TECHNISCHE UNIVERSITÄT MÜNCHEN
TUM School of Natural Sciences

Collisionless Dark Matter in Cosmology

Vlasov Perturbation Theory for Large-Scale Structure Formation with Dark Matter Velocity Dispersion and Higher Cumulants

Dominik Laxhuber

Vollständiger Abdruck der von der TUM School of Natural Sciences der Technischen Universität München zur Erlangung eines

Doktors der Naturwissenschaften (Dr. rer. nat.)

genehmigten Dissertation.

Vorsitz:		Prof. Dr. Sherry Suyu
Prüfer der Dissertation:	1.	Priv.-Doz. Dr. Mathias Garny
	2.	Prof. Dr. Björn Garbrecht

Die Dissertation wurde am 21.08.2023 bei der Technischen Universität München eingereicht und durch die TUM School of Natural Sciences am 12.09.2023 angenommen.

Abstract

This thesis explores an extension of the Standard Perturbation Theory (SPT) used in cosmic structure formation. The extension, called Vlasov Perturbation Theory or VPT, incorporates higher cumulants generated by the crossing of particle orbits. VPT offers a deterministic approach that addresses issues with SPT, such as the backreaction of small-scale modes on larger scales. The thesis derives both linear and nonlinear solutions of VPT, illustrating the clustering of collisionless dark matter with velocity dispersion and higher-order cumulants. The results show that VPT can be formulated similarly to SPT, but with additional perturbation variables and nonlinear interactions. Importantly, the nonlinear kernels of VPT exhibit a decoupling property that suppresses individual momenta after crossing the dispersion scale into the nonlinear regime. This property allows for the computation of nonlinear corrections to power spectra, even for cosmologies with highly blue power-law input spectra. The comparison of results to N-body simulations demonstrates good agreement up to the nonlinear scale. The thesis also explores the generation of vorticity and its role in maintaining momentum conservation. The correct scaling of the vorticity power spectrum at the two-loop order is verified. Additionally, the thesis applies the VPT framework to compute a stochastic background of gravitational waves generated by nonlinear velocity dispersion. Overall, the findings of this thesis suggest that our understanding of collisionless dynamics can lead to systematic improvements in techniques for studying dark matter clustering.

Zusammenfassung

Diese Dissertation untersucht die Erweiterung der Standard Störungstheorie (SPT), die in der kosmischen Strukturbildung verwendet wird. Diese Erweiterung, namens Vlasov Störungstheorie oder VPT, bezieht höhere Kumulanten ein, die durch das Durchqueren von Teilchenbahnen entstehen. VPT bietet einen deterministischen Ansatz, der die Entkopplung von kleinskaligen Moden berücksichtigt und Probleme von SPT angeht, wie zum Beispiel die starken Auswirkungen kleinskaliger Moden auf größere Skalen. Dies berücksichtigt beispielsweise die Bildung von Dunkler Materie Halos, die sich von der kosmische Expansion entkoppeln. In der Dissertation werden lineare und nichtlineare Lösungen von VPT hergeleitet, die das Clustern von kollisionsfreier Dunkler Materie mit Geschwindigkeitsdispersion und höheren Kumulanten darstellen. Die Ergebnisse zeigen, dass VPT ähnlich wie SPT formuliert werden kann, jedoch mit zusätzlichen Störungsvariablen und nichtlinearen Wechselwirkungen. Am wichtigsten ist, dass die nichtlinearen Kernels von VPT eine Entkopplungseigenschaft aufweisen, die verhindert, dass Moden bis über die Dispersionsgrenze hinaus anwachsen und in den nichtlinearen Bereich gelangen. Diese Eigenschaft ermöglicht die Berechnung nichtlinearer Korrekturen zu Leistungsspektren, selbst für Kosmologien mit stark blauen Potenzgesetzen. Die Ergebnisse werden mit N-Body-Simulationen verglichen und zeigen eine gute Übereinstimmung bis zur nichtlinearen Skala. Die Dissertation untersucht auch die Erzeugung von Vortizität und ihre Rolle bei der Aufrechterhaltung der Impulserhaltung. Die korrekte Skalierung des Vortizitätleistungsspektrums in der zweiten nicht-trivialen Ordnung wird verifiziert. Darüber hinaus wird die VPT-Methode verwendet, um einen stochastischen Hintergrund von Gravitationswellen zu berechnen, der durch nichtlineare Geschwindigkeitsdispersion erzeugt wird. Insgesamt legen die Ergebnisse der Dissertation nahe, dass durch ein physikalisches Verständnis der kollisionsfreien Dynamiken die Techniken zur Clusterbildung der Dunklen Materie systematisch verbessert werden können.

Preface

This thesis focuses on the theoretical modeling of cosmological observables. It is the outcome of research conducted during my tenure as a Ph.D. candidate at the Physics Department of the Technical University of Munich from 2020 to 2023. The thesis aims to contextualize our findings for non-experts. To achieve this, the initial three chapters offer an introductory overview of physical cosmology, particularly emphasizing the modeling of the universe's large-scale structure. The subsequent chapters delve into the primary results of the papers listed below.

In embarking on this academic journey, I am humbled to present this thesis as the culmination of years of research, exploration, and dedicated effort. I am immensely thankful for the support I have received along the way. First and foremost, I want to express my gratitude to my advisor, Mathias Garny, for his unwavering guidance, patience, and expertise that have been instrumental in shaping the direction of this research. His supervision has been pivotal in molding my academic growth and instilling the pursuit of excellence in me. His passion for physics serves as a remarkable example to me.

I would like to extend a special acknowledgment to my uncle, Ludwig Laxhuber who not only played a crucial role in shaping my academic journey but also served as an exceptional mentor throughout the course of my Ph.D. thesis. His innovative insights and unwavering support, extending beyond academic matters, have proven invaluable. I am deeply grateful for the privilege of gaining from his wisdom and expertise, which have broadened my horizons and equipped me to tackle upcoming challenges.

I am profoundly grateful to my family, in particular to my parents Udo and Gudrun, as this achievement would not have been attainable without them. Their unconditional love and support have been the cornerstone of my achievements. Their sacrifices and encouragement have been a constant source of motivation. Finally, I am incredibly grateful to my significant other, Nina, for her persistent patience, understanding, and everlasting support during the challenging phases of this endeavor. Her presence has provided me with solace and encouragement, reminding me of the importance of maintaining a work-life balance, a feeling that frequently brightened my mood.

Dominik Laxhuber
August, 2023

List of publications

[1] M. Garny, D. Laxhuber and R. Scoccimarro, *Perturbation theory with dispersion and higher cumulants: Framework and linear theory*, *Phys. Rev. D* **107** (2023) 063539 [2210.08088].

[2] M. Garny, D. Laxhuber and R. Scoccimarro, *Perturbation theory with dispersion and higher cumulants: Nonlinear regime*, *Phys. Rev. D* **107** (2023) 063540 [2210.08089].

Contents

1 Introduction

Cosmology is the scientific study of how the universe began, what it is made of, and how it evolved to its current state. It therefore deals with some of the most fundamental questions of existence. As a field of scientific inquiry, it is relatively youthful, potentially tracing its origins back just a century [1]. Its inception is closely linked to Einstein's formulation of General Relativity (GR) [2] as well as Hubble's discovery of an expanding universe [3]. This coincided with advancements in telescope technology that facilitated investigations extending beyond our Milky Way galaxy, revealing the broader cosmic picture through innovative concepts and tools [4, 5]. Presently, cosmology has evolved into a widespread and industrious scientific pursuit, engaging a global community of over a thousand astronomers and physicists. Formerly characterized by uncertainties predominantly residing in the exponents, the field of cosmology was once marked by a dearth of data [5]. However, in the current landscape, precision cosmology has materialized, showcasing cosmology as a prime exemplar of data-rich science [6]. Impressively, these strides have empowered us to offer well-informed responses to the queries mentioned above, yet a number of significant puzzles still await resolution.

Cosmology's observational journey encompasses various probes, including the Cosmic Microwave Background (CMB) anisotropies first measured by COBE [7], light element abundance measurements [8], and Type Ia Supernovae distance measurements, where the latter have unveiled a remarkable observation: the universe is undergoing an acceleration in its expansion, pointing towards the presence of an enigmatic entity called dark energy [9, 10]. These make the hot Big Bang model as state-of-the-art science for the origin and evolution of the universe. Probing the universe's large-scale structure (LSS) is a significant endeavor in precision cosmology today. Over billions of years, structures formed from tiny fluctuations in the early universe due to gravitational collapse, offering vital insights into fundamental physics. Redshift surveys measure the angular position of and distance to objects like galaxies and galaxy clusters, initiated with measurements of thousands and eventually expanded to encompass hundreds of thousands of galaxies [11, 12], confirming theoretic expactions of the largest patterns of the universe [13].

The recent gravitational wave (GW) detection and the James Webb Space Telescope provide novel insights into cosmic and early galaxy evolution [14–17]. In addition, the brand-new discovery of a possible GW background by the NANOGrav collaboration provides a step forward to see past the last scattering surface of the CMB of the very early universe [18, 19]. The ΛCDM model, the prevailing concordant model, describes the universe a fraction of a second after its origin until today, 13.8 billion years later [20–22], backed by consistent data, yet fundamental challenges remain: about dark components, inflation, and matter-antimatter asymmetry. Ongoing and future probes promise novel insights into these enigmas, exploring dark matter, gravity, dark energy, inflation, and neutrino mass [23–28].

In the last decade, significant progress has been made in surveying the universe to achieve precision cosmology. It began with surveys like the 6dF Galaxy Redshift Survey (6dFGRS) [29] and the WiggleZ Dark Energy Survey [30], which provided valuable data for precision cosmology.

The Baryon Oscillation Spectroscopic Survey (BOSS) [31], one of the projects within the Sloan Digital Sky Survey-III (SDSS-III) [32], followed and measured the Baryon Acoustic Oscillation (BAO) scale at an accuracy of about 1% [33]. BAOs refer to regularly spaced fluctuations in the distribution of galaxies and matter in the universe, resulting from sound waves that traveled in the early universe and left an imprint on the large-scale structure which helps us to understand its expansion history. In the latest phase of the SDSS [12], the enhanced Baryon Oscillation Spectroscopic Survey (eBOSS) [34], significantly increased the number of objects and redshifts at which BAO and redshift space distortions (RSD) were measured. RSD refers to the apparent distortion of the distribution of galaxies caused by their peculiar velocities along the line of sight, distinct from their recession velocity due to cosmic expansion. Building on these achievements, ongoing and near-future surveys such as the Dark Energy Spectroscopic Instrument (DESI) [35], Euclid [36], the Vera Rubin Observatory [25], the Prime Focus Spectrograph (PFS) [28], SPHEREx [24], and the Nancy Grace Roman Space Telescope [27] are expected to provide unprecedented maps of the structure of the universe.

In addition to galaxy surveys, there are photometric surveys like the Kilo-Degree Survey (KiDS) [37], and the Dark Energy Survey (DES) [38] that contribute to cosmology. These surveys measure galaxy shear, which is the distortion of images of distant sources caused by gravitational lensing from massive structures. This allows to probe the dark matter structures of the universe and determine relative distances between objects, providing insights into the expansion history of the universe. Another method to study LSS is through the Lyman-α forest, which consists of absorption lines in light from distant quasars caused by the Lyman-α transition in natural hydrogen. The position and depth of these absorption features provide information about the position (redshift) and amount of hydrogen, which traces the underlying dark matter distribution. The BOSS and eBOSS surveys have observed the BAO feature in the Lyman-α forest by studying hundreds of thousands of quasars [39].

Why invest extensively in probing LSS when CMB measurements have precisely constrained ΛCDM parameters [40, 41], with upcoming CMB Stage IV improvements [42]? LSS offers independent modes beyond CMB due to mode limitations. The available LSS modes grow with the third power of the maximum wavenumber (smallest scale) up to which data can be reliably analyzed, which significantly exceeds the CMB modes as LSS utilizes galaxy distribution. This yields numerous additional modes as survey volumes and k_{max} expand. Further, LSS surveys are tomographic, capturing multi-redshift structure, unlike fixed CMB redshift, and they probe the vacuum energy-dominated universe era, enhancing dark energy insights.

To extract meaningful insights from cosmological investigations, robust theoretical predictions are crucial. The hierarchical model of structure formation, driven by cold dark matter (CDM) and gravity, involves smaller scales collapsing first, followed by larger ones. While LSS observables offer richer information than the CMB, their extraction is complex due to gravitational collapse and dark matter dominance. Perturbative methods are key to unraveling LSS evolution, particularly for CDM clustering, emerging for quasi-linear fluctuations on large scales, and requiring simulations or empirical models for nonlinear scales [43]. These models have been effective in analyzing BOSS galaxy clustering data [44, 45], accounting for next-to-leading order (NLO) and two-loop (NNLO) corrections for precision, although they entail simplifications like neglecting relativistic effects and treating baryons as dark matter. While these approximations suffice at the few percent level, anticipated (sub-)percent precision of future LSS surveys necessitates further scrutiny, especially for mildly nonlinear scales ($k \simeq 0.1 - 0.3\,h\,\mathrm{Mpc}^{-1}$) with small fluctuations enabling perturbative expansion. Understanding gravitational clustering's dynamics in cosmology hinges on perturbative techniques, particularly in the context of CDM

clustering. Our exploration is grounded in the Vlasov equation, which describes the evolution of the CDM phase-space distribution function (DF) coupled to gravity via the Poisson equation for scales below the Hubble radius. Standard perturbation theory (SPT) provides a useful approximation, but it is limited by the neglect of higher cumulants of the DF.

To accurately describe the nonlinear regime, the Vlasov-Poisson equation in 3+3 dimensional phase space is used. However, it is challenging to solve this equation numerically [46]. As an alternative, N-body simulations are employed, where the phase-space distribution is represented by a number of artificial test particles. These particles follow Newtonian equations of motion in the gravitational potential and their density distribution is used to obtain the matter density. The simulation parameters, such as box size, number of particles, and treatment of close encounters, depend on the scales and resolution required for the simulation. From N-body simulations, it is observed that nonlinear overdensities form bound gravitational halos, which can be arranged in filaments, sheets, and separated by voids, forming the cosmic web in agreement with the observed galaxy distribution. Small halos merge into larger ones over time.

A key motivation for this thesis stems from the discrepancies observed in simulations and SPT predictions. Simulations have indicated that nonlinear growth is suppressed for initial conditions with blue spectra, assuming a power-law initial spectrum $P_0 \sim k^{n_s}$, contrasting the behavior for red or CDM-like spectra [47]. This discrepancy becomes more pronounced for bluer spectra (larger n_s), exposing the limitations of SPT which exhibits UV (small-scale) divergences for spectral indices $n_s \geq -1$ [48, 49]. Furthermore, the challenge of understanding how nonlinear modes decouple from large-scale quasilinear modes arises [50, 51], especially considering the formation of stable objects like dark matter halos. The conventional SPT approach does not account for this decoupling. Groups of galaxies appear elongated along the line of sight due to their random motions within these groups, blurring their appearance and affecting our measurements of distances and positions. This "fingers-of-god" effect is known to be highly sensitive to velocity dispersion and higher moments of the velocity distribution [52]. Additionally, in the nonlinear regime, the vector part of the dark matter velocity flow (related to vorticity) becomes relevant, with vorticity being generated by nonlinear processes [53].

Recent efforts involving effective field theory (EFT) [54, 55] have tried to bridge the gap between SPT and simulations by introducing counter-terms derived from a derivative expansion of the stress tensor that would be absent in SPT and appears in the Euler equation, however is still only valid at large scales. While EFT offers a way to improve predictions, it relies on a large set of free parameters and lacks physical insight into the decoupling of UV modes and the underlying dynamics driving it. This motivates one to develop a predictive framework within perturbation theory which is able to describe the decoupling of UV modes that improves over SPT without the need of additional free parameters.

The Vlasov equation introduces the concept of orbit crossing, where higher cumulants of the DF beyond density and velocity fields become significant, giving rise to the Vlasov hierarchy [53]. Our approach involves expanding the equations of motion about a new linear theory that considers these cumulants, leading to what we term Vlasov Perturbation Theory or VPT, see Fig. 1.1. Linearized solutions derived in VPT offer richer insights compared to SPT, particularly regarding the backreaction of orbit crossing on linear modes. Furthermore, we delve into the realm of nonlinear solutions within the VPT framework. We demonstrate that VPT can be expressed in a manner analogous to SPT but with added variables, nonlinear interactions, and a more intricate propagation. This formalism is derived from the Vlasov-Poisson equation, offering a more systematic approach to perturbation theory that captures the decoupling of UV modes. In the nonlinear regime, the screening of UV modes mirrors the physical behavior, particularly in

the context of stable dark matter halos. In the case of CDM spectra, this phase is marked by the "virial turnover", where nonlinear power grows with wavenumber slower compared to the weakly nonlinear phase. The stable clustering concept [56–58] partially explains this phenomenon, attributing it to pairwise velocities that counteract the Hubble flow. Our investigations extend beyond theory; we compare our predictions with N-body simulations for various statistics, confirming the validity of our approach. Prior research on corrections to SPT stemming from the Vlasov equation has paved the way for our work, but VPT consolidates these insights into a comprehensive framework. Our main objective is to enhance the accuracy of perturbative techniques for understanding large-scale structure formation, leveraging the inherent collisionless dynamics of the universe to refine our predictions.

The focus in this thesis is to enhance perturbative methods within gravitational clustering using collisionless dynamics. This extends prior Vlasov hierarchy exploration truncated at the second cumulant, addressing large-scale mode corrections via a low-k expansion [59] and systematic methods [60, 61], with the latter addressing nonlinear background dispersion evolution while maintaining linear fluctuations. For instance, [53] derives the equation of motion for the Vlasov cumulant generating function hierarchy, aligning with post-shell-crossing Vlasov solutions. They close the hierarchy using stress tensor measurements and assess shell-crossing's backreaction on density and velocity divergence power spectra, including vorticity growth. Furthermore, Lagrangian perturbation theory (LPT) has investigated velocity dispersion growth and shell-crossing [62–74], including incorporation into dark matter halos [75–79]. Particular Lagrangian approaches compute vorticity growth from velocity dispersion in [68, 71]. Complementary insights from collisionless dynamics arise from numerical phase-space distribution tracking [46, 80–87] and Schrödinger equation modeling [88–97], with various strategies to close the Vlasov hierarchy presented in [92].

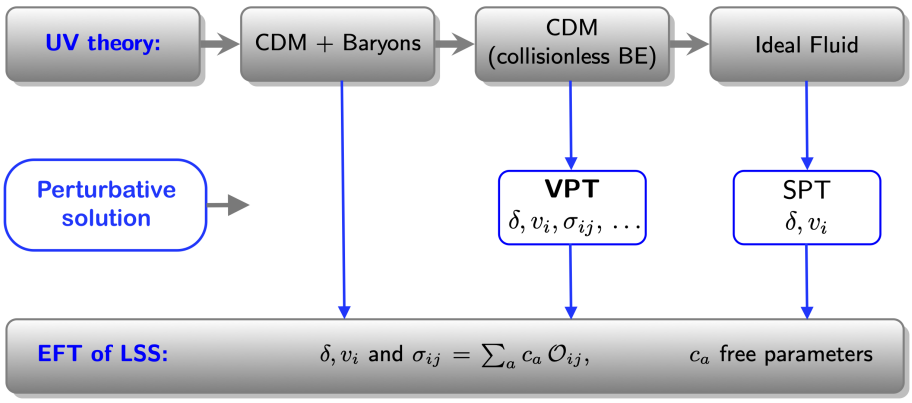

Figure 1.1: In this thesis, the VPT framework was developed to study structure formation at UV (small) scales. We computed power- and bispectra, analogously as in SPT, using the evolution equations of variables δ, v_i, $\sigma_{ij}, \ldots$, being density, velocity vector, and velocity dispersion tensor as well as higher cumulants. The VPT framework provides a complementary description of structure formation, taking into account higher cumulants of the dark matter distribution function. We offer a comprehensive investigation of the "complete" UV theory for cold dark matter (CDM), while simpler models, based on the ideal fluid approximation, have been extensively studied in the existing literature. The effective field theory approach for large-scale structure (EFTofLSS) provides a further means in this direction but involves additional parameters that require empirical determination and have no physical insight.

Outline of the thesis

This thesis is structured as follows: To begin, the basis is laid in Chapter 2, offering a concise introduction and overview of the fundamentals of physical cosmology. We outline the expanding universe as homogeneous and isotropic, overlaid with density fluctuations. Given the thesis' emphasis on large-scale structure formation, Chapter 3 is dedicated to describing cosmological perturbation theory in the context of an ideal fluid framework, known as Standard Perturbation Theory or SPT.

We proceed in Chapter 4 by introducing an extended framework of cosmological perturbation theory for large-scale structure, dubbed Vlasov Perturbation Theory (VPT), exploring the cumulant generating function and Vlasov dynamics. We derive the extension of SPT by considering the second cumulant in Section 4.1, which encompasses the velocity dispersion tensor. Appendices A to C provide comprehensive equations of motion and vertex results. We also discuss the extension of the framework to higher cumulants in Section 4.2 and include corresponding vertices in Appendix D. Comparisons to a collisional fluid with viscosity are discussed. In Chapter 5, we derive coupled equations up to arbitrary cumulant orders within the linear approximation, ensuring stability through analytical conditions. Applying the formalism to a scaling universe in Chapter 6, we attain self-consistent solutions for cumulant expectation values (up to the eighth cumulant) and discuss truncation order effects. The outcomes up to this point have been discussed in **Paper I** [98].

In Chapter 7, we introduce nonlinear kernels, investigating their scaling in the small wavenumber limit compared to the dispersion scale. Additionally, we numerically study cases where wavenumbers cross the dispersion scale, highlighting UV mode screening. The properties of these kernels, especially symmetry properties, are thoroughly explored for various cumulant hierarchy truncations. In Chapter 8, we delve into vorticity generation and vector/tensor modes of the velocity dispersion tensor. Comparisons of VPT predictions to simulation measurements are presented in Chapter 9, encompassing density power spectrum, bispectrum, velocity divergence power spectrum, cross-spectrum between density and velocity divergence, and vorticity power spectrum. Finally, in Chapter 10, we showcase an applied computation, specifically the generation of a stochastic gravitational wave background due to nonlinear velocity dispersion. The subsequent findings were detailed in **Paper II** [99], except for the final chapter.

For the sake of convenience, we have compiled the key variables of VPT in Table 1.1 below, providing concise descriptions and references to their corresponding equations. This table serves as a valuable reference for tracking various quantities while navigating through the text.

Notation

We work in natural units where the speed of light c, the Planck constant $\hbar$ as well as the Boltzmann constant k_B is set to unity. We adopt the metric signature $(-,+,+,+)$ and use Greek letters like $\mu = \{0,1,2,3\}$ for spacetime indices, while Latin indices indicate conventional summations starting from 1. We adhere to Einstein's summation convention. Bold letters like $\boldsymbol{q}$ represent three-dimensional vectors, and their magnitudes are denoted by italics, $|\boldsymbol{q}| = q$. The Dirac delta function is denoted as δ_D, and the Kronecker delta function is δ^K. Lastly, we adhere to the following convention for the three-dimensional Fourier transform:

$$\tilde{f}(\boldsymbol{k}) = \int \frac{\mathrm{d}^3x}{(2\pi)^3}\, e^{-\mathrm{i}\,\boldsymbol{k}\cdot\boldsymbol{x}}\, f(\boldsymbol{x})\,, \quad f(\boldsymbol{x}) = \int \mathrm{d}^3k\, e^{\mathrm{i}\,\boldsymbol{k}\cdot\boldsymbol{x}}\, \tilde{f}(\boldsymbol{k})\,. \tag{1.1}$$

Table 1.1: Provided below is a concise overview of the essential variables within the VPT framework. In the first column (from the left), we present the corresponding symbol along with a brief description. The third and fourth columns reference the equations where these symbols and their equations of motion are defined, respectively. For the sake of brevity, the argument is occasionally omitted; however, each quantity is time and wavenumber dependent. Furthermore, the symbols in the first category do also depend on the external parameter $\boldsymbol{L}$. The application of a Taylor expansion in $\boldsymbol{L}$ results in the subsequent block of expressions for the symbols. It is important to note that each cumulant order n has been rescaled by the time-dependent factor $(-\mathcal{H}f)^n$ (as indicated in Eq. 4.10).

Variable	Description	Definition	Equation of motion
$\widetilde{\mathcal{C}}$	cumulant generating function	Eqs. (4.3, 4.86), see also Eq. (4.93)	Eq. (4.90)
$\mathcal{E}(\eta, L^2)$	ensemble average of $\widetilde{\mathcal{C}}$	Eq. (4.91), see also Eq. (4.94)	Eq. (4.92)
$Q_{\mathcal{E}}(\eta, L^2)$	source term for $\mathcal{E}$	Eq. (4.92, 5.7)	-
$\delta\widetilde{\mathcal{C}}$	perturbation of $\widetilde{\mathcal{C}}$	Eq. (4.100)	Eq. (4.101)
$\mathcal{C}_\ell$	multipole decomposition of $\delta\widetilde{\mathcal{C}}$	Eqs. (5.1, 5.3)	Eq. (5.5) (linear)
$\widetilde{\mathcal{C}}_{i_1,\ldots,i_n}$	**n^{th} cumulant**	Eqs. (4.87, 4.88)	-
$\mathcal{E}_{2n}(\eta)$	background value of $2n^{\text{th}}$ (even) cumulant	Eqs. (4.95)	Eqs. (5.17, 5.23) (linear)
$Q_{\mathcal{E}_{2n}}(\eta)$	source term for $\mathcal{E}_{2n}$	Eq. (5.18)	-
$\mathcal{C}_{\ell,2n}$	transfer functions up to cumulant order $\ell + 2n$	Eqs. (5.9, 5.21)	Eqs. (5.13, 5.22) (linear)
$\ln(1+\delta)$	**0^{th} cumulant** (density contrast)	Eq. (3.3)	Eqs. (4.11, 4.44)
u_i	**1^{st} cumulant** (peculiar velocity)	Eq. (3.4)	Eq. (4.12)
θ	velocity divergence (scalar mode of u_i)	Eq. (3.23)	Eqs. (4.18, 4.45)
w_i	vorticity (vector mode of u_i)	Eq. (3.23)	Eqs. (4.22, A.4)
ϵ_{ij}	**2^{nd} cumulant** (velocity dispersion)	Eq. (3.7)	Eq. (4.13)
$\epsilon(\eta)$	background value of ϵ_{ij}	Eq. (4.14)	Eq. (4.15)
$Q(\eta)$	source term for $\epsilon(\eta)$	Eqs. (4.16, 4.105)	-
$\delta\epsilon$, g	scalar modes of ϵ_{ij}	Eq. (4.26)	Eqs. (4.34, A.5, A.6)
ν_i	vector modes of ϵ_{ij}	Eq. (4.27)	Eqs. (4.39, A.7)
t_{ij}	tensor modes of ϵ_{ij}	Eq. (4.28)	Eqs. (4.39, A.8)
π_{ijk}	**3^{rd} cumulant**	Eq. (4.87)	Eq. (4.102)
π, χ	scalar modes of π_{ijk}	Eq. (4.106)	Eq. (4.107) (linear)
Λ_{ijkl}	**4^{th} cumulant**	Eq. (4.87)	Eq. (4.103)
$\omega(\eta)$	background value of Λ_{ijkl}	Eq. (4.89)	Eq. (4.105)
$Q_\omega(\eta)$	source term for $\omega(\eta)$	Eqs. (4.99, 4.105)	-
κ, ξ, ζ	scalar modes of Λ_{ijkl}	Eq. (4.106)	Eq. (4.107) (linear)

2 Foundations of modern cosmology

Cosmology deals with the origin and evolution of the universe along its constituents. Einstein's discovery of general relativity in 1915 enabled us, for the first time in history, to establish a testable theory of the entire universe [2]. Together with the discovery of the expansion of the universe by Edwin Hubble in 1929 [3] a compelling *Big Bang model* eventually emerged as the leading theory of physical cosmology. It combines fundamental physics with our understanding of the conditions of the early universe. Remarkably, the abundance of light elements as well as the existence of the cosmic microwave background radiation was confirmed by observations, providing firm evidence of the model [100, 101]. In this chapter, we present a brief overview of the concordance model of cosmology and focus on the physics relevant for this thesis. It is by far not complete, a more pedagogical introduction on cosmology can be found in [1, 4, 20–22, 102, 103]. In Sec. 2.1 we review an expanding space and the homogeneous evolution of all the constituents of the universe. Then in Sec. 2.2 we give a brief overview of the most important events within cosmological evolution, starting from the Big Bang all the way to the present state. Finally, we discuss the inhomogeneous universe consisting of rich structures in more detail in Sec. 2.3, including observables such as the power spectrum and the CMB temperature anisotropies.

2.1 Expanding universe

The concordance model of cosmology is based on two pillars: general relativity and the *cosmological principle*. GR is a theory of gravity that describes how mass and energy warps the fabric of spacetime, influencing the motion of objects and the geometry of the universe. This behaviour is described by the Einstein field equations [2]

$$G_{\mu\nu} = 8\pi G\, T_{\mu\nu}\,, \tag{2.1}$$

with G being Newton's gravitational constant. The Einstein tensor $G_{\mu\nu}$ contains the information on spacetime while the stress-energy-momentum tensor $T_{\mu\nu}$ represents the density and flux of energy and momentum at each point in spacetime. The Einstein tensor can be written in terms of the *metric tensor* $g_{\mu\nu}$ relating observer-dependent coordinates x^μ to the invariant line element via $\mathrm{d}s^2 = g_{\mu\nu}\mathrm{d}x^\mu \mathrm{d}x^\nu$.

The cosmological principle states that the universe is *homogeneous* and *isotropic* on large scales, with no preferred locations or directions. The most general metric describing a spacetime compatible with the cosmological principle is the *Friedmann-Lemaître-Robertson-Walker* (FLRW) metric, given by the following line element [104–107]:

$$\mathrm{d}s^2 = -\mathrm{d}t^2 + a^2(t)\left[\frac{\mathrm{d}r^2}{1-Kr^2} + r^2\left(\mathrm{d}\theta^2 + \sin^2\theta\,\mathrm{d}\phi^2\right)\right]. \tag{2.2}$$

The expansion of space is quantified by the scale factor a, which only depends on physical time t and whose present value is set to unity by convention. Thus, it characterizes the relative size of the universe at any instant of time. r, θ and ϕ are *comoving* spherical coordinates. Note that in an expanding space the comoving distance between two objects at rest is constant while their physical distance evolves with time and is proportional to a. Finally, K describes the curvature of a three-dimensional spatial slice of the universe. It is therefore related to the geometry of the universe and manifests itself when following two parallel particle trajectories. Their paths could stay parallel forever corresponding to a *flat* or Euclidean universe ($K = 0$). In an open ($K = -1$) or closed ($K = 1$) universe the trajectories eventually start to diverge or converge, respectively.

The expansion of space itself affects radiation which propagates therein. Thus, the physical wavelength of light emitted from a distant object is stretched out proportionally to the scale factor. Therefore the observed wavelength is larger than the one at which light was emitted. This stretching factor is quantified by the *redshift* z via

$$1 + z \equiv \frac{\lambda_{\text{obs}}}{\lambda_{\text{emit}}} = \frac{a_{\text{obs}}}{a_{\text{emit}}} = \frac{1}{a_{\text{emit}}} \,. \tag{2.3}$$

This implies for observers today $1 + z = 1/a$. The evolution of the scale factor a with cosmic time t is crucial to understand the history of the universe. In fact, this evolution depends on the energy content of the universe, whose connection to a is provided by general relativity. This suggests that apart from physical time t we have in addition the scale factor a as well as the redshift z as a measure of cosmological time-evolution. There exists a critical energy density, denoted as ρ_{cr}, that, when taken as the energy content of the universe, precisely corresponds to a flat geometry of the universe. If the actual energy density is lower or higher than ρ_{cr} the universe is open or closed, respectively. Usually, the change in the scale factor and its relation to energy is quantified by the *Hubble rate*

$$H(t) \equiv \frac{1}{a}\frac{\mathrm{d}a}{\mathrm{d}t} \,, \tag{2.4}$$

which measures the speed of expansion of the universe. The expansion rate today, $H(t_0) \equiv H_0$ defines the *Hubble constant*:

$$H_0 = (67.66 \pm 0.42)\,\mathrm{km\,s^{-1}Mpc^{-1}} \,, \tag{2.5}$$

with the quoted value being the measurement (68 % C.L.) from the Planck CMB experiment [41]. The astronomical length scale of a megaparsec (Mpc) is equal to 3.0856×10^{19} km. The Hubble constant is also often written as $H_0 = 100\,h\,\mathrm{km\,s^{-1}Mpc^{-1}}$ moving the uncertainty to the reduced Hubble constant h. For this reason, it is convenient to use $h^{-1}\,\mathrm{Mpc}$ as the unit of length in cosmology. With this unit, the Hubble constant drops out of many computations, such that they become insensitive to its precise value in light of current controversial discussions [108]. We follow this convention throughout the thesis. The stress-energy-momentum tensor compatible with homogeneity and isotropy on large scales is that of a perfect fluid, given in the rest frame as

$$T^{\mu}{}_{\nu} = \mathrm{diag}\left[-\rho(t), P(t), P(t), P(t)\right] \,, \tag{2.6}$$

where ρ is the energy density and P is the pressure of the perfect fluid. Both depend on time only to respect homogeneity. Therefore, there is a relationship between the evolution of energy density and pressure and the scale factor or rather Hubble rate, which can be obtained by

inserting the metric Eq. (2.2) and the time-time component of the source term Eq. (2.6) into the Einstein equation Eq. (2.1) yielding the first *Friedmann equation* [4]

$$H^2(t) = \frac{8\pi G}{3}\left[\rho(t) + \frac{\rho_{\rm cr} - \rho(t_0)}{a^2(t)}\right], \tag{2.7}$$

where $\rho(t_0)$ is the energy density today and $\rho_{\rm cr} = 3H_0^2/(8\pi G)$ is the aforementioned *critical density*, which with Eq. (2.5) turns out to be tiny, $\rho_{\rm cr} = 1.88\,h^2 \times 10^{-29}\,\mathrm{g\,cm^{-3}}$. The second term in the square brackets corresponds to the case when today the total energy density of the universe does not adopt the critical value, which implies nonzero curvature which is related to the parameter K, as given in the metric Eq. (2.2). Note that this geometric contribution scales with a^{-2}. The space-space component of Eq. (2.6) yields the second Friedmann equation involving the pressure which is of no importance for our purposes and we do not show it. The generalized energy-momentum conservation equation within general relativity is $\nabla_\nu T^\mu{}_\nu = 0$. For the perfect fluid, the zeroth component of this equation yields an equation for the conservation of energy density,

$$\frac{\mathrm{d}\rho}{\mathrm{d}t} + 3H(\rho + P) = 0\,. \tag{2.8}$$

In fact, ρ and P are the total energy density and pressure of all constituents of the universe: (cold) dark matter, baryons, photons, neutrinos, and dark energy. The former is a type of matter that does not emit, absorb, or reflect light, making it invisible to traditional observations. It is inferred to exist due to its gravitational effects on visible matter and its role in shaping the large-scale structure of the universe. Despite its significance in the cosmos, the nature and composition of dark matter remain a major unsolved mystery in astrophysics, see the following reviews for possible candidates and methods of detection [109–111]. In cosmology, "baryons" refer to nuclei and electrons. Unlike dark matter, dark energy does not cluster around galaxies or structures; instead, it exerts a repulsive force that counteracts gravity on large scales. The nature of dark energy is still only purely understood.

So, we have *radiation* (photons and ultra-relativistic neutrinos in the early universe) and *matter* (baryons and non-baryonic dark matter as well as nonrelativistic neutrinos in the late universe) constituents while a *dark energy* component provides a further constituent. We will see in a bit that the division into those three categories is sufficient to track the background evolution of the universe.

Cosmological evolution

We now assume a certain equation of state for each species s given by $P_s = w_s\rho_s$ with *equation of state* parameter w_s. Inserting this relation into the conservation equation Eq. (2.8) one directly obtains the dependence of the energy density on the scale factor as

$$\rho_s \propto a^{-3(1+w_s)}\,, \tag{2.9}$$

which implies that the evolution of the energy density evolves differently for a given species. Note that the energy density entering the Friedmann equation is the sum over each individual energy density, thus it is important to know the dependence for each component. Consider first *nonrelativistic matter* whose energy content is dominated by its rest mass and over the course of cosmological expansion its density dilutes with the volume expansion. The corresponding pressure is then much less than the energy density, so we have $w \to 0$ implying a scaling $\rho \propto a^{-3}$.

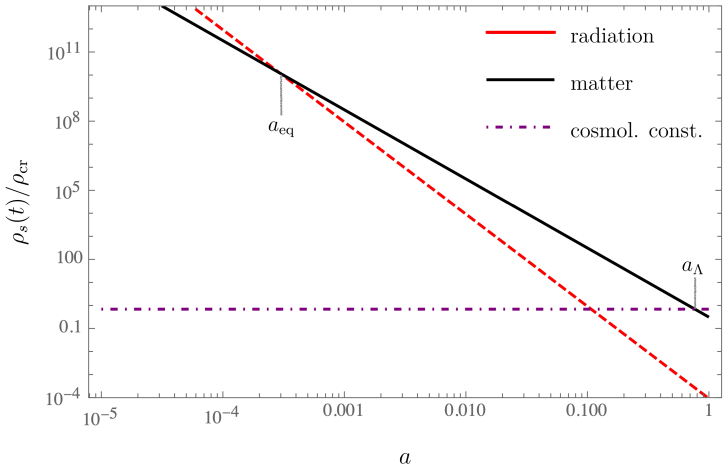

Figure 2.1: Energy density varies with the scale factor across various components of the Euclidean cosmology, characterized by parameters specified in Eq. (2.18). These components include nonrelativistic matter ($\propto a^{-3}$), radiation ($\propto a^{-4}$), and a cosmological constant ($\propto a^{0}$), all measured in terms of the current critical density. While matter and the cosmological constant seem dominant in the present era, it is worth noting that during early times, radiation density held the highest significance. The point in time when matter and radiation energy densities become equal is referred to as a_{eq} and the juncture at which matter and cosmological constant densities reach equality is termed as a_Λ and occured rather recently.

Apart from matter, a sea of massless (relativistic) particles, in particular photons, permeates the universe, as first discovered in 1965 [112]. These photons have traveled freely since the universe was very young and constitute the so-called *cosmic microwave background radiation* (CMB). As for the matter, their number density gets diluted with the volume expansion. In addition, their wavelength get stretched during propagation as $\lambda = c/\nu \propto a$ (or equivalently their frequency ν decays as $1/a$) which for CMB photons lies in the microwave regime today. In total, the energy density decays as $\rho \propto a^{-4}$ with the expansion, which implies for the equation of state parameter $w = 1/3$[1]. The CMB has a perfect black-body spectrum whose energy density scales with temperature as $\rho \propto T^4$. Therefore the temperature of radiation as a function of time is given by $T(t) = T_0/a(t)$, with a very well-measured temperature of $T_0 = (2.7255 \pm 0.0006)\,\mathrm{K}$ today [113]. This tells us that radiation decays with cosmological expansion more strongly than any matter component.

Moreover, the current energy budget of the universe is dominated by a further unknown component, dubbed dark energy. The most favourable model is that of a *cosmological constant* Λ corresponding to a constant energy density $\rho \propto a^0$ or equivalently $w = -1$. Due to its constant energy density Λ affects cosmological evolution at late times, i.e. today and is supposed to drive the *accelerated expansion* of the universe which only started "recently" [9, 10]. Einstein's equations allow for an additional term that can be related to the cosmological constant. Therefore, the origin of dark energy could equivalently arise from a modified theory of gravity. We refer to Refs. [114–117] for discussions of dark energy and modified gravity in the context of cosmology. In total we have three different scalings, given by

[1] This value can equivalently be derived from quantum statistics calculating the radiation pressure of a relativistic gas of photons.

$$\rho \propto \begin{cases} a^{-4} & \text{for radiation } (w = 1/3)\,, \\ a^{-3} & \text{for matter } (w = 0)\,, \\ a^{0} & \text{cosmological constant } (w = -1)\,. \end{cases} \tag{2.10}$$

The scaling laws indicate that different components dominate the universe's energy content at different cosmic epochs, as shown in Fig. 2.1. During the early radiation-dominated era, when the scale factor is small, radiation prevails as the dominant energy density. As the universe expands, radiation dilutes faster than matter, resulting in a point called *matter-radiation equality* when their energy densities become equal corresponding to a redshift of about $z_{\rm eq} \simeq 3400$. Subsequently, during the matter-dominated era, dark energy eventually becomes dominant at $z_\Lambda \simeq 0.30$, known as *matter-dark energy equality*. By understanding which component dominates, we can derive the time-dependent behavior of the scale factor from the Friedmann equation Eq. (2.7),

$$a(t) \propto \begin{cases} t^{\frac{2}{3(1+w)}}\,, & w \neq -1\,, \\ e^{Ht}\,, & w = -1\,. \end{cases} \tag{2.11}$$

Although this result is strictly applicable only to a universe with a single dominant component, it serves as an excellent approximation during the different cosmic eras when either radiation, matter, or dark energy plays the dominant role. We observe that as long as $w \neq -1$ the scale factor follows a power-law with physical time. However, when the universe is dominated by the cosmological constant ($w = -1$) the scale factor grows exponentially giving rise to the accelerated expansion of the universe and is also referred to as *de Sitter expansion*.

Furthermore, it is convenient to divide all energy densities by the critical density today and define the *dimensionless energy density parameters*,

$$\Omega_s \equiv \frac{\rho_s(t_0)}{\rho_{\rm cr}}\,, \tag{2.12}$$

where s stands for any species of the universe. In terms of this parameter, we can write the original density of constituent s as a function of scale factor as

$$\rho_s(a) = \Omega_s \rho_{\rm cr}\, a^{-3(1+w_s)}\,, \tag{2.13}$$

assuming that its equation of state parameter w_s is time-independent. Note in this convention Ω_s is also time-independent as it is the ratio of densities today. Using Eq. (2.7), we can rewrite the Friedmann equation in terms of redshift as

$$H(z) = H_0 \sqrt{\Omega_r (1+z)^4 + \Omega_m (1+z)^3 + \Omega_K (1+z)^2 + \Omega_\Lambda}\,, \tag{2.14}$$

where Ω_r, $\Omega_m = \Omega_{\rm cdm} + \Omega_{\rm b}$ and Ω_Λ are the radiation, matter and cosmological constant density parameters. In addition, we defined $\Omega_K = -K/H_0^2$, treating curvature as an effective additional constituent of the universe, although it is not a physical energy density in the usual sense. For a flat unvierse all Ω_s sum up to unity. CMB measurements suggest that the curvature component contributes a negligible fraction of the total energy density of the universe today, amounting to only about a thousandth of the total [41]. We will thus neglect the curvature from now on.

Finally we define a new time variable, the *conformal time* τ via $\mathrm{d}\tau \equiv \mathrm{d}t/a$ which will be needed later on when discussing perturbation theory. Then, the flat FLRW metric can be written as

$$\mathrm{d}s^2 = a^2(\tau) \left[-\mathrm{d}\tau^2 + \mathrm{d}r^2 + r^2 \left(\mathrm{d}\theta^2 + \sin^2\theta\, \mathrm{d}\phi^2 \right) \right]\,, \tag{2.15}$$

with radial, light-like geodesics given by $\Delta\tau = \Delta r$. The comoving distance,

$$\tau(t) = \int_0^t \frac{\mathrm{d}t'}{a(t')} \tag{2.16}$$

is referred to as the *comoving horizon* and corresponds to the maximum distance information can have propagated since the Big Bang. In addition, we define the conformal Hubble rate as

$$\mathcal{H} \equiv \frac{1}{a}\frac{\mathrm{d}a}{\mathrm{d}\tau} = aH\,, \tag{2.17}$$

which will be used throughout in the subsequent chapters.

ΛCDM: the concordance model of cosmology

The currently most widely accepted cosmological model is the ΛCDM model, which agrees well with observations and is described by only six parameters [41]. This model assumes a spatially flat FLRW metric and includes baryons, cold dark matter, photons, neutrinos (with fixed mass), and a homogeneous dark energy component with $w = -1$ corresponding to a cosmological constant Λ. The term "Cold Dark Matter" (CDM) stems from the requirement that dark matter particles clump efficiently in the early universe, ruling out hot dark matter candidates like neutrinos. GR (describing the evolution of large-scale structure in the universe), nuclear physics (applied to Big Bang Nucleosynthesis or BBN), and atomic physics (for interpreting the CMB) established a robust theoretical framework. The combination of structure formation, light-element ratios from BBN, and the black-body spectrum of the CMB formed a solid observational basis and support the existence of non-baryonic dark matter, which outweighs visible matter by roughly five times. The prevailing idea is that dark matter consists of elementary particles formed during the early moments of the Big Bang. Though its exact nature and formation remain a subject of ongoing experimental investigation, current evidence points to dark matter being cold and composed of fundamental relics from the early universe. Introducing a cosmological constant to explain dark energy poses a challenge for physicists. While particles dilute in an expanding universe, the idea that empty space holds energy, so that the density remains constant even as the universe expands, aligns with quantum mechanics and Heisenberg's uncertainty principle, where virtual particles briefly appear. However, attempts to quantify the cosmological constant using quantum field theory result in values much higher than needed to explain observations [118], making dark energy a major unsolved puzzle in physics, generating numerous ideas and papers.

The Planck CMB measurements provide the most stringent constraints on the ΛCDM model [41]:

$$\begin{aligned} \Omega_{\mathrm{cdm}}h^2 &= 0.1193 \pm 0.0009\,, \qquad \Omega_{\mathrm{b}}h^2 = 0.0224 \pm 0.0001\,, \\ \Omega_m &= 0.3111 \pm 0.0056\,, \qquad \Omega_\Lambda = 0.6889 \pm 0.0056\,, \end{aligned} \tag{2.18}$$

revealing that the dark components dominate the cosmic energy budget today, with dark energy constituting almost 70% and dark matter contributing 26% of the energy density. The remaining parameters control the amplitude and tilt of the primordial power spectrum and describe the amount of reionization during the late stages of star formation [119].

2.2 A nutshell history of the universe

The expanding universe's history indicates increasing density and temperature in the past. GR and thermodynamics show that matter was in thermal equilibrium at various epochs. The hot Big Bang theory describes such a universe. Moving forward in time, and, accordingly to lower temperatures, significant periods in cosmological evolution emerge, which we briefly summarize:

- ***Inflation***: In the very early universe ($t \ll 10^{-5}\,\mathrm{s}$), rapid expansion causes a small, smooth patch to exponentially grow and encompass the observable universe [120–123]. Although not yet experimentally verified, this hypothesis offers explanations for some puzzles within the hot Big Bang model. For instance, it addresses questions like why the CMB appears almost uniform across different parts of the sky (even regions that wouldn't have had time to influence each other), and why the curvature of the universe is exceptionally close to flat. It also serves as the leading explanation for the origin of the initial perturbations that led to the current observed structure. When inflation terminates, the universe enters a phase called *reheating*, during which the energy stored in the hypothetical inflaton field gets transferred back to the familiar standard model particles. This transition shifts the universe's evolution from de Sitter expansion to the radiation dominated phase.

- ***Primordial soup***: From the end of inflation ($t \ll 10^{-5}\,\mathrm{s}$) until quarks form hadrons ($t \sim 10^{-5}\,\mathrm{s}$) the universe was mostly in thermal equilibrium. However two nonequilibrium events at about $T \sim 100\,\mathrm{GeV}$, corresponding to about $z \sim 10^{15}$, occurred: *baryogenesis*, a phase which generates a slight excess of baryons over antibaryons, quantified by the baryon-to-photon ratio $n_\mathrm{b}/n_\gamma \sim 10^{-9}$, and the creation of dark matter particles. In the early universe, if matter and anti-matter were present in equal amounts, their interaction would have led to annihilation, resulting in a universe dominated solely by radiation. Hence, theories of baryogenesis aim to propose mechanisms that could explain the emergence of an imbalance between matter and anti-matter.

- ***Neutrino decoupling***: After the temperature has dropped to $T \sim 1\,\mathrm{MeV}$, or $z \sim 10^9$, weak interactions between electrons and neutrinos become inefficient and neutrinos decouple from the thermal plasma. So, they were in thermal equilibrium with the rest of matter, and once the universe was about a second old, i.e. long before photons decoupled, they began to freely propagate through the universe.

- ***Big Bang Nucleosynthesis (BBN)***: At lower temperatures $T \sim 0.1\,\mathrm{MeV}$, roughly determined by nuclear binding energies ($1 - 10\,\mathrm{MeV}$), a significant cosmological epoch takes place. Initially, protons and neutrons existead freely in cosmic plasma, but as the universe cooled due to expansion, neutrons were captured into nuclei. This process led to the formation of light nuclei with a significant amount of helium-4 and trace amounts of deuterium, helium-3, and lithium-7, while heavier elements weren't produced during this early phase called Big Bang Nucleosynthesis. BBN, occurring from about 1 to 300 seconds after the Big Bang, or correspondingly at $z \sim 10^8$, is directly studied using GR and known microphysics, and the agreement between BBN theory and observations is a crucial component of the early universe theory.

- ***Recombination***: At some point in the history of the universe, ordinary matter began to exist as neutral gas, primarily as hydrogen atoms. In earlier stages, at higher temperatures, the binding energy couldn't retain electrons in atoms, leading to a baryon-electron-photon

plasma state. The epoch of recombination, when this plasma turned into gas, occurred at around $T \simeq 0.25\,\mathrm{eV}$, roughly marked by the binding energy of hydrogen atoms. Before recombination, photons actively scattered off electrons in the plasma, but afterwards, the gas became transparent to photons and they decouple at $z \simeq 1100$. The CMB we observe today, originated from the last scattering of photons, provides us with a snapshot of the universe at that specific point in time. This reveals properties of the universe when its temperature was about $T \sim 3000\,\mathrm{K}$ and age around 380,000 years.

- ***Structure formation***: At matter-radiation equality ($z_{\mathrm{eq}} \simeq 3400$) the universe entered the phase of matter domination, even before the recombination epoch, around 64,000 years after the Big Bang. Rapid growth of density perturbations occurs at that stage of cosmological expansion where baryons started to fall into gravitational potential wells created by the CDM particles. Regions of higher density act as sources of gravitational potential, attracting surrounding matter and amplifying density. This gravitational instability drives the formation of objects like protostars and protogalaxies. Once the overdensity is large enough, the overdense region becomes gravitationally bound and decouples from the cosmological expansion. This process was influenced by the pressure exerted by photons, leading to a phenomenon known as *baryonic acoustic oscillations* (BAO). These oscillations persisted until recombination was terminated. Subsequently, photons were able to travel freely, giving rise to the CMB. During this period, structure began to take shape in a hierarchical manner, starting from galaxies and extending to clusters of galaxies and superclusters. Recently, the universe entered yet another epoch, the phase of *cosmic acceleration*, when dark energy starts to become the dominant contributor to the cosmic energy budget at $z_\Lambda \simeq 0.30$, about 5 billion years ago. The attractive gravity of dark matter eventually becomes subdominant, inhibiting the formation of larger structures (i.e. galaxy clusters).

2.3 Structure in the universe

In the initial 25 years of Cosmic Microwave Background (CMB) surveying, the significant insight gained was that the early universe appeared remarkably smooth without detected anisotropies. This smoothness was a cornerstone of the Big Bang theory. However, the COBE satellite mission in 1992 uncovered *small anisotropies* in the CMB, revealing fractional temperature fluctuations around $\delta T/T \sim 10^{-5}$ [7], in particular this temperature fluctuation corresponding to a certain direction $\hat{\boldsymbol{p}}$ on the sky, can be modelled as

$$\Theta(\tau, \boldsymbol{x}, \hat{\boldsymbol{p}}) \equiv \frac{T(\tau, \boldsymbol{x}, \hat{\boldsymbol{p}}) - T(\tau)}{T(\tau)}\,, \tag{2.19}$$

with $T(\tau)$ being the usual mean temperature $\propto 1/a$ with $T_0 = (2.7255 \pm 0.0006)\,\mathrm{K}$ the value of today [113]. Over time, these fluctuations have been meticulously mapped, by NASA's Wilkinson Microwave Anisotropy Probe (WMAP) in 2003 [40], and even better by ESA's Planck in 2013 [41], see Fig. 2.2. Ongoing research is investigating even more subtle effects like CMB polarization and gravitational lensing due to matter perturbations. This calls for an understanding of *inhomogeneities* or deviations from a smooth background universe, often referred to as *structure*. A natural observable for inhomogeneities is the *density contrast* δ,

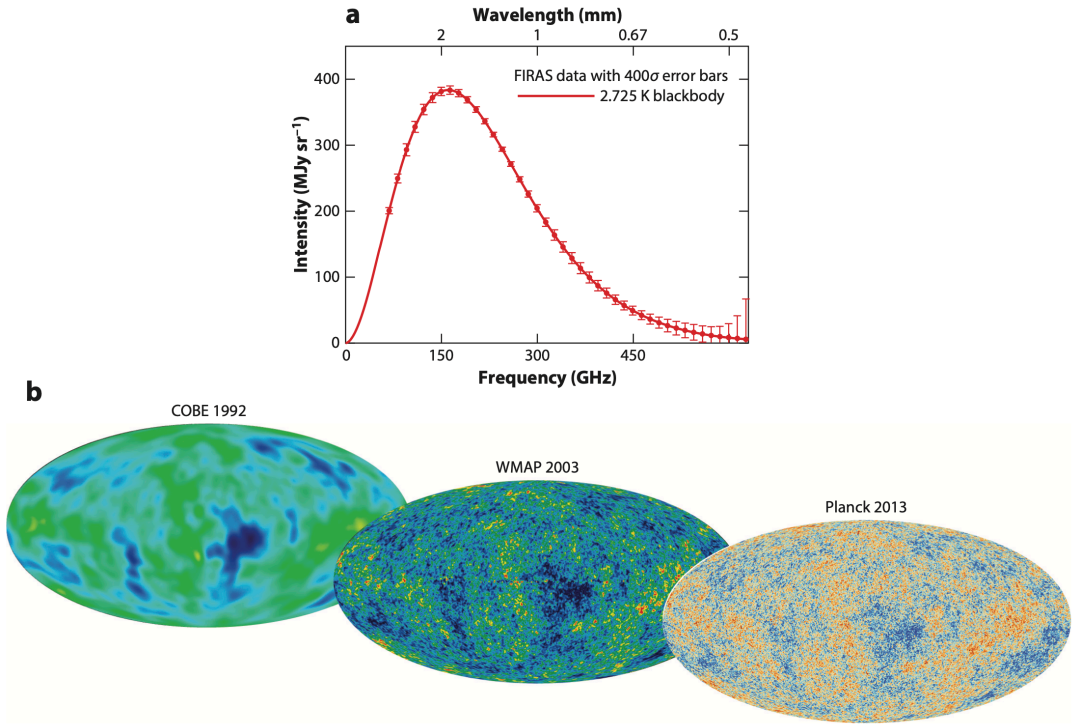

Figure 2.2: (*a*) The perfect blackbody spectrum measured by the FIRAS instrument on COBE with error bars inflated by a factor 400 to make them visible. (*b*) The cosmic microwave background anisotropy progression, with increasing sensitivity and resolution, from COBE to WMAP to Planck. Collage taken from [5].

describing the fractional departure of the background energy density $\bar{\rho}$ as

$$\delta_s(\tau, \boldsymbol{x}) \equiv \frac{\rho_s(\tau, \boldsymbol{x}) - \bar{\rho}_s(\tau)}{\bar{\rho}_s(\tau)}\,, \tag{2.20}$$

for a given species s and which depends on the location $\boldsymbol{x}$ within the universe giving rise to overdense and underdense regions. $\bar{\rho}_s$ denotes the mean background energy density described in Sec. 2.1.

The presence of structure in the universe was recognized long before detecting CMB anisotropies. Early efforts to map galaxy distributions revealed non-uniform patterns, with surveys like the Sloan Digital Sky Survey (SDSS) [12] and the Two Degree Field Galaxy Redshift Survey (2dF) [11] playing significant roles, see the galaxy map in Fig. 2.3. These surveys and subsequent projects provide increasingly detailed galaxy maps. The structure in these maps highlights the need to study perturbations around a smooth background, particularly on large scales. To compare theories with observations effectively, it is essential to focus on anisotropies in the CMB and inhomogeneities in the large-scale structure (LSS) since small-scale perturbations become nonlinear over time, making CMB anisotropies and LSS key sources for understanding cosmic evolution.

The density fluctuations in the universe are thought to have originated from small initial perturbations in its early stages, amplified over time by gravitational instability. While we lack direct measurements of these primordial fluctuations, the most compelling explanation for their

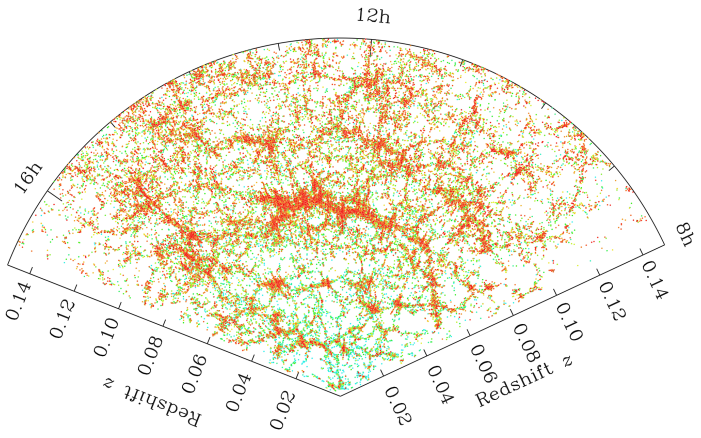

Figure 2.3: A cross-section of the main galaxy sample distribution in the northern segment of the SDSS survey, observed from our viewpoint at the bottom center ($z = 0$). Each dot indicates a galaxy's position, with color reflecting the galaxy's actual color (e.g., red dots represent redder galaxies) [4].

origin is the inflationary theory. In inflation models, these perturbations arise from quantum fluctuations in the inflaton field driving inflation. As a result, they have a statistical nature, giving rise to cosmological observables that are inherently probabilistic rather than deterministic. Additionally, cosmological evolution occurs over a much longer timescale than our observational window, leading us to model the universe as an ensemble of universes with statistical properties. To study these properties, we use the ergodic theorem to transform ensemble averages into spatial averages, assuming uncorrelated fields on large scales.

The statistical features of fields are described by moments of the probability density function (PDF), known as correlation functions or $\mathcal{N}$-point functions, involving $\mathcal{N}$ fields. In the case of Gaussian random variables, the two-point correlation function contains all relevant information. Fields are statistically homogeneous and isotropic if their PDF or moments remain unchanged under spatial translations and rotations. Based on the cosmological principle for large scales, we assume that cosmic fields follow statistically homogeneous and isotropic distributions.

The focus of cosmology lies in the progression of the entire universe, rather than the destiny of individual particles. The emphasis is on the collective and averaged characteristics of matter and radiation, governed by statistical mechanics. In this context, virtually all cosmological findings can be deduced by combining two key equations: the Einstein equations Eq. (2.1) governing gravity, and the Boltzmann equations of statistical mechanics governing matter and radiation.[2] The evolution of density perturbations inevitably leads to gravitational effects influencing the metric. One usually assumes perturbations around the FLRW background metric given by

$$\mathrm{d}s^2 = a^2(\tau)\left[-(1+2\psi)^2\,\mathrm{d}\tau^2 + (1+2\phi)^2\,\delta^K_{ij}\mathrm{d}x^i\mathrm{d}x^j\right]\,, \tag{2.21}$$

where δ^K_{ij} is the Kronecker symbol and the choice of this line element is also referred to as conformal Newtonian gauge [124]. The *scalar metric perturbations* are denoted by the

[2] The Boltzmann equation e.g. for cold dark matter, relevant for this thesis, is given below by Eq. (3.1) and is also known as the Vlasov equation.

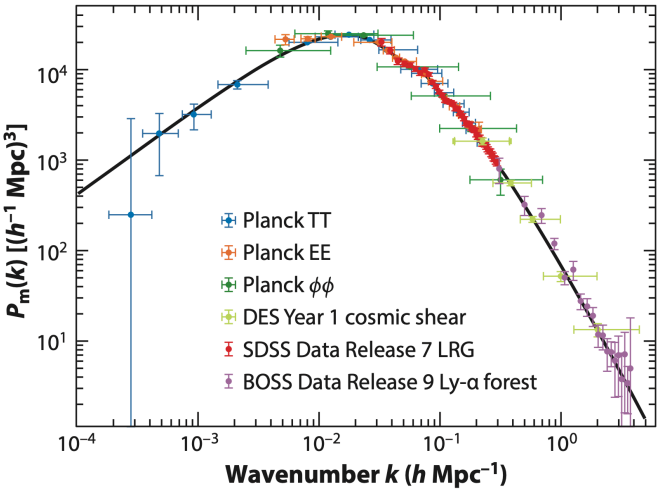

Figure 2.4: Planck compilation of the power spectrum of inhomogeneities, the curve shows the predictions of the ΛCDM model, given by Eq. (2.25) with its maximal value at k_{eq}. Reprinted from [5].

gravitational potential fluctuations $\phi(\boldsymbol{x}, \tau)$ and $\psi(\boldsymbol{x}, \tau)$. Its relation to the matter and radiation fields is governed by the linearized Einstein equation[3]

$$-\nabla^2\phi + 3\mathcal{H}(\phi' - \mathcal{H}\psi) = 4\pi G a^2 \sum_s \rho_s \delta_s \,, \tag{2.22}$$

where for times relevant for structure formation (i.e. in the matter-dominated phase) radiation (photons and neutrinos) is subdominant. It states that density perturbations source fluctuations in gravitational potentials and can be seen as the generalized form of the Poisson equation. Next, we will consider density perturbations in more detail. The corresponding evolution of perturbations are the basis to explain the pattern of CMB anisotropies and the large-scale structure of the universe.

Large-scale structure

As the density perturbations in the universe evolve from small initial conditions, it becomes practical to characterize observables as deviations around the background value. Utilizing the ergodic theorem, the first moment or average of these fluctuation fields cancels out entirely. Consequently, the first significant moment that emerges is the two-point correlation function for the density contrast. It is defined as the joint ensemble average of the density at two different locations, $\xi(r) = \langle \delta(\boldsymbol{x})\delta(\boldsymbol{x}+\boldsymbol{r})\rangle$, and can be considered as the typical separation scale of two point-like galaxies. Due to the assumption of statistical homogeneity and isotropy, it can only depend on the distance r. Galaxies evolve in the matter and dark energy dominated epochs, in the gravitational potential wells created by dark matter (dominantly) and baryons, however note that dark energy is homogeneous and only contributes to the homogeneous background evolution. To effectively compare maps such as the one depicted in Fig. 2.3 with theoretical predictions it is crucial to isolate large and small scales. Then, one useful approach involves taking the

[3]There is a second independent Einstein equation relating matter and radiation perturbations to metric perturbations. It essentially states that second moments of the distribution function source deviations between both ϕ and ψ. Assuming that these quantities are negligible yields approximately $\phi \simeq -\psi$.

Fourier transform of the distribution, which facilitates the separation of different scales. In both CMB and LSS analyses, the primary statistic of significance is the power spectrum, the Fourier transform of the two-point correlation function. Hence, correlators in Fourier space can be expressed as follows

$$\langle \delta_m(\boldsymbol{k}) \delta_m(\boldsymbol{k}') \rangle \equiv \delta_{\mathrm{D}}^{(3)}(\boldsymbol{k} + \boldsymbol{k}')\, P_m(k)\,, \tag{2.23}$$

where $\delta_{\mathrm{D}}^{(3)}$ is the Dirac delta function, $\delta_m(\boldsymbol{k})$ the Fourier transform of the matter density contrast and we defined the *matter density power spectrum* as $P_m(k)$. However, we do not have a direct way of measuring the matter power spectrum; after all, the bulk of matter is in form of dark matter, and lots of baryonic matter is not readily observable (e.g., dilute hot gas). The map in Fig. 2.3 shows a population of galaxies. As it turns out, galaxies can be used as *tracers* of the large-scale matter distribution such that the density perturbations of galaxies and the total matter field can be related by so-called bias parameters [125]. This is beyond the scope of this work and we henceforth only discuss matter perturbations. Due to statistical homogeneity and isotropy, the power spectrum only depends on the norm of the wavenumber k. It is by far the most common descriptor of clustering in the linear and mildly nonlinear regime and plays a central role in cosmology [103] and will be one of the main observables modeled and discussed in this thesis.

The simplest inflationary models suggest initial conditions that are nearly scale-invariant, adiabatic, and closely Gaussian. These predictions align well with Planck's measurements of the CMB [41], which indicate that the primordial non-Gaussianity is significantly smaller than the Gaussian component. Hence, for the purposes of this thesis, we will work with Gaussian initial conditions. The initial density fluctuations can be described by the primordial power spectrum formula:

$$P_{\mathrm{prim}}(k) = A_m \left(\frac{k}{k_{\mathrm{p}}} \right)^{n_s} \tag{2.24}$$

where A_m is the amplitude, k_{p} a reference scale (typically $k_{\mathrm{p}} = 0.05\,\mathrm{Mpc}^{-1}$), and the spectral index n_s determines the tilt of the spectrum. Almost scale-invariant conditions correspond to $n_s \simeq 1$, most inflation models suggest a slightly lower value [126]. Present CMB data measures $n_s = (0.9645 \pm 0.0004)$ at a 68% confidence level [41], yet it lacks the sensitivity to detect deviations from power-law initial conditions, such as a scale-dependent or "running" spectral index [127]. The power spectrum is influenced by various events and processes between the inflationary period and the present time, resulting in a "processed" version of the primordial power spectrum. This modification can be represented as

$$P_m(k, \tau) = D_+^2(\tau) T^2(k) P_{\mathrm{prim}}(k)\,, \tag{2.25}$$

where D_+ is a time-dependent *growth factor* (see Sec. 3.1 for its time-evolution) and T is the *transfer function* that describes the evolution of the density perturbations through decoupling. The scale-dependent part simply refers to $P_m(k)$ as defined in Eq. (2.23). As the universe evolves, progressively larger comoving regions come within causal contact as they enter the comoving horizon set by the Hubble rate $\sim 1/\mathcal{H}$. The size of the wavenumber k determines when it enters the horizon, specifically when $k\tau = 1$ or when $k \simeq \mathcal{H}$. It is useful to distinguish modes that enter the horizon during radiation domination from those during matter domination, denoted by $k > k_{\mathrm{eq}}$ and $k < k_{\mathrm{eq}}$, respectively. Here, k_{eq} represents the mode that enters exactly at the point of matter-radiation equality. This distinction is important because during radiation domination, the growth of structure is inhibited by radiation pressure, causing density contrast

to increase logarithmically ($\delta \propto \ln a$), while during matter domination, it grows linearly as $\delta \propto a$ [4, 22]. Therefore, we anticipate a distinct power shape for scales that enter the horizon before and after equality, displaying a turnover at $k_{\rm eq} \simeq 0.02\,h\,\mathrm{Mpc}^{-1}$. One finds

$$T(k) \propto \begin{cases} 1 & \text{for } k < k_{\rm eq} \\ \frac{\ln^2(k)}{k^4} & \text{for } k > k_{\rm eq} \end{cases} . \tag{2.26}$$

In the radiation-dominated period, perturbations in the baryon-photon fluid undergo oscillations due to gravitational attraction and radiation pressure. Before recombination, baryons and photons are tightly coupled through effective Compton scatterings. As a result, baryons also experience these oscillations before they become decoupled. This phenomenon gives rise to the BAO imprint on the matter power spectrum. The BAO feature is characterized by a set of wiggles observed in the power spectrum, typically occurring around the wavenumber $k \simeq 0.1\,h\,\mathrm{Mpc}^{-1}$, as displayed in Fig. 2.4.

Finally, using the statistic description of the Boltzmann equations one is able to obtain evolution equations for the perturbations. In Sec. 2.1 we have described the characteristics of various components in the universe using average density and pressure, which are macroscopic measures. However, on a microscopic level, matter and radiation consist of numerous interacting or non-interacting particles of various species within a specific volume. These particles can be statistically described through their *distribution functions* which in turn allows us to derive all macroscopic properties of the collection of particles, such as density, velocity and pressure. Phase-space conservation then yields evolution equations e.g. for baryon density and velocity given by

$$\delta_{\rm b}' + \mathrm{i}kv_{\rm b} + 3\phi' = 0\,, \tag{2.27}$$

$$v_{\rm b}' + \mathcal{H}v_{\rm b} + \mathrm{i}k\psi = -\tau'\frac{1}{R}(v_\gamma - v_{\rm b})\,, \tag{2.28}$$

where $' \equiv \mathrm{d}/\mathrm{d}\tau$ is the time-derivative with respect to conformal time. The term on the right-hand side is a collision term which incorporates direct particle interactions. The prefactor of the collision term contains the scattering rate of photons. Its integral over time, τ (not to be confused with conformal time), gives the average number of collisions, known as *optical depth*. In addition, R scales with a. The coherent flow of the baryon fluid apart from the cosmic expansion is characterized by the peculiar velocity $v_{\rm b}$. We see here, that efficient Compton scattering tends to equalize the baryon and photon velocities, i.e. we get a so-called *Compton drag* term, leading to a single baryon-photon fluid. Similarly, one obtains the corresponding linearized equations of motion for cold dark matter as

$$\delta_{\rm cdm}' + \mathrm{i}kv_{\rm cdm} + 3\phi' = 0\,, \tag{2.29}$$

$$v_{\rm cdm}' + \mathcal{H}v_{\rm cdm} + \mathrm{i}k\psi = 0\,, \tag{2.30}$$

where we emphasize the *collisionless* nature of dark matter, having no collision term on the right-hand side. This is essentially the reason why dark matter cluster so early showing off its dominant role for structure formation. Eqs. (2.29) and (2.30) govern the evolution of density and velocity of cold dark matter. The Euler equation Eq. (2.30) lacks the standard $(\boldsymbol{v}\cdot\nabla)\boldsymbol{v}$ term due to its nonlinear nature (appearing in Ch. 3). For the nonrelativistic components of dark matter and baryons, the Boltzmann equation can be simplified significantly by taking

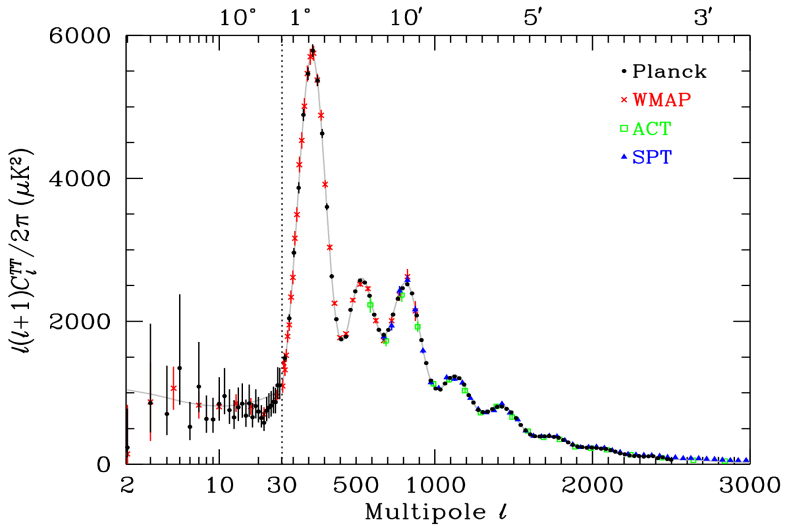

Figure 2.5: CMB temperature anisotropy power spectrum obtained from various experiments including Planck, WMAP, ACT [128–130], and SPT [131, 132]. The x-axis is logarithmic for lower multipole moments ℓ (large angular scales) to highlight the Sachs-Wolfe plateau and linear for other multipoles. The y-axis is the variance of the temperature fluctuations as a function of scale. The observed acoustic peaks and damping region are clearly visible, and the curve represents the best-fit Planck ΛCDM model. Reprinted from [133].

moments in terms of the particle momentum, and keeping only the lowest-order moments being the overdensity δ and peculiar velocity v satisfying fluid equations. Relativistic particles like photons and neutrinos are more complex to describe. Their distribution depends on position, time, and the photon's propagation direction, $\hat{\boldsymbol{p}}$, involving monopole, dipole, quadrupole and higher moments, which will be discussed next.

Cosmic microwave background

The primary measure of Cosmic Microwave Background (CMB) anisotropies is the two-point function, specifically in terms of intensity across the sky. The incorporation of anisotropies in all directions $\hat{\boldsymbol{p}}$, results in a two-dimensional map situated on a spherical surface, making it beneficial to expand these anisotropies, Eq. 2.19, using spherical harmonics as

$$\Theta(\tau, \boldsymbol{x}, \hat{\boldsymbol{p}}) = \sum_{\ell,m} a_{\ell m}(\tau, \boldsymbol{x}) Y_{\ell m}(\hat{\boldsymbol{p}})\,, \tag{2.31}$$

and their expansion coefficients $a_{\ell m}$. Given statistical isotropy, different values of m (running from $-\ell$ to ℓ) are equivalent, implying no preferred direction. Assuming Gaussian initial conditions, we can describe the statistical properties using

$$\langle a_{\ell m} \rangle = 0\,, \qquad \langle a_{\ell m} a^*_{\ell' m'} \rangle = \delta^K_{\ell\ell'} \delta^K_{mm'} C_\ell\,, \tag{2.32}$$

where the variance C_ℓ measures the degree of temperature anisotropies depending on the multipole moment ℓ and its the two-dimensional distribution is analogous to the three-dimensional power spectrum. The CMB power spectrum, C_ℓ, has been measured with high precision by various groups, see Fig. 2.5 showing the result normalized by the inverse of $\ell(\ell+1)$. The

Planck observations of the CMB currently offer the most stringent limitations on the ΛCDM cosmological model [41]. Future CMB Stage IV experiments, like Simons Observatory [134], LiteBIRD [135], and CMB-S4 [42], along with potential satellite projects like CORE-M5 [136] and PICO [137], are anticipated to enhance these constraints. These experiments will achieve greater precision in measuring the small-scale anisotropies and polarization of CMB photons, surpassing the capabilities of the Planck mission.

CMB temperature anisotropies are influenced by the complete cosmological evolution, especially the fluctuations of the photon fluid from the early universe until recombination, as well as various effects between recombination and the present day. The evolution of the temperature anisotropy is governed by the Boltzmann equation for photons and is in linear approximation[4] given by

$$\Theta' + \mathrm{i}k\mu\Theta + \phi' + \mathrm{i}k\mu\psi = -\tau' \left(\Theta_0 - \Theta + \mu v_\mathrm{b}\right) , \tag{2.33}$$

$$\mathcal{N}' + \mathrm{i}k\mu\mathcal{N} + \phi' + \mathrm{i}k\mu\psi = 0 . \tag{2.34}$$

In the absence of a bulk velocity for the electrons ($v_\mathrm{b} = 0$), efficient Compton scattering tends to drive Θ to Θ_0, the so-called *monopole* ($\ell = 0$) of the photon perturbation which yields an angle-averaged photon flux and is thus related to the photon density contrast δ_γ. Strong scattering implies a short mean free path for photons. Photons reaching a point recently scattered off nearby electrons with similar temperature. Consequently, photons from all directions share the same temperature, resulting in equal flux from all angles. All anisotropies (i.e. higher moments) are therefore washed out and the photon distribution gets completely isotropized. When including a non-zero bulk velocity, scatterings drive the photon distribution to $\Theta \to \Theta_0 + \mu v_\mathrm{b}$, where μ is the cosine of the angle between wavenumber $\boldsymbol{k}$ and the photon direction $\hat{\boldsymbol{p}}$. Since photons are "dragged" along electrons (or also vice-versa), the μv_b contribution is sometimes called "drag term". In total, fully efficient Compton scattering would produce a situation where the photon distribution is completely characterized by the density (i.e. by the angle-average or zeroth moment) and the mean velocity v_γ (first moment, related to the dipole Θ_1), and wash out higher moments of the distribution function. In this type of situation, photons would behave like a "perfect fluid". However, this ceases to be true after baryon-photon decoupling, so photons no longer behave like a fluid after recombination. Nevertheless, for all modes with wavelengths much larger than their mean free path, we have $\Theta_\ell \ll \Theta_{\ell-1}$ (i.e. higher multipoles are suppressed), and the Boltzmann approach remains valid after decoupling when the photons freely stream to us. There is an analogous equation for the (relativistic) neutrino temperature anisotropy $\mathcal{N}$ but without an collision term which is negligible for weak interactions. To track the evolution of neutrino anisotropies after recombination significant changes are required with higher multipoles being more important due to the lack of Compton scattering.

The integration of Boltzmann equations into fluid equations leads to a hierarchy where each integrated equation for the lth moment depends on the next moment of order $l + 1$. This is one way of solving the Boltzmann equation for the photons Eq. (2.33). In the case of cold dark matter, we close the hierarchy by setting the second moment to zero, resulting in a self-consistent system. For particles with higher velocities like massive neutrinos, this closure is more complex and higher moments must be considered. In fact, also *higher moments of cold dark matter* distribution become relevant during nonlinear structure formation which will be discussed in-depth from Ch. 4 onwards and is the main address of this thesis.

[4] Here we neglected the quadrupole ($\ell = 2$) and polarization anisotropies of CMB photons.

Contrasting the CMB map with current universe structure maps reveals a transition from a smooth early universe to the clumpy present state, driven by gravity's role in accumulating matter into overdense regions. This growth of structure is a central focus in cosmology, revealing insights into both the universe's background evolution and its gravitational instability. This interplay between growth and expansion serves as a stringent test for our cosmological and general relativity theories. The workhorse for describing gravitational instability is perturbation theory which accounts for important nonlinear effects during structure formation which will be reviewed in the next chapter.

3 Growth of structure: beyond linear theory

This chapter delves into the utilization of large-scale structure (LSS) as a tool for exploring cosmology. We explore how the process of structure formation can be understood within the context of the perfect fluid picture, employing perturbation theory beyond linear order. In the linear regime, it is sufficient to some extent to use density contrast and velocity to adequately describe the matter distribution. However, in the nonlinear regime, this approximation eventually breaks down due to the occurrence of *shell crossing* and *multi-streaming* effects. Shell crossing happens when infalling matter particles from different directions meet and cross through each other, resulting in the matter distribution being described by a superposition of multiple streams. This leads to the breakdown of the single-valued velocity field and the generation of higher moments of the distribution function which will be addressed in Ch. 4.

Before doing this, in this chapter we provide a comprehensive review, introducing the Eulerian setup of the so-called *Standard Perturbation Theory* (SPT) description (see [138] for an extensive review). We use a notation suitable for extending the SPT framework which is presented in the subsequent chapters.

3.1 Vlasov-Poisson system

The probability of finding a particle in a phase space volume $\mathrm{d}^3x\,\mathrm{d}^3p$ at conformal time τ is given by the distribution function $f(\boldsymbol{x},\boldsymbol{p},\tau)$. In the limit of noninteracting, collisionless dark matter particles, the phase-space density is conserved along the particle trajectories $\mathrm{d}f/\mathrm{d}\tau = 0$. This is the collisionless Boltzmann equation and describes the evolution of perturbations. For scales smaller than the Hubble radius, relevant for nonlinear large-scale structure formation, the nonrelativistic limit suffices, which is called *Vlasov equation* and reads

$$0 = \frac{\partial f}{\partial \tau} + \frac{p_i}{ma}\frac{\partial f}{\partial x_i} - am(\nabla_i\phi)\frac{\partial f}{\partial p_i}\,, \tag{3.1}$$

with scale factor $a(\tau)$, comoving momentum $\boldsymbol{p}$ and ϕ obeying the Poisson equation

$$\nabla^2\phi = 4\pi G a^2\bar{\rho}\delta = \frac{3}{2}\mathcal{H}^2\Omega_m\delta\,, \tag{3.2}$$

where $\Omega_m(\tau) = \bar{\rho}(\tau)/\rho_{\mathrm{cr}}(\tau)$ is the time-dependent density parameter given in Eq. (3.12) below, and $\rho_{\mathrm{cr}} = 3H(\tau)^2/(8\pi G)$ the time-dependent critical energy density. The dark matter particles move along the characteristics, $\boldsymbol{v} = \mathrm{d}\boldsymbol{x}/\mathrm{d}\tau = \boldsymbol{p}/(ma)$ and $\mathrm{d}\boldsymbol{p}/\mathrm{d}\tau = -am\nabla\phi$. This distribution function implies phase-space conservation and is obeyed by collisionless dark matter. Solely the deviation from the homogeneous part enters as source for the potential. This refers to the *Vlasov-Poisson system* and is a seven-dimensional nonlinear differential set of equations which is very difficult to solve.

Fluid equations

CDM is per definition cold or in other words dark matter particles move relatively slowly. Therefore, instead of assuming a form for the distribution function f, in practice one takes moments or cumulants of the distribution function with respect to the momentum. We only keep the lowest order moments (zeroth and first order) while neglecting terms $\propto (p/m)^2$. This means we include the bulk flow of dark matter, but not its velocity dispersion which allows one to treat dark matter as a *perfect fluid*. Note that, as we will see later, this *pressureless perfect fluid approximation* eventually breaks down during later stages of structure formation. When taking the momentum average one obtains the density contrast δ given by the zeroth moment, or more precisely cumulant of the distribution function,

$$1 + \delta = \int \mathrm{d}^3p \, f(\tau, \boldsymbol{x}, \boldsymbol{p}) \,, \tag{3.3}$$

where we have normalized the distribution function by its background number density $\bar{n} = \bar{\rho}/m$, which was also implicitly assumed in Eq. (3.1). The first moment corresponds to the peculiar velocity field

$$(1 + \delta) v_i = \int \mathrm{d}^3p \, \frac{p_i}{ma} \, f(\tau, \boldsymbol{x}, \boldsymbol{p}) \,. \tag{3.4}$$

Integrating the Vlasov equation over $\int \mathrm{d}^3p$ yields the *continuity equation* for the density contrast

$$\partial_\tau \delta + \nabla_i [(1 + \delta) v_i] = 0 \,, \tag{3.5}$$

and first multiplying with p_i/am and then integrating over $\int \mathrm{d}^3p$ gives the *Euler equation* for the peculiar velocity field

$$\begin{aligned} \partial_\tau v_i + \mathcal{H} v_i + v_j \nabla_j v_i + \nabla_i \phi &= -\frac{1}{1+\delta} \nabla_j \left((1+\delta) \sigma_{ij} \right) \\ &= -\sigma_{ij} \nabla_j \ln(1+\delta) - \nabla_j \sigma_{ij} \,. \end{aligned} \tag{3.6}$$

The widely used framework of SPT is based on a perturbative solution of these fluid equations obtained when neglecting the right-hand side of the Euler equation, that contains the velocity dispersion tensor

$$\sigma_{ij} = \frac{1}{1+\delta} \int \mathrm{d}^3p \, \frac{p_i}{ma} \frac{p_j}{ma} \, f(\tau, \boldsymbol{x}, \boldsymbol{p}) - v_i v_j \,. \tag{3.7}$$

However, it is well-known that velocity dispersion and all higher moments are generated via orbit-crossing during nonlinear structure formation [53], even for almost vanishing velocity dispersion initially, as appropriate for cold dark matter. In Ch. 4 we explicitly develop a framework to also include velocity dispersion and higher order moments in perturbation theory which is an essential feature of this thesis. But before doing this, in this section we review SPT which resembles a pressureless perfect fluid approximation.

Closing the Vlasov hierarchy

When taking moments of the Vlasov equation Eq. (3.1) we get differential equations with terms coupling the n-th cumulant to the $(n+1)-$cumulant which eventually leads to an infinite set of equations. This is referred to as Boltzmann or Vlasov hierarchy. One could close the set of

continuity and Euler equations with an anstatz for the velocity dispersion tensor σ_{ij} motivated from standard fluid dynamics by splitting it into isotropic and anisotropic parts [139]

$$\sigma_{ij} = -p\delta^K_{ij} + \zeta\delta^K_{ij}\boldsymbol{\nabla}\cdot\boldsymbol{v} + \eta\left(\nabla_i v_j + \nabla_j v_i - \frac{2}{3}\boldsymbol{\nabla}\cdot\boldsymbol{v}\delta^K_{ij}\right), \tag{3.8}$$

where p is the pressure, and ζ and η are viscosity coefficients. Moreover, and more correctly, σ_{ij} can also chosen to be proportional to the density perturbation (as only the gradient of σ_{ij} appears in the Euler equation) and an effective sound speed c_s as $\sigma_{ij} \propto \delta^K_{ij}c_s^2\delta$ revealing an dispersion-induced effective pressure driven by collisionless small-scale perturbations. In this sense dark matter is treated as an *effective fluid*. This would indeed modify linear dynamics and we present in detail the correct extension within perturbation theory to get an improved closure of the hierarchy in Ch. 4.

The common lore in SPT is to set all moments of second and higher order exactly to zero. One is then left with three variables δ, v_i, ϕ which actually forms a closed set and no higher moments will be generated (see details in Ch. 4). This Vlasov-Poisson system is particularly simple and is able to predict the density and velocity at large, quasi-linear scales. Our focus is on CDM clustering during early stages of gravitational collapse, where its velocity dispersion is negligible compared to its velocity flow due to its near-uniform initial state. Velocity dispersion signifies deviation from a single coherent flow, disappearing prior to shell-crossing, when gravity-induced multiple streams intersect. This assumption of $\sigma_{ij} = 0$ is termed the *single stream approximation*. Thus, it is still a good approximation in the first stages of gravitational instability where structures did not have time to collapse and virialize. The distribution function in this case reads

$$f(\boldsymbol{x},\boldsymbol{p},\tau) = (1+\delta)\,\delta_{\rm D}^{(3)}\left(\boldsymbol{p} - am\boldsymbol{v}\right), \qquad \text{(no velocity dispersion)} \tag{3.9}$$

hence requiring that all particles at a given point move with the same velocity. As time progresses, gravitational collapse causes larger scales to collapse, resulting in multiple flows whose analytical description is challenging, often requiring N-body simulations. Nevertheless, the single stream approximation proves useful for analyzing numerous large-scale structure effects. Initially, this approximation is employed to establish perturbative solutions for the nonlinear equations below. However, its inconsistency on scales pertinent to mildly nonlinear corrections becomes apparent, leading to perturbation theory breakdown in the ideal, pressureless fluid scenario. This issue is addressed by incorporating a non-zero anisotropic stress tensor within the so-called Vlasov Perturbation Theory (VPT) to restore the predictive power of perturbative theory, presented in Ch. 4.

Linear growth factor

Now, we consider the time-dependent growth factor entering the matter power spectrum, Eq. (2.25), and seek a solution at linear level. To obtain an evolution for the scale-independent part of matter fluctuations one has to go back to the linearized continuity and Euler equation for dark matter. Multiplying Eq. (2.29) by a and taking the derivative with respect to τ yields after combining with Eq. (2.30) and Eq. (2.22)

$$[a\delta']' = ak^2\phi = \frac{3}{2}H_0^2\Omega_m\delta\,, \tag{3.10}$$

where we assumed $\phi = -\psi$ and neglected time-derivatives of the potential, as appropriate for sub-horizon scales. This results to a second-order differential equation for δ given by

$$\delta'' + \mathcal{H}\delta' = \frac{3}{2}\Omega_m(\tau)\mathcal{H}^2\delta\,, \tag{3.11}$$

whose solution is actually scale-independent as only time derivatives are acting on the density field. We thus can factorize $\delta(\boldsymbol{x},\tau) = D(\tau)\delta_0(\boldsymbol{x})$ with $D(\tau)$ the so-called *linear growth factor* and δ_0 the initial density contrast at some fixed reference epoch and we introduced the time-dependent matter density parameter

$$\Omega_m(\tau) = \frac{H_0^2}{H^2(\tau)}\Omega_m a(\tau)^{-3}\,, \tag{3.12}$$

$$H^2(\tau) = H_0^2\left(\Omega_m\, a(\tau)^{-3} + \Omega_\Lambda\right)\,. \tag{3.13}$$

$D(\tau)$ governs the growth of density perturbations, satisfying the following equation of motion:

$$D'' + \mathcal{H}D' = \frac{3}{2}\Omega_m(\tau)\mathcal{H}^2 D\,. \tag{3.14}$$

Its two independent solutions are denoted by the growing mode $D_+(\tau)$ and decaying mode $D_-(\tau)$ and the evolution of the density is then

$$\delta(\boldsymbol{x},\tau) = D_+(\tau)\delta_+(\boldsymbol{x}) + D_-(\tau)\delta_-(\boldsymbol{x})\,, \tag{3.15}$$

where δ_+ and δ_- describe the initial density configuration. The solution of the growth factor actually depends on the cosmology. To solve it, it is more convenient to exchange the time variable from τ to a which gives the following differential equation

$$\frac{\mathrm{d}^2 D}{\mathrm{d}a^2} + \frac{\mathrm{d}D}{\mathrm{d}a}\frac{\mathrm{d}\ln(a^3H)}{\mathrm{d}a} - \frac{3}{2}\frac{\Omega_m H_0^2}{a^5 H^2}D = 0\,. \tag{3.16}$$

For a cosmology with matter and a cosmological constant, with Hubble rate given by Eq. (3.13), one obtains an integral representation for the growing mode given by

$$D_+(a) = \frac{5\Omega_m}{2}\frac{H_0}{H(a)}\int_0^a \frac{\mathrm{d}a'}{\left(a'H(a')/H_0\right)^3}\,, \tag{3.17}$$

whose solution can be found analytically [140]

$$D_+(a) = \frac{a\left(8\,{}_2F_1\left(-\frac{1}{2},\frac{5}{6};\frac{11}{6};-x\right) - (2x+5)\,{}_2F_1\left(\frac{1}{2},\frac{5}{6};\frac{11}{6};-x\right)\right)}{3\,(1+x)^{1/2}}\,, \tag{3.18}$$

where $x = a^3\Omega_\Lambda/\Omega_m$. The decaying solution is simply

$$D_-(a) = \frac{H(a)}{H_0}\,. \tag{3.19}$$

One can define the corresponding *growth rates*

$$f(a) \equiv \frac{\mathrm{d}\ln D_+(a)}{\mathrm{d}\ln a}, \qquad g(a) \equiv \frac{\mathrm{d}\ln D_-(a)}{\mathrm{d}\ln a}\,, \tag{3.20}$$

where the former satisfies

$$\frac{\mathrm{d}f}{\mathrm{d}\ln a} + f^2 + \left(1 + \frac{\mathrm{d}\ln(aH)}{\mathrm{d}\ln a}\right) f - \frac{3}{2}\Omega_m(\tau) = 0\,. \tag{3.21}$$

In an Einstein-de Sitter (EdS) cosmology with ($\Omega_m = 1$, $\Omega_\Lambda = 0$) one simply obtains

$$D_+(a) = a, \quad D_-(a) = a^{-3/2}, \qquad f(a) = 1, \quad g(a) = -3/2 \tag{3.22}$$

This means, in a purely matter dominated Universe the growth factor D_+ and correspondingly the density contrast grows with a until today (cf. Eq. (3.18) with $x \to 0$). The second independent solution, the decaying mode, *decays* as $a^{-3/2}$. As soon as we include some form of dark energy like a cosmological constant we should expect deviations from this where the growth factor is suppressed at late times ($f < 1$) and we have to use Eq. (3.18). It seems reasonable that in the following we can neglect the decaying mode solution D_- since after a sufficient amount of time the growing mode solution completely dominates. For further discussion with different cosmological setups we refer to [138].

Velocity divergence and vorticity

In the following it is convenient to consider the two velocity-related fields

$$\begin{aligned} \theta &\equiv \frac{\nabla_i v_i}{-\mathcal{H}f} = \nabla_i u_i \\ w_i &\equiv \frac{(\boldsymbol{\nabla}\times\boldsymbol{v})_i}{-\mathcal{H}f} = (\boldsymbol{\nabla}\times\boldsymbol{u})_i \end{aligned} \tag{3.23}$$

where the divergence θ (curl-free) denotes the scalar mode and the vorticity w_i (divergence-free) the vector modes of the rescaled velocity field $u_i = v_i/(-\mathcal{H}f)$. This notation further simplifies the equations where the growth rate f is defined as in Eq. (3.20) and we switch to time variable $\eta = \ln D_+(\tau)$ which then leads to

$$\begin{aligned} \partial_\tau \delta &= \frac{\mathrm{d}\ln a}{\mathrm{d}\tau}\frac{\mathrm{d}\ln D_+}{\mathrm{d}\ln a}\frac{\partial}{\partial \ln D_+}\delta\,, \\ &= \mathcal{H}f\,\partial_\eta\delta\,. \end{aligned} \tag{3.24}$$

Applying the decomposition Eq. (3.23) to the Euler equation (3.6) with σ_{ij} being neglected, one obtains

$$\begin{aligned} \theta' + \left(\frac{3}{2}\frac{\Omega_m}{f^2} - 1\right)\theta - \frac{3}{2}\frac{\Omega_m}{f^2}\delta &= \nabla_i(u_j\nabla_j u_i)\,, \\ w_i' + \left(\frac{3}{2}\frac{\Omega_m}{f^2} - 1\right) w_i &= (\boldsymbol{\nabla}\times(u_j\nabla_j\boldsymbol{u}))_i\,, \end{aligned} \tag{3.25}$$

where $' = \partial_\eta$ and we used Eq. (3.21) to obtain

$$\partial_\tau(\mathcal{H}f) = \mathcal{H}^2\left(\frac{3}{2}\Omega_m(\tau) - f(\tau) - f^2(\tau)\right)\,. \tag{3.26}$$

This decomposition allows us to use the Poisson equation for ϕ via Eq. (3.2). The continuity equation now becomes

$$\delta' - \theta = \nabla_i[\delta\, u_i]\,. \tag{3.27}$$

In the *linear regime* where the fluctuation fields are small compared to the homogeneous contribution we can set the terms on the right-hand side to zero which means we can also neglect the vorticity field since its linearized solution in the matter era where $\Omega_m/f^2 \to 1$ only decays away as $\boldsymbol{w}(\eta) \propto a^{-1/2}$. Its evolution equation shows that the dynamics depends on the vorticity itself meaning if it is small but nonzero initially it remains small throughout even in the nonlinear regime for a vanishing stress tensor $T_{ij} = (1+\delta)\sigma_{ij}$ (see Eq 3.6). If also σ_{ij} becomes nonzero we get source terms for the vorticity which does not contain the vorticity itself. This means vorticity can be amplified nonlinearly through the velocity dispersion tensor. This is in fact the dominant contribution for vorticity generation, as we will see in Ch. 8. Written in terms of η the linear evolution equation (3.11) reads

$$\delta'' + \left(\frac{3}{2}\frac{\Omega_m}{f^2} - 1\right)\delta' - \frac{3}{2}\frac{\Omega_m}{f^2}\delta = 0\,. \tag{3.28}$$

The linear solution is thus given by $\delta^{(1)}(\boldsymbol{x},\eta) \equiv e^{\eta}\delta_0(\boldsymbol{x})$ and the linearized divergence is simply $\theta^{(1)} = \delta^{(1)\prime} = \delta^{(1)}$ (motivating the rescaling Eq. 3.23).

3.2 Perturbation theory in the mildly nonlinear regime

We now turn to the *nonlinear regime*, that is we consider all nonlinear terms on the right-hand side in Eqs. (4.18, 4.11). Within the single stream approximation, $\sigma_{ij} = 0$, the dynamical variables are δ and θ which both are coupled through the Poisson equation. A second order solution to the evolution equations is obtained by plugging in the linear solution, thus

$$\begin{aligned} \delta^{(2)\prime} - \theta^{(2)} &= \nabla_i[\delta^{(1)}\, u_i^{(1)}]\,, \\ \theta^{(2)\prime} + \left(\frac{3}{2}\frac{\Omega_m}{f^2} - 1\right)\theta^{(2)} - \frac{3}{2}\frac{\Omega_m}{f^2}\delta^{(2)} &= \nabla_i(u_j^{(1)}\nabla_j u_i^{(1)})\,, \end{aligned} \tag{3.29}$$

where we can replace the linear velocity field by

$$u_i^{(1)} = \frac{\nabla_i}{\nabla^2}\delta^{(1)}\,. \tag{3.30}$$

This means, $\delta^{(2)}$ and $\theta^{(2)}$ are sourced by terms which correspond to the square of the linear density field $\delta^{(1)}$. At sufficiently large scales the linear field is small, the square of it is even smaller, so $\delta^{(2)}$ accounts to a small correction to $\delta^{(1)}$. This iterative approach suggests that we can expand the nonlinear fields as

$$\begin{aligned} \delta &= \delta^{(1)} + \delta^{(2)} + \cdots + \delta^{(n)}\,, \\ \theta &= \theta^{(1)} + \theta^{(2)} + \cdots + \theta^{(n)}\,, \end{aligned} \tag{3.31}$$

where $\delta^{(n)}, \theta^{(n)}$ involve n powers of the linear fields such that each term in the series Eq. (3.31) is smaller than the previous one. Given this, the perturbation theory should become more accurate as one includes higher-order terms. Hence, one is motivated to apply a perturbative treatment in the mildly nonlinear regime.

Nonlinear kernels

We henceforth switch to the equations of motion in the *Fourier representation*. In the linear regime different Fourier modes (k-modes) evolve independently. However when nonlinear terms are taken into account different Fourier modes couple. We use the convention

$$\tilde{\xi}(\boldsymbol{k},\eta) = \int \frac{\mathrm{d}^3x}{(2\pi)^3}\, e^{-\mathrm{i}\,\boldsymbol{k}\cdot\boldsymbol{x}}\,\xi(\boldsymbol{x},\eta)\,, \tag{3.32}$$

$$\xi(\boldsymbol{x},\eta) = \int \mathrm{d}^3k\, e^{\mathrm{i}\,\boldsymbol{k}\cdot\boldsymbol{x}}\,\tilde{\xi}(\boldsymbol{k},\eta)\,, \tag{3.33}$$

identical to Eq. (1.1). For brevity we also define the following short-hand notation for Fourier space variables: $\tilde{\xi}(\boldsymbol{k},\eta) \equiv \xi_k$. We assume the flow to be directed along the gravitational potential gradient, which means we can neglect the vorticity field, so we can write in Fourier space $u_{k,i} = k_i\alpha$ [103]. With $\theta_k = \mathrm{i}k_iu_{k,i}$ we obtain $\alpha = -\mathrm{i}\theta_k k^{-2}$ and hence at any order

$$u_{k,i} = -\frac{\mathrm{i}k_i}{k^2}\theta_k\,. \tag{3.34}$$

Transforming the second order equations, Eq (3.29), and using Eq. (3.34), we obtain in Fourier space

$$\begin{aligned}
\delta_k^{(2)\prime} - \theta_k^{(2)} &= D_+^2 \int d^3p\, d^3q\, \delta_{\mathrm{D}}^{(3)}(\boldsymbol{k}-\boldsymbol{p}-\boldsymbol{q})\frac{\boldsymbol{k}\cdot\boldsymbol{p}}{p^2}\delta_{p0}\delta_{q0}\,,\\
\theta_k^{(2)\prime} + \left(\frac{3}{2}\frac{\Omega_m}{f^2} - 1\right)\theta_k^{(2)} - \frac{3}{2}\frac{\Omega_m}{f^2}\delta_k^{(2)} &= D_+^2 \int d^3p\, d^3q\, \delta_{\mathrm{D}}^{(3)}(\boldsymbol{k}-\boldsymbol{p}-\boldsymbol{q})\frac{k^2(\boldsymbol{p}\cdot\boldsymbol{q})}{2p^2q^2}\delta_{p0}\delta_{q0}\,,
\end{aligned} \tag{3.35}$$

where $\delta_{\mathrm{D}}^{(3)}$ denotes the 3D Dirac delta distribution and $\boldsymbol{k} = \boldsymbol{p}+\boldsymbol{q}$ ensures momentum conservation as required by translation invariance in a spatially homogeneous Universe. While the linear terms on the left-hand side are easy to convert to Fourier space we obtain convolution integrals on the right-hand side for the nonlinear term after inserting the linear solution. Let us define the scale-dependent integral on the right-hand side of the second-order continuity equation as $S_\delta(\boldsymbol{k})$ and the one of the second-order Euler equation as $S_\theta(\boldsymbol{k})$.
We notice that only the source terms in Eq. (3.35) are explicitly time-dependent via D_+ (by using the approximation $\Omega_m/f^2 \to 1$). This allows one to make a power-law ansatz for the solution of $\delta^{(2)}$ and $\theta^{(2)}$:

$$\delta^{(2)}(\boldsymbol{k},\tau) = A_\delta(\boldsymbol{k})D_+^2(\tau)\,; \qquad \theta^{(2)}(\boldsymbol{k},\tau) = A_\theta(\boldsymbol{k})D_+^2(\tau)\,. \tag{3.36}$$

Plugging this into Eq. (3.35) we can solve for the scale-dependent part which yields

$$\begin{aligned}
A_\delta(\boldsymbol{k}) &= \frac{5}{7}S_\delta(\boldsymbol{k}) - \frac{2}{7}S_\theta(\boldsymbol{k})\,,\\
A_\theta(\boldsymbol{k}) &= -\frac{3}{7}S_\delta(\boldsymbol{k}) + \frac{4}{7}S_\theta(\boldsymbol{k})\,.
\end{aligned} \tag{3.37}$$

Thus, the solution at second order is

$$\begin{aligned}
\delta_k^{(2)} &= D_+^2 \int d^3p\, d^3q\, \delta_{\mathrm{D}}^{(3)}(\boldsymbol{k}-\boldsymbol{p}-\boldsymbol{q})F_2(\boldsymbol{p},\boldsymbol{q})\delta_{p0}\delta_{q0}\,,\\
\theta_k^{(2)} &= D_+^2 \int d^3p\, d^3q\, \delta_{\mathrm{D}}^{(3)}(\boldsymbol{k}-\boldsymbol{p}-\boldsymbol{q})G_2(\boldsymbol{p},\boldsymbol{q})\delta_{p0}\delta_{q0}\,,
\end{aligned} \tag{3.38}$$

where the second-order *kernels* are given by

$$F_2(\boldsymbol{p},\boldsymbol{q}) = \frac{5}{7}+\frac{1}{2}\frac{\boldsymbol{p}\cdot\boldsymbol{q}}{pq}\left(\frac{p}{q}+\frac{q}{p}\right)+\frac{2}{7}\frac{(\boldsymbol{p}\cdot\boldsymbol{q})^2}{p^2q^2}\,,$$
$$G_2(\boldsymbol{p},\boldsymbol{q}) = \frac{3}{7}+\frac{1}{2}\frac{\boldsymbol{p}\cdot\boldsymbol{q}}{pq}\left(\frac{p}{q}+\frac{q}{p}\right)+\frac{4}{7}\frac{(\boldsymbol{p}\cdot\boldsymbol{q})^2}{p^2q^2}\,, \tag{3.39}$$

which completely describe the scale-dependence of the second-order solutions. They are symmetrized in their arguments since they are integrated against a symmetric integrand. When going e.g. to third-order one has to insert products of $\delta^{(1)}$ and $\delta^{(2)}$, $\theta^{(2)}$ to capture the third-order source terms. This can be continued to any higher order. The nth order solution will be

$$\delta_k^{(n)} = D_+^n\int_{q_{1\ldots n}} F_n(\boldsymbol{q}_1,\ldots,\boldsymbol{q}_n)\delta_{q_1 0}\ldots\delta_{q_n 0}\,,$$
$$\theta_k^{(n)} = D_+^n\int_{q_{1\ldots n}} G_n(\boldsymbol{q}_1,\ldots,\boldsymbol{q}_n)\delta_{q_1 0}\ldots\delta_{q_n 0} \tag{3.40}$$

where $\int_{q_{1\ldots n}} = \int \mathrm{d}^3q_1\ldots\mathrm{d}^3q_n\,\delta_{\rm D}^{(3)}(\boldsymbol{k}-\sum_{i=1}^n\boldsymbol{q}_i)$. Each nth order solution $\delta^{(n)},\theta^{(n)}$ simply evolves with time as D_+^n as initialized in the growing mode. This compact result exactly determines how structure in the Universe evolves nonlinearly in SPT. By defining the mode coupling terms in Eq. (3.35) via[1]

$$\alpha_{pq}\equiv\frac{\boldsymbol{k}\cdot\boldsymbol{p}}{p^2},\qquad \beta_{pq}\equiv\frac{k^2(\boldsymbol{p}\cdot\boldsymbol{q})}{2p^2q^2} \tag{3.41}$$

where $\boldsymbol{k}\equiv\boldsymbol{p}+\boldsymbol{q}$ and using the convention $\int_{pq}\equiv\int\mathrm{d}^3p\,\mathrm{d}^3q\,\delta_{\rm D}^{(3)}(\boldsymbol{k}-\boldsymbol{p}-\boldsymbol{q})$ we can write down the set of evolution equations for the full nonlinear fields as

$$\delta_k'-\theta_k = \int_{pq}\alpha_{pq}\theta_p\delta_q\,,$$
$$\theta_k'+\left(\frac{3}{2}\frac{\Omega_m}{f^2}-1\right)\theta_k-\frac{3}{2}\frac{\Omega_m}{f^2}\delta_k = \int_{pq}\beta_{pq}\theta_p\theta_q\,, \tag{3.42}$$

where the evolution of δ_k, θ_k is determined by the coupling of fields at all pairs of wave vectors $\boldsymbol{p}$ and $\boldsymbol{q}$ whose sum is $\boldsymbol{k}$. F_n and G_n in Eq. (3.40) are dimensionless and homogeneous functions of the wave vectors $\{\boldsymbol{q}_1,\ldots,\boldsymbol{q}_n\}$ which are constructed from the fundamental mode coupling functions α_{pq} and β_{pq} according to the recursion relations which are obtained by solving the nth order equation analogously as for the $n=2$ case [141, 142]:

$$F_n(\boldsymbol{q}_1,\ldots,\boldsymbol{q}_n) = \sum_{m=1}^{n-1}\frac{G_m(\boldsymbol{q}_1,\ldots,\boldsymbol{q}_m)}{(2n+3)(n-1)}[(2n+1)\alpha_{pq}F_{n-m}(\boldsymbol{q}_{m+1},\ldots,\boldsymbol{q}_n)$$
$$+2\beta_{pq}G_{n-m}(\boldsymbol{q}_{m+1},\ldots,\boldsymbol{q}_n)]\,,$$
$$G_n(\boldsymbol{q}_1,\ldots,\boldsymbol{q}_n) = \sum_{m=1}^{n-1}\frac{G_m(\boldsymbol{q}_1,\ldots,\boldsymbol{q}_m)}{(2n+3)(n-1)}[3\alpha_{pq}F_{n-m}(\boldsymbol{q}_{m+1},\ldots,\boldsymbol{q}_n)$$
$$+2n\beta_{pq}G_{n-m}(\boldsymbol{q}_{m+1},\ldots,\boldsymbol{q}_n)]\,, \tag{3.43}$$

[1] Note that β_{pq} is symmetric in its argument while α_{pq} is not since the latter couples in general two different fields.

where $\boldsymbol{p} \equiv \boldsymbol{q}_1 + \cdots + \boldsymbol{q}_m$, $\boldsymbol{q} \equiv \boldsymbol{q}_{m+1} + \cdots + \boldsymbol{q}_n$, $\boldsymbol{k} \equiv \boldsymbol{p} + \boldsymbol{q}$ and $F_1 = G_1 \equiv 1$. Due to the underlying symmetry those kernels satisfy certain relations [138]:

(*i*) When the total sum $\boldsymbol{k} = \boldsymbol{q}_1 + \cdots + \boldsymbol{q}_n$ goes to zero but the individual $\boldsymbol{q}_i$ do not, the kernels scale as

$$F_n^{(s)} \propto k^2 \,. \tag{3.44}$$

(*ii*) When the total sum $\boldsymbol{k}$ stays fixed but some of the arguments $\boldsymbol{q}_i$ get large, the kernels are suppressed. That is for a particular $p \gg q_i$, we get:

$$F_n^{(s)}(\boldsymbol{q}_1, \ldots, \boldsymbol{q}_{n-2}, \boldsymbol{p}, -\boldsymbol{p}) \propto \frac{k^2}{p^2} \,. \tag{3.45}$$

(*iii*) When on the other hand an individual $\boldsymbol{q}_i$ goes to zero we get an infrared divergence

$$F_n^{(s)} \propto \frac{\boldsymbol{q}_i}{q_i^2} \,, \tag{3.46}$$

coming from the infrared behaviour of α_{pq} and β_{pq}.

Points (*ii*) and (*iii*) also hold for G_n. Note that the relations above only hold for a symmetrized version of the kernels $F_n^{(s)}$, which is obtained by a summation of F_n with all possible permutations of the variables.

3.3 Equations of motion in matrix form

It is convenient to define a vector of the perturbation variables as

$$\psi \equiv (\delta, \theta) \,. \tag{3.47}$$

The equations of motion, Eq. (3.42) can then be brought into a matrix form [143]

$$\psi'_{k,a}(\eta) + \Omega_{ab}(\eta)\, \psi_{k,b}(\eta) = \int_{pq} \gamma_{abc}(\boldsymbol{p}, \boldsymbol{q}) \psi_{p,b}(\eta) \psi_{q,c}(\eta) \,, \tag{3.48}$$

where the subscript again labels the wavenumber as well as the component of the vector ψ. In addition, it is assumed that repeated indices are summed over. The linear dynamics is captured by the matrix Ω_{ab} and reads

$$\Omega = \begin{pmatrix} 0 & -1 \\ -\frac{3}{2}\frac{\Omega_m}{f^2} & \frac{3}{2}\frac{\Omega_m}{f^2} - 1 \end{pmatrix} \overset{\text{EdS}}{=} \begin{pmatrix} 0 & -1 \\ -\frac{3}{2} & \frac{1}{2} \end{pmatrix} , \tag{3.49}$$

which we note is constant in the EdS case. The nonlinear terms on the right-hand side are described by the mode coupling functions $\gamma_{abc}(\boldsymbol{p}, \boldsymbol{q})$, which we refer to as *vertices*. It is implicitly assumed that the mode a adopts wave vector $\boldsymbol{k}$, and b, c adopt $\boldsymbol{p}, \boldsymbol{q}$ respectively. In fact, they have only two entries being

$$\gamma_{\delta\theta\delta}(\boldsymbol{p}, \boldsymbol{q}) = \frac{1}{2}\alpha_{pq} = \frac{\boldsymbol{k} \cdot \boldsymbol{p}}{2p^2} \,, \tag{3.50}$$

$$\gamma_{\theta\theta\theta}(\boldsymbol{p}, \boldsymbol{q}) = \beta_{pq} = \frac{k^2 (\boldsymbol{p} \cdot \boldsymbol{q})}{2p^2 q^2} \,. \tag{3.51}$$

The first vertex $\gamma_{\delta\theta\delta}$ is identical to the coupling function defined in Eq. (3.41) up to a factor 1/2 since we are aiming for integrands which are symmetric in their arguments $\boldsymbol{p}$ and $\boldsymbol{q}$ and thus also account for $\gamma_{\delta\delta\theta} = \alpha_{qp}/2$ where δ and θ swap their arguments. In $\gamma_{\theta\theta\theta}$ we can already perform the symmetrization at the vertex level since it describes the coupling of two identical fields, i.e. $b = c$. It is worth noting that in the large-scale limit $\boldsymbol{k} \to 0$, Eq. (3.42) recovers the linear theory since α_{pq} and β_{pq} vanish in the limit where the sum of their arguments go to zero. In matrix notation the perturbative expansion becomes

$$\psi_{k,a}(\eta) = \sum_{n=1}^{\infty} e^{n\eta} \psi_{k,a}^{(n)} \tag{3.52}$$

where now $\psi_k^{(n)} = \left(\delta_k^{(n)}, \theta_k^{(n)}\right)$ is time-independent and the summand is equivalent to Eq. (3.40). This is analogous to Eq. (3.36) for nth order in perturbation theory with $\Omega_m/f^2 = 1$. The solution is thus separable in scale and time which allows us to obtain analytical expressions for $\psi_{k,a}^{(n)}$. Inserting the expansion in Eq. (3.48) yields

$$(n\delta_{ab} + \Omega_{ab})\psi_{k,b}^{(n)} = \int_{pq} \gamma_{abc}(\boldsymbol{p}, \boldsymbol{q}) \sum_{m=1}^{n-1} \psi_{p,b}^{(n-m)} \psi_{q,c}^{(m)} \,. \tag{3.53}$$

By defining $s_{ab}^{-1}(n) = (n\delta_{ab} + \Omega_{ab})$ we then get

$$\psi_{k,a}^{(n)} = s_{ab}(n) \int_{pq} \gamma_{bcd}(\boldsymbol{p}, \boldsymbol{q}) \sum_{m=1}^{n-1} \psi_{p,c}^{(n-m)} \psi_{q,d}^{(m)} \,, \tag{3.54}$$

where

$$s(n) = \frac{1}{(2n+3)(n-1)} \begin{pmatrix} 2n+1 & 2 \\ 3 & 2n \end{pmatrix} . \tag{3.55}$$

The linear solution ($n = 1$) is simply given by the initial condition $\psi_{k,a}^{(1)} = i_a \, \delta_{k0}(\eta_{\rm ini})$ with $i = (1, 1)$ and $\eta_{\rm ini}$ corresponds to an initial reference epoch. Then the repeated application of Eq. (3.54) gives $\psi_{k,a}^{(n)} = i_a \, \mathcal{O}\left([\delta_{k0}]^n\right)$ which then amounts to Eq. (3.40), but now we factored out the growth factors as

$$\psi_{k,a}^{(n)} = \int_{q_{1\ldots n}} F_{n,a}(\boldsymbol{q}_1, \ldots, \boldsymbol{q}_n) \delta_{q_1 0} \ldots \delta_{q_n 0} \,, \tag{3.56}$$

where $F_{n,a} = (F_n, G_n)$. This can be used to obtain solutions for the nth order kernels $F_{n,a}$ by inserting Eq. (3.56) into Eq. (3.54) which gives

$$F_{n,a}(\boldsymbol{q}_1, \ldots, \boldsymbol{q}_n) = s_{ab}(n) \sum_{m=1}^{n-1} \left[\gamma_{bcd}(\boldsymbol{q}_{1\ldots m}, \boldsymbol{q}_{m+1\ldots n}) F_{m,c}(\boldsymbol{q}_1, \ldots, \boldsymbol{q}_m) F_{n-m,d}(\boldsymbol{q}_{m+1}, \ldots, \boldsymbol{q}_n)\right]^{(s)} , \tag{3.57}$$

where $\boldsymbol{q}_{1\ldots m} = \boldsymbol{q}_1 + \cdots + \boldsymbol{q}_m$ and so on. The right-hand side is understood to be symmetrized with respect to permutations exchanging momenta in the $\{\boldsymbol{q}_1, \ldots, \boldsymbol{q}_m\}$ set with momenta in the $\{\boldsymbol{q}_{m+1}, \ldots, \boldsymbol{q}_n\}$ set, i.e. summing over all permuted expressions and dividing by the total number of permutations $N_m = \frac{n!}{m!(n-m)!}$. This way, the nth order kernel will be symmetric under exchange of momentum arguments provided that all lower order kernels are. The unsymmetrized recursion relations in terms of the vertices in Eq. (3.43) are obtained in this way. We initialize with $F_{1,a} = i_a$.

In fact, the ansatz in Eq. (3.52) only represents the asymptotic time-dependence given by the growing mode ($\propto D_+^n$). To capture also any transient behavior one can derive the following solution for the Fourier amplitude (see [144] for details)

$$\psi_{k,a}(\eta) = g_{ab}(\eta)\psi^{(1)}_{k,b} + \int_{\eta_{\rm ini}}^{\eta} \mathrm{d}\eta' \int_{pq} g_{ab}(\eta-\eta')\gamma_{bcd}(\boldsymbol{p},\boldsymbol{q})\psi_{p,c}(\eta')\psi_{q,d}(\eta')\,, \tag{3.58}$$

where the *linear propagator* $g_{ab}(\eta)$ is defined as

$$g_{ab}(\eta) = \frac{e^{\eta}}{5}\begin{pmatrix} 3 & 2 \\ 3 & 2 \end{pmatrix} + \frac{e^{-3\eta/2}}{5}\begin{pmatrix} 2 & -2 \\ -3 & 3 \end{pmatrix}. \tag{3.59}$$

In the limit $\eta \to 0$ we have $g_{ab} \to \delta_{ab}$. The first term corresponds to the growing mode and the second one to the decaying mode (see Eq. 3.22). The nonlinear correction to the propagator is given by the integral in Eq. (3.58). To obtain the standard asymptotic time-dependence in the growing mode one has to take the growing mode initial conditions $\psi^{(1)}_{k,a} \propto (1,1)$ with the initial time being set to $\eta_{\rm ini} \to -\infty$, placing the initial conditions "infinitely far away" in the past.

Power spectrum

The results so far showed us that perturbation theory can predict statistics of the nonlinear density in terms of the statistics of the linear field δ_{k0}. We can write the full equal-time power spectrum of $\psi_{k,a}(\eta)$ as the ensemble average

$$\langle \psi_{k,a}(\eta)\,\psi_{k',b}(\eta)\rangle = \sum_{n,l=1,2,\ldots}^{n+l\,\text{even}} e^{(n+l)\eta}\left\langle \psi^{(n)}_{k,a}\,\psi^{(l)}_{k',b}\right\rangle. \tag{3.60}$$

This tells us that we still have to sum up infinitely many terms which is not very practical. In perturbation theory one has to truncate the series anyways as long as the neglected terms are smaller than the ones we include which represents perturbative validity. The first four terms read

$$\langle \psi_{k,a}(\eta)\,\psi_{k',b}(\eta)\rangle = e^{2\eta}\left\langle \psi^{(1)}_{k,a}\,\psi^{(1)}_{k',b}\right\rangle + e^{4\eta}\left\langle \psi^{(2)}_{k,a}\,\psi^{(2)}_{k',b}\right\rangle + e^{4\eta}\left\langle \psi^{(1)}_{k,a}\,\psi^{(3)}_{k',b}\right\rangle + e^{4\eta}\left\langle \psi^{(3)}_{k,a}\,\psi^{(1)}_{k',b}\right\rangle + \ldots\,, \tag{3.61}$$

where the first term corresponds to the linear power spectrum and for growing mode initial conditions with $F_{1,a} = i_a = (1,1)$ it simplifies to $e^{2\eta}\,\langle \delta_{k0}\,\delta_{k'0}\rangle = e^{2\eta}\delta_{\rm D}^{(3)}(\boldsymbol{k}+\boldsymbol{k'})P_0(k)$ for all $a,b = \delta,\theta$. In particular if $a = b$ we are dealing with the auto power spectrum whereas $a \neq b$ refers to the cross power spectrum. The input power spectrum $P_0(k)$ can be referred to the realistic ΛCDM matter power spectrum, as defined in Eq. (2.23) and shown in Fig. 2.4 which will be used in Sec. 3.4 and Ch. 10. On the other hand, one could also use toy models like power-law behaviors without the turnover in the input power spectrum, mostly used in this thesis. Note that $e^{\eta} = a(\tau)$ in EdS. The remaining terms correspond to the first nonlinear correction to the power spectrum, i.e. the *next-to-leading order* (NLO) result. Assuming that δ_{k0} is a Gaussian random field all terms where $n+l$ is odd correspond to expectation values of an odd number of Gaussian fields which vanish. This means that the *next-to-next-to-leading order* (NNLO) consists of terms where $n+l = 6$ and so forth. The NLO correction can be calculated

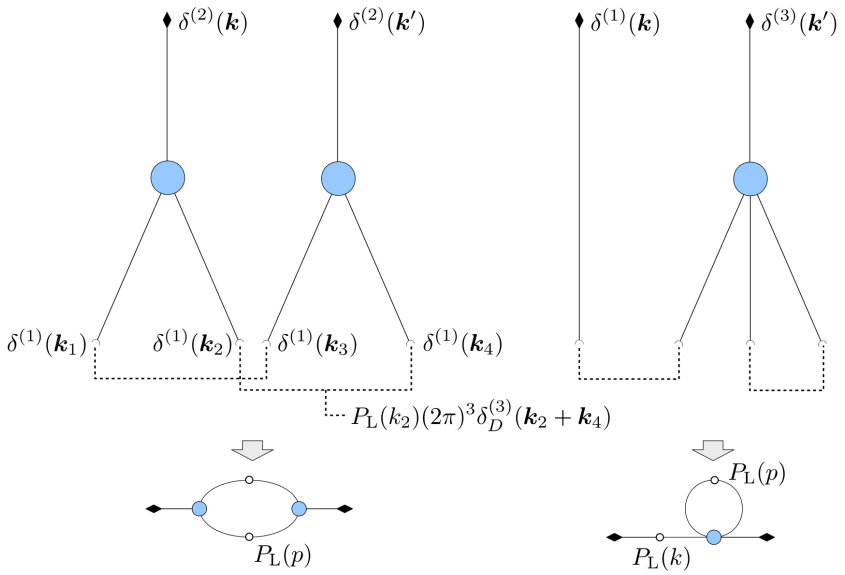

Figure 3.1: This figure illustrates the next-to-leading-order contributions to the matter power spectrum. The upper diagrams depict calculations by connecting linear density fields using dashed lines, yielding linear power spectra and Dirac deltas. The lower diagrams use open circles to represent connections of linear fields, clarifying the "one-loop" terminology as each loop corresponds to an integral over wavenumber [4].

with Eqs. (3.56, 3.57) and using Wick's theorem [145]

$$\begin{aligned}\langle\delta_{k_10}\,\delta_{k_20}\,\delta_{k_30}\,\delta_{k_40}\rangle &= \delta_{\rm D}^{(3)}(\boldsymbol{k}_1+\boldsymbol{k}_2)\delta_{\rm D}^{(3)}(\boldsymbol{k}_3+\boldsymbol{k}_4)P_0(k_1)P_0(k_3)\\ &\quad+\delta_{\rm D}^{(3)}(\boldsymbol{k}_1+\boldsymbol{k}_3)\delta_{\rm D}^{(3)}(\boldsymbol{k}_2+\boldsymbol{k}_4)P_0(k_1)P_0(k_2)\\ &\quad+\delta_{\rm D}^{(3)}(\boldsymbol{k}_1+\boldsymbol{k}_4)\delta_{\rm D}^{(3)}(\boldsymbol{k}_2+\boldsymbol{k}_3)P_0(k_1)P_0(k_2)\,. \end{aligned}\tag{3.62}$$

The two NLO terms consist of two power spectra which can be represented in a diagrammatic way (see Fig. 3.1). Each of it contains two linear power spectra (see Eq. 3.62). The linear power spectrum arises from a connection of two lines (P_L in the figure). For the nonlinear fields we first have two identical second-order fields connected symmetrically illustrated by the left diagram and can also be referred to $P_{\delta\delta}^{(22)}$ as part of the NLO correction. The remaining diagram corresponds to the coupling of a linear field with a third-order field where two lines of the latter one form a *loop* (right diagram corresponding to other NLO correction $P_{\delta\delta}^{(13)}$). Therefore, the NLO correction is more commonly called the *one-loop correction* to the linear power spectrum as the corresponding diagrams (similar as Feynman diagrams in quantum field theory) contain exactly one loop. The NNLO correction would correspond to diagrams containing two loops and so on. We mostly concentrate on one-loop corrections throughout the thesis except in Sec. 9.4 where we discuss nonlinear vorticity generation. In this language, the linear power spectrum is also called *tree-level* contribution. In total, the nonlinear power spectrum becomes

$$P_{ab}(k,\eta) = P_{ab}^{\rm lin}(k,\eta)+P_{ab}^{1-\rm loop}(k,\eta)+P_{ab}^{2-\rm loop}(k,\eta)+\dots\,,\tag{3.63}$$

and in general, one can define the *L-loop power spectrum* by [146]

$$\delta_D(\boldsymbol{k}+\boldsymbol{k}')P_{ab}^{L-\mathrm{loop}}(k,\eta) \equiv \sum_{m=1}^{2L+1} e^{2(L+1)\eta}\langle \psi_{k,a}^{(m)}\psi_{k',b}^{(2L+2-m)}\rangle\,, \tag{3.64}$$

where for example the linear and one-loop contributions are given by [48, 147]

$$\begin{aligned} P_{ab}^{\mathrm{lin}}(k,\eta) &= e^{2\eta}F_{1,a}F_{1,b}P_0(k)\,,\\ P_{ab}^{1-\mathrm{loop}}(k,\eta) &= P_{ab}^{(22)}(k,\eta)+2P_{ab}^{(13)}(k,\eta)\,, \end{aligned} \tag{3.65}$$

with

$$\begin{aligned} P_{ab}^{(22)}(k,\eta) &\equiv e^{4\eta}\int \mathrm{d}^3q\Big\{2F_{2,a}(\boldsymbol{k}-\boldsymbol{q},\boldsymbol{q})F_{2,b}(\boldsymbol{k}-\boldsymbol{q},\boldsymbol{q})P_0(|\boldsymbol{k}-\boldsymbol{q}|)P_0(q)\Big\}\,,\\ 2P_{ab}^{(13)}(k,\eta) &\equiv e^{4\eta}\int \mathrm{d}^3q\Big\{3F_{1,a}F_{3,b}(\boldsymbol{k},\boldsymbol{q},-\boldsymbol{q})P_0(k)P_0(q)\\ &\quad +3F_{3,a}(\boldsymbol{k},\boldsymbol{q},-\boldsymbol{q})F_{1,b}P_0(k)P_0(q)\Big\}\,. \end{aligned} \tag{3.66}$$

Here q is referred to as the loop momentum. The time-dependence is completely determined by powers of the growth factor $D_+(\tau)$ in SPT. The wavenumber-dependence is captured by the corresponding nonlinear kernels. We have explicitly written down where the *linear* kernels would enter the results although they are exactly one for all $a,b=\delta,\theta$. This will be important subsequently when we go beyond the perfect fluid approximation where the linear kernels differ from unity. The SPT kernels are obtained via the recursion equation Eq. (3.43). We omitted the superscript (s) and assume in the following that all kernels when calculated are symmetrized. The input spectrum $P_0(k)$ (or $P_L(k)$) can be computed by using numerical Boltzmann solvers such as CLASS [148] or CAMB [149]. In the one-loop calculation there is a delicate cancellation taking place, namely when $q \ll k$ there are large contributions of individual terms which cancel upon summation. It is advantageous for the numerical Monte Carlo integration to shift this cancellation to the integrand level by introducing $2\Theta(|\boldsymbol{k}-\boldsymbol{q}|-|\boldsymbol{q}|)$ where $\Theta(x)$ denotes the Heaviside function and then symmetrizing it with respect to the substitution $\boldsymbol{q}\to-\boldsymbol{q}$ [150].

3.4 Next-to-leading order matter power spectrum

As we have seen, in order to calculate the NLO or one-loop result for the matter density power spectrum $P_{\delta\delta}$ one needs to solve third-order perturbation theory. We briefly sketch how one can find analytical results for the nonlinear kernels and thereby determine the asymptotic behavior of the NLO correction. To compute the third-order kernel in Eq. (3.66) we use the recursion relation Eq. (3.43) which gives

$$\begin{aligned} F_3(\boldsymbol{q}_1,\boldsymbol{q}_2,\boldsymbol{q}_3) &= \frac{1}{18}[7\alpha_{pq}F_2(\boldsymbol{q}_2,\boldsymbol{q}_3)+2\beta_{pq}G_2(\boldsymbol{q}_2,\boldsymbol{q}_3)]\\ &\quad +\frac{G_2(\boldsymbol{q}_1,\boldsymbol{q}_2)}{18}[7\alpha_{pq}+2\beta_{pq}]\,. \end{aligned} \tag{3.67}$$

Note that the summation over m yields two terms and the symmetrization process includes all the 3! permutations of the three wavevectors. Using from Eq. (3.39), that $F_2(\boldsymbol{q},-\boldsymbol{q})=G_2(\boldsymbol{q},-\boldsymbol{q})=0$

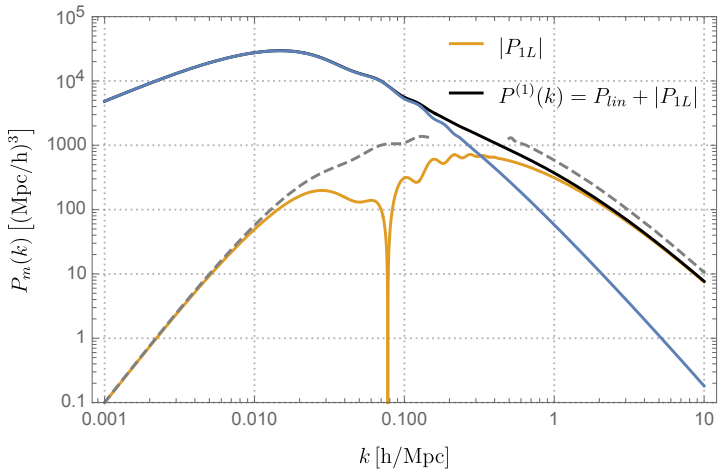

Figure 3.2: The one-loop contribution to the linear power spectrum (brown) as well as the sum of both denoting the nonlinear power spectrum (up to one-loop) for ΛCDM (see Eq. (2.25)). For comparison the linear power spectrum (blue) is also plotted which deviates from the nonlinear power spectrum at small scales as expected. The dashed lines show the asymptotic behavior at small k (see Eq. (3.72), since it is dominated by the $P_{\delta\delta}^{(13)}(k)$-limit), and at large k (see Eq. (3.78)).

and considering the fact that the parameters $\boldsymbol{p}$ and $\boldsymbol{q}$ of the mode coupling functions α_{pq} and β_{pq} depend differently on the wave vectors $\boldsymbol{q}_i$ for $m = 1$ and $m = 2$ respectively after adding the permutations one arrives at

$$\begin{aligned} 108 \cdot F_3^{(s)}(\boldsymbol{k}, \boldsymbol{q}, -\boldsymbol{q}) = {} & G_2(\boldsymbol{k}, \boldsymbol{q})\ [14\alpha(\boldsymbol{k}+\boldsymbol{q}, -\boldsymbol{q}) + 8\beta(\boldsymbol{k}+\boldsymbol{q}, -\boldsymbol{q})] \\ & + F_2(\boldsymbol{k}, \boldsymbol{q})\, 14\alpha(-\boldsymbol{q}, \boldsymbol{k}+\boldsymbol{q}) \\ & + G_2(\boldsymbol{k}, -\boldsymbol{q})\ [14\alpha(\boldsymbol{k}-\boldsymbol{q}, \boldsymbol{q}) + 8\beta(\boldsymbol{k}-\boldsymbol{q}, \boldsymbol{q})] \\ & + F_2(\boldsymbol{k}, -\boldsymbol{q})\, 14\alpha(\boldsymbol{q}, \boldsymbol{k}-\boldsymbol{q})\,. \end{aligned} \tag{3.68}$$

Consider $P^{(13)}$, to put this expression into a form with scalar variables, we use spherical coordinates and rewrite the scalar products as $\boldsymbol{k} \cdot \boldsymbol{q} = kq\cos\theta$ where θ is the angle between $\boldsymbol{k}$ and $\boldsymbol{q}$. Using the definitions Eqs. (3.39, 3.41), it is possible to perform the angular integrations ($\int \mathrm{d}^3q = \int q^2 \mathrm{d}q\, \mathrm{d}\phi\, \mathrm{d}\cos\theta$) and obtain [151]

$$2P_{\delta\delta}^{(13)}(k, \eta) = 6e^{4\eta} \int \mathrm{d}q\, q^2\, g(k/q) P_0(k) P_0(q)\,, \tag{3.69}$$

where

$$g(x) = \frac{2\pi}{756}\left(50 - 79x^2 - 21\frac{1}{x^2} + 6x^4 + \frac{3}{4}\frac{(-7 + 19x^2 - 15x^4 + x^6 + 2x^8)\ln\frac{(1-x)^2}{(1+x)^2}}{x^3}\right)\,. \tag{3.70}$$

Using the small-/large-x behavior of this function,

$$\frac{g(x)}{2\pi} \to \begin{cases} -\frac{61}{945}x^2 & \text{for } x \to 0\,, \\ -\frac{1}{9}x^2 & \text{for } x \to \infty\,, \end{cases} \tag{3.71}$$

we find the IR/UV sensitivity of the loop correction to be

$$P_{\delta\delta}^{(13)}(k,\eta) \to e^{4\eta} \times \begin{cases} -\frac{61}{105}\sigma_d^2 k^2\, P_0(k) & \text{for } k \to 0\,, \\ -\frac{1}{2}\sigma_d^2 k^2\, P_0(k) & \text{for } k \to \infty\,, \end{cases} \tag{3.72}$$

where

$$\sigma_d^2 \equiv \frac{4\pi}{3}\int_0^\infty \mathrm{d}q\, P_0(q) \simeq 8870\ (\mathrm{Mpc/h})^2\,. \tag{3.73}$$

Next, we look at $P^{(22)}$ which can be written as

$$P_{\delta\delta}^{(22)}(k,\eta) = 4e^{4\eta}\int_\Theta q^2 g_2(k/q,\cos(\theta)) P_0(q) P_0(|\boldsymbol{k}-\boldsymbol{q}|)\,. \tag{3.74}$$

The same procedure as above can be applied but now $g_2(x,\cos(\theta))$ and $P_0(|\boldsymbol{k}-\boldsymbol{q}|)$ are angle dependent which in general makes it impossible to reduce it to a 1D integral. Instead a reduction to a 2D integral is possible, after integrating over $\cos(\theta)$ one gets the following limits

$$\frac{g_2(x)}{2\pi} \to \begin{cases} \frac{9}{98}x^4 & \text{for } x \to 0 \\ \frac{1}{6}x^2 & \text{for } x \to \infty. \end{cases} \tag{3.75}$$

Note that to first order $P_0(|\boldsymbol{k}-\boldsymbol{q}|)$ does not depend on the angle in both limits. There is a singularity also for $P^{(13)}$, $g(x) \propto x^2$ for $x \to \infty$ which cancels against $P^{(22)}$ contributions. In addition the integrand has a symmetry for $q \leftrightarrow |\boldsymbol{k}-\boldsymbol{q}|$. Introducing a Heaviside function one can circumvent the singularity at $|\boldsymbol{k}-\boldsymbol{q}| \to 0$ which from a numerical point of view is less stable than the infrared limit $q \to 0$. With this method one can therefore enhance the numerical stability of the integration by using the symmetry of the integrand. More precisely, we use following integration limits

$$\begin{aligned} 2\int_\Theta &\equiv \int \mathrm{d}q \int \mathrm{d}\cos(\theta)\Theta(|\boldsymbol{k}-\boldsymbol{q}|-q) \\ &= \int_0^{k/2}\mathrm{d}q\int_{-1}^{1}\mathrm{d}\cos(\theta) + \int_{k/2}^{\infty}\mathrm{d}q\int_{-1}^{\frac{k}{2q}}\mathrm{d}\cos(\theta)\,. \end{aligned} \tag{3.76}$$

We find the following IR/UV behavior for $P^{(22)}$

$$P_{\delta\delta}^{(22)}(k,\eta) \to e^{4\eta} \times \begin{cases} \frac{36}{49}\pi k^4 \int \mathrm{d}q\, P_0(q)^2/q^2 & \text{for } k \to 0\,, \\ \sigma_d^2 k^2\, P_0(k) & \text{for } k \to \infty\,. \end{cases} \tag{3.77}$$

with $\int \mathrm{d}q\, P(q)^2/q^2 \approx 2.09 \cdot 10^{11}\ (\mathrm{Mpc/h})^7$. For numerical evaluation one instead uses Λ as the scale at which we cut off the initial power spectrum, and which is typically taken as the nonlinear scale where perturbation theory is expected to break down. One notes that for $k \to \infty$ both contributions $(2P_{\delta\delta}^{(13)} + P_{\delta\delta}^{(22)})$ exactly cancel up to first order in q/k (see Eqs. (3.72, 3.77)). $P_{\delta\delta}^{(22)}$ is positive definite and describes the effects of mode-coupling between waves with wavenumbers $\boldsymbol{k}-\boldsymbol{q}$ and $\boldsymbol{q}$. Imprints of acoustic oscillations in this contribution are therefore washed out. In general $P_{\delta\delta}^{(13)}$ is negative leading to effects of previrialization. It does not contain the aforementioned mode-coupling.

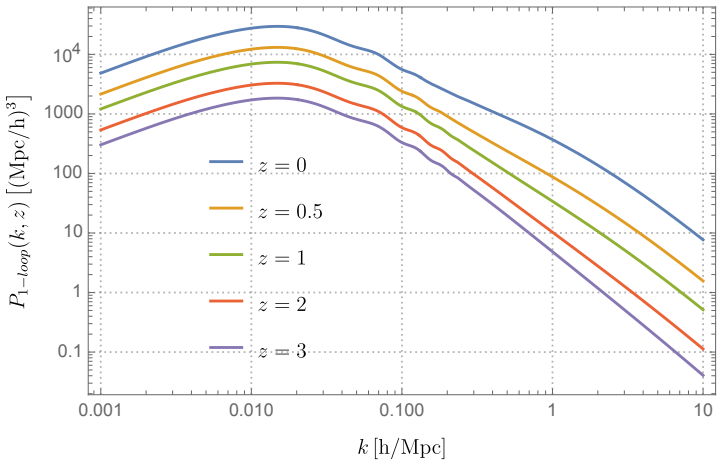

Figure 3.3: Nonlinear power spectrum up to one-loop for various redshifts. The small bump at low redshift at small scales denoting high one-loop contribution eventually vanishes at high redshift.

Finally the total one-loop contribution is shown in Fig. 3.2 (brown) evaluated today $\eta = 0$. Hence the NLO result (black line) deviates significantly from the linear power spectrum at small scales which is also observed from galaxy surveys [22]. To obtain the limiting behavior of $P^{1L}_{\delta\delta}(k,\eta)$ for large k one has to expand both $g(x)$ and $g_2(x)$ to next orders and also $P_0(|\boldsymbol{k}-\boldsymbol{q}|)$ gets new terms dependent on k, q aside from $P_0(k)$. All this was treated in Ref. [152] arriving at

$$P^{1L}_{\delta\delta}(k,\eta) \to e^{4\eta}\left(\frac{2519}{2205} - \frac{23}{42}k\partial_k + \frac{1}{10}[k\partial_k]^2\right) P_0(k)\sigma_l(k)^2\,, \tag{3.78}$$

where

$$\sigma_l^2(k) \equiv 4\pi \int^k \mathrm{d}q\, q^2 P_0(q)\,. \tag{3.79}$$

The simple time-dependence of the NLO power spectrum is shown in Fig. 3.3 as well as for the dimensionless power spectrum $\Delta_m(k) \equiv k^3 P_m(k)/(2\pi^2)$ in Fig. 3.4 by plotting the spectra for different redshift z. The time-dependence of the one loop contribution is suppressed by $a(\tau)^2$ compared to the linear contribution. Therefore, as we go to earlier epochs the one-loop contribution decreases in amplitude and becomes only visible at smaller scales.

The linear approximation breaks down when δ is of order unity corresponding to $\Delta_m(k)|_{k=k_{\mathrm{nl}}(z)} = 1$, which defines the *nonlinear scale* $k_{\mathrm{nl}}(z)$. From Fig. 3.4 one sees that small scales (i.e. large k-modes) cross the dotted line at $\Delta_m(k) = 1$ earlier which means that small scales turn nonlinear first, and with time larger and larger scales turn nonlinear and form gravitationally bound objects. This is known as *hierarchical clustering*.

Asymptotic behavior for power-law spectras

From mass and momentum conservation one knows that for any nth order kernel

$$F_n(\boldsymbol{k}_1, \ldots, \boldsymbol{k}_n) \propto k^2 \tag{3.80}$$

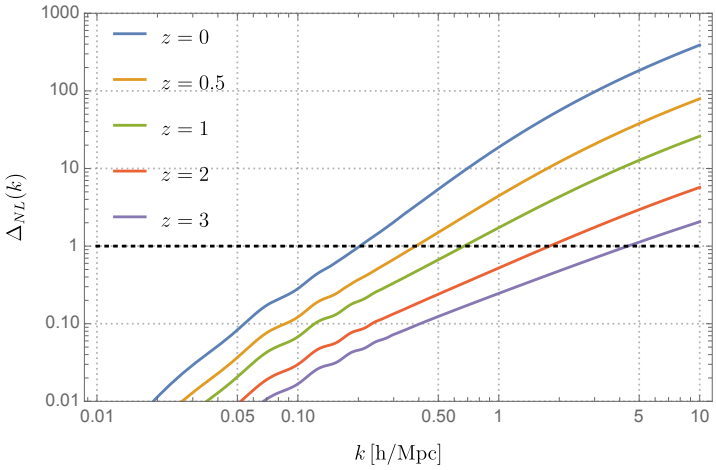

Figure 3.4: The dimensionless one-loop power spectrum demonstrates that small scales turn nonlinear first. The time dependence of the nonlinear scale $k_{\rm nl}$ can be clearly extracted. In the past ever smaller scales are reliable in the linear theory.

in the large-scale limit, i.e. when the sum $\boldsymbol{k} \equiv \sum_i \boldsymbol{k}_i$ of wave vectors goes to zero. For any internal loop wave vector $q \equiv \max_i |k_i|$ (such that $k \ll q$) we obtain [138]

$$F_n(\boldsymbol{k}_1, \ldots, \boldsymbol{k}_n) \propto \frac{k^2}{q^2} \tag{3.81}$$

for $k \to 0$. This allows one to study the UV limit for the integrand at e.g. one-loop. It is defined as

$$P_{\delta\delta}^{1L}(k,\eta) = \int \mathrm{d}\ln q \, P_{\rm Integrand}(k,q,\eta) \tag{3.82}$$

and has two contributions which can be extracted from Eq. (3.66). We now assume power-law input spectra, $P_0(k,\eta) = D_+^2 \, P_0(k) = A \, D_+^2 \, k^{n_s}$. In such a scale-free cosmology one can set the nonlinear scale $k_{\rm nl} = 1\,h/\mathrm{Mpc}$ so that the normalization factor $A = \frac{1}{4\pi}$. This will be motivated in detail in Ch. 6. Both contributions then lead to a UV sensitivity as

$$\begin{aligned} P_{\rm Integrand}^{(13)}(k,q,\eta) &\propto q^{n_s+1} \\ P_{\rm Integrand}^{(22)}(k,q,\eta) &\propto q^{2n_s-1} \end{aligned} \tag{3.83}$$

for $k \ll q$. This means as long as $n_s < 2$ the UV sensitivity is dominated by $P_{\rm Integrand}^{(13)}$. Hence, for input spectra with blue spectral indices, i.e. for $n_s \geq -1$ the one-loop contribution becomes *UV divergent*. Consequently, SPT fails to predict nonlinear corrections in this case. At two-loop, we have following UV limits for its various contributions,

$$\begin{aligned} P_{\rm Integrand}^{(15)}(k,q,\eta) &\propto q^{n_s+1}\,, \\ P_{\rm Integrand}^{(24)}(k,q,\eta) &\propto q^{2n_s-1}\,, \\ P_{\rm Integrand}^{(33),\,\mathrm{I}}(k,q,\eta) &\propto q^{n_s-1}\,, \\ P_{\rm Integrand}^{(33),\,\mathrm{II}}(k,q,\eta) &\propto q^{2n_s-1}\,. \end{aligned} \tag{3.84}$$

In principle $P^{(33),\mathrm{I}}_{\mathrm{Integrand}}$ would converge for $-1 \leq n_s < 1$, but this is irrelevant since the next-to-leading (one-loop) correction is divergent for this range of n_s.

In summary, Standard Perturbation Theory (SPT) has been a foundational framework in cosmology for understanding the growth of cosmic structures. By systematically expanding the equations of motion for density and velocity fields in terms of perturbations, SPT provides valuable insights into the growth of large-scale structures over cosmic time. While powerful in describing the initial stages of structure formation, SPT encounters challenges as perturbations grow nonlinear and interact in complex ways. In addition, its convergence becomes problematic in the nonlinear regime, leading to inaccuracies in predicting power spectra and other observables. Higher order terms introduce UV sensitivity, where small-scale modes dominate the results, making SPT less reliable in highly nonlinear regions. Additionally, SPT does not account for vorticity backreaction and higher cumulants, which are important factors in accurately describing the evolution of density and velocity fields. As a result, an improved approach is needed to overcome these limitations and provide more accurate predictions. This will be tackled in the subsequent chapters by introducing Vlasov Perturbation Theory (VPT).

4 Perturbation theory with higher cumulants

In this chapter, we develop a systematic extension of SPT that includes velocity dispersion and higher cumulants of the distribution function. That is we systematically solve the Vlasov equation perturbatively which we will refer to as *Vlasov Perturbation Theory* (VPT). The aim is to address the shortcomings of the pressureless perfect fluid approximation, and thus obtain a more accurate description of structure formation in the mildly nonlinear regime. We describe the general structure of the extension in perturbation theory including the second cumulant in Sec. 4.1 as well as even higher cumulants in Sec. 4.2. In addition, we discuss linearized solutions in each truncation order. But first of all, we show the physical origin of velocity dispersion and higher cumulants in the simplified setup of spherical collapse.

It is known that eventually during structure formation higher moments will be important [53]. Once one enters the nonlinear regime the SPT description with a well-defined density contrast δ and average velocity v_i, with higher moments being suppressed, breaks down since when perturbations become large, the infalling matter from different directions will meet, and cross each other. When infalling matter streams meet they penetrate each other (*shell-crossing*), and at each point in space the matter distribution is now described by a superposition of two or more streams. The single-stream approximation in which a unique velocity is assigned to each point in space breaks down since now the velocity field is not single valued anymore, a phenomenon known as *multi-streaming*. These new degrees of freedom can be described by including the second cumulant of the distribution function, namely the velocity dispersion. At times when multiple shell crossings occur all higher cumulants are generated [53]. The effect of velocity dispersion may be small initially but can evolve to accountable corrections at late times and small scales [153], as we will see below. Fig. 4.1 sketches from left to right the time evolution of the formation of a bound dark matter structure starting from cold initial conditions. SPT is completely agnostic about higher moments and therefore fails to properly describe structure formation.

The starting point in VPT is to derive the equations of motion of the higher cumulants (SPT follows only the two lowest moments, the density and veloctiy fields). The equation for σ_{ij} as defined in Eq. (3.7) can be obtained by taking the second moment of the Vlasov equation, Eq. (3.1), and reads

$$\begin{aligned} \partial_\tau \sigma_{ij} \quad &+ \quad 2\mathcal{H}\sigma_{ij} + v_k \nabla_k \sigma_{ij} + \sigma_{jk}\nabla_k v_i + \sigma_{ik}\nabla_k v_j \\ &= \quad -\nabla_k \mathcal{C}_{ijk} - \mathcal{C}_{ijk}\nabla_k \ln(1+\delta)\,. \end{aligned} \tag{4.1}$$

As emphasized in Ch. 3, σ_{ij} is coupled to the third cumulant of the distribution function $\mathcal{C}_{ijk}$

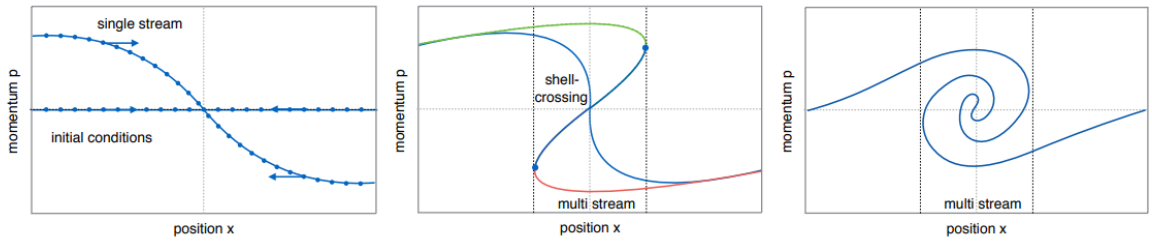

Figure 4.1: Cold initial conditions imply a initial flat phase-space sheet which subsequently bends due to the coherent infall caused by gravitational interaction (*left panel*). Once shell-crossing occurs the pressureless perfect fluid (PPF) approximation breaks down and the single stream splits into three fluid streams (*middle panel*). After crossing the gravitational potential decelerates the dark matter particles eventually pulling them back to the center. This process repeats several times resulting to a wound up phase-space sheet generating multiple streams (*right panel*) [154].

whose evolution equation

$$\begin{aligned} \partial_\tau \mathcal{C}_{ijk} &+ 3\mathcal{H}\mathcal{C}_{ijk} + v_m \nabla_m \mathcal{C}_{ijk} \\ &+ \sigma_{km}\nabla_m \sigma_{ij} + \sigma_{im}\nabla_m \sigma_{kj} + \sigma_{jm}\nabla_m \sigma_{ik} \\ &+ \mathcal{C}_{jkm}\nabla_m v_i + \mathcal{C}_{ikm}\nabla_m v_j + \mathcal{C}_{ijm}\nabla_m v_k \\ &= -\nabla_m \mathcal{C}_{ijkm} - \mathcal{C}_{ijkm}\nabla_m \ln(1+\delta)\,, \end{aligned} \tag{4.2}$$

is in turn coupled to the fourth cumulant $\mathcal{C}_{ijkm}$ and so forth, giving rise to the Vlasov hierarchy. Expressions of the cumulants and their evolution equations can be obtained straightforwardly by introducing a generic *cumulant generating function* $\mathcal{C}$ via

$$\exp\left[\mathcal{C}(\tau, \boldsymbol{x}, \boldsymbol{l})\right] = \int \mathrm{d}^3 p \, \exp\left(\frac{\boldsymbol{l}\cdot\boldsymbol{p}}{ma}\right) f(\tau, \boldsymbol{x}, \boldsymbol{p})\,. \tag{4.3}$$

Taylor expanding $\mathcal{C}$ around its external parameter $\boldsymbol{l}$ gives

$$\begin{aligned} \mathcal{C}(\tau, \boldsymbol{x}, \boldsymbol{l}) &\equiv \ln\left[\int \mathrm{d}^3 p \, \exp\left(\frac{\boldsymbol{l}\cdot\boldsymbol{p}}{ma}\right) f(\tau, \boldsymbol{x}, \boldsymbol{p})\right] \\ &= \ln(1+\delta) + \mathcal{C}_i l_i + \mathcal{C}_{ij}\frac{l_i l_j}{2!} + \mathcal{C}_{ijk}\frac{l_i l_j l_k}{3!} + \dots\,, \end{aligned} \tag{4.4}$$

where the coefficients in the series are given by the cumulants. This means that all the cumulants are generated by applying successive derivates with respect to $\boldsymbol{l}$ that is then set to zero,

$$\mathcal{C}_{ijk\dots}(\tau, \boldsymbol{x}) = \nabla_{l_i}\nabla_{l_j}\nabla_{l_k}\cdots\mathcal{C}|_{\boldsymbol{l}=0}\,, \tag{4.5}$$

in particular

$$\mathcal{C}|_{\boldsymbol{l}=0} = \ln(1+\delta),\ \mathcal{C}_i = v_i,\ \mathcal{C}_{ij} = \sigma_{ij}\,, \tag{4.6}$$

which is equivalent to Eqs. (3.3, 3.4, 3.7). The pressureless perfect fluid approximation, on which SPT is based, corresponds to an ansatz for $\mathcal{C}$ containing only constant and linear terms in $\boldsymbol{l}$ in the Taylor expansion of the cumulant generating function, see Eq. (4.4),

$$\mathcal{C}_{\mathrm{SPT}} = \ln(1+\delta) + \boldsymbol{l}\cdot\boldsymbol{v}\,. \tag{4.7}$$

When going beyond the pressureless perfect fluid approximation one has to include quadratic and higher-order terms in $\boldsymbol{l}$. Remarkably however, this approximation is stable under time evolution and does not generate higher cumulants. This feature can be understood when inspecting the evolution equation of $\mathcal{C}$, given by

$$\partial_\tau \mathcal{C} + \mathcal{H}(\boldsymbol{l}\cdot\nabla_l)\mathcal{C} + (\nabla\mathcal{C})\cdot(\nabla_l\mathcal{C}) + (\nabla\cdot\nabla_l)\mathcal{C} = -\boldsymbol{l}\cdot\nabla\phi\,, \tag{4.8}$$

which results when replacing f by the Vlasov equation in Eq. (4.4). The equations of motion of the cumulants, like the continuity and Euler equation Eqs. (3.5, 3.6) as well as Eqs. (4.1, 4.2) for second and third cumulant are obtained by taking derivatives of Eq. (4.8) with respect to $\boldsymbol{l}$. When $\mathcal{C}$ contains at most linear terms in $\boldsymbol{l}$ no higher-order terms in $\boldsymbol{l}$ will be generated. However as soon as $\mathcal{C} = \mathcal{O}(\boldsymbol{l}^2)$, the nonlinear term in Eq. (4.8) immediately generates terms $\propto \boldsymbol{l}^3$ and so on. Effectively, this means once second cumulant (velocity dispersion) is turned on all higher cumulants will be generated as well and it is a priori not clear how to truncate the hierarchy when extending SPT. This issue will be addressed in detail in the subsequent chapters. Moreover, the nonlinear term in the nth order cumulant evolution equation couples fields which have in total cumulant order $n+1$. Thus, the higher order cumulants always enter through the coupling to the log-density field $\ln(1+\delta)$, i.e. the zeroth cumulant. As soon as orbit crossing occurs the ansatz in Eq. (4.7) breaks down due to a singularity in the density contrast (see Eq. 3.9). This singularity is cured when initializing with an arbitrarily small velocity dispersion, which then from Eq. (4.8) generates all cumulants [53].

There is a contradiction between the Vlasov formal solution and the time evolution of the cumulant hierarchy due to singularities arising at orbit crossing. This necessitates a regularization procedure to reconcile the two. Although CDM's slight velocity dispersion can naturally regulate these singularities in the cumulant hierarchy, the final *large-scale* density and velocity fields should not significantly depend on CDM velocity dispersion. Rather, self-gravity of regions undergoing orbit crossing should lead to self-consistent regularization. Two approaches are possible: 1) Introduce a non-zero initial velocity dispersion $\sigma_{\rm ini}$ and evolve using the cumulant hierarchy without the development of singularities. For CDM-like cases, corrections for infinitesimal $\sigma_{\rm ini}$ are needed. 2) Work with coarse-grained variables, taking into account their interaction with time evolution. Regularization sources higher-order cumulants from density and velocity fields, implying an effective equation of state for dark matter, but a consistent hierarchy closure remains a challenge [53, 155]. We will see in the subsequent chapters that we aim exactly for the first approach.

In the next section we focus on the inclusion of velocity dispersion, and then extend the formalism to include also higher cumulants in Sec. 4.2 and Ch 5.

4.1 Second cumulant

Now we switch to rescaled quantities,

$$\widetilde{\mathcal{C}}_{i_1 i_2 \ldots i_n} = \frac{\mathcal{C}_{i_1 i_2 \ldots i_n}}{(-\mathcal{H}f)^n}\,, \tag{4.9}$$

which we already introduced for the velocity, see Eq. (3.23), in the previous chapter. For the first four cumulants we define

$$\begin{aligned} u_i &= \frac{v_i}{-\mathcal{H}f}, \quad \epsilon_{ij} = \frac{\sigma_{ij}}{(\mathcal{H}f)^2}\,, \\ \pi_{ijk} &= \frac{\mathcal{C}_{ijk}}{(-\mathcal{H}f)^3}, \quad \Lambda_{ijkm} = \frac{\mathcal{C}_{ijkm}}{(\mathcal{H}f)^4}\,, \end{aligned} \tag{4.10}$$

where $f = d\ln D/d\ln a$ is the usual growth rate, with $D(a)$ being the conventional growth factor as introduced in Eq. (3.20). In the following, we switch again from conformal time τ to $\eta = \ln(D)$ using $\partial_\tau = \mathcal{H}f\partial_\eta$ and Eq. (3.26). In this section we focus on the second cumulant, namely the velocity dispersion ϵ_{ij}, while neglecting the third and higher order cumulants. The full set of evolution equations in this setup reads

$$\delta' - \theta = \nabla_i[\delta\, u_i]\,, \tag{4.11}$$

$$u_i' + \left(\frac{3}{2}\frac{\Omega_m}{f^2} - 1\right) u_i - \nabla_i\widetilde{\phi} = u_j\nabla_j u_i + \nabla_j\epsilon_{ij} + \epsilon_{ij}\nabla_j\ln(1+\delta)\,, \tag{4.12}$$

$$\begin{aligned} \epsilon_{ij}' + 2\left(\frac{3}{2}\frac{\Omega_m}{f^2} - 1\right)\epsilon_{ij} &= u_l\nabla_l\epsilon_{ij} + \epsilon_{jl}\nabla_l u_i + \epsilon_{il}\nabla_l u_j \\ &\quad + \nabla_l\pi_{ijl} + \pi_{ijl}\nabla_l\ln(1+\delta)\,, \end{aligned} \tag{4.13}$$

where $\widetilde{\phi} = \phi/(\mathcal{H}f)^2$ is the rescaled gravitational potential satisfying $\nabla^2\widetilde{\phi} = \frac{3}{2}\frac{\Omega_m}{f^2}\delta$.

Background value and perturbations of the velocity dispersion tensor

The density and peculiar velocity field does not have an average value which is guaranteed by mass conservation and statistical isotropy, i.e. this implies $\langle\delta(\eta,\boldsymbol{x})\rangle \equiv 0$ and $\langle\boldsymbol{u}(\eta,\boldsymbol{x})\rangle \equiv 0$. This is not true anymore when dealing with the square of the density or velocity fields. Also higher cumulants are expected to have nonzero expectation (or average) values compatible with isotropy, corresponding to rotationally invariant stochastic fields. The second cumulant is the first example where this occurs,

$$\langle\epsilon_{ij}(\eta,\boldsymbol{x})\rangle = \epsilon(\eta)\,\delta^K_{ij}\,, \tag{4.14}$$

with time-dependent, homogeneous expectation value $\epsilon(\eta)$ multiplying the 3×3 unit matrix δ^K_{ij} and corresponding to the background value of the velocity dispersion. The equation of motion for $\epsilon(\eta)$ can be obtained by taking the trace as well as the ensemble average of Eq. (4.13), giving

$$\epsilon' + 2\left(\frac{3}{2}\frac{\Omega_m}{f^2} - 1\right)\epsilon = Q(\eta)\,, \tag{4.15}$$

with source term

$$Q(\eta) \equiv \frac{1}{3}\langle u_l\nabla_l\epsilon_{ii}\rangle + \frac{2}{3}\langle\epsilon_{il}\nabla_l u_i\rangle + \frac{1}{3}\langle\pi_{iil}\nabla_l\ln(1+\delta)\rangle\,, \tag{4.16}$$

using $\langle\pi_{ijk}\rangle = 0$ due to isotropy (see also [59] and [60, 61] for the case without third cumulant). Therefore, velocity dispersion is sourced by the cross power spectrum of peculiar velocity and the perturbations of ϵ_{ij}, as well as a cross spectrum between the third cumulant and the logarithm of the density field perturbations.

Our strategy for solving this system perturbatively is then as follows: we first split all quantities in a background value and perturbations, in particular

$$\epsilon_{ij}(\eta, \boldsymbol{x}) = \epsilon(\eta)\, \delta^K_{ij} + \delta\epsilon_{ij}(\eta, \boldsymbol{x})\,, \tag{4.17}$$

for the velocity dispersion tensor. Then we can determine a solution to these equations linear in perturbations where the background expectation values enter as they are treated similarly to other background quantities such as the background Hubble rate $\mathcal{H}$ or the background matter density $\Omega_m(\eta)$. The common assumption that the average background dispersion simply decays as $\epsilon(\eta) \propto a^{-1}$ is only true when strictly limiting to the *linear* case, i.e. $Q(\eta) = 0$. The fact that the source $Q(\eta)$ is given as an integration over all space, implies that, one cannot expect $Q(\eta)$, and therefore $\epsilon(\eta)$, to be a small quantity; what enters is not small on *all scales*. Therefore, we will not treat ϵ perturbatively.

In fact, $Q(\eta)$ evolves with time and can be amplified at late times through power spectra *even at quasi-linear level* when computing linear power spectra in Eq. (4.16) using Eq. (3.65). Inspecting the last term on the left hand side of Eq. (4.8), we notice that higher cumulants will have an impact on lower cumulants even at linear level. In our approach, we intentionally do not make assumptions about the extent of velocity dispersion effects. This approach enables us to demonstrate the anticipated decoupling of UV modes caused by halo formation at small scales, as discussed in Ch. 1. For a detailed discussion of the linear solutions along the UV screening, see Sec. 4.1 (last subsection).

The next step is to expand around the linear solutions including nonlinear terms in the perturbation variables. This then gives solutions to the coupled equations of motion for the cumulant perturbations δ, u_i, $\delta\epsilon_{ij}$, π_{ijk}, ..., which can be used to calculate $Q(\eta)$. This allows us to self-consistently solve the evolution equation for $\epsilon(\eta)$, Eq. (4.15). Alternatively, the background dispersion can be obtained by an external input, such as from simulations or from the theory of halo formation, see [98].

SVT decomposition and equations of motion

We henceforth decompose the cumulants into their irreducible scalar, vector and tensor degrees of freedom, analogously as for the peculiar velocity field u_i within SPT, see Eq. (3.23). In comparison to the fluid equations in SPT we now have to account for the velocity dispersion tensor ϵ_{ij}, which modifies the Euler equation as given in Eq. (4.12). The velocity divergence $\theta = \nabla_i u_i$ yields after inserting Eq. (4.17),

$$\theta' + \left(\frac{3}{2}\frac{\Omega_m}{f^2} - 1\right)\theta - \frac{3}{2}\frac{\Omega_m}{f^2}\delta = \nabla_i(u_j\nabla_j u_i) + q_\theta\,, \tag{4.18}$$

where the extra term compared to SPT is given by

$$q_\theta = \epsilon(\eta)\nabla^2 A + \nabla_i\nabla_j\delta\epsilon_{ij} + \nabla_i(\delta\epsilon_{ij}\nabla_j A)\,. \tag{4.19}$$

Note that we also introduced a short-hand notation for the log-density field,

$$A \equiv \ln(1+\delta)\,. \tag{4.20}$$

As already hinted above, the first two terms in Eq. (4.19) contribute to the linear solution when velocity dispersion is present and the last term is another nonlinear contribution. In fact,

we incorporate *the field A* into our perturbation theory framework in order to avoid Taylor expanding the log, that is we systematically take further nonlinearities coming from A into account, see details below.
In Sec. 3.1 we argued that as soon as velocity dispersion enters the Euler equation there is no reason to neglect the vorticity field anymore,

$$w_i = \varepsilon_{ijk}\nabla_j u_k = (\boldsymbol{\nabla}\times\boldsymbol{u})_i\,, \tag{4.21}$$

which is governed by the Euler equation Eq. (4.12), reading

$$w_i' + \left(\frac{3}{2}\frac{\Omega_m}{f^2} - 1\right) w_i = (\boldsymbol{\nabla}\times(u_j\nabla_j\boldsymbol{u}))_i + (q_w)_i\,, \tag{4.22}$$

with

$$(q_w)_i = \varepsilon_{ijk}\nabla_j(\nabla_l\delta\epsilon_{kl} + \delta\epsilon_{kl}\nabla_l A)\,, \tag{4.23}$$

where ε_{ijk} is the Levi-Civita symbol. The vorticity evolution is affected by velocity dispersion also at linear level, given by the first term in Eq. (4.23). In total, the peculiar velocity field can also be written in terms of its divergence (one scalar mode) and vorticity (two vector modes),

$$u_i = u_i^S + u_i^V = \frac{\nabla_i}{\nabla^2}\theta - \frac{\varepsilon_{ijk}\nabla_j}{\nabla^2}w_k\,, \tag{4.24}$$

where $\nabla_i w_i = 0$ and within SPT the curl part u_i^V is simply set to zero. The operator $1/\nabla^2$ becomes $-1/k^2$ in Fourier space acting on fields at wavenumber $\boldsymbol{k}$.

We similarly decompose the dispersion tensor into

$$\delta\epsilon_{ij} \;=\; \delta\epsilon_{ij}^S + \delta\epsilon_{ij}^V + \delta\epsilon_{ij}^T\,, \tag{4.25}$$

with

$$\delta\epsilon_{ij}^S \;=\; \delta_{ij}^K\,\delta\epsilon + \frac{\nabla_i\nabla_j}{\nabla^2}g\,, \tag{4.26}$$

$$\delta\epsilon_{ij}^V \;=\; -\frac{\varepsilon_{ilk}\nabla_l\nabla_j}{\nabla^2}\nu_k - \frac{\varepsilon_{jlk}\nabla_l\nabla_i}{\nabla^2}\nu_k\,, \tag{4.27}$$

$$\delta\epsilon_{ij}^T \;=\; t_{ij} \equiv P^T_{ij,ls}\delta\epsilon_{ls}\,, \tag{4.28}$$

and the *tensor projection operator*

$$\begin{aligned} P^T_{ij,ls} \;=\; & \frac{1}{2}\left(\delta^K_{is} - \frac{\nabla_i\nabla_s}{\nabla^2}\right)\left(\delta^K_{jl} - \frac{\nabla_j\nabla_l}{\nabla^2}\right) \\ & + \frac{1}{2}\left(\delta^K_{js} - \frac{\nabla_j\nabla_s}{\nabla^2}\right)\left(\delta^K_{il} - \frac{\nabla_i\nabla_l}{\nabla^2}\right) \\ & - \frac{1}{2}\left(\delta^K_{ij} - \frac{\nabla_i\nabla_j}{\nabla^2}\right)\left(\delta^K_{ls} - \frac{\nabla_l\nabla_s}{\nabla^2}\right)\,. \end{aligned} \tag{4.29}$$

With this decomposition we fully characterize the perturbations of the dispersion tensor by two scalar modes $\delta\epsilon$, g; two vector modes ν_i with $\nabla_i\nu_i = 0$ (divergence-free) and two tensor modes t_{ij} with $t_{ii} = 0$, $\nabla_i t_{ij} = \nabla_j t_{ij} = 0$ (traceless-transverse and symmetric). In total, this gives six

independent degrees of freedom of the symmetric velocity dispersion tensor ϵ_{ij}, which can finally be written as

$$\begin{aligned}\epsilon_{ij} &= \langle\epsilon_{ij}\rangle + \delta\epsilon^S_{ij} + \delta\epsilon^V_{ij} + \delta\epsilon^T_{ij} \\ &= \underbrace{\epsilon(\eta)\delta^K_{ij}}_{\text{background value}} + \underbrace{\delta\epsilon\,\delta^K_{ij} + \frac{\nabla_i\nabla_j}{\nabla^2}g}_{\text{scalar perturbations}} - \underbrace{\frac{(\varepsilon_{ilk}\nabla_j + \varepsilon_{jlk}\nabla_i)\nabla_l}{\nabla^2}\nu_k}_{\text{vector perturbations}} + \underbrace{t_{ij}}_{\text{tensor perturbations}}. \end{aligned} \tag{4.30}$$

Inserting the decompositions of Eqs. (4.24, 4.30) in the source term for the background dispersion, Eq. (4.16), we obtain

$$Q(\eta) = \frac{1}{3}\int d^3k\,(P_{\theta\tilde{g}}(k,\eta) + 2P_{w_i\nu_i}(k,\eta))\,, \tag{4.31}$$

where $\tilde{g} \equiv g - \delta\epsilon$, and $P_{w_i\nu_i}(k,\eta)$ is the cross power spectrum of vorticity and the vector perturbation, summed over $i = 1,2,3$. Here we neglected the third cumulant π_{ijk} and higher cumulants; we will come back to them in Sec. 4.2 and Ch. 5. Written this way it is again clear that, the peculiar velocities impact the velocity dispersion background through their correlation (power spectrum in Fourier space) with dispersion fluctuations.

Finally, we need to find the equations of motion for the modes of $\delta\epsilon_{ij}$. First, we use Eq. (4.13) from which we subract Eq. (4.15) times δ^K_{ij}. This gives an equation of motion for $\delta\epsilon_{ij}$. Then we can use

$$\delta\epsilon = \frac{1}{2}\left(\delta^K_{ij} - \frac{\nabla_i\nabla_j}{\nabla^2}\right)\delta\epsilon_{ij}\,, \tag{4.32}$$

$$g = -\frac{1}{2}\left(\delta^K_{ij} - 3\frac{\nabla_i\nabla_j}{\nabla^2}\right)\delta\epsilon_{ij}\,, \tag{4.33}$$

to obtain evolution equations for the scalar modes which are given by

$$\delta\epsilon' + 2\left(\frac{3}{2}\frac{\Omega_m}{f^2} - 1\right)\delta\epsilon = q_\epsilon\,, \tag{4.34}$$

$$g' + 2\left(\frac{3}{2}\frac{\Omega_m}{f^2} - 1\right)g - 2\epsilon\theta = q_g\,, \tag{4.35}$$

where

$$\begin{aligned} q_\epsilon &= \frac{1}{2}u_l\nabla_l(3\delta\epsilon + g) + \delta\epsilon_{il}\nabla_l u_i - \frac{1}{2}\frac{\nabla_i\nabla_j}{\nabla^2}(u_l\nabla_l\delta\epsilon_{ij}) \\ &\quad - \frac{\nabla_i\nabla_j}{\nabla^2}(\delta\epsilon_{il}\nabla_l u_j) - Q(\eta)\,, \\ q_g &= -\frac{1}{2}u_l\nabla_l(3\delta\epsilon + g) - \delta\epsilon_{il}\nabla_l u_i + \frac{3}{2}\frac{\nabla_i\nabla_j}{\nabla^2}(u_l\nabla_l\delta\epsilon_{ij}) \\ &\quad + 3\frac{\nabla_i\nabla_j}{\nabla^2}(\delta\epsilon_{il}\nabla_l u_j)\,. \end{aligned} \tag{4.36}$$

Most importantly, the term $-2\theta\epsilon$ shows that the g mode is *generated linearly* in presence of a background dispersion $\epsilon(\eta)$. The nonlinear source term q_g generates additional modifications. In contrast, $\delta\epsilon$ has no source terms at linear level, which means that it decays as $\delta\epsilon \propto a^{-1}$.

However the nonlinear terms in q_ϵ can amplify it through the coupling between velocity and velocity dispersion fields including vorticity and vector fields. The fact that the source term $Q(\eta)$ appears in q_ϵ ensures that $\delta\epsilon$ has a vanishing expectation value and arises due to the specific projection necessary to get Eq. (4.34). On a more technical level, tadpole diagram contributions will be removed by the appearance of the source term, see Eq. (4.55) below.

To proceed, in order to obtain equations of motion for the vector and tensor modes we use

$$\nu_i = \varepsilon_{ijk}\frac{\nabla_j\nabla_l}{\nabla^2}\,\delta\epsilon_{kl}\,, \tag{4.37}$$

$$t_{ij} = P^T_{ij,kl}\,\delta\epsilon_{kl}\,, \tag{4.38}$$

from which we obtain

$$\begin{aligned}\nu_i' + 2\left(\frac{3}{2}\frac{\Omega_m}{f^2} - 1\right)\nu_i - \epsilon\, w_i &= \varepsilon_{ijk}\frac{\nabla_j\nabla_l}{\nabla^2}q_{kl}\,,\\ t_{ij}' + 2\left(\frac{3}{2}\frac{\Omega_m}{f^2} - 1\right)t_{ij} &= P^T_{ij,kl}\;q_{kl}\,.\end{aligned} \tag{4.39}$$

Nonlinear terms in perturbations are contained in

$$q_{kl} \equiv u_n\nabla_n\delta\epsilon_{kl} + \delta\epsilon_{ln}\nabla_n u_k + \delta\epsilon_{kn}\nabla_n u_l\,. \tag{4.40}$$

We notice that the vector mode mixes with the vorticity already at linear level through the term ϵw_i such that both vector modes ν_i, w_i are coupled to each other. The tensor mode however does not mix with any other mode at linear level. Up to the second cumulant we work in total with following perturbation variables

δ,	θ,	$\delta\epsilon$, g	scalar	4×1 d.o.f.,
	w_i,	ν_i	vector	2×2 d.o.f.,
		t_{ij}	tensor	1×2 d.o.f..

Moreover, as already defined in Eq. (4.20) we incorporate the log-density field A as an *additional perturbation variable*. Although it is not an independent degree of freedom of course, it is advantageous since we do not have to expand the log giving rise to higher order nonlinearities. This means we complement the set of scalar modes with the variable A and simultaneously solve its equation of motion. It is obtained by dividing Eq. (4.11) by $1+\delta$:

$$A' - \theta = u_i\nabla_i A\,, \tag{4.41}$$

which holds at any order in perturbation theory. The solution of Eq. (4.41) can be used to calculate the backreaction of A in the Euler equation, see Eq. (4.19). Importantly, A has a nonzero expectation value

$$\langle A\rangle = \mathcal{A}\,, \tag{4.42}$$

whose evolution equation can be derived by taking the ensemble average of Eq. (4.41) and reads

$$\mathcal{A}' = Q_A(\eta) \equiv -\int \mathrm{d}^3k\, P_{\theta A}(k,\eta)\,, \tag{4.43}$$

where the part coming from the vorticity vanishes when taking the ensemble average. However, the average value $\mathcal{A}$ is not of interest in practice: Inspecting the evolution equations for the cumulants, $A = \mathcal{A} + \delta A$ only enters with a spatial derivative acting on it leaving only the perturbation. This means in practice we do not care about the difference between A and δA and just use A as perturbation variable. Although A could be an interesting observable due to statistical reasons (see [156–159]) we do not explicitly care about its solution but rather its impact on the cumulants which is automatically accounted in the VPT framework.

Equations of motion in Fourier space

We are now armed with a new set of perturbation variables whose equations of motion can be written in Fourier space similar to Eq. (3.42) in SPT. For the continuity equation we get

$$\delta_k' - \theta_k = \int_{pq} \left\{ \alpha_{pq} \theta_p \delta_q + \frac{(\boldsymbol{p} \times \boldsymbol{q}) \cdot \boldsymbol{w}_p}{p^2} \delta_q \right\} , \tag{4.44}$$

where $\alpha_{pq} = \boldsymbol{k} \cdot \boldsymbol{p}/p^2$, as defined in Eq. (3.41), is the only nonlinear mode coupling function of SPT. In addition, we get a backreaction from the vorticity field on the density contrast which emphasizes that scalar modes nonlinearly couple to vector modes. The Euler equation now becomes

$$\begin{aligned} &\theta_k' + \left(\frac{3}{2} \frac{\Omega_m}{f^2} - 1 \right) \theta_k - \frac{3}{2} \frac{\Omega_m}{f^2} \delta_k + k^2 \left(\delta\epsilon_k + g_k + \epsilon A_k \right) \\ &= \int_{pq} \left\{ \beta_{pq} \theta_p \theta_q + \left(1 + \frac{2p \cdot q}{q^2} \right) \frac{(\boldsymbol{p} \times \boldsymbol{q}) \cdot \boldsymbol{w}_p}{p^2} \theta_q - \frac{(\boldsymbol{p} \times \boldsymbol{q}) \cdot \boldsymbol{w}_p}{p^2} \frac{(\boldsymbol{p} \times \boldsymbol{q}) \cdot \boldsymbol{w}_q}{q^2} \right. \\ &\quad \left. - \boldsymbol{k} \cdot \boldsymbol{p} A_p \delta\epsilon_q - \boldsymbol{k} \cdot \boldsymbol{q} \, \frac{\boldsymbol{q} \cdot \boldsymbol{p}}{q^2} A_p g_q + \left(1 + \frac{2p \cdot q}{q^2} \right) A_p (\boldsymbol{p} \times \boldsymbol{q}) \cdot \boldsymbol{\nu}_q - A_p p_i p_j t_{q,ij} \right\} , \end{aligned} \tag{4.45}$$

where $\boldsymbol{k} = \boldsymbol{p} + \boldsymbol{q}$ as required by momentum conservation. Hence, the Euler equation dramatically changes as soon as one takes velocity dispersion into account. First, we focus on the first line, i.e. the linear part. The term proportional to k^2 describes a suppression which is similar to the Jeans suppression that arises from the velocity dispersion perturbation modes $\delta\epsilon_k$, g_k as well as from the dispersion background ϵA_k. Interestingly, this damping at linear level depends on the isotropic (ϵ, $\delta\epsilon$) *and* anisotropic (g) part of the dispersion tensor, see Eqs. (4.32, 4.33). Actually the *stress-tensor* contribution $[(1+\delta)\epsilon_{ij}]$ enters the Euler equation which explains the fact that both background and perturbations of the velocity dispersion enter here.

Note that the suppression of growth which arises in this context has a different physical origin than the familiar Jeans suppression [160]. In the latter case, the fluid encounters small-scale damping due to particle collisions which counteract gravitational collapse. This yields a pressure or sound speed contribution responsible for the suppression. The last term of the first line of Eq. (4.45) would correspond to such a contribution, as can be seen when approximating $k^2 \epsilon \, [\ln(1+\delta)]_k \sim k^2 \epsilon \, \delta_k$, motivating the effective fluid ansatz mentioned in Sec. 3.1. On the contrary, the Euler equation in Eq. (4.45) describes a *collisionless* system which prevents particles to collide at small scales. This means particles can cross through each other without interacting. In other words they *shell-cross* and the resulting velocity dispersion also yields an effective pressure. Thus, although the physical situation is quite different with that of a fluid, the net effect is very similar.

Another misleading comparison is that, in linear theory $g \sim \epsilon\theta$ (see Eq. 4.35 and Eq. 4.61) looks very similar to a viscosity contribution in the Navier-Stokes equation, see Eq. (3.8). Again, the Vlasov equation, which is collisionless, does not include dissipation which is an essential feature in the energy conservation equation, see Sec. VII in [98].

One may wonder whether this damping at small scales is always guaranteed given the different physical origin. This is an important question since we seek small-scale decoupling including the screening (suppression) of high-k modes. This will also be required to have convergence within

VPT when computing nonlinear loop corrections (see Ch. 7). However, as we will see below, when going beyond the second cumulant the collisionless dynamics also allows for *instabilities*, i.e. small-scale enhancement. This behavior actually depends on the expectation values of the cumulants (see Ch. 6). In the fluid picture this would not be possible as stability is always guaranteed below the Jeans length.

Finally, the second and third line of Eq. (4.45) contain nonlinear terms. The only nonlinearity within SPT is given by β_{pq}, see Eq. (3.41). Additional backreactions within VPT stem from the vorticity (second line) as well as couplings between A_k and all dispersion modes (third line).

Analogous equations of motion for the remaining perturbation variables $\delta\epsilon$, g, A, w_i, ν_i, t_{ij} in Fourier space can be obtained in a similar way. Due to the great amount of additional mode coupling functions, i.e. vertices, they are rather lengthy and we shift them to Appendix A. We also include the continuity and Euler equations for completeness. The explicit expressions of all vertices up to the second cumulant can be found in Appendix B.

In the following it is convenient to put the perturbation variables into a single vector

$$\psi \equiv (\delta, \theta, g, \delta\epsilon, A, w_i, \nu_i, t_{ij})\,. \tag{4.46}$$

In analogy with SPT, the equations of motion can then be brought into a matrix equation [143]

$$\psi'_{k,a}(\eta) + \Omega_{ab}(k,\eta)\,\psi_{k,b}(\eta) = \int_{pq} \gamma_{abc}(\boldsymbol{p},\boldsymbol{q})\psi_{p,b}(\eta)\psi_{q,c}(\eta)\,, \tag{4.47}$$

as introduced in Eq. (3.48) in Sec. 3.3. The vector $\psi_{k,a}$ can in principle be further extended when including perturbations of higher cumulants, see Sec 4.2. The index a runs through the modes as well as their components (for vector and tensor fields). Now we set third and higher cumulants to zero so that the nonlinear vertices γ_{abc} are those given in Appendix B. An important difference to Eq. (3.48) is that the linear matrix $\Omega_{ab}(k,\eta)$ now becomes *scale- and time-dependent*. Since scalar, vector and tensor modes are independent of each other at linear level it has a block-diagonal form when defining $\psi = (\psi^S, \psi^V, \psi^T)$ into subsets of SVT modes, and is given by

$$\Omega = \begin{pmatrix} \Omega^S & & \\ & \Omega^V & \\ & & \Omega^T \end{pmatrix}, \tag{4.48}$$

with vanishing off-diagonal entries as claimed above. The scalar part reads

$$\Omega^S = \begin{pmatrix} & -1 & & & \\ -\frac{3}{2}d & \frac{1}{2}e & k^2 & k^2 & k^2\epsilon \\ & -2\epsilon & e & & \\ & & & e & \\ & -1 & & & \end{pmatrix}, \tag{4.49}$$

using $\psi^S = (\delta, \theta, g, \delta\epsilon, A)$ and $d(\eta) \equiv \Omega_m/f^2$, $e(\eta) \equiv 3d(\eta) - 2$, with $d, e \mapsto 1$ in the EdS approximation. The upper left two-by-two matrix corresponds to the linear matrix in SPT, see Eq. (3.49). The second row gives the coefficients of the linear terms in the Euler equation where the third, fourth and fifth column correspond to the damping term which is discussed below Eq. (4.45). Note that the linear part of δ (first row) and A (fifth row) are identical since to first order we have $\delta \approx A$. As we will see in the next subsection the emergence of the background

dispersion ϵ already at linear level accounts for the screening of UV (high-k) modes. This is the case when modes pass over a certain scale

$$k_\sigma(\eta) \equiv \frac{1}{\sqrt{\epsilon(\eta)}}\,, \qquad \text{(dispersion scale)} \tag{4.50}$$

above which velocity dispersion becomes important, i.e. for $k \gtrsim k_\sigma$. The vector and tensor parts are given by

$$\Omega^V = \begin{pmatrix} \frac{1}{2}e & k^2 \\ -\epsilon & e \end{pmatrix}\,, \quad \Omega^T = e\,, \tag{4.51}$$

where the vector matrix shows the mixing of vorticity and the vector field of the velocity dispersion tensor. The components of the doublet $(w_i,\, \nu_i)$ are understood to apply separately to each $i = x, y, z$ as well as for the ij components of t_{ij}. That is each spatial component of vector and tensor fields evolve separately from each other at linear level.

The nonlinear vertices γ_{abc}, given in Appendix B contain all nonlinearities which arise when accounting for a nonzero velocity dispersion. In e.g. the continuity equation the velocity backreactions to the density contrast read

$$\gamma_{\delta\theta\delta}(\boldsymbol{p},\boldsymbol{q}) = \frac{1}{2}\alpha_{pq}, \quad \gamma_{\delta w_i\delta}(\boldsymbol{p},\boldsymbol{q}) = \frac{1}{2}\frac{(\boldsymbol{p}\times\boldsymbol{q})_i}{p^2}\,, \tag{4.52}$$

where the first one corresponds to the usual SPT expression and the latter one to the vorticity backreaction. They can be read off from Eq. (4.44). Moreover, we assume all vertices to be symmetric, i.e.

$$\gamma_{abc}(\boldsymbol{p},\boldsymbol{q}) = \gamma_{acb}(\boldsymbol{q},\boldsymbol{p})\,, \tag{4.53}$$

which gives additional factors $1/2$ for $b \neq c$. Note that when exchanging perturbation types b and c the wavenumbers as well as the components for the vector and tensor fields must be exchanged. In addition, the vertices

$$\gamma_{w_iA(\delta\epsilon)} = \frac{1}{2}(\boldsymbol{p}\times\boldsymbol{q})_i, \quad \gamma_{w_iAg} = -\frac{1}{2}\frac{\boldsymbol{p}\cdot\boldsymbol{q}}{q^2}(\boldsymbol{p}\times\boldsymbol{q})_i \tag{4.54}$$

are responsible for vorticity generation. They show that two scalar modes ($A_p\delta\epsilon_q$ and A_pg_q) couple to create a vorticity mode. This will be discussed in detail in Sec. 8.3. Note that in the following we will denote the mode $\delta\epsilon$ in γ_{abc} simply as ϵ (such that $\gamma_{w_iA(\delta\epsilon)} \mapsto \gamma_{w_iA\epsilon}$) to avoid confusion.

In fact, when deriving the equations of motion for the perturbation variables by subtracting the equations of motion for the homogenous background values from the original ones, what one actually obtains is

$$\psi'_{k,a}(\eta) + \Omega_{ab}(k,\eta)\psi_{k,b}(\eta) = \int_{pq} \hat{\gamma}_{abc}(\boldsymbol{p},\boldsymbol{q})\psi_{p,b}(\eta)\psi_{q,c}(\eta) - Q_a(\eta)\delta_{\mathrm{D}}^{(3)}(\boldsymbol{k})\,, \tag{4.55}$$

which differs from Eq. (4.47) and contains vertices $\hat{\gamma}_{abc}(\boldsymbol{p},\boldsymbol{q})$ which are derived from the Vlasov equation when one strictly uses $a = \delta A$ instead of A as perturbation variable keeping track of the homogenous background value $\langle A\rangle = \mathcal{A}$. In addition, when subtracting the background part $\langle\epsilon_{ij}\rangle$ the last term in Eq. (4.55) arises also in the equation for $\delta\epsilon$, see Eq. (4.34) and therefore gives a contribution at $\boldsymbol{k} = 0$ for the modes $a = \delta\epsilon$, δA ($Q_a = 0$ otherwise) which do possess average values. In the following, we use the fact that the contribution coming from $-Q_a(\eta)\delta_{\mathrm{D}}^{(3)}(\boldsymbol{k})$ can

be skipped in the evolution equations when replacing the vertices $\hat{\gamma}_{abc}(\boldsymbol{p},\boldsymbol{q})$ by vertices $\gamma_{abc}(\boldsymbol{p},\boldsymbol{q})$ given by

$$\gamma_{abc}(\boldsymbol{p},\boldsymbol{q}) \equiv \begin{cases} \hat{\gamma}_{abc}(\boldsymbol{p},\boldsymbol{q}) & \boldsymbol{p}+\boldsymbol{q} \neq 0\,, \\ 0 & \boldsymbol{p}+\boldsymbol{q} = 0\,. \end{cases} \tag{4.56}$$

This is so because so-called "tadpole" contributions, given by

$$T_a(\boldsymbol{k},\eta) \equiv \delta^{(3)}(\boldsymbol{k}) \int \mathrm{d}^3p\, \gamma_{abc}(\boldsymbol{p},\boldsymbol{q})\Big|_{\boldsymbol{p}+\boldsymbol{q}\to 0} P_{bc}(p,\eta)\,, \tag{4.57}$$

where $P_{bc}(p,\eta)$ denotes the power spectrum at time η, will be exactly canceled by the source term insertions $Q_a(\eta)\delta_{\mathrm{D}}^{(3)}(\boldsymbol{k})$. This can be seen when setting for example $a = \delta\epsilon$ and evaluating the corresponding vertices $\gamma_{\epsilon bc}$ in the limit $\boldsymbol{p}+\boldsymbol{q}\to 0$, we then exactly obtain in Eq. (4.57) the expression for $Q(\eta)$ in Eq. (4.31) such that those vertices will be canceled. In practice we simply set *all* vertices for $\boldsymbol{p}+\boldsymbol{q}=0$ to zero which is implicitly assumed in γ_{abc}, thus we do not need to take care of the source term contributions in the equations of motion and henceforth use Eq. (4.47). This works at any loop order, see [99] for further details.

We emphasize that the structure of Eq. (4.47) allows to find solutions analogous to SPT. We will assume that at some initial time η_{ini}, long after recombination and before the onset of nonlinearities, the effects of velocity dispersion and higher cumulants are negligible such that *all* the fluctuation fields are proportional to the initial density field δ_{k0} for the case of adiabatic initial conditions. This seems reasonable for sufficiently cold dark matter and we may then formally Taylor expand the perturbation vector $\psi_{k,a}$ into powers of δ_{k0} as

$$\psi_{k,a}(\eta) = \sum_{n\geq 1} \int_{k_i} F_{n,a}(\boldsymbol{k}_1,\ldots,\boldsymbol{k}_n,\eta)\, e^{n\eta}\, \delta_{k_1 0}\cdots\delta_{k_n 0}\,, \tag{4.58}$$

analogous to the SPT-ansatz in Eqs. (3.52, 3.56) and $\int_{k_i} \equiv \int \mathrm{d}^3k_1\cdots\mathrm{d}^3k_n\,\delta^{(3)}(\boldsymbol{k}-\sum_i \boldsymbol{k}_i)$. The perturbative expansion is furnished by the nth order nonlinear kernels $F_{n,a}$ for variable a and are assumed to be symmetrized under arbitrary permutations in their arguments. Even if initially all the cumulant *perturbations* are exactly zero they will be generated in the presence of background values of the cumulants. The perturbations in turn source the background values which in principle requires to self-consistently solve the system of evolution equations and we come back to those determinations in Ch. 6. The first two entries of ψ correspond to $a=\delta$, θ in analogy to SPT. However, the corresponding kernels $F_{n,\delta}$ and $F_{n,\theta}$ are modified compared to the ones from SPT due to the presence of velocity dispersion and higher cumulants as captured by the evolution equations Eq. (4.44, 4.45).

Apart from the extended set of variables, Eq. (4.46), and the large number of additional vertices, the time-dependence of the linear matrix $\Omega_{ab}(k,\eta)$ does in general not factorize when compared to the SPT-case, see Eq. (3.49). Hence, the nonlinear kernels have an additional time-dependence apart from the growing mode factor $e^{n\eta}$ which is already factored out from the kernels but henceforth we keep it inside of $\psi_{k,a}(\eta)$, in contrast to Eq. (3.56). Thus, we have to generalize the well-known recursion relations of the nonlinear kernels (see Eq. 3.43) leading to differential equations given by

$$\begin{aligned}(\partial_\eta\delta_{ab} + n\delta_{ab} + \Omega_{ab}(k,\eta))F_{n,b}(\boldsymbol{k}_1,\ldots,\boldsymbol{k}_n,\eta) \;&=\; \sum_{m=1}^{n-1}\Big\{\gamma_{abc}(\boldsymbol{q}_1+\cdots+\boldsymbol{q}_m,\boldsymbol{q}_{m+1}+\cdots+\boldsymbol{q}_n) \\ &\times\; F_{m,b}(\boldsymbol{q}_1,\ldots,\boldsymbol{q}_m,\eta)F_{n-m,c}(\boldsymbol{q}_{m+1},\ldots,\boldsymbol{q}_n,\eta)\Big\}^s,\end{aligned} \tag{4.59}$$

which is obtained by inserting Eq. (4.58) into Eq. (4.47). $\{\cdots\}^s = \sum_{\text{perm}}\{\cdots\}/|\text{perm}|$ denotes an average over all $|\text{perm}| = n!/m!/(n-m)!$ possibilities to choose the subset of wave vectors $\{\boldsymbol{q}_1, \ldots, \boldsymbol{q}_m\}$ from $\{\boldsymbol{k}_1, \ldots, \boldsymbol{k}_n\}$, and $k \equiv |\sum_i \boldsymbol{k}_i|$. As emphasized above when completely neglecting velocity dispersion and higher cumulants, the equations reduce to the time-independent recursion relations, given in Eq. (3.43) with $F_1 = G_1 = 1$. Instead, when taking them into account one has to solve the coupled equations for all $F_{n,a}$ satisfied by Eq. (4.59), and no analytical solutions can be found, so one has to resort to numerical methods where in this case we follow the algorithm presented in [161, 162]. Then the kernels do depend on time and even the linear solutions given by $F_{1,a}(k,\eta)$ will develop scale- and time-dependence which we discuss in the next subsection. The expressions for the power spectra $P_{ab}(k,\eta)$ including its loop corrections are identical to Eqs. (3.63 – 3.66) except that the linear kernels now become $F_{1,a} \mapsto F_{1,a}(k,\eta)$.

VPT analogously allows to calculate the two-loop (see Ch. 8 and [150, 162, 163]). Also the NLO correction to the bispectrum can be calculated similarly when using the modified kernels from VPT and the integration procedure from [150].

Finally, it is still possible to find analytical solutions of the nonlinear kernels as long as dispersion effects remain small, i.e. for $k \lesssim k_\sigma$. We present analytical results for the nonlinear kernels in Ch. 7. In fact, for a specific setup linear solutions can be obtained analytically without the restriction to low-k values. Again, the treatment of using both δ and A as variables allows us to capture all quadratic nonlinearities in ψ which is important to efficiently calculate higher-order nonlinear corrections in perturbation theory.

Linear solutions

Now we focus on the linear approximation of the coupled system of equations, i.e. we set all nonlinear vertices to zero. Moreover, we take the background dispersion $\epsilon(\eta)$ as given. As highlighted above, we expect the density contrast for modes $k \gtrsim k_\sigma$ to be suppressed due to the screening of UV scales by velocity dispersion even at linear level, see Eq. (4.50). This arises from two effects: directly due to the presence of the background dispersion $\epsilon(\eta)$ in the linear Euler equation and indirectly due to the dispersion fields g and $\delta\epsilon$ that are in turn sourced by $\epsilon(\eta)$.

Since vector and tensor modes cannot be generated at linear level we can neglect them for now. Although vorticity will be generated by velocity dispersion, this will only happen at nonlinear level. In other words, vector and tensor have no growing modes when neglecting nonlinear contributions. Since they also evolve independently to the growing modes coming from scalar perturbations, see Eq. (4.48), they simply decay to first order. We are then left with the scalar part of the linear matrix Ω_{ab}, Eq. (4.49). This can be further simplified, since $\delta = A$ at linear level and following the previous discussion, $\delta\epsilon$ decays at linear level as $e^{-\eta} = 1/D$. Thus, we are left with

$$\begin{aligned} \delta_k' &= \theta_k\,, \\ \theta_k' &= -\frac{1}{2}\theta_k + \frac{3}{2}\delta_k - k^2 g_k - \epsilon k^2 \delta_k\,, \\ g_k' &= -g_k + 2\epsilon\theta_k\,. \end{aligned} \tag{4.60}$$

The equation for g has a formal solution given by

$$g_k(\eta) = \int^\eta \mathrm{d}\eta'\, e^{\eta'-\eta}\, 2\epsilon(\eta')\theta_k(\eta')\,. \tag{4.61}$$

Inserting this in the Euler equation in Eq. (4.60) one obtains a correction term proportional to k^2 compared to SPT which is nonlocal in time. Since this modification is consistent with the most general structure allowed by symmetries [164], adding second and higher cumulants by using the Vlasov-Poisson dynamics to the perturbative treatment gives a deterministic *UV completion* to SPT.

One could naively replace Eq. (4.61) by $g_k \mapsto c_{\rm vis}^2 \theta_k$ that corresponds to a dissipative viscosity term in the Euler equation which is local in time. While this seems reasonable it actually violates energy conservation. When instead using the nonlocal solution given by Eq. (4.61) which is obtained by the nondissipative Vlasov-Poisson system (Eq. 4.60) the dynamics does indeed obey the cosmic energy equation [165], to first order in perturbation theory given by the sum of kinetic and potential energy (see Apendix E in [98]). Furthermore, when including higher cumulants the solution for g_k will be modified while still obeying nondissipative energy evolution. This shows that a naive fluidlike description with dissipative viscosity cannot explain the actual dynamics which is, as we find below, significantly more complex.

To first order we know from SPT (valid when $k^2\epsilon \ll 1$) that one can approximate $\theta_k^{(1)}(\eta') = \delta_k^{(1)}(\eta') \propto e^{\eta'}$ which gives

$$g_k(\eta) \to 2\delta_k(\eta) \int^\eta {\rm d}\eta'\, e^{2(\eta'-\eta)}\, \epsilon(\eta')\,, \tag{4.62}$$

when inserting the approximation into Eq. (4.61). Replacing this into the Euler equation one can factor out $\delta_k(\eta)$. This yields a scale of the "Jeans-like" suppression as

$$\frac{1}{k^2_{\text{J-like}}(\eta)} = \epsilon(\eta) + 2\int^\eta {\rm d}\eta'\, e^{2(\eta'-\eta)}\epsilon(\eta')\,. \tag{4.63}$$

By introducing the "Jeans-like" suppression scale one could in principle get rid off the equation for g_k dealing only with continuity and Euler equation including the suppression term from Eq. (4.63) to capture velocity dispersion effects. While this modification takes place only at linear level we know that second and higher cumulants also modify nonlinear evolution whose effects go far beyond adding a Jeans-like term. Furthermore, we seek solutions which are also valid when $k^2\epsilon$ is not small and the simplified modification of Eq. (4.63) cannot be used for all scales even at linear level.

Therefore, we have to solve the system of equations explicitly including the g_k-mode, Eq. (4.60). The solution of the full linear system will then be used as starting point for a perturbative solution of the nonlinear system later in Ch. 7. To obtain solutions of Eq. (4.60), knowledge of the background dispersion $\epsilon(\eta)$ is required. In this section we refrain from finding solutions of its evolution equation, Eq. (4.15). For illustration and for simplicity we make instead a power-law ansatz

$$\epsilon(\eta) = \epsilon_0 e^{\alpha\eta}\,, \tag{4.64}$$

with value ϵ_0 today and a power-law parameter α which specifies the growth index. As we will see further below this ansatz is motivated by the limit of a scaling universe described by a power-law initial spectrum $P_0 \sim k^{n_s}$ with index given by

$$\alpha = \frac{4}{n_s + 3}\,, \tag{4.65}$$

which is governed by the underlying symmetry (see Ch. 6). For specific redshift intervals this can be treated as an approximate description within the ΛCDM cosmology with initial spectrum given by Eq. (2.25).

We henceforth consider the g-mode rescaled by the background dispersion, that is we work with

$$\bar{g}_k(\eta) \equiv g_k(\eta)/\epsilon(\eta)\,. \tag{4.66}$$

We can then rewrite the linear system into a matrix equation, given by

$$\bar{\psi}_k' + (\Omega_0 + \epsilon k^2 \Omega_1)\bar{\psi}_k = 0\,, \tag{4.67}$$

with vector $\bar{\psi}_k = (\delta_k, \theta_k, \bar{g}_k)$ and

$$\Omega_0 = \begin{pmatrix} 0 & -1 & 0 \\ -\frac{3}{2} & \frac{1}{2} & 0 \\ 0 & -2 & 1+\alpha \end{pmatrix}\,, \quad \Omega_1 = \begin{pmatrix} 0 & 0 & 0 \\ 1 & 0 & 1 \\ 0 & 0 & 0 \end{pmatrix}\,. \tag{4.68}$$

When going to the limit $k^2\epsilon \ll 1$ (or setting $\Omega_1 \to 0$) we obtain the zeroth order growing mode solution as

$$\bar{\psi}_k \to \bar{\psi}_k^{(0)} \equiv \begin{pmatrix} 1 \\ 1 \\ \frac{2}{2+\alpha} \end{pmatrix} e^{\eta}\delta_{k0}\,, \tag{4.69}$$

in accordance with Eq. (4.62). Here δ_{k0} denotes the usual initial density field. This equation also tells us that in the limit $k^2\epsilon \ll 1$ for both δ_k, θ_k we obtain the identical linear growing mode $e^{\eta}\delta_{k0}$ in analogy to SPT where $F_1 = G_1 = 1$. We can expand around the zeroth order solution to obtain a general solution by an iteration in powers of Ω_1, expanding $\bar{\psi}_k(\eta) = \sum_j \bar{\psi}_k^{(j)}(\eta)$, with

$$\bar{\psi}_k^{(j)}(\eta) = \int^{\eta} \mathrm{d}\eta' g_0(\eta-\eta') \left(-k^2\epsilon(\eta')\Omega_1\right) \bar{\psi}_k^{(j-1)}(\eta')\,, \tag{4.70}$$

where g_0 denotes the linear propagator including all decaying modes in the limit $k^2\epsilon \ll 1$. It is the Green function in the limit $\Omega_1 \to 0$ and contains the SPT propagator given in Eq. (3.59) in the upper left 2×2 block,

$$\begin{aligned} g_0(\eta-\eta') \;=\; & \frac{1}{5}\begin{pmatrix} 3 & 2 & 0 \\ 3 & 2 & 0 \\ \frac{6}{2+\alpha} & \frac{4}{2+\alpha} & 0 \end{pmatrix} e^{\eta-\eta'} + \frac{1}{5}\begin{pmatrix} 2 & -2 & 0 \\ -3 & 3 & 0 \\ -\frac{12}{2\alpha-1} & \frac{12}{2\alpha-1} & 0 \end{pmatrix} e^{-3(\eta-\eta')/2} \\ & + \begin{pmatrix} 0 & 0 & 0 \\ 0 & 0 & 0 \\ \frac{6}{(2\alpha-1)(\alpha+2)} & \frac{-4(1+\alpha)}{(2\alpha-1)(\alpha+2)} & 1 \end{pmatrix} e^{-(1+\alpha)(\eta-\eta')}\,. \end{aligned} \tag{4.71}$$

From the first column in the first term ($\propto e^{\eta}$) one can read off the leading order result from Eq. (4.69). Relative to SPT an additional decaying mode ($\propto e^{-(1+\alpha)\eta}$) emerges due to the presence of velocity dispersion. When using the growing mode initial conditions Eq. (4.69), one obtains

$$\bar{\psi}_k^{(j)}(\eta) = \begin{pmatrix} c_\delta^{(j)} \\ c_\theta^{(j)} \\ c_{\bar{g}}^{(j)} \end{pmatrix} \left(\epsilon(\eta)k^2\right)^j e^{\eta}\delta_{k0}\,, \tag{4.72}$$

with coefficients that can be found recursively by using Eq. (4.70),

$$c_\delta^{(j)} = -\frac{2(4+3\alpha j-2\alpha)}{\alpha j(5+2\alpha j)(2+\alpha j)} c_\delta^{(j-1)}\,, \tag{4.73}$$

and

$$c_{\bar{g}}^{(j)} = \frac{2(1+\alpha j)}{2+\alpha j+\alpha} c_{\delta}^{(j)}\,, \quad c_{\theta}^{(j)} = (1+\alpha j) c_{\delta}^{(j)}\,. \tag{4.74}$$

Then the explicit form of the recursive solution yields

$$c_{\delta}^{(j)} = \left(-\frac{3}{\alpha^2}\right)^j \frac{1}{j!} \frac{\Gamma\left(j+\frac{4+\alpha}{3\alpha}\right)}{\Gamma\left(\frac{4+\alpha}{3\alpha}\right)} \frac{\Gamma\left(\frac{5}{2\alpha}+1\right)}{\Gamma\left(j+\frac{5}{2\alpha}+1\right)} \frac{\Gamma\left(\frac{2}{\alpha}+1\right)}{\Gamma\left(j+\frac{2}{\alpha}+1\right)}\,. \tag{4.75}$$

Performing the sum $\sum_j$ over Eq. (4.72) gives an expression in terms of a generalized hypergeometric function, ${}_1F_2$. This gives a closed-form result for the perturbation modes

$$\psi_{k,a}(\eta) = F_{1,a}(k,\eta)\, e^{\eta} \delta_{k0}\,, \tag{4.76}$$

with linear kernels for the density contrast,

$$F_{1,\delta}(k,\eta) = {}_1F_2\left(\frac{4+\alpha}{3\alpha}; 1+\frac{2}{\alpha}, 1+\frac{5}{2\alpha}; \frac{-3k^2\epsilon(\eta)}{\alpha^2}\right)\,, \tag{4.77}$$

and for the velocity divergence and the rescaled velocity dispersion mode,

$$\begin{aligned}
F_{1,\theta}(k,\eta) &= F_{1,\delta}(k,\eta) - \frac{2(4+\alpha)k^2\epsilon}{(2+\alpha)(5+2\alpha)}\, {}_1F_2\left(\frac{4+4\alpha}{3\alpha}; 2+\frac{2}{\alpha}, 2+\frac{5}{2\alpha}; \frac{-3k^2\epsilon}{\alpha^2}\right)\,, \\
F_{1,\bar{g}}(k,\eta) &= \frac{2}{2+\alpha}\left[{}_1F_2\left(\frac{4+\alpha}{3\alpha}; 2+\frac{2}{\alpha}, 1+\frac{5}{2\alpha}; \frac{-3k^2\epsilon}{\alpha^2}\right)\right. \\
&\quad \left. - \frac{(4+\alpha)k^2\epsilon}{(1+\alpha)(5+2\alpha)}\, {}_1F_2\left(\frac{4+4\alpha}{3\alpha}; 3+\frac{2}{\alpha}, 2+\frac{5}{2\alpha}; \frac{-3k^2\epsilon}{\alpha^2}\right)\right]\,.
\end{aligned} \tag{4.78}$$

Note that in the limit $k^2\epsilon \to 0$ we recover the asymptotic solution Eq. (4.69) and that the full linear results given in Eq. (4.77) and Eq. (4.78) are valid for arbitrary values of $k^2\epsilon$. We show these expressions in Fig. 4.2 for $\alpha = 2$ where we scaled out the time-dependence by normalizing the scale to the dispersion scale k_σ, which characterizes the scale above which velocity dispersion effects become important. That is we expect UV screening to set in when the ratio k/k_σ becomes of the order one. In the limit $k^2\epsilon \ll 1$ (or equivalently $k/k_\sigma \ll 1$) we recover the zeroth order solution, Eq. (4.69), in analogy to SPT. But keep in mind even in this limit we have a nonzero contribution from $F_{1,\bar{g}}$ (see Fig. 4.2). Note also that the ratio $k/k_\sigma(\eta)$ is *time-dependent*. This means the scale above which we expect the suppression to take place changes with time and enters as $k^2\epsilon$ in the hypergeometric functions above. For example the lack of suppression of small-k modes can be somewhat compensated by the growth of velocity dispersion at late times rendering the term $k^2\epsilon$ to unity leading to suppression. On the other hand, large-k modes (which are suspected to be suppressed) can still grow as $\propto e^{\eta}$ as long as velocity dispersion has not built up which is the case for early times, so we get small $k^2\epsilon$ and no suppression.

Following the discussion of the expansion in Eq. (4.72) the next-order result proportional to $k^2\epsilon$ is given by

$$\begin{pmatrix} F_{1,\delta} \\ F_{1,\theta} \\ F_{1,\bar{g}} \end{pmatrix} \to \begin{pmatrix} 1 \\ 1 \\ \frac{2}{2+\alpha} \end{pmatrix} - \begin{pmatrix} 1 \\ 1+\alpha \\ 1 \end{pmatrix} \frac{2(4+\alpha)k^2\epsilon(\eta)}{\alpha(2+\alpha)(5+2\alpha)} + \mathcal{O}(k^4\epsilon^2)\,, \tag{4.79}$$

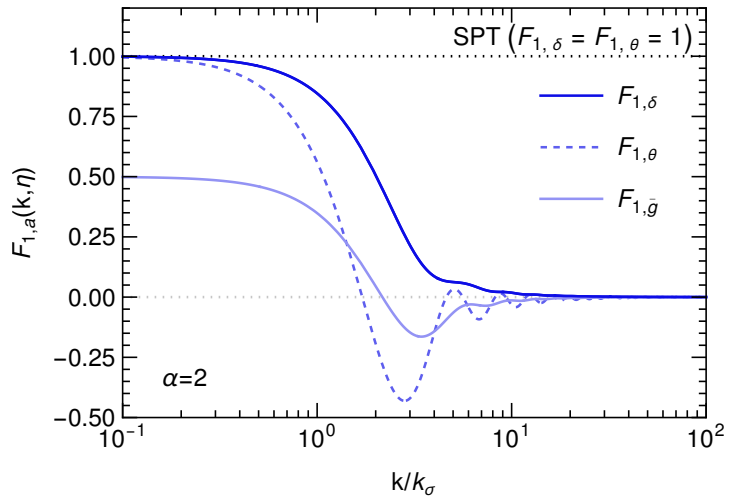

Figure 4.2: Linear kernels $F_{1,a}(k,\eta)$ for the modes $a = \delta$, θ, $\bar{g}$ that show the suppression relative to SPT around the dispersion scale $k \simeq k_\sigma$. We set $\eta = 0$, $\alpha = 2$. In the limit $k \to 0$ one recovers the SPT kernels $F_{1,\delta} = F_{1,\theta} = 1$. However, also the rescaled dispersion mode $\bar{g} = g/\epsilon$ is nonvanishing in this limit and possesses a growing mode, $F_{1,\bar{g}} \to 2/(2+\alpha)$. In addition, the time-dependence is scaled out by rescaling k with $k_\sigma = 1/\sqrt{\epsilon(\eta)}$. Reprinted from [98].

valid in the limit $k^2\epsilon \to 0$. The first term recovers the zeroth order solution of Eq. (4.69). The fact that the term proportional to $k^2\epsilon$ will be subtracted leads to a *suppression* relative to SPT (for $\alpha > 0$) and captures the onset of "Jeans-like" suppression discussed above which indeed depends on the precise form of the background dispersion $\epsilon(\eta)$. Eq. (4.79) agrees with the low-k approach in [59]. It is also noteworthy that velocity divergence θ is even more suppressed relative to the suppression of the density contrast δ by a factor of $1+\alpha$ which was also found in [59, 166] and can be seen in Fig. 4.2.

In the opposite limit $k^2\epsilon \gg 1$ one finds that the decay happens with a power-law scaling. The asymptotic expansion when neglecting the second line of Ω_0 in Eq. (4.68) for large $k^2\epsilon$ looks as

$$F_{1,a}(k,\eta) \to D_a s_k^{-d_a} + E_a s_k^{-e_a} \cos\left(\frac{2s_k}{\alpha} + \varphi_a\right) , \tag{4.80}$$

where $s_k^2 \equiv 3k^2\epsilon(\eta)$ with coefficients given in Table 4.1. It can be rewritten by the form

$$\begin{pmatrix} F_{1,\delta} \\ F_{1,\theta} \\ F_{1,\bar{g}} \end{pmatrix} \to \begin{pmatrix} 1 \\ -\frac{1+\alpha}{3} \\ -1 \end{pmatrix} \frac{D_\delta}{s_k^{d_\delta}} + 2\,\mathrm{Re}\left[\begin{pmatrix} 1 \\ is_k \\ 2 \end{pmatrix} \frac{E_\delta e^{i\left(\frac{2s_k}{\alpha}+\varphi_\delta\right)}}{s_k^{e_\delta}}\right] , \tag{4.81}$$

where one notes that the coefficients d_δ, e_δ tell us whether the nonoscillating power-law decay ($\propto 1/k^{d_\delta}$) or the oscillating decay ($\propto 1/k^{e_\delta}$) dominates. For $F_{1,\delta}$ and $F_{1,\bar{g}}$ we have

$$d_\delta = \frac{16+4\alpha}{6\alpha} \quad < \quad e_\delta = \frac{19+7\alpha}{6\alpha} , \tag{4.82}$$

such that the nonoscillating part dominates as long as $\alpha > 0$. For $F_{1,\theta}$ this is only true for $0 < \alpha < 1$, while the oscillating part dominates for $\alpha > 1$ because of the additional factor is_k in

Table 4.1: Coefficients in the expansion Eq. (4.80) of the linear kernels $F_{1,a}(k,\eta)$ for large $k^2\epsilon$.

a	d_a	e_a	D_a	E_a	φ_a
δ	$\frac{2}{3\alpha}(4+\alpha)$	$\frac{19+7\alpha}{6\alpha}$	$\frac{5\alpha^{\frac{2-\alpha}{3\alpha}}\Gamma(\frac{2}{\alpha})\Gamma(\frac{5}{2\alpha})}{\Gamma(\frac{4\alpha+7}{6\alpha})\Gamma(\frac{2(1+\alpha)}{3\alpha})}$	$-\frac{5\alpha^{\frac{19-5\alpha}{6\alpha}}\Gamma(\frac{2}{\alpha})\Gamma(\frac{5}{2\alpha})}{\sqrt{\pi}\Gamma(\frac{4+\alpha}{3\alpha})}$	$\frac{5\alpha-19}{12\alpha}\pi$
θ	$\frac{2}{3\alpha}(4+\alpha)$	$\frac{19+\alpha}{6\alpha}$	$-\frac{5\alpha^{\frac{2-\alpha}{3\alpha}}(\alpha+1)\Gamma(\frac{2}{\alpha})\Gamma(\frac{5}{2\alpha})}{3\Gamma(\frac{4\alpha+7}{6\alpha})\Gamma(\frac{2(1+\alpha)}{3\alpha})}$	$-\frac{5\alpha^{\frac{19-5\alpha}{6\alpha}}\Gamma(\frac{2}{\alpha})\Gamma(\frac{5}{2\alpha})}{\sqrt{\pi}\Gamma(\frac{4+\alpha}{3\alpha})}$	$\frac{11\alpha-19}{12\alpha}\pi$
$\bar{g}$	$\frac{2}{3\alpha}(4+\alpha)$	$\frac{19+7\alpha}{6\alpha}$	$-\frac{5\alpha^{\frac{2-\alpha}{3\alpha}}\Gamma(\frac{2}{\alpha})\Gamma(\frac{5}{2\alpha})}{\Gamma(\frac{4\alpha+7}{6\alpha})\Gamma(\frac{2(1+\alpha)}{3\alpha})}$	$-\frac{10\alpha^{\frac{19-5\alpha}{6\alpha}}\Gamma(\frac{2}{\alpha})\Gamma(\frac{5}{2\alpha})}{\sqrt{\pi}\Gamma(\frac{4+\alpha}{3\alpha})}$	$\frac{5\alpha-19}{12\alpha}\pi$

the second line of Eq. (4.81). This can also be seen from Fig. 4.2 where the oscillating nature is only visible in $F_{1,\theta}$ for $\alpha = 2$.

However, as emphasized above, small-scale suppression is not always guaranteed in particular when including cumulants beyond second order, a feature expected for a collisionless system [160], in contrast to fluids. Remarkably, when restricting to second cumulant approximation we find no evidence of instability, leading to stable solutions when going to higher orders in perturbation theory. We will discuss stability conditions in Ch. 5.

Finally, so far we only discussed the leading growing mode solutions at linear order in perturbation theory. The general solution including all eigenmodes can be also found and is given by

$$\begin{aligned}\delta_k &= A\, e^{\eta}\, {}_1F_2\left(\frac{4+\alpha}{3\alpha}; 1+\frac{2}{\alpha}, 1+\frac{5}{2\alpha}; \frac{-3k^2\epsilon(\eta)}{\alpha^2}\right)\\ &+ B\, e^{-\frac{3}{2}\eta}\, {}_1F_2\left(\frac{-7+2\alpha}{6\alpha}; 1-\frac{1}{2\alpha}, 1-\frac{5}{2\alpha}; \frac{-3k^2\epsilon(\eta)}{\alpha^2}\right)\\ &+ C\, e^{-\eta}\, {}_1F_2\left(\frac{-2+\alpha}{3\alpha}; 1-\frac{2}{\alpha}, 1+\frac{1}{2\alpha}; \frac{-3k^2\epsilon(\eta)}{\alpha^2}\right),\end{aligned} \tag{4.83}$$

with free coefficients A, B, C. In the limit $k^2\epsilon \to 0$ the hypergeometric functions become unity and we recover the usual growing and decaying modes known from SPT plus an additional decaying mode coming from the velocity dispersion mode g_k (not $\bar{g}_k$ here). A full treatment of the scalar modes including all the decaying modes means we have to account for $\delta\epsilon_k$ and A_k. This leads to two additional terms for δ_k with free coefficients D, E in Eq. (4.83). An analysis shows that one of them is zero ($D = 0$) and the second is given by

$$\delta_k|_{A=B=C=0} = E\,\left[{}_2F_3\left(1, p_1; q_1, q_2, q_3; x\right) - 1\right], \tag{4.84}$$

where

$$p_1 \equiv \frac{1+\alpha}{3\alpha}, \qquad q_1 \equiv \frac{\alpha-1}{\alpha}, \qquad q_2 \equiv \frac{\alpha+1}{\alpha}, \qquad q_3 \equiv \frac{\alpha+\frac{3}{2}}{\alpha}, \tag{4.85}$$

and $x \equiv -3k^2\epsilon(\eta)/\alpha^2$. It scales with e^0 and is thus related to the freedom to chose different initial conditions for δ_k and A_k. We refer to [98] for further details about this and the derivation of a generalized propagator including velocity dispersion. The solutions given in Eq. (4.77) and Eq. (4.78) are obtained when setting $B = C = D = E = 0$, i.e. neglecting the decaying modes.

This is justified given $\epsilon(\eta)$ grows with time at late times and we henceforth use these generalized growing mode initial conditions (first line in Eq. 4.83).

Before considering nonlinear solutions within the second cumulant approximation we first turn to the inclusion of higher cumulants beyond second order and discuss an updated linear approximation. The nonlinear regime will be discussed in Ch. 7.

4.2 Higher cumulants

In this section we want to extend the framework presented so far to go beyond the second cumulant approximation, that is we discuss how to incorporate third and higher cumulants of the distribution function into the VPT framework. In a hydrodynamic context where the distribution function is close to thermal equilibrium higher cumulants are expected to be even more suppressed. However, shell-crossing generates all cumulants beyond first order at once which accounts for a highly nontrivial distribution function at small scales. An example of this can be seen when discussing background values of the cumulants within halo models, see [98]. Nevertheless, within the regime of perturbative validity, i.e. in the mildly nonlinear regime the impact of higher cumulants is expected to become negligible at some point. Hence, we want to quantify the impact coming from cumulants beyond second order.

Split of cumulant generating function into background values and perturbation modes

First, it is convenient to define the rescaled cumulant generating function

$$\widetilde{\mathcal{C}}(\eta, \boldsymbol{x}, \boldsymbol{L}) \equiv \mathcal{C}(\tau, \boldsymbol{x}, \boldsymbol{l})\,, \qquad \boldsymbol{l} = \frac{\boldsymbol{L}}{(-f\mathcal{H})}\,, \tag{4.86}$$

where $\eta = \ln(D(\tau))$. Setting

$$\widetilde{\mathcal{C}}_{i_1,\ldots,i_n} \equiv \nabla_{L_{i_1}} \cdots \nabla_{L_{i_n}} \widetilde{\mathcal{C}}|_{\boldsymbol{L}=0}\,, \tag{4.87}$$

which is equivalent to Eq. (4.9) and we get the rescaled cumulants up to fourth order,

$$u_i = \widetilde{\mathcal{C}}_i, \quad \epsilon_{ij} = \widetilde{\mathcal{C}}_{ij}, \quad \pi_{ijk} = \widetilde{\mathcal{C}}_{ijk}, \quad \Lambda_{ijkl} = \widetilde{\mathcal{C}}_{ijkl}\,, \tag{4.88}$$

in accordance with Eq. (4.10). Including higher cumulants means we also have to account for their homogeneous expectation values which are nonzero for even cumulants, respecting statistical isotropy, that is we have

$$\begin{aligned} \langle \pi_{ijk} \rangle &= 0\,, \\ \langle \Lambda_{ijkl} \rangle &= \left(\delta^K_{ij}\delta^K_{kl} + 2 \text{ cyc.} \right) \frac{\omega(\eta)}{5}\,, \end{aligned} \tag{4.89}$$

with $\omega(\eta)$ the homogeneous background value of the fourth cumulant Λ_{ijkl}. It is normalized as $\langle \Lambda_{ijkk} \rangle = \omega(\eta)\delta^K_{ij}$ with δ^K_{ij} the unit matrix. The corresponding equations of motion can be obtained analogously as for the second cumulant variables by applying additional derivatives with respect to $\boldsymbol{L}$ in Eq. (4.8). But first we deal with the equation of motion of $\widetilde{\mathcal{C}}$ itself. Switching to the η-dependence yields

$$\partial_\eta \widetilde{\mathcal{C}} + \left(\frac{3}{2}\frac{\Omega_m}{f^2} - 1 \right) (\boldsymbol{L}\cdot\nabla_L)\widetilde{\mathcal{C}} - (\nabla\widetilde{\mathcal{C}})\cdot(\nabla_L\widetilde{\mathcal{C}}) - (\nabla\cdot\nabla_L)\widetilde{\mathcal{C}} = \boldsymbol{L}\cdot\nabla\widetilde{\phi}\,. \tag{4.90}$$

Next, we can define a generic ensemble average of the generating functional,

$$\mathcal{E}(\eta, L^2) \equiv \langle \widetilde{\mathcal{C}}(\eta, \boldsymbol{x}, \boldsymbol{L}) \rangle \,, \tag{4.91}$$

which according to statistical homogeneity and isotropy only depends on even powers of $\boldsymbol{L}$. The corresponding evolution equation can be obtained by taking the ensemble average of Eq. (4.90) plus taking the average over $\boldsymbol{L}$,

$$\left[\partial_\eta + \left(\frac{3}{2}\frac{\Omega_m}{f^2} - 1\right)\frac{\partial}{\partial \ln L}\right]\mathcal{E} = Q_\mathcal{E} \equiv \int \frac{\mathrm{d}\Omega_L}{4\pi} \langle \nabla\widetilde{\mathcal{C}} \cdot \nabla_L \widetilde{\mathcal{C}} \rangle \,. \tag{4.92}$$

Analogously as in Eq. (4.4), $\widetilde{\mathcal{C}}$ can be written in terms of a Taylor expansion in $\boldsymbol{L}$,

$$\widetilde{\mathcal{C}} = A + L_i u_i + \frac{1}{2} L_i L_j \epsilon_{ij} + \frac{1}{6} L_i L_j L_k \pi_{ijk} + \frac{1}{24} L_i L_j L_k L_l \Lambda_{ijkl} + \dots \,, \tag{4.93}$$

with fifth and higher cumulants hidden in the ellipsis. For $\mathcal{E}$ we can also write down the corresponding Taylor expansion

$$\mathcal{E} = \mathcal{A}(\eta) + \frac{1}{2}\epsilon(\eta) L^2 + \frac{1}{24}\frac{3\omega(\eta)}{5} L^4 + \mathcal{O}(L^6) \,, \tag{4.94}$$

which is obtained by taking the ensemble average of Eq. (4.93) and using the definitions of the expectation values in Eqs. (4.14, 4.42) and (4.89) of the zeroth, second and fourth cumulant, respectively.

In Ch. 5 we discuss an extension going beyond fourth cumulant order dealing with the full hierarchy. For this purpose it is convenient to write down

$$\mathcal{E} = \sum_n \mathcal{E}_{2n}(\eta) \frac{L^{2n}}{(2n)!} \,, \tag{4.95}$$

where

$$\mathcal{E}_0 = \mathcal{A} \,, \quad \mathcal{E}_2 = \epsilon \,, \quad \mathcal{E}_4 = \frac{3}{5}\omega \,, \tag{4.96}$$

where background values of sixth and higher cumulants are denoted by $\mathcal{E}_6$, $\mathcal{E}_8$ and so on. For the expectation values given in Eq. (4.96) we obtain their equations of motion by inserting Eqs. (4.93, 4.94) into Eq. (4.92),

$$\begin{aligned}
\partial_\eta \mathcal{A} &= Q_A \equiv Q_\mathcal{E}\big|_{L^0} \,, \\
\left[\partial_\eta + 2\left(\frac{3}{2}\frac{\Omega_m}{f^2} - 1\right)\right]\epsilon &= Q \equiv 2Q_\mathcal{E}\big|_{L^2} \,, \\
\left[\partial_\eta + 4\left(\frac{3}{2}\frac{\Omega_m}{f^2} - 1\right)\right]\omega &= Q_\omega \equiv 24\frac{5}{3}Q_\mathcal{E}\big|_{L^4} \,,
\end{aligned} \tag{4.97}$$

where the generalized source term $Q_\mathcal{E}$ as defined in Eq. (4.92) is evaluated at a given order in powers of L^2. It can be obtained by inserting Eq. (4.94) into Eq. (4.92). Performing the angular integrations using

$$\begin{aligned}
\int \frac{d\Omega_L}{4\pi} L_i L_j &= \frac{1}{3} L^2 \delta^K_{ij} \,, \\
\int \frac{d\Omega_L}{4\pi} L_i L_j L_k L_l &= \frac{1}{15} L^4 \left(\delta^K_{ij}\delta^K_{kl} + 2 \text{ cyc.}\right) \,,
\end{aligned} \tag{4.98}$$

then the resulting equations for $\mathcal{A}$ and ϵ from Eq. (4.97) recover Eqs. (4.15) and (4.43). In addition, we then easily get the equation of motion of the expectation value of the fourth order cumulant $\omega(\eta)$ which arises at order L^4,

$$\begin{aligned} Q_\omega &= \frac{1}{3}\Big\{\langle(\nabla_i A)\widetilde{\mathcal{C}}_{ijjkk}\rangle + 4\langle(\nabla_i u_j)\Lambda_{ijkk}\rangle \\ &\quad + 2\langle(\nabla_i \epsilon_{jj})\pi_{ikk}\rangle + 4\langle(\nabla_i \epsilon_{jk})\pi_{ijk}\rangle \\ &\quad + 4\langle(\nabla_i \pi_{jkk})\epsilon_{ij}\rangle + \langle(\nabla_i \Lambda_{jjkk})u_i\rangle\Big\}\,. \end{aligned} \tag{4.99}$$

In order to get equations of motion for the perturbation variables we first define

$$\delta\widetilde{\mathcal{C}}(\eta, \boldsymbol{x}, \boldsymbol{L}) \equiv \widetilde{\mathcal{C}}(\eta, \boldsymbol{x}, \boldsymbol{L}) - \mathcal{E}(\eta, L^2)\,, \tag{4.100}$$

then subtract Eq. (4.92) from Eq. (4.90) which gives

$$\left[\partial_\eta + \left(\frac{3}{2}\frac{\Omega_m}{f^2} - 1\right)(\boldsymbol{L}\cdot\nabla_L) - 2\frac{\partial\mathcal{E}}{\partial L^2}\boldsymbol{L}\cdot\nabla - (\nabla\cdot\nabla_L)\right]\delta\widetilde{\mathcal{C}} = (\nabla\delta\widetilde{\mathcal{C}})\cdot(\nabla_L\delta\widetilde{\mathcal{C}}) + \boldsymbol{L}\cdot\nabla\widetilde{\phi} - Q_{\mathcal{E}}\,, \tag{4.101}$$

from which one can derive the equations of motion for all the perturbation variables by Taylor expanding in L_i. Up to the second cumulant the evolution equations are given in Appendix A. The term proportional to $\partial\mathcal{E}/\partial L^2 = \epsilon/2 + L^2\omega/20 + \mathcal{O}(L^4)$ can actually be seen as the generalization of the terms in Eq. (4.45) which generate terms that describes the above discussed "Jeans-like" suppression.

Third and fourth cumulant

In the following we focus on the third $\pi_{ijk} \equiv \delta\pi_{ijk}$ and fourth cumulant $\Lambda_{ijkl} = \langle\Lambda_{ijkl}\rangle + \delta\Lambda_{ijkl}$ with potential expectation value given in Eq. (4.89). That is we set fifth and higher cumulants to zero. The equation of motion for the third cumulant for our notation becomes

$$\begin{aligned} \partial_\eta\pi_{ijk} &+ 3\left(\frac{3}{2}\frac{\Omega_m}{f^2} - 1\right)\pi_{ijk} - \epsilon(\eta)\left(\nabla_k\delta\epsilon_{ij} + \nabla_i\delta\epsilon_{kj} + \nabla_j\delta\epsilon_{ik}\right) \\ &- \frac{\omega(\eta)}{5}\left(\delta^K_{ij}\nabla_k + \delta^K_{ik}\nabla_j + \delta^K_{jk}\nabla_i\right)A - \nabla_m\,\delta\Lambda_{ijkm} \\ &= \delta\epsilon_{km}\nabla_m\delta\epsilon_{ij} + \delta\epsilon_{im}\nabla_m\delta\epsilon_{kj} + \delta\epsilon_{jm}\nabla_m\delta\epsilon_{ik} + \delta\Lambda_{ijkm}\nabla_m A \\ &\quad + u_m\nabla_m\pi_{ijk} + \pi_{jkm}\nabla_m u_i + \pi_{ikm}\nabla_m u_j + \pi_{ijm}\nabla_m u_k \quad , \end{aligned} \tag{4.102}$$

which comes originally from Eq. (4.2) and we inserted the "background + fluctuation" splitting of the cumulants into the expressions. For the background values of second and fourth cumulant we used $\epsilon(\eta)$ and $\omega(\eta)$, respectively. While the equation for π_{ijk} is complete, we expand the one for Λ_{ijkl} up to linear order in perturbations for brevity, and since we never use nonlinear terms when discussing solutions at fourth cumulant order. The corresponding equation then reads

$$\begin{aligned} &\partial_\eta\Lambda_{ijkl} + 4\left(\frac{3}{2}\frac{\Omega_m}{f^2} - 1\right)\Lambda_{ijkl} - \epsilon(\eta)\left(\nabla_i\pi_{jkl} + \nabla_j\pi_{ikl} + \nabla_k\pi_{ijl} + \nabla_l\pi_{ijk}\right) \\ &- \frac{\omega(\eta)}{5}\left[\delta^K_{ij}(\nabla u)_{kl} + \delta^K_{ik}(\nabla u)_{jl} + \delta^K_{jk}(\nabla u)_{il} + \delta^K_{il}(\nabla u)_{jk} + \delta^K_{jl}(\nabla u)_{ik} + \delta^K_{kl}(\nabla u)_{ij}\right] = 0\,, \end{aligned} \tag{4.103}$$

where we used the short-hand notation $(\nabla u)_{ij} = \nabla_i u_j + \nabla_j u_i$ for brevity.

We take the full set of *scalar* perturbations of them into account by decomposing

$$\begin{aligned}
\pi^S_{ijk} &= -\left(\delta^K_{ij}\frac{\nabla_k}{\nabla^2} + 2 \text{ cyc.}\right)\frac{\chi}{5} - \frac{\nabla_i\nabla_j\nabla_k}{\nabla^4}(\pi - \chi)\,, \\
\delta\Lambda^S_{ijkl} &= \left(\delta^K_{ij}\delta^K_{kl} + 2 \text{ cyc.}\right)\frac{\zeta}{5} + \left(\delta^K_{ij}\frac{\nabla_k\nabla_l}{\nabla^2} + 5 \text{ cyc.}\right)\frac{\kappa - \xi - 2\zeta}{2} \\
&\quad + \frac{\nabla_i\nabla_j\nabla_k\nabla_l}{\nabla^4}(7\zeta + 5\xi - 4\kappa)\,,
\end{aligned} \tag{4.104}$$

with scalar modes $\pi, \chi, \kappa, \xi, \zeta$ defined such that $\pi = -\nabla_i\pi_{ijj}$, $\kappa = \Lambda_{iijj}$ and $\xi = \nabla_i\nabla_j/\nabla^2\Lambda_{ijkk}$. The superscript means that we only account for the scalar mode contributions while neglecting vector, tensor and higher-spin fields of third and fourth cumulant since we expect that the dominant contributions coming from third and fourth cumulants are given by the scalar perturbations. Now we recall that third cumulant perturbations enter the equation for the velocity dispersion ϵ_{ij}, see Eq. (4.13). At the background level we can calculate the source terms for second and fourth cumulant expectation values by inserting the scalar modes given in Eq. (4.104) into Eqs. (4.16) and (4.99),

$$\begin{aligned}
\left[\partial_\eta + 2\left(\frac{3}{2}\frac{\Omega_m}{f^2} - 1\right)\right]\epsilon &= \frac{1}{3}\Big\{\langle A\pi\rangle + \langle\theta(g - \delta\epsilon)\rangle + 2\langle w_i\nu_i\rangle\Big\}\,, \\
\left[\partial_\eta + 4\left(\frac{3}{2}\frac{\Omega_m}{f^2} - 1\right)\right]\omega &= \frac{1}{3}\Big\{\langle\theta(4\xi - \kappa)\rangle + 2\langle(g + 3\delta\epsilon)\pi\rangle - \frac{8}{5}\langle g\chi\rangle\Big\}\,,
\end{aligned} \tag{4.105}$$

where e.g. $\langle A\pi\rangle = \int d^3k\, P_{A\pi}(k,\eta)$ which is in fact the only change in the source term for ϵ when compared to the second cumulant approximation, even when allowing for higher cumulant orders. The source term for ω in the second line contains cross power spectra between first and fourth as well as second and third cumulant perturbations. Note that this is not the complete set of power spectra entering Q_ω since e.g. vector and tensor modes as well as cross spectra between zeroth and fifth cumulant perturbations are neglected in the current approximation which would play a role here.

In order to obtain equations of motion for the scalar perturbations we use

$$\begin{aligned}
\pi^{(3)} &= (-\nabla_i\delta_{kj})\,\pi_{ijk}\,, \\
\chi^{(3)} &= \frac{5}{2}\left(\frac{\nabla_i\nabla_j\nabla_k}{\nabla^2} - \nabla_i\delta_{kj}\right)\pi_{ijk}\,, \\
\kappa^{(4)} &= \left(\delta^K_{ij}\delta^K_{kl}\right)\,\delta\Lambda_{ijkl}\,, \\
\xi^{(4)} &= \left(\frac{\nabla_i\nabla_j}{\nabla^2}\delta^K_{kl}\right)\,\delta\Lambda_{ijkl}\,, \\
\zeta^{(4)} &= \frac{5}{8}\left[\frac{\nabla_i\nabla_j\nabla_k\nabla_l}{\nabla^4} + \delta^K_{ij}\left(\delta^K_{kl} - 2\frac{\nabla_k\nabla_l}{\nabla^2}\right)\right]\,\delta\Lambda_{ijkl}\,,
\end{aligned} \tag{4.106}$$

where the superscript indicates the cumulant order to which the scalar mode belongs to. This notation is only used here for clarification. In Fourier space, in addition to Eq. (4.105), the

complete set of scalar modes up to the fourth cumulant in the linear approximation becomes

$$\begin{aligned}
\partial_\eta \delta_k &= \theta_k \,, \\
\left[\partial_\eta + \left(\frac{3}{2}\frac{\Omega_m}{f^2} - 1\right)\right] \theta_k &= \frac{3}{2}\frac{\Omega_m}{f^2}\delta_k - \epsilon k^2 A_k - k^2(g_k + \delta\epsilon_k) \,, \\
\left[\partial_\eta + 2\left(\frac{3}{2}\frac{\Omega_m}{f^2} - 1\right)\right] g_k &= 2\epsilon\theta_k - \pi_k + \frac{3}{5}\chi_k \,, \\
\left[\partial_\eta + 2\left(\frac{3}{2}\frac{\Omega_m}{f^2} - 1\right)\right] \delta\epsilon_k &= -\frac{1}{5}\chi_k \,, \\
\left[\partial_\eta + 3\left(\frac{3}{2}\frac{\Omega_m}{f^2} - 1\right)\right] \pi_k &= \omega k^2 A_k + \epsilon k^2(3g_k + 5\delta\epsilon_k) + k^2\xi_k \,, \\
\left[\partial_\eta + 3\left(\frac{3}{2}\frac{\Omega_m}{f^2} - 1\right)\right] \chi_k &= \omega k^2 A_k + \epsilon k^2(5\delta\epsilon_k) + \frac{1}{2}k^2(5\kappa_k - 5\xi_k - 8\zeta_k) \,, \\
\left[\partial_\eta + 4\left(\frac{3}{2}\frac{\Omega_m}{f^2} - 1\right)\right] \kappa_k &= 4\omega\theta_k - 4\epsilon\pi_k \,, \\
\left[\partial_\eta + 4\left(\frac{3}{2}\frac{\Omega_m}{f^2} - 1\right)\right] \xi_k &= \frac{16}{5}\omega\theta_k - 4\epsilon\pi_k + \frac{4}{5}\epsilon\chi_k \,, \\
\left[\partial_\eta + 4\left(\frac{3}{2}\frac{\Omega_m}{f^2} - 1\right)\right] \zeta_k &= 0 \,,
\end{aligned} \tag{4.107}$$

as well as $\partial_\eta A_k = \theta_k$ such that $A_k = \delta_k$ in the linear approximation. We notice that the background values of second, fourth, ... cumulant first enter in the first, third, ... cumulant perturbation equations. This means, the dispersion background ϵ already enters the Euler equation (second line) and the background value ω first enters the equation for the scalar mode π_k of the third cumulant (fifth line) both leading to the "Jeans-like" suppression terms. The full nonlinear equations in this truncation scheme also take the form of Eq. (4.47), with an extended set of variables in the scalar sector

$$\psi^S = (\delta, \theta, g, \delta\epsilon, A, \pi, \chi, \kappa, \xi, \zeta) \,, \tag{4.108}$$

and the corresponding linear matrix is given by

$$\Omega^S = \begin{pmatrix}
 & -1 & & & & & & & & \\
-3/2 & 1/2 & k^2 & k^2 & k^2\epsilon & & & & & \\
 & -2\epsilon & 1 & & & 1 & -3/5 & & & \\
 & & & 1 & & & 1/5 & & & \\
 & -1 & & & & & & & & \\
 & & -3k^2\epsilon & -5k^2\epsilon & -k^2\omega & 3/2 & & & -k^2 & \\
 & & & -5k^2\epsilon & -k^2\omega & & 3/2 & -5/2k^2 & 5/2k^2 & 4k^2 \\
 & -4\omega & & & & 4\epsilon & & 2 & & \\
 & -16/5\omega & & & & 4\epsilon & -4/5\epsilon & & 2 & \\
 & & & & & & & & & 2
\end{pmatrix} , \tag{4.109}$$

in the approximation $\Omega_m/f^2 \to 1$. In addition, the set of vertices increases which are listed in Appendix D. Therein, vertices are given where the scalar modes π, χ of the third cumulant as

well as all other scalar modes or at most one vorticity, vector or tensor mode up to the second cumulant appear (see Eq. 4.46). That is we do not include vertices where scalar modes of the fourth cumulant appear which means we only solve the linear equations for κ, ξ, ζ (last three lines of Eq. 4.107) in accordance with Eq. (4.103).

After discussing linear solutions up to the fourth cumulant, we extend the cumulant expansion beyond fourth order in linear approximation in Ch. 5.

Linear solutions

Now we consider linear solutions by solving the system of equations including third and fourth cumulant in the linear approximation which is given by Eq. (4.107). For illustration, we assume a constant dimensionless ratio for the fourth cumulant expectation value

$$\bar{\omega} \equiv \frac{\omega(\eta)}{\epsilon(\eta)^2}\,, \tag{4.110}$$

due to dimensional reasons and which is also motivated within the scaling solutions considered in Ch. 6. Henceforth, we work with dimensionless perturbation variables

$$\bar{g} \equiv \frac{g}{\epsilon},\;\; \delta\bar{\epsilon} \equiv \frac{\delta\epsilon}{\epsilon},\;\; \bar{\pi} \equiv \frac{\pi}{\epsilon},\;\; \bar{\chi} \equiv \frac{\chi}{\epsilon},\;\; \bar{\kappa} \equiv \frac{\kappa}{\epsilon^2},\;\; \bar{\xi} \equiv \frac{\xi}{\epsilon^2},\;\; \bar{\zeta} \equiv \frac{\zeta}{\epsilon^2}\,. \tag{4.111}$$

Note that as discussed in the second cumulant approximation at linear level only scalar modes contribute. The evolution equations for the dimensionless quantities for the Fourier mode k using $\Omega_m/f^2 \to 1$ then read

$$\begin{aligned}
\partial_\eta \delta_k &= \theta_k\,,\\
\left[\partial_\eta + \frac{1}{2}\right]\theta_k &= \frac{3}{2}\delta_k - \epsilon k^2\left(\delta_k + \bar{g}_k + \delta\bar{\epsilon}_k\right)\,,\\
\left[\partial_\eta + 1 + \alpha\right]\bar{g}_k &= 2\theta_k - \bar{\pi}_k + \frac{3}{5}\bar{\chi}_k\,,\\
\left[\partial_\eta + 1 + \alpha\right]\delta\bar{\epsilon}_k &= -\frac{1}{5}\bar{\chi}_k\,,\\
\left[\partial_\eta + \frac{3}{2} + \alpha\right]\bar{\pi}_k &= \epsilon k^2\left(\bar{\omega}\delta_k + 3\bar{g}_k + 5\delta\bar{\epsilon}_k + \bar{\xi}_k\right)\,,\\
\left[\partial_\eta + \frac{3}{2} + \alpha\right]\bar{\chi}_k &= \epsilon k^2\left(\bar{\omega}\delta_k + 5\delta\bar{\epsilon}_k + \frac{1}{2}\left(5\bar{\kappa}_k - 5\bar{\xi}_k - 8\bar{\zeta}_k\right)\right)\,,\\
\left[\partial_\eta + 2 + 2\alpha\right]\bar{\kappa}_k &= 4\bar{\omega}\theta_k - 4\bar{\pi}_k\,,\\
\left[\partial_\eta + 2 + 2\alpha\right]\bar{\xi}_k &= \frac{16}{5}\bar{\omega}\theta_k - 4\bar{\pi}_k + \frac{4}{5}\bar{\chi}_k\,,\\
\left[\partial_\eta + 2 + 2\alpha\right]\bar{\zeta}_k &= 0\,.
\end{aligned} \tag{4.112}$$

For this set of evolution equations one can find growing mode initial conditions for $k^2\epsilon \to 0$ as

$$\begin{aligned}
\bar{\psi}_k &\equiv \left(\delta_k,\, \theta_k,\, \bar{g}_k,\, \delta\bar{\epsilon}_k,\, \bar{\pi}_k,\, \bar{\chi}_k,\, \bar{\kappa}_k,\, \bar{\xi}_k,\, \bar{\zeta}_k\right)\\
&\to \left(1,\, 1,\, \frac{2}{2+\alpha}, 0, 0, 0, \frac{4\bar{\omega}}{3+2\alpha},\, \frac{16\bar{\omega}}{5(3+2\alpha)}, 0\right) e^{\eta}\delta_{k0}\,,
\end{aligned} \tag{4.113}$$

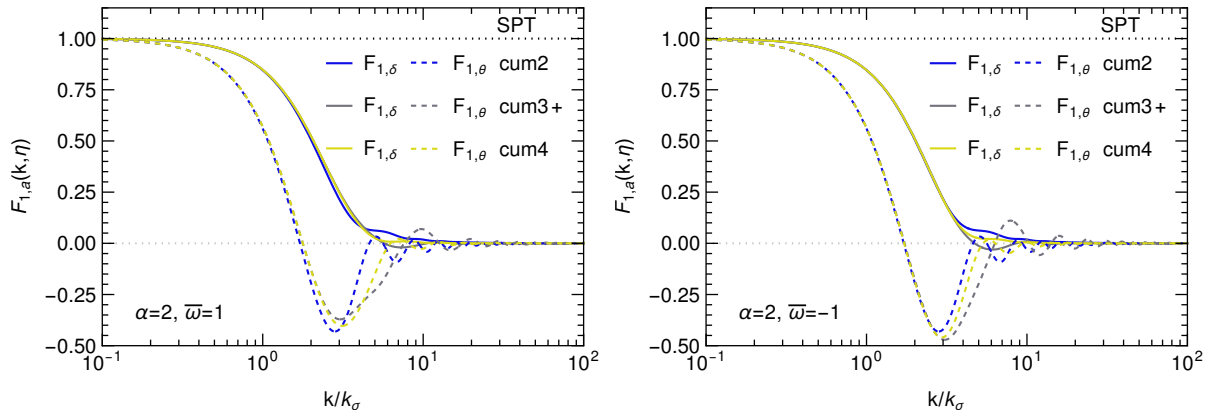

Figure 4.3: Linear Kernels $F_{1,\delta}(k,\eta)$ (solid lines) and $F_{1,\theta}(k,\eta)$ (dashed lines) when including second, third and fourth cumulant, respectively. The left panel shows $\bar{\omega} = +1$ and the right panel $\bar{\omega} = -1$. In addition, $\alpha = 2$, $\eta = 0$ and $k_\sigma = 1/\sqrt{\epsilon(\eta)}$. Reprinted from [98].

in accordance with Eq. (4.69) in the second cumulant approximation. Note that now the situation changes also for the modes $\bar{g}_k$, $\delta\bar{\epsilon}_k$ of the second cumulant, where the latter can be generated at linear level due to the presence of mode $\bar{\chi}_k$ which in turn gets generated by terms proportional to $k^2\epsilon$. Also $\bar{\pi}_k$ will be generated in time by terms proportional to $k^2\epsilon$. Having initialized we can write down the corresponding linear kernels for all variables as

$$\bar{\psi}_{k,a}(\eta) \equiv F_{1,a}(k,\eta)\, e^{\eta}\delta_{k0}\,. \tag{4.114}$$

The solution of these kernels can be calculated within different approximation schemes capturing the successive impact of higher cumulants:

cum2: second cumulant approximation $(\delta_k, \theta_k, \bar{g}_k, \delta\bar{\epsilon}_k$ and background dispersion $\epsilon(\eta))$,

cum3+: third cumulant approximation for perturbation modes $(+\,\bar{\pi}_k, \bar{\chi}_k)$, and fourth cumulant approximation for expectation values $(+\,\omega(\eta))$,

cum4: fourth cumulant approximation $(+\,\bar{\kappa}_k, \bar{\xi}_k, \bar{\zeta}_k)$,

where the modes given in the parenthesis denote the ones which are included in the given approximation scheme. The **cum2** scheme corresponds to the second cumulant approximation given by the analytical results from Eq. (4.77) and Eq. (4.78). In addition, **cum3+** includes further modes $\bar{\pi}_k, \bar{\chi}_k$ from the third cumulant as well as the expectation value $\omega(\eta)$ of the fourth cumulant. Here, Eq. (4.102) will be used where all terms involving $\delta\Lambda_{ijkl}$ are neglected. So, only the expectation value of the fourth cumulant is taken into account. Finally, **cum4** takes also the modes $\bar{\kappa}_k, \bar{\xi}_k, \bar{\zeta}_k$ into account and one works with the full set Eq. (4.107) in linear approximation. The treatment of comparing results for different approximation schemes allows one to quantify the impact of higher cumulants. In Fig. 4.3 we show the kernels $F_{1,\delta}$ (solid lines) and $F_{1,\theta}$ (dashed lines) for all three approximations where for **cum3+** and **cum4** the equations have to be solved numerically including the linear kernel of $F_{1,\delta\bar{\epsilon}}$ which is absent in **cum2**.

Both panels in Fig 4.3 use identical setups except for the choice of $\bar{\omega}$ (left $+1$ and right -1). On scales up to the dispersion scale $k \lesssim 3k_\sigma$ there is hardly any difference between the different

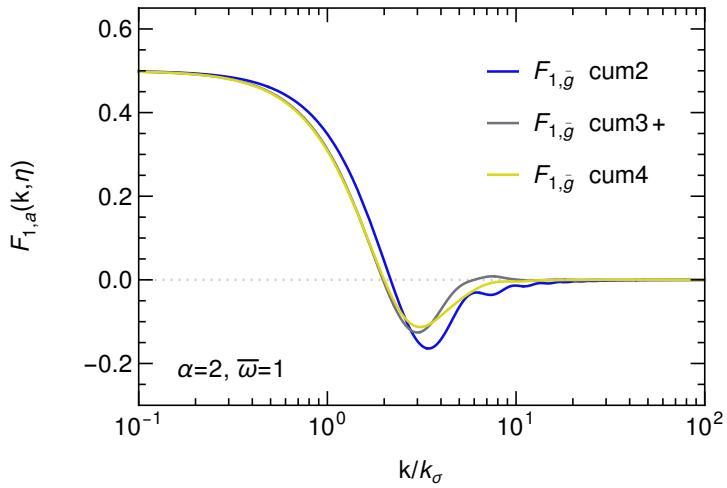

Figure 4.4: Linear kernel for $F_{1,\bar{g}}(k,\eta)$ for second, third and fourth cumulant approximations, respectively. Here $\alpha = 2$, $\eta = 0$ and $\bar{\omega} = +1$. Reprinted from [98].

approximations while higher cumulants becoming important for even smaller scales $k \gtrsim 3k_\sigma$ in the damping tail. For negative $\bar{\omega}$ the impact seems to be even less pronounced. For $F_{1,\bar{g}}$ there is a mild shift when including the third cumulant (**cum3+**) while adding the fourth cumulant the additional difference is rather small (**cum4**), see Fig. 4.4.

It is possible to find an approximate analytical solution for the schemes **cum3+** and **cum4** when considering $k^2\epsilon \to 0$ given by

$$F_{1,\bar{g}} \to \frac{1}{2} - k^2\epsilon \times \begin{cases} \frac{1}{6} & \text{cum2}\,, \\ \frac{1}{6} + \frac{1+4\bar{\omega}/15}{26} & \text{cum3+}\,, \\ \frac{1}{6} + \frac{1+4\bar{\omega}/15}{26} + \frac{2\bar{\omega}}{273} & \text{cum4}\,, \end{cases} \tag{4.115}$$

where we set $\alpha = 2$. In fact, at order $\mathcal{O}(k^2\epsilon)$, fifth and higher cumulants do not change this result.

Overall, while **cum2**, i.e. the second cumulant approximation significantly changes the dynamics even at linear order, see Sec. 4.1, taking higher cumulants (**cum3+** and **cum4**) into account we do not observe appreciable differences for the linear δ and θ kernels in the transition region between the ideal fluid behavior for $k \ll k_\sigma$ and the strongly suppressed regime for $k \gg k_\sigma$. The emergence of the background dispersion ϵ at linear order is mainly responsible for the screening of small scales for $k \gtrsim \epsilon^{-1/2}$. Due to dimensional reasons we expect the background value of the fourth cumulant being relevant when $k \gtrsim \omega^{-1/4}$. For $\omega \sim \epsilon^2$ this coincides with the dispersion scale. Thus, since all cumulants are generated at once, one expects the relevant scales of all the cumulants to be in the same range.[1] Despite this and in addition the complicated coupling between different cumulants, it is remarkable that, as the numerical evaluation shows, even the third order cumulant is significantly less important than the second cumulant at the relevant scales and, along with the fourth cumulant, plays only a role at very high k values.

[1] Provided that $\mathcal{E}_{2n} \propto \epsilon^n$ for even n, see Sec. 5.3 for details.

In the next chapter we introduce a framework where one is able to include an arbitrary cumulant order and discuss further linear solutions. Nonlinear results will be presented in Ch. 7.

5 Full hierarchy of cumulants

So far the perturbative treatment to include dispersion and higher cumulants allowed us to calculate solutions in linear approximation. Also nonlinear solutions within this framework can be found and we present them in Ch. 7. In the following we introduce an alternative formulation to include an arbitrary number of higher cumulants beyond fourth order, however it is restricted to linear order in perturbations. This formulation can be used to study the convergence of linear kernels in the cumulant hierarchy in Sec. 5.1. In addition, we present stability conditions in Sec. 5.4 to ensure convergence of the Vlasov hierarchy within linear approximation.

To proceed, we introduce the Fourier decomposition of the cumulant generating function perturbation $\delta\widetilde{\mathcal{C}}$, Eq. (4.100),

$$\delta\widetilde{\mathcal{C}}(\eta, \boldsymbol{x}, \boldsymbol{L}) = \int \mathrm{d}^3k \, e^{\mathrm{i}\boldsymbol{k}\cdot\boldsymbol{x}} \, \delta\widetilde{\mathcal{C}}(\eta, \boldsymbol{k}, \boldsymbol{L}) \,. \tag{5.1}$$

We henceforth use adiabatic cold dark matter initial conditions as before. This gives rise to growing mode initial conditions for the density contrast and velocity divergence whereas vorticity as well as higher cumulants vanish relative to the density contrast at early times. Thus, when expanding to linear order, all perturbation variables are proportional to the initial density contrast, i.e. this implies $\delta\widetilde{\mathcal{C}}(\eta, \boldsymbol{k}, \boldsymbol{L}) \propto e^{\eta}\delta_{k0}$. As before, the proportionality factor will be given by a linear kernel, derived from the linearized equations Eq. (4.101), while the dependence on the initial stochastic density field δ_{k0} as well as the leading time-dependence e^{η} are factored out. To linear order, we know from rotational invariance that the linear kernel shall depend on the wave vector $\boldsymbol{k}$ and the auxiliary vector $\boldsymbol{L}$ only via their magnitudes k, L as well as the scalar projection $\mu \equiv \boldsymbol{k} \cdot \boldsymbol{L}/kL$. It is convenient to introduce the multipole decomposition

$$\delta\widetilde{\mathcal{C}}(\eta, \boldsymbol{k}, \boldsymbol{L}) = \sum_{\ell} i^{-\ell}(2\ell + 1)\mathcal{C}_{\ell}(\eta, k, L)P_{\ell}(\mu)e^{\eta}\delta_{k0} \,, \tag{5.2}$$

with the Legendre polynomials $P_{\ell}(\mu)$ and the *multipoles* are given by

$$\mathcal{C}_{\ell}(\eta, k, L) \equiv i^{\ell} \int_{-1}^{1} \frac{\mathrm{d}\mu}{2} \delta\widetilde{\mathcal{C}}(\eta, \boldsymbol{k}, \boldsymbol{L}) \frac{P_{\ell}(\mu)}{e^{\eta}\delta_{k0}} \,. \tag{5.3}$$

The quantity $\mathcal{C}_{\ell}$ denotes the evolution of *perturbations*. We prefer to denote it by $\mathcal{C}_{\ell}$ instead of $\delta\mathcal{C}_{\ell}$ since the initial density perturbation is here already factored out and it is then more closely

related to "transfer functions". The first four multipoles are given by

$$\begin{aligned}
\mathcal{C}_0 &= F_{1,A} + \frac{\epsilon L^2}{6}(F_{1,\bar{g}} + 3F_{1,\delta\bar{\epsilon}}) + \frac{\epsilon^2 L^4}{5!}F_{1,\bar{\kappa}} + \mathcal{O}(L^6)\,,\\
\mathcal{C}_1 &= \frac{L}{k}\left(\frac{F_{1,\theta}}{3} - \frac{\epsilon L^2}{30}F_{1,\bar{\pi}} + \mathcal{O}(L^4)\right),\\
\mathcal{C}_2 &= -\frac{\epsilon L^2}{15}F_{1,\bar{g}} + \frac{2\epsilon^2 L^4}{7\cdot 5!}(F_{1,\bar{\kappa}} - 3F_{1,\bar{\xi}}) + \mathcal{O}(L^6)\,,\\
\mathcal{C}_3 &= \frac{L}{k}\left(\frac{\epsilon L^2}{105}(F_{1,\bar{\pi}} - F_{1,\bar{\chi}}) + \mathcal{O}(L^4)\right),\\
\mathcal{C}_4 &= \frac{\epsilon^2 L^4}{9\cdot 7\cdot 5\cdot 3}\left(-4F_{1,\bar{\kappa}} + 5F_{1,\bar{\xi}} + 7F_{1,\bar{\zeta}}\right) + \mathcal{O}(L^6)\,.
\end{aligned} \tag{5.4}$$

They are obtained by Taylor expanding $\delta\widetilde{\mathcal{C}}$ in L_i (analogously as in Eq. (4.93) but instead with the perturbations of the cumulants only) and evaluating the integral in Eq. (5.3). Notice that the multipoles are related to the linear kernels only, with $e^{\eta}\delta_{k0}$ being factored out. From the Taylor series mentioned before each second term vanishes due to the μ-integration in each $\mathcal{C}_\ell$ with leading order power given by $\mathcal{C}_\ell \propto L^\ell$. This means that each multipole contains a tower of higher cumulants multiplied by powers of L^2, with lowest power being L^ℓ. Here only scalar modes contribute since we only expand to linear order in perturbations, which allows us to replace $F_{1,A} \to F_{1,\delta}$ in $\mathcal{C}_0$.

From the equation of motion Eq. (4.101) of the cumulant generating function perturbation one can obtain a corresponding equation of motion for the multipoles

$$\begin{aligned}
\left[\partial_\eta + 1 + \left(\frac{3}{2}\frac{\Omega_m}{f^2} - 1\right)(L\cdot\partial_L)\right]\mathcal{C}_\ell &= \frac{k}{2\ell+1}\left[2\frac{\partial\mathcal{E}}{\partial L^2}L + \partial_L\right]((\ell+1)\mathcal{C}_{\ell+1} - \ell\mathcal{C}_{\ell-1})\\
&+ \frac{k}{2\ell+1}\frac{1}{L}((\ell+1)(\ell+2)\mathcal{C}_{\ell+1} + \ell(\ell-1)\mathcal{C}_{\ell-1})\\
&- \frac{k}{3}LF_{1,\widetilde{\phi}}\delta^K_{\ell 1}\,,
\end{aligned} \tag{5.5}$$

where the quadratic term in the equation for $\delta\widetilde{\mathcal{C}}$ was neglected. $\delta^K_{\ell 1}$ is the Kronecker symbol and

$$F_{1,\widetilde{\phi}} \equiv \frac{\widetilde{\phi}_k}{e^{\eta}\delta_{k0}} = \frac{3}{2}\frac{\Omega_m}{f^2}\frac{F_{1,\delta}}{k^2} = \frac{3}{2}\frac{\Omega_m}{f^2}\frac{\mathcal{C}_0}{k^2}\Big|_{L=0}\,. \tag{5.6}$$

Similarly, for the source term of the generalized expectation value $\mathcal{E}$, Eq. (4.92), one can insert the multipole decomposition which gives

$$Q_{\mathcal{E}} = 4\pi\int_0^\infty \mathrm{d}k\, k^3 e^{2\eta}P_0(k)\sum_\ell(\ell+1)\left(\mathcal{C}_{\ell+1}\partial_L\mathcal{C}_\ell - \mathcal{C}_\ell\partial_L\mathcal{C}_{\ell+1} - \frac{2(\ell+1)}{L}\mathcal{C}_{\ell+1}\mathcal{C}_\ell\right), \tag{5.7}$$

where $P_0(k)$ is the usual linear input power spectrum with time-dependence $e^{2\eta}$ being factored out. The impact of the cumulants from the Vlasov dynamics is contained in the multipoles $\mathcal{C}_\ell$. By inserting Eq. (5.4) into Eq. (5.5) one gets the linear evolution equations Eq. (4.107) (using Eq. 4.114) of **cum4** when Taylor expanding up to order L^4. In addition, to recover the equations for the source terms in Eq. (4.105) one has to expand Eq. (5.7) in L up to the order given by Eq. (4.94). Finally, using Eq. (5.4) and Eq. (3.65) yields the desired result.

5.1 Linear kernels beyond fourth cumulant order

The treatment so far allows us to incorporate cumulants beyond fourth order. It is convenient to factor out the leading L^ℓ dependence of $\mathcal{C}_\ell$ as well as a factor of $1/k$ for odd ℓ, giving

$$\mathcal{C}_\ell(\eta,k,L) = L^\ell \times \begin{cases} \check{\mathcal{C}}_\ell(\eta,k,L) & \ell \text{ even}\,, \\ \check{\mathcal{C}}_\ell(\eta,k,L)/k & \ell \text{ odd}\,. \end{cases} \tag{5.8}$$

We analogously expand the rescaled multipoles as

$$\check{\mathcal{C}}_\ell(\eta,k,L) = \sum_n \frac{L^{2n}}{(2n)!}\mathcal{C}_{\ell,2n}(\eta,k)\,. \tag{5.9}$$

The above mentioned vanishing of each second term in the Taylor series L arises due to the symmetry of the Legendre decomposition such that in $\check{\mathcal{C}}_\ell$ only even powers of L appear. The multipole coefficients are then directly related to the linear kernels in accordance with Eq. (5.4), e.g.

$$\mathcal{C}_{0,0}(\eta,k) = F_{1,\delta}(\eta,k), \quad \mathcal{C}_{1,0}(\eta,k) = \frac{1}{3}F_{1,\theta}(\eta,k), \quad \mathcal{C}_{2,0}(\eta,k) = -\frac{\epsilon}{15}F_{1,\bar{g}}(\eta,k)\,. \tag{5.10}$$

Note that the additional factors of ϵ only arise due to the notation given in Eq. (4.111). One can define an analogous expression for the ensemble averages of the cumulants (identical to Eq. 4.95) as

$$\mathcal{E}(\eta,L^2) = \sum_n \frac{L^{2n}}{(2n)!}\mathcal{E}_{2n}(\eta)\,, \tag{5.11}$$

such that the background values of zeroth, second and fourth expectation values are given by

$$\mathcal{E}_0 = \mathcal{A},\ \mathcal{E}_2 = \epsilon,\ \mathcal{E}_4 = \frac{3\omega}{5}\,, \tag{5.12}$$

where only even cumulants possess a nonzero expectation value, due to statistical isotropy. By inserting the expansions given above into Eq. (5.5) we can derive an equation of motion for the $\mathcal{C}_{\ell,2n}$, given by

$$\left[\partial_\eta + 1 + \left(\frac{3}{2}\frac{\Omega_m}{f^2} - 1\right)(\ell+2n)\right]\mathcal{C}_{\ell,2n} \;=\; \frac{\{1,k^2\}}{2\ell+1}\mathcal{R}_{\ell,2n} + \frac{1}{2}\delta^K_{\ell 1}\delta^K_{n0}\frac{\Omega_m}{f^2}\mathcal{C}_{0,0}\,, \tag{5.13}$$

where $\{A,B\} = A$ for even ℓ, and B for odd ℓ, δ^K_{ij} is the Kronecker symbol, and

$$\begin{aligned} \mathcal{R}_{\ell,2n} \;\equiv\; & \sum_{m=0}^{n} \frac{(2n)!\,\mathcal{E}_{2m+2}}{(2m+1)!(2n-2m)!} \\ & \times \Big((\ell+1)(2n-2m)(2n-2m-1)\mathcal{C}_{\ell+1,2(n-m-1)} - \ell\mathcal{C}_{\ell-1,2(n-m)}\Big) \\ & +(\ell+1)\,(2\ell+3+2n)\,\mathcal{C}_{\ell+1,2n} - \frac{\ell}{2n+1}\mathcal{C}_{\ell-1,2(n+1)}\,. \end{aligned} \tag{5.14}$$

To solve them we set the growing mode initial conditions as

$$\begin{aligned} \mathcal{C}_{0,0} &\to 1\,, \\ \mathcal{C}_{1,0} &\to \frac{1}{3}\,, \\ \mathcal{C}_{\ell,2n} &\to 0, \qquad \ell+2n \geq 2\,, \end{aligned} \tag{5.15}$$

for $\eta \to -\infty$, as appropriate for cold dark matter and adiabatic initial conditions. The sum $\ell + 2n$ gives information about the maximal cumulant order $c_{\max}$ we take into account. We henceforth consider different cumulant truncations with a specific $c_{\max}$, that is we include perturbations $\mathcal{C}_{\ell,2n}$ with

$$\ell + 2n \leq c_{\max}\,, \tag{5.16}$$

while setting those with $\ell + 2n > c_{\max}$ to zero. The truncations with $c_{\max} \leq 4$ in linear approximation we already discussed in the previous chapter where the approximation schemes used there are now related to $c_{\max}$ as

$$\begin{aligned} \textbf{cum2}: &\quad c_{\max} = 2\,, \\ \textbf{cum3+}: &\quad c_{\max} = 3\,, \\ \textbf{cum4}: &\quad c_{\max} = 4\,. \end{aligned}$$

We know already that not only perturbations govern the dynamics, also background values are important and do enter here, see Eq. (5.14). For odd $c_{\max}$ they contribute for all $2n \leq c_{\max} + 1$ whereas for even $c_{\max}$ for all $2n \leq c_{\max}$. This essentially explains the + in **cum3+** since for $c_{\max} = 3$ we know that the fourth (3+1) cumulant expectation value enters in the evolution equations. This pattern is extended to higher order cumulants correspondingly.

Analogously, the differential equations for $\mathcal{E}_{2n}$ can be obtained by Taylor expanding the source term Eq. (5.7) in L. They are given by

$$\left[\partial_\eta + \left(\frac{3}{2}\frac{\Omega_m}{f^2} - 1\right) 2n\right] \mathcal{E}_{2n} = Q_{\mathcal{E}_{2n}}\,, \tag{5.17}$$

with

$$\begin{aligned} Q_{\mathcal{E}_{2n}} \;=\; & 4\pi \int_0^\infty dk\, k^2\, e^{2\eta}\, P_0(k) \sum_{\ell=0}^{n} (\ell+1) \sum_{m_1,m_2=0}^{n-\ell} \delta^K_{m_1+m_2,n-\ell} \frac{(2n)!}{(2m_1)!(2m_2)!} \\ & \times (2m_2 - 2m_1 - 2\ell - 3) \mathcal{C}_{\ell+1,2m_1} \mathcal{C}_{\ell,2m_2}\,. \end{aligned} \tag{5.18}$$

Hence, in order to find linear (kernels) solutions for an arbitrary cumulant order in principle we have to solve both Eq. (5.13) and Eq. (5.14) correspondingly. We refer the reader to Ch. 6 for self-consistent solutions of both perturbations and background values.

Instead, we now consider solutions where we take the $\mathcal{E}_{2n}$ as given. Thus, we only have to solve Eq. (5.13) using the $\mathcal{E}_{2n}$ as external input, as before. In Fig. 5.1 we show the linear density kernel $F_{1,\delta} \equiv \mathcal{C}_{0,0}$ for various $c_{\max} = 2 \ldots 20$, when assuming the power-law growth of the background dispersion as in the linear solutions of the previous chapter, and in addition we set all remaining background values to zero, that is we have

$$\mathcal{E}_2(\eta) \equiv \epsilon(\eta) = \epsilon_0 e^{\alpha\eta}, \qquad \mathcal{E}_{2n}(\eta) = 0 \quad \text{for} \quad 2n \geq 4\,. \tag{5.19}$$

We checked that the linear kernels of the solutions obtained for **cum2, cum3+** and **cum4** are identical to the ones for $c_{\max} = 2, 3, 4$. For example the top line in Fig 5.1 is the same as the one from Fig 4.2. In particular, we use the quadratic late-time growth of the velocity dispersion $\epsilon \propto a^2$ (or more correctly $\propto D_+^2$). We emphasize that this choice of vanishing $\mathcal{E}_{2n}$ for $2n \geq 4$ we only used here, in particular we derive constraints on the values of $\mathcal{E}_{2n}$ to ensure stability in Sec. 5.4 and present self-consistent solutions of them in Ch. 6. We observe in Fig. 5.1 that for any particular wavenumber k the linear kernel gets more suppressed when including higher

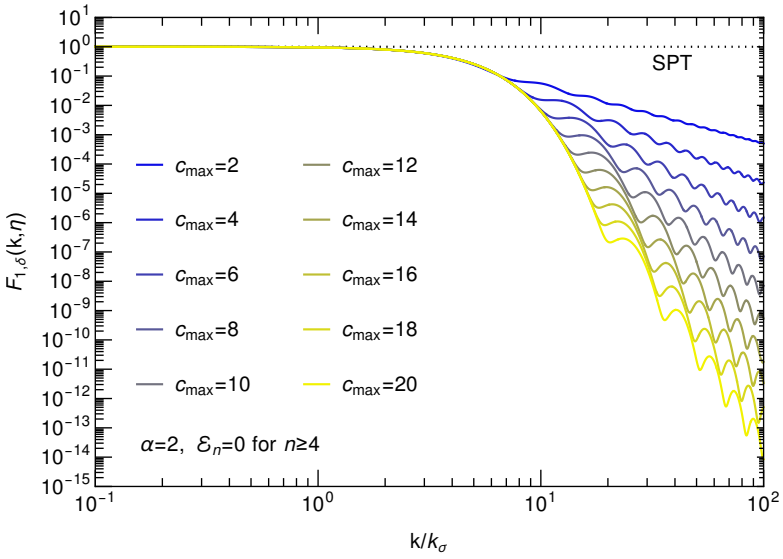

Figure 5.1: Linear VPT kernels for the density $F_{1,\delta} = \mathcal{C}_{0,0}$ when taking up to twenty cumulants ($c_{\max} = 20$) into account. For a given $c_{\max}$ we include all perturbations $\mathcal{C}_{\ell,2n}$ with $\ell + 2n \leq c_{\max}$. Here we set $\eta = 0$, $\alpha = 2$ and $\mathcal{E}_{2n}$. In addition, we scaled out the time-dependence by normalizing each scale with the time-dependent dispersion scale $k_\sigma = 1/\sqrt{\epsilon(\eta)}$. The inclusion of higher cumulants (beyond second order) only reinforces the suppression and indicates the convergence of VPT within this approximation.

cumulants, i.e. if $c_{\max}$ is increased. They even approach a common limit, which is depicted by the yellow envelope. To obtain convergence, for higher wavenumbers a larger value of $c_{\max}$ is required. For the lowest truncation (**cum2**) we see that the approximation is sufficient for wavenumbers of $k \lesssim 7k_\sigma$. At that value the kernel is already suppressed by a factor of 10 relative to the SPT value which is unity. When going to smaller scales the kernel gets strongly suppressed, especially for higher cumulant truncations. For the fourth cumulant truncation, $c_{\max} = 4$, we find convergence for values of $k \lesssim 9k_\sigma$, with a damping of around two orders of magnitude. For the highest truncation order we chose, $c_{\max} = 20$, the convergence reaches down to scales of $k \lesssim 18k_\sigma$, corresponding to a suppression of 10^{-7}. All in all, we found that in linear approximation higher cumulants are important to capture the correct amount of suppression for very large k while cumulants beyond second order are rather negligible to describe the transition region between ideal fluid behavior and the onset of suppression, i.e. for scales around $k \simeq k_\sigma$, as illustrated by the convergence limit. Therefore, within the VPT approximation we are using here the cumulant hierarchy converges.

5.2 Rescaling to dimensionless variables

In the following we want to study the behavior when also including expectation values of higher cumulants. It is convenient to rescale them to dimensionless quantities,

$$\bar{\mathcal{E}}_{2n} \equiv \frac{\mathcal{E}_{2n}}{\epsilon^n} = \frac{\mathcal{E}_{2n}}{\mathcal{E}_2^n}\,, \tag{5.20}$$

as already done for $\mathcal{E}_4 \propto \omega(\eta)$ in Sec. 4.2 leading to the quantity $\bar{\omega}$. One can correspondingly define dimensionless linear kernels

$$T_{\ell,2n} \equiv \frac{\mathcal{C}_{\ell,2n}}{\epsilon^{n+[\ell/2]}}\,, \tag{5.21}$$

where $[\ell/2] = \ell/2$ for even ℓ, and $(\ell-1)/2$ for odd ℓ. The corresponding differential equations of the dimensionless quantities then become

$$\begin{aligned}\left[\partial_\eta + 1 + \left(\frac{3}{2}\frac{\Omega_m}{f^2} - 1\right)(\ell+2n) \quad + \quad (n + \{\ell/2, (\ell-1)/2\})\,(\partial_\eta \ln\epsilon)\right] T_{\ell,2n} \\ = \quad \frac{\{1,\epsilon k^2\}}{2\ell+1}\bar{\mathcal{R}}_{\ell,2n} + \frac{1}{2}\delta^K_{\ell 1}\delta^K_{n0}\frac{\Omega_m}{f^2}T_{0,0}\,,\end{aligned} \tag{5.22}$$

where again $\{A, B\} = A$ for even ℓ, B for odd ℓ, and

$$\left[\partial_\eta + \left(\frac{3}{2}\frac{\Omega_m}{f^2} - 1\right)2n + n(\partial_\eta \ln\epsilon)\right]\bar{\mathcal{E}}_{2n} = \bar{Q}_{\mathcal{E}_{2n}}\,, \tag{5.23}$$

with $\bar{\mathcal{R}}_{\ell,2n} = \mathcal{R}_{\ell,2n}|_{\mathcal{C}\to T,\,\mathcal{E}\to\bar{\mathcal{E}}}$ and $\bar{Q}_{\mathcal{E}_{2n}} = Q_{\mathcal{E}_{2n}}|_{\mathcal{C}\to T}$ from Eq. (5.14) and Eq. (5.18), respectively. One is then able to collect the perturbation variables into a single vector, as before,

$$\bar{\psi}_k' + (\Omega_0 + \epsilon k^2 \Omega_1)\bar{\psi}_k = 0\,, \tag{5.24}$$

which is equivalent to Eq. (4.67), where now the number of rows of $\bar{\psi}_k$ (and equivalently the number of rows and columns of Ω_0 and Ω_1) are given by all scalar variables with $\ell + 2n \leq c_{\max}$. So we have $4, 6, 9, 12, 16$ scalar variables for $c_{\max} = 2, 3, 4, 5, 6$, respectively. Again, $c_{\max}$ denotes the maximal order in the cumulant expansion we take into account with their perturbation variables collected in $\bar{\psi}_k$. The background values $\bar{\mathcal{E}}_{2n}$ $(2n \geq 4)$ will enter the matrices Ω_1 *and* Ω_0, what can be extracted from Eq. (4.109), where $\Omega^S = \Omega_0 + k^2\epsilon\,\Omega_1$. For even $c_{\max}$ the background values $\bar{\mathcal{E}}_4, \bar{\mathcal{E}}_6, \ldots \bar{\mathcal{E}}_{c_{\max}}$ contribute, while for odd $c_{\max}$ the perturbation equations depend on $\bar{\mathcal{E}}_4, \bar{\mathcal{E}}_6, \ldots \bar{\mathcal{E}}_{c_{\max}+1}$.

Assuming again the power-law growth of the velocity dispersion with $\mathcal{E}_2(\eta) = \epsilon(\eta) = \epsilon_0 \exp[\alpha\eta]$ with constant $\alpha = \partial_\eta \ln\epsilon$ and the approximation $\Omega_m/f^2 \to 1$. In addition, we assume constant dimensionless ratios $\bar{\mathcal{E}}_{2n}$, as before for the treatment of the fourth cumulant. In Ch. 6 it will be seen that these assumptions are consistent for a scaling universe and may be seen as a starting point for a more general treatment. In this case, the matrices Ω_0 and Ω_1 are constant in time and the time-dependence is completely contained in the quantity ϵk^2.

5.3 Scaling in the limit $\epsilon \to 0$

All cumulants except for the density and velocity have vanishing initial conditions. Due to the presence of the background dispersion ϵ (and background values of higher cumulants) all other cumulants will be generated in time. Therefore, second and higher cumulants or more precisely their perturbation variables have to vanish in the limit $\epsilon \to 0$, and when assuming dimensionless quantities $T_{\ell,2n}$ they have to approach constant values (e.g. $T_{2,0} \propto F_{1,\bar{g}} \to 2/(2+\alpha)$ for $\epsilon \to 0$). In fact, we expect that higher cumulants are more strongly suppressed when $\epsilon \to 0$. To see this we consider Eq. (5.24) in the limit $\epsilon k^2 \to 0$, whose solutions are determined by the eigenmodes

of Ω_0. When considering systems containing at least the SPT variables (plus the background dispersion) with $c_{\max} \geq 1$ the Ω_0–eigenmodes always comprise the usual growing and decaying modes known from SPT, and additional decaying modes for $c_{\max} \geq 2$. Inspecting the term $\{1, \epsilon k^2\}$ in Eq. (5.22) one notes that the Taylor expansion in powers of ϵk^2 starts with a constant term for even ℓ, while for odd ℓ it contains at least one factor of ϵk^2. There is one exception related to the velocity divergence ($\ell = 1$, $n = 0$) which gives $T_{1,0} = F_{1,\theta}/3 = 1/3 + \mathcal{O}(\epsilon k^2)$. The reason behind this is the Poisson term in the Euler equation for θ. Using Eq. (5.21) one then obtains the following counting

$$\mathcal{C}_{\ell,2n} \propto \begin{cases} \epsilon^{n+\ell/2} \times [1 + \mathcal{O}(\epsilon k^2) + \dots] & \ell \text{ even}\,, \\ \epsilon^0 \times [1 + \mathcal{O}(\epsilon k^2) + \dots] & \ell = 1, n = 0\,, \\ \epsilon^{n+(\ell-1)/2} \times [\mathcal{O}(\epsilon k^2) + \dots] & \ell \text{ odd}, \ \ell + 2n \geq 3\,, \end{cases} \tag{5.25}$$

which shows that higher cumulants with order $\ell + 2n$ are correspondingly more suppressed by the background dispersion ϵ for $\epsilon \to 0$. For the dimensionless cumulant perturbations $T_{\ell,2n}$ one obtains a power counting as given in the square brackets. The condition $\ell + 2n \geq 3$ only arises due to the above mentioned exception for $\ell = 1$, $n = 0$. The next possibility where ℓ is odd gives at least $\ell + 2n = 3$. Overall, the counting assumes that the dimensionless ratios $\bar{\mathcal{E}}_{2n}$ are of order unity which effectively implies for the background values of the $2n$th cumulant $\mathcal{E}_{2n} \propto \epsilon^n$. This means that perturbation variables $\mathcal{C}_{\ell,2n}$ of the same cumulant order equally scale with ϵ.

Looking at the differential equations of the perturbations of the cumulant generating function Eq (4.101), one finds a generalized scaling for the cumulants with leading contribution

$$\begin{aligned} \delta, A, \theta &\propto \mathcal{O}(\epsilon^0)\,, \\ w_i = (\boldsymbol{\nabla} \times \boldsymbol{u})_i &\propto \mathcal{O}(\epsilon^1)\,, \\ \epsilon_{ij} &\propto \mathcal{O}(\epsilon^1)\,, \\ \mathcal{C}_{ijk} &\propto \mathcal{O}(\epsilon^2)\,, \\ \mathcal{C}_{ijkl} &\propto \mathcal{O}(\epsilon^2)\,, \\ \mathcal{C}_{ijklm} &\propto \mathcal{O}(\epsilon^3)\,, \\ \mathcal{C}_{ijklmn} &\propto \mathcal{O}(\epsilon^3)\,, \end{aligned} \tag{5.26}$$

in the limit $\epsilon \to 0$. Simply said, the number of indices of a given cumulant denote the cumulant order and this will hold correspondingly for higher orders (7, 8, ...). Again, the only exception is θ which already contributes at ϵ^0 despite being of first cumulant order. Note that the other part of the velocity, namely the vorticity, obeys the generalized counting structure since the Poisson term cancels in the vorticity equation.

This is a remarkable result, since all the perturbation variables are coupled between different cumulant orders, however using Eq. (4.101) this self-consistency can be checked and this holds for any cumulant order. In addition, it is also valid beyond the linear approximation and will hold for the full nonlinear Vlasov hierarchy.

5.4 Stability conditions

As already mentioned, within the collisionless Vlasov-Poisson system stability is not always guaranteed as can be expected. In this section we present under which circumstances instabilities can occur within the linear approximation and derive stability conditions which give constraints

on the background values of the cumulants. However note that we only highlight the most important results and refer to [98] for an in-depth view of further details and the derivation therein. We also emphasize that within the *collisional* fluid picture we can always expect small-scale suppression, i.e. stability due to microscopic pressure and viscosity.

First of all, in Sec. 5.1 we found a configuration of the collisionless dynamics where stability was fulfilled and observed permanent damping of perturbations, as shown in Fig. 5.1. Those solutions were characterized by the fact that, no matter which cumulant order we took into account we set background values of all order $\mathcal{E}_{2n}$ to zero but solely included the background dispersion $\mathcal{E}_2 = \epsilon$ in the perturbation equations.

When instead including background values $\mathcal{E}_{2n}$ of higher cumulants the solutions of the linear kernels yield essentially analogous results provided the dimensionless quantities $\bar{\mathcal{E}}_{2n}$ (see Eq. 5.20) are of order unity. However, for large ϵk^2 the solutions can establish instabilities when the values of $\bar{\mathcal{E}}_{2n}$ become too large. Demanding those exponential instabilities to be absent imposes restrictions on the background values of the cumulants.

These can be derived when considering Eq. (5.24) in the limit $\epsilon k^2 \gg 1$. Taking an additional time-derivative yields

$$\bar{\psi}_k'' - [\Omega_0 \cdot \Omega_0 + \epsilon k^2(\Omega_0 \cdot \Omega_1 + \Omega_1 \cdot \Omega_0 - \alpha\Omega_1)]\bar{\psi}_k = 0\,, \tag{5.27}$$

where we used $\Omega_1 \cdot \Omega_1 = 0$. When switching from η to the variable

$$s_k \equiv \sqrt{3\epsilon(\eta)k^2}\,, \tag{5.28}$$

we obtain

$$\partial_\eta = \frac{1}{2}(\partial_\eta \ln\epsilon)s_k\partial_{s_k} = \frac{\alpha}{2}s_k\partial_{s_k}\,. \tag{5.29}$$

where we used $\alpha = \partial_\eta \ln\epsilon$ =const. Finally, we obtain following differential equation

$$\left[\frac{\alpha^2}{4}s_k^2\partial_{s_k}^2 - \Omega_0\cdot\Omega_0 - \frac{\alpha}{2}\Omega_0 - \frac{s_k^2}{3}\left(\Omega_0\cdot\Omega_1 + \Omega_1\cdot\Omega_0 - \frac{\alpha}{2}\Omega_1\right)\right]\bar{\psi}_k = 0\,. \tag{5.30}$$

Then the solution is a linear combination of eigenmodes which have leading time-dependence in the limit $s_k \gg 1$,

$$T_{\ell,2n} \propto e^{\pm 2\sqrt{\lambda}\,s_k/\alpha} \qquad \text{for } s_k \gg 1\,, \tag{5.31}$$

where λ are the eigenvalues of the matrix

$$M_{c_{\max}} \equiv \frac{1}{3}\left(\Omega_0\cdot\Omega_1 + \Omega_1\cdot\Omega_0 - \frac{\alpha}{2}\Omega_1\right)\,, \tag{5.32}$$

which depends on the truncation order $c_{\max}$. If any $\sqrt{\lambda}$ has a nonzero real part we will obtain an exponential instability. Therefore, we require

$$\mathrm{Im}(\lambda) = 0, \quad \mathrm{Re}(\lambda) \leq 0\,, \tag{5.33}$$

such that no instability can occur. These conditions can be translated into a condition for the roots of the characteristic polynomial

$$p_{c_{\max}}(\lambda) \equiv \det(\lambda\,\mathbf{1} - M_{c_{\max}})\,, \tag{5.34}$$

which should be zero or lie on the negative real axis. For the truncations we considered so far we obtain

$$\begin{aligned} p_1(\lambda) &= \left(\frac{1}{3}+\lambda\right)^2, \\ p_2(\lambda) &= \lambda^2(1+\lambda)^2, \\ p_3(\lambda) &= \left(\frac{1}{3}+\lambda\right)^2\left(\lambda^2+2\lambda+\frac{1}{9}(3-\bar{\mathcal{E}}_4)\right)^2, \\ p_4(\lambda) &= \lambda^3(1+\lambda)^2\left(\lambda^2+\frac{10}{3}\lambda+\frac{5}{9}(3-\bar{\mathcal{E}}_4)\right)^2. \end{aligned} \tag{5.35}$$

First of all, we find that the roots do not depend on $\alpha = \partial_\eta \ln \epsilon$ which can also be extended to higher $c_{\max}$. This means, that the emergence of instabilities is not sensitive to the time-dependence of the background dispersion. This argument can be turned around, the time-dependence of the background dispersion will not be constrained by the stability conditions. Also, the size of the background dispersion $\mathcal{E}_2 = \epsilon$ is not constrained by the background dispersion, what was also found in Sec. 5.1. Hence, only fourth and higher cumulant expectation values are restricted by stability conditions.

For $c_{\max} = 1, 2$ we find no constraints coming from stability. Truncating at first order means essentially we have continuity and Euler equations identical to the ones from SPT but with an additional "Jeans-like" term $(k^2\epsilon\delta)$ in the Euler equation coming from the background dispersion. This slight modification relative to SPT yields already nontrivial oscillatory solutions since $\lambda = -1/3$ which leads to stability. Next, $c_{\max} = 2$ corresponds to **cum2** whose solutions were already discussed in Sec. 4.1 and the roots $\lambda = 0, -1$ exactly correspond to the exponential factors of the linear density kernel given in Eq. (4.81). The additional power-law dependence on s_k is not captured in the leading contribution in the limit $s_k \gg 1$ considered above.

For $c_{\max} = 3, 4$ (equivalent to **cum3+** and **cum4**, respectively) the expectation value of the fourth cumulant $\bar{\mathcal{E}}_4$ enters the equations of motion. Demanding that the corresponding roots of $p_3(\lambda), p_4(\lambda)$ are real and nonpositive yields

$$\begin{aligned} c_{\max} = 3: &\qquad -6 \le \bar{\mathcal{E}}_4 \le 3, \\ c_{\max} = 4: &\qquad -2 \le \bar{\mathcal{E}}_4 \le 3, \end{aligned} \tag{5.36}$$

constraining the size of the expectation value $\bar{\mathcal{E}}_4 = 3\bar{\omega}/5$. In addition, we find that the roots within $c_{\max} = 3$ contain the ones from $c_{\max} = 1$, while the ones within $c_{\max} = 4$ contain roots of $c_{\max} = 2$. This recursive structure can be extended to higher truncation orders. To find the full *sufficient* set of stability conditions also for higher cumulant truncations $c_{\max} \ge 4$ we simply give the results, while referring to [98] for the detailed derivation of them. For $c_{\max} = 5$ we obtain

$$\begin{aligned} -2 &\le \bar{\mathcal{E}}_4 \le 3, \\ 15(\bar{\mathcal{E}}_4 - 1) &\le \bar{\mathcal{E}}_6 \le 10(6 - \bar{\mathcal{E}}_4), \\ 0 &\le 100\left(24 + 12\bar{\mathcal{E}}_4 - 6\bar{\mathcal{E}}_4^2 + 5\bar{\mathcal{E}}_4^3\right) \\ &\quad -40\bar{\mathcal{E}}_6(2 + 3\bar{\mathcal{E}}_4) - \bar{\mathcal{E}}_6^2, \end{aligned} \tag{5.37}$$

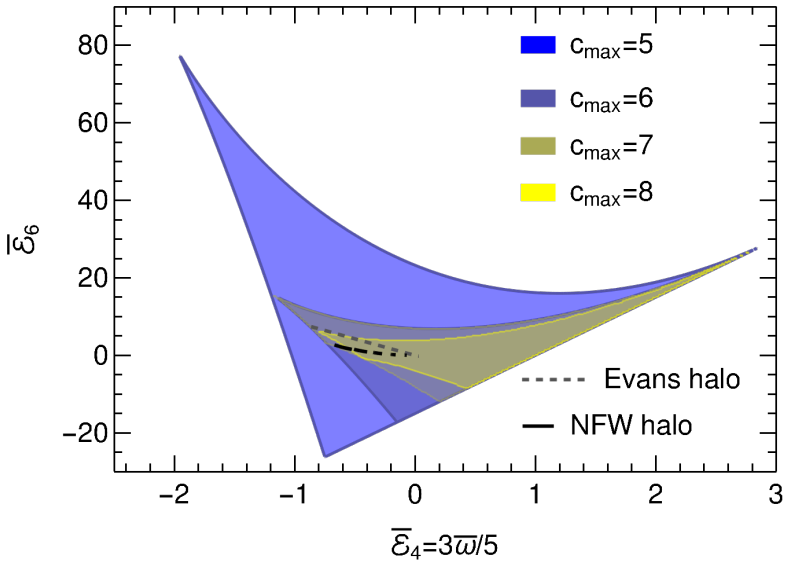

Figure 5.2: Allowed region for the size of the background values $\bar{\mathcal{E}}_4$ and $\bar{\mathcal{E}}_6$ to ensure stability. The fact that the stable region lies within a two-dimensional parameter space $(\bar{\mathcal{E}}_4, \bar{\mathcal{E}}_6)$ takes into account that the stability conditions on $\bar{\mathcal{E}}_4$ depend on $\bar{\mathcal{E}}_6$ and vice versa, for maximal cumulant orders $c_{\max} = 5, 6$. For $c_{\max} = 7, 8$ we get an additional dependence on $\bar{\mathcal{E}}_8$ which is projected onto the $(\bar{\mathcal{E}}_4, \bar{\mathcal{E}}_6)$ plane. The constraints are obtained from the linearized evolution equations of the perturbation modes where the background values $\bar{\mathcal{E}}_4$, $\bar{\mathcal{E}}_6$, $\bar{\mathcal{E}}_8$ first enter for $c_{\max} = 3, 5, 7$, respectively. The grey dashed and black solid line corresponds to the estimates for Evans and NFW halos, respectively. Both halo predictions satisfy the stability conditions, i.e. lie within the stable region which makes linear VPT trustable for a perturbative expansion. Reprinted from [98].

and for $c_{\max} = 6$ we obtain

$$\begin{aligned} -\frac{6}{5} &\leq \bar{\mathcal{E}}_4 \leq 3\,, \\ 15(\bar{\mathcal{E}}_4 - 1) &\leq \bar{\mathcal{E}}_6 \leq 10(2 + \bar{\mathcal{E}}_4/3)\,, \\ 0 &\leq 20\left(216 + 324\bar{\mathcal{E}}_4 + 90\bar{\mathcal{E}}_4^2 + 175\bar{\mathcal{E}}_4^3\right) \\ &\quad -108\bar{\mathcal{E}}_6(4 + 10\bar{\mathcal{E}}_4) - 27\bar{\mathcal{E}}_6^2\,. \end{aligned} \tag{5.38}$$

We confirm that the constraints from $c_{\max} = 3, 4$ are contained in those of $c_{\max} = 5, 6$ while the latter ones further restrict the value of $\bar{\mathcal{E}}_4$. Thus, when going to higher $c_{\max}$ the values of the background values get more and more restricted. The constraints for $c_{\max} = 7, 8$ are given in Ref. [98]. One can check that $\bar{\mathcal{E}}_{2n} = 0$ for $2n \geq 4$ satisfies the stability conditions for all cases. Then, stability sets an upper limit on the size of the $\bar{\mathcal{E}}_{2n}$, which determines how strongly non-Gaussian the distribution function can become.

Overall, there are no constraints coming from the two simplest truncations $c_{\max} = 1, 2$, which makes the equations always stable. For $c_{\max} = 3, 4$ we have constraints restricting the size of $\bar{\mathcal{E}}_4$, given by Eq. (5.36), while for $c_{\max} = 5, 6$ we found additional constraints for $\bar{\mathcal{E}}_4$ as well as

a constraint for the size of $\bar{\mathcal{E}}_6$, as indicated in Eq. (5.37) and Eq. (5.38). The latter two cases then correspond to an allowed finite region in the two-dimensional $(\bar{\mathcal{E}}_4, \bar{\mathcal{E}}_6)$ parameter space, as illustrated in Fig. 5.2.

As claimed above, the point $(\bar{\mathcal{E}}_4, \bar{\mathcal{E}}_6) = (0, 0)$ lies within the stable region. Allowing for higher cumulant truncations further shrinks the stable region while they are contained within the allowed regions for lower $c_{\max}$. Note that when using $c_{\max} = 7, 8$ also $\bar{\mathcal{E}}_8$ enters the equations. Here the allowed region lies within the three-dimensional parameter space $(\bar{\mathcal{E}}_4, \bar{\mathcal{E}}_6, \bar{\mathcal{E}}_8)$ and we only show the projection on the $(\bar{\mathcal{E}}_4, \bar{\mathcal{E}}_6)$ plane. See [98] for more details. In addition, we compared this with predictions coming from halo models (dashed for Evans halo and solid for NFW halo in Fig. 5.2) which were performed in [98]. Here one can extract averaged cumulants from virialized halos. Remarkably, the stable region coming from perturbation theory when linearizing the Vlasov hierarchy covers the predictions from the halos. This means the halo cumulants are automatically within the stable region. They touch the stability boundary either when their shape approaches the unphysical limit of extremely oblateness (Evans halos) or when their mass become very high (NFW halos) which should be exponentially suppressed within a halo mass spectrum. All physical values are therefore allowed.

The fact that the perturbative constraints on the non-Gaussianity of the distribution function is also satisfied by halo calculations is impressive and suggests that the linear approximation of VPT is a good starting point to further develop the perturbative analysis for expectation values of higher cumulants.

In the following we introduce the so-called scaling universe, for which we present self-consistent solutions of the background values in various cumulant truncations.

6 Velocity dispersion in a scaling universe

We considered solutions so far where we took the background dispersion $\mathcal{E}_2 = \epsilon$ (see Sec. 4.1) as well as the background value of the fourth cumulant $\bar{\mathcal{E}}_4 = 3\bar{\omega}/5$ (Sec. 4.2) in the equations for the perturbation modes as given. In this section, we go back to the equations of motion of the background values themselves and recall Eqs. (4.15) and (4.105) as well as Eqs. (4.92) and (4.97). The equations dictate that the background values depend on the perturbations via their source terms and we present self-consistent solutions of the perturbation and background equations in various cumulant truncations in Secs. 6.1 to 6.3. Now, we consider a scaling universe, for which the differential equations for the background values turn into algebraic equations, as presented below.

First of all, we introduce the main features of a scaling universe with EdS background ($\Omega_m = 1$). It is described by a power-law initial spectrum as

$$P_0(k) = A\, k^{n_s}\,, \tag{6.1}$$

where n_s is the scalar spectral index. The linear power spectrum in SPT is then given by

$$P^{\rm lin}_{\rm SPT}(k,\eta) = e^{2\eta} P_0(k)\,, \tag{6.2}$$

with time-dependence $e^{2\eta} = D_+^2$ which is the square of the scale factor in EdS. Then the dimensionless linear power spectrum $\Delta \equiv 4\pi k^3 P$ is given by

$$\Delta^{\rm lin}_{\rm SPT}(k,\eta) = 4\pi e^{2\eta} A\, k^{n_s+3} \equiv \left(\frac{k}{k_{\rm nl}(\eta)}\right)^{n_s+3}\,, \tag{6.3}$$

which depends only on the ratio $k/k_{\rm nl}(\eta)$ with

$$k_{\rm nl}(\eta) = k_{\rm nl}\, e^{-2\eta/(n_s+3)}\,, \tag{6.4}$$

and $k_{\rm nl} = (4\pi A)^{-1/(n_s+3)}$ being the nonlinear scale today ($\eta = 0$). The dimensionless power spectrum obeys a scaling symmetry (for any $r > 0$)

$$k \to rk, \qquad e^{\eta} \to r^{-(n_s+3)/2} e^{\eta}\,, \tag{6.5}$$

such that the nonlinear power spectrum only depends on the ratio

$$\Delta(k,\eta) = \Delta(k/k_{\rm nl}(\eta))\,. \tag{6.6}$$

As before, the background dispersion introduces the time-dependent dispersion scale

$$k_\sigma(\eta) \equiv \frac{1}{\sqrt{\epsilon(\eta)}}\,. \tag{6.7}$$

Then the scaling symmetry implies that the ratio $k_\sigma(\eta)/k_{\rm nl}(\eta)$ is constant which leads to

$$\epsilon(\eta) = \epsilon_0 e^{\alpha\eta}, \qquad \alpha = \frac{4}{n_s+3}\,. \tag{6.8}$$

The value of the background dispersion today gives $k_\sigma \equiv 1/\sqrt{\epsilon_0}$ without time-argument. Given these assumptions, the dimensionless ratios $\bar{\mathcal{E}}_4 = 3\bar{\omega}/5$ as well as all remaining $\bar{\mathcal{E}}_{2n}$ are constant in time. The solutions in linear approximation in Ch. 4 and Ch. 5 explicitly used the time-dependence in Eq. (6.8) and therefore the expressions of the kernels derived therein are applicable within a scaling universe.

The linear matter power spectrum within VPT becomes

$$P^{\rm lin}_{\delta\delta}(k,\eta) = F_{1,\delta}(k,\eta)^2\, e^{2\eta} P_0(k)\,, \tag{6.9}$$

where $F_{1,\delta}(k,\eta)$ is the linear density kernel and is obtained from a linearized version of the perturbation equations. In general, for any perturbation mode we have

$$P^{\rm lin}_{ab}(k,\eta) = F_{1,a}(k,\eta) F_{1,b}(k,\eta)\, e^{2\eta} P_0(k)\,. \tag{6.10}$$

We have seen in Ch. 4 and Ch. 5 that the linear kernels $F_{1,a}(k,\eta) = F_{1,a}(s)$ depend on time and scale only via the dimensionless variable

$$s \equiv s_k(\eta) = \sqrt{3\epsilon(\eta)k^2}\,, \tag{6.11}$$

regardless of the truncation order. Then the dimensionless power spectrum can be written as

$$\Delta^{\rm lin}_{ab}(k,\eta) = x\, \hat{\Delta}^{\rm lin}_{ab}(s)\,, \tag{6.12}$$

where the quantity

$$x \;\equiv\; \left(\frac{k_\sigma}{\sqrt{3}k_{\rm nl}}\right)^{n_s+3} = \left(\frac{1}{3\epsilon_0 k_{\rm nl}^2}\right)^{\frac{n_s+3}{2}} \tag{6.13}$$

does not depend on time, so we can write down

$$\hat{\Delta}^{\rm lin}_{ab}(s) \equiv F_{1,a}(s) F_{1,b}(s) s^{n_s+3}\,. \tag{6.14}$$

This can be extended to the nonlinear power spectrum within VPT including loop corrections. The loop expansion can be written as

$$\Delta_{ab}(k,\eta) = \sum_{L\geq 0} \Delta^{L-{\rm loop}}_{ab}(k,\eta)\,, \tag{6.15}$$

with $L=0$ being the linear solution and furnished by the modified nonlinear kernels from VPT satisfying the differential equations Eq. (4.59). For example the one-loop correction ($L=1$) is given in Eq. (3.66). As each L-loop integral contains exactly $L+1$ factors of $P_0 \propto A \propto x$, one has

$$\Delta^{L-{\rm loop}}_{ab}(k,\eta) = x^{L+1}\, \hat{\Delta}^{L-{\rm loop}}_{ab}(s)\,, \tag{6.16}$$

while for $L=0$ we obtain the linear power spectrum Eq. (6.12).

Now we can discuss self-consistent solutions for the velocity dispersion $\epsilon(\eta)$. Its equation of motion including the source term is given by Eqs. (4.15) and (4.105). Turning to dimensionless variables, we get

$$\frac{\epsilon'(\eta)}{\epsilon(\eta)} + 1 = \frac{1}{3}\int_0^\infty \frac{\mathrm{d}k}{k}\,\left(\Delta_{\theta\bar{g}} - \Delta_{\theta\delta\bar{\epsilon}} + 2\Delta_{w_i\bar{\nu}_i} + \Delta_{A\bar{\pi}}\right)\,, \tag{6.17}$$

where $\bar{g} = g/\epsilon$, $\delta\bar{\epsilon} = \delta\epsilon/\epsilon$ and $\bar{\nu}_i = \nu_i/\epsilon$ the dimensionless scalar and vector modes of the dispersion tensor, $\bar{\pi} = \pi/\epsilon$ the scalar mode of third cumulant and we use $\Omega_m/f^2 \to 1$ as before. With the time-dependence given in Eq. (6.8) the left-hand side is constant and becomes $\alpha + 1 = (n_s + 7)/(n_s + 3)$. We obtain a consistent ansatz of the time-dependence for ϵ when also the right-hand side is constant. Inspecting Eq. (6.16) we see that the dimensionless power spectrum apart from the time-independent factor x depends on time only via the variable s. After integration over $k \propto s$ in Eq. (6.17) the right-hand side is indeed constant in time. Then we have

$$\frac{n_s + 7}{n_s + 3} = \frac{1}{3}\sum_{L\geq 0} x^{L+1} I^{L-\mathrm{loop}}(n_s)\,, \tag{6.18}$$

where

$$I^{L-\mathrm{loop}}(n_s) \equiv \int_0^\infty \frac{\mathrm{d}s}{s}\Big(\hat{\Delta}_{\theta\bar{g}}(s) - \hat{\Delta}_{\theta\delta\bar{\epsilon}}(s) + 2\hat{\Delta}_{w_i\bar{\nu}_i}(s) + \hat{\Delta}_{A\bar{\pi}}(s)\Big)^{L-\mathrm{loop}}\,, \tag{6.19}$$

which is an algebraic equation for the variable x. At linear order we get

$$I^{\mathrm{lin}}(n_s) = \int_0^\infty \mathrm{d}s\, s^{n_s+2}\Big(F_{1,\theta}(s)(F_{1,\bar{g}}(s) - F_{1,\delta\bar{\epsilon}}(s)) + F_{1,\delta}(s)F_{1,\bar{\pi}}(s)\Big)\,, \tag{6.20}$$

where we used that vector modes do not contribute at linear order and $A \mapsto \delta$. When going to any loop order L, Eq. (6.18) becomes a polynomial equation for x with degree $L + 1$. From Eq. (6.13) one can write down

$$k_\sigma/k_{\mathrm{nl}} = \sqrt{3}x_*^{1/(n_s+3)}\,, \tag{6.21}$$

where x_* corresponds to the particular (self-consistent) solution(s) for the ratio k_σ/k_{nl} and hence gives an estimate of the overall magnitude of the background dispersion $\epsilon_0 = 1/k_\sigma^2$. In linear approximation, it is given by

$$x_*^{\mathrm{lin}} = \frac{3(n_s + 7)}{(n_s + 3)I^{\mathrm{lin}}(n_s)}\,. \tag{6.22}$$

Nonlinear corrections can significantly change the results, dealing with polynomials of higher degrees.

Finally, there is another simplification for the power- and bispectrum within a scaling universe. Scaling symmetry can be used to rescale power spectra computed for a given reference value of the background dispersion $\epsilon_0^{\mathrm{ref}}$ to any other value ϵ_0, but keeping the dimensionless ratios of any higher cumulants fixed, in particular $\bar{\omega}$, i.e. the dimensionless ratio of the fourth cumulant background value. Then we assess the dependence on ϵ_0 via

$$P_{\bar{a}\bar{b}}(k, \eta; \epsilon_0) = P_{ab}(k, \eta; \epsilon_0)/\epsilon^{d_a+d_b}(\eta) \tag{6.23}$$

and have introduced dimensionless perturbation variables $\bar{a} = a/\epsilon^{d_a}(\eta)$ and $\bar{b} = b/\epsilon^{d_b}(\eta)$, with appropriate powers d_a, d_b. For example, $d_\delta = d_\theta = d_A = d_{w_i} = 0$, $d_g = d_{\delta\epsilon} = d_{\nu_i} = d_{t_{ij}} = d_\pi = d_\chi = 1$, see Eq. (4.111). Then the dimensionless power spectrum $4\pi k^3 P_{\bar{a}\bar{b}}$ depends only on dimensionless ratios of k, k_σ and k_{nl}, which we take to be k/k_σ and k_σ/k_{nl}. For the L-loop

power spectrum factors of $P_0^{L+1} \propto A^{L+1}$ are involved, which implies Eq. (6.16) for the rescaled variables $\bar{a}$ and $\bar{b}$. Using Eq. (6.13) we then obtain the rescaling relation for the original power spectrum,

$$P_{ab}^{L-\text{loop}}(k,\eta;\epsilon_0) = \left(\frac{\epsilon_0^{\text{ref}}}{\epsilon_0}\right)^{\frac{(n_s+3)(L+1)-3}{2}-d_a-d_b} P_{ab}^{L-\text{loop}}\left(k\left(\frac{\epsilon_0}{\epsilon_0^{\text{ref}}}\right)^{1/2},\eta;\epsilon_0^{\text{ref}}\right). \tag{6.24}$$

Similarly, for the bispectrum we find

$$B_{abc}^{L-\text{loop}}(k_1,k_2,k_3,\eta;\epsilon_0) = \left(\frac{\epsilon_0^{\text{ref}}}{\epsilon_0}\right)^{\frac{(n_s+3)(L+2)-6}{2}-d_a-d_b-d_c} B_{abc}^{L-\text{loop}}(k_1',k_2',k_3',\eta;\epsilon_0^{\text{ref}}), \tag{6.25}$$

where $k_i' = k_i \times (\epsilon_0/\epsilon_0^{\text{ref}})^{1/2}$ for $i = 1,2,3$. Note also that the dependence on time η is uniquely given by the factor $k/k_\sigma(\eta)$ or equivalently by $s_k(\eta)$, see Eq. (6.11) and recall that $k_\sigma(\eta)/k_{\text{nl}}(\eta) = \text{const}$. This gives

$$P_{ab}(k,\eta;\epsilon_0) = \left(\frac{\epsilon(\eta')}{\epsilon(\eta)}\right)^{-3/2-d_a-d_b} P_{ab}(k',\eta';\epsilon_0) \tag{6.26}$$

for the power spectrum and

$$B_{abc}(k_1,k_2,k_3,\eta;\epsilon_0) = \left(\frac{\epsilon(\eta')}{\epsilon(\eta)}\right)^{-6/2-d_a-d_b-d_c} B_{abc}(k_1',k_2',k_3',\eta';\epsilon_0) \tag{6.27}$$

for the bispectrum, where now $k' = k \times (\epsilon(\eta)/\epsilon(\eta'))^{1/2} = ke^{2(\eta-\eta')/(n_s+3)}$ and analogously for k_i'.

We now present self-consistent solutions in linear approximation for various truncations in order to estimate the impact of higher cumulants in this regard. We first start by only including velocity dispersion.

6.1 Self-consistent solution in second cumulant approximation

When neglecting third and higher cumulants, we can evaluate the integral Eq. (6.20) by using the analytical expressions for the kernels $F_{1,\theta}$, $F_{1,\bar{g}}$, given in Eq. (4.78), while setting $F_{1,\bar{\pi}} = F_{1,\delta\bar{\epsilon}} = 0$. So we are only left with the growing modes in **cum2**.

We need the integral $I^{\text{lin}}(n_s)$ to converge such that self-consistent solutions can exist. For very small wavenumbers $k \propto s \to 0$ the kernels approach $F_{1,\theta} \to 1$ and $F_{1,\bar{g}} \to 2/(2+\alpha)$. We require $\alpha > 0$, i.e. a growth of velocity dispersion, which means the integral is infrared-finite for $n_s > -3$. In the opposite limit, $k \propto s \gg 1$ the kernels take the asymptotic form given in Eq. (4.80). An analysis shows using Table 4.1 that for $n_s > -53/11 \approx -4.8$ the integral is absolutely convergent [98]. So there is only a constraint coming from the red spectrum meaning that even for very blue spectral indices (large n_s) the integral converges and a solution exists. Therefore, high initial power at small scales (large k) will be compensated by the damping due to velocity dispersion making the integral converge. In total, the whole integral is convergent for $n_s > -3$. Furthermore, when approaching $n_s \to -3$ from above the sensitivity to small scales grows [98]. The lack of velocity dispersion will enhance the small-scale sensitivity approaching a similar situation to the one from SPT.

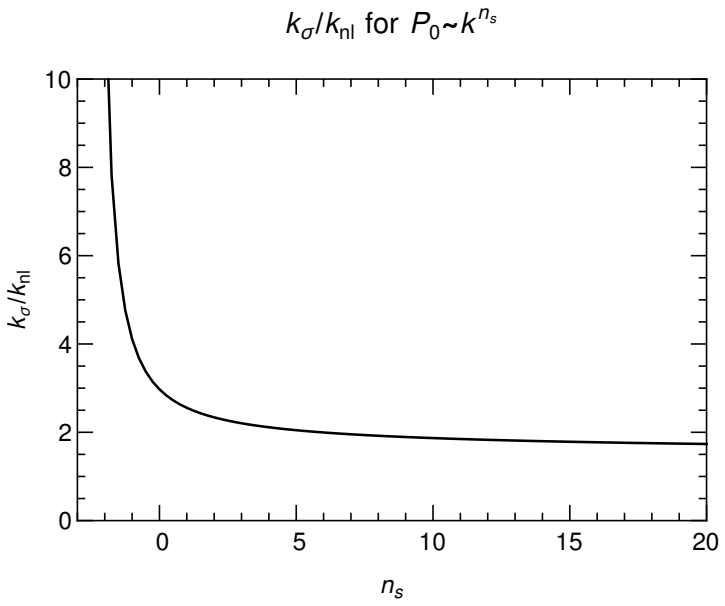

Figure 6.1: Ratio of the velocity dispersion scale $k_\sigma = 1/\sqrt{\epsilon}$ to the nonlinear scale $k_{\rm nl}$ versus n_s for a power-law initial spectrum $P \propto k^{n_s}$ when solving the linear equation of the background dispersion ϵ in the second cumulant approximation.

In Fig. 6.1 the ratio $k_\sigma/k_{\rm nl}$ versus n_s is shown as obtained from the self-consistent linear solutions $x_*^{\rm lin}$ within the second cumulant approximation, see Eq. (6.22). The ratio is always larger than one and becomes very large when $n_s \to -3$. This explains the discussion above, for large n_s the solution is not very sensitive to small scales and approaches a constant value, while for very low n_s the sensitivity grows and nonlinear corrections become more relevant.

6.2 Self-consistent solution in third and fourth cumulant approximation

Now we turn to the inclusion of third and fourth cumulant perturbations as well as the background value of the fourth cumulant $\omega(\eta)$ where the latter enters the perturbation equations of the third cumulant. This means the integral Eq. (6.20) is now implicitly dependent on ω and now all terms therein have to be considered. In addition, we have to solve for the corresponding evolution equation for ω which for $\Omega_m/f^2 \to 1$ can be rewritten as

$$\frac{\omega' + 2\omega}{\epsilon^2} = \frac{1}{3}\int_0^\infty \frac{\mathrm{d}k}{k}\left(4\Delta_{\theta\bar{\xi}} - \Delta_{\theta\bar{\kappa}} + 2\Delta_{\bar{g}\bar{\pi}} + 6\Delta_{\delta\bar{\epsilon}\bar{\pi}} - \frac{8}{5}\Delta_{\bar{g}\bar{\chi}}\right), \tag{6.28}$$

where $\bar{\pi}, \bar{\chi}$ and $\bar{\xi}, \bar{\kappa}$ are the dimensionless perturbation modes of the third and fourth cumulant, respectively. Let us assume the scaling $\omega(\eta) \propto \epsilon(\eta)^2$ and the dimensionless constant quantity $\bar{\omega} = \omega/\epsilon^2$ as used before. Inserting this on the left-hand side we note that it becomes constant and is given by $2(\alpha+1)\bar{\omega} = 2(n_s+7)\bar{\omega}/(n_s+3)$. For the right-hand side the same argument holds as in the previous section for the second cumulant approximation. It is also constant in time despite the implicit dependence on $\bar{\omega}$ since it is constant. So the scaling of $\omega(\eta) \propto \epsilon(\eta)^2$ is consistent with its equation of motion.

Now we have to solve for both $k_\sigma/k_{\rm nl}$ (Eq. 6.18) and $\bar{\omega}$ (Eq. 6.28) at the same time giving rise to the coupled system of equations,

$$\begin{aligned} \frac{n_s+7}{n_s+3} &= \frac{1}{3}\sum_{L\geq 0} x^{L+1} I^{L-\text{loop}}(n_s,\bar{\omega})\,, \\ 2\frac{n_s+7}{n_s+3}\bar{\omega} &= \frac{1}{3}\sum_{L\geq 0} x^{L+1} J^{L-\text{loop}}(n_s,\bar{\omega})\,, \end{aligned} \tag{6.29}$$

with unknowns x, $\bar{\omega}$ and polynomial dependence on x for a given loop number L and an implicit dependence on $\bar{\omega}$ which has to be determined numerically in general. In addition, we defined

$$J^{L-\text{loop}}(n_s,\bar{\omega}) \equiv \int_0^\infty \frac{\mathrm{d}s}{s}\Big(4\hat{\Delta}_{\theta\bar{\xi}}(s) - \hat{\Delta}_{\theta\bar{\kappa}}(s) + 2\hat{\Delta}_{\bar{g}\bar{\pi}}(s) + 6\hat{\Delta}_{\delta\bar{\epsilon}\bar{\pi}}(s) - \frac{8}{5}\hat{\Delta}_{\bar{g}\bar{\chi}}(s)\Big)^{L-\text{loop}}\,. \tag{6.30}$$

Also the $I^{L-\text{loop}}(n_s,\bar{\omega})$ is the same expression as in Eq. (6.28) but evaluated with kernels and vertices including third and fourth cumulant perturbations and an additional implicit dependence on $\bar{\omega}$.

In linear approximation we can eliminate the dependence on x by taking the ratio of both equations in Eq. (6.29) which leads to an implicit equation for $\bar{\omega}$,

$$\bar{\omega} = \frac{1}{2}\frac{J^{\rm lin}(n_s,\bar{\omega})}{I^{\rm lin}(n_s,\bar{\omega})}\,. \tag{6.31}$$

Its linear solution $\bar{\omega}_*$ can be obtained numerically using Eq. (6.20) and an analogous expression for $J^{\rm lin} = J^{0-\text{loop}}$. The power spectra entering both integrals are then expressed by their linear kernels which can be obtained by solving the linear equations of motion Eq. (4.112) and using Eq. (4.114). The dispersion scale can then be obtained by using the linear solution for x given by Eq. (6.22) with $I^{\rm lin} = I^{\rm lin}(n_s,\bar{\omega}_*^{\rm lin})$ evaluated at $\bar{\omega} = \bar{\omega}_*^{\rm lin}$.

When truncating the equations at third cumulant oder, as denoted by **cum3+** or equivalently $c_{\rm max} = 3$ one finds that Eq. (6.31) indeed has a solution at linear level. The obtained values for $k_\sigma/k_{\rm nl}$ as well as for $\bar{\omega}$ are given in Table 6.1 for spectral indices $n_s = -1, 0, 1, 2$. We note that the dimensionless fourth cumulant expectation value is of order unity which is in accordance with the scaling ansatz $\omega(\eta) \propto \epsilon(\eta)^2$, and that higher cumulants are relevant quantitatively at the same order as the background dispersion. Furthermore, we see a shift in the ratio $k_\sigma/k_{\rm nl}$ when going to third cumulant order which is sizeable but still within the same order of magnitude. In this regard, higher cumulants have a quantitative impact but do not invalidate the qualitative dynamics within the second cumulant approximation.

Within the fourth cumulant truncation we find that no self-consistent solution exist which may be subject to the shortcomings of the linear approximation. In the next section we estimate the impact of higher cumulants.

6.3 Self-consistent solutions for the full cumulant hierarchy

Now, we further extend the self-consistent solutions to incorporate cumulants beyond fourth order following the treatment introduced in Ch. 5. The generalized expectation values $\mathcal{E}_{2n}$ satisfy Eq. (5.17). For $2n = 2$ and $2n = 4$ they are equivalent to ϵ and $3\omega/5$ and yield the results

Table 6.1: Self-consistent values of the dispersion scale $k_\sigma = \epsilon^{-1/2} = \mathcal{E}_2^{-1/2}$ relative to the nonlinear scale $k_{\rm nl}$ as well as the dimensionless ratios of the background values $\bar{\mathcal{E}}_{2n} = \mathcal{E}_{2n}/\epsilon^n$ of higher cumulants. We show results for various spectral indices $n_s = -1, 0, 1, 2$ and in addition for different cumulant truncations $c_{\rm max} = 2, 3, 6, 7$ for which solutions in linear approximation and within a scaling universe exist. The cases $c_{\rm max} = 2, 3$ are equivalent to **cum2** and **cum3+**, respectively, with $\bar{\mathcal{E}}_4 = 3\bar{\omega}/5$.

	$n_s = -1$				$n_s = 0$				$n_s = 1$				$n_s = 2$			
$c_{\rm max}$	$k_\sigma/k_{\rm nl}$	$\bar{\mathcal{E}}_4$	$\bar{\mathcal{E}}_6$	$\bar{\mathcal{E}}_8$	$k_\sigma/k_{\rm nl}$	$\bar{\mathcal{E}}_4$	$\bar{\mathcal{E}}_6$	$\bar{\mathcal{E}}_8$	$k_\sigma/k_{\rm nl}$	$\bar{\mathcal{E}}_4$	$\bar{\mathcal{E}}_6$	$\bar{\mathcal{E}}_8$	$k_\sigma/k_{\rm nl}$	$\bar{\mathcal{E}}_4$	$\bar{\mathcal{E}}_6$	$\bar{\mathcal{E}}_8$
2	4.1	-	-	-	3.0	-	-	-	2.6	-	-	-	2.3	-	-	-
3	3.4	0.45	-	-	2.5	0.40	-	-	2.2	0.37	-	-	2.0	0.35	-	-
6	3.8	0.37	0.86	-	2.7	0.34	0.92	-	2.3	0.31	0.93	-	2.1	0.29	0.92	
7	3.8	0.36	0.78	3.5	2.7	0.36	0.94	4.5	2.3	0.35	1.03	5.1	2.1	0.34	1.08	5.3

discussed in Secs. 6.1 and 6.2. When assuming constant dimensionless ratios $\bar{\mathcal{E}}_{2n}$ within a scaling universe we obtain a generalized set of implicit equations in linear approximation ($L = 0$)

$$n\,\frac{n_s+7}{n_s+3}\bar{\mathcal{E}}_{2n} = x\, I^{\rm lin}_{\bar{\mathcal{E}}_{2n}}(n_s, \bar{\mathcal{E}}_4, \bar{\mathcal{E}}_6, \dots)\,, \tag{6.32}$$

with

$$I_{\bar{\mathcal{E}}_{2n}} = \int_0^\infty \mathrm{d}s\, s^{n_s+2} \sum_{\ell=0}^{n}(\ell+1) \sum_{m_1,m_2=0}^{n-\ell} \delta^K_{m_1+m_2,n-\ell}\, \frac{(2n)!(2(m_2-m_1-\ell)-3)}{(2m_1)!(2m_2)!} T_{\ell+1,2m_1}(s) T_{\ell,2m_2}(s)\,, \tag{6.33}$$

where $\delta^K_{i,j}$ is the Kronecker symbol, and $T_{\ell,2m}(s)$ are the dimensionless linear kernels for perturbation modes of cumulant order $\ell + 2m$ defined in Eq. (5.21). They are obtained numerically using Eq. (5.22) and have scale- and time-dependence only via the term $s = \sqrt{3\epsilon(\eta)}k^2$. In addition, they parametrically depend on $\alpha = \partial_\eta \ln\epsilon = 4/(3+n_s)$ and on $\bar{\mathcal{E}}_4, \bar{\mathcal{E}}_6, \dots$ which are constant for a scaling universe. Thus, Eq. (6.32) is a highly implicit and coupled set of equations for the self-consistent values of $\bar{\mathcal{E}}_{2n}$ and $k_\sigma/k_{\rm nl}$ where the latter is parametrized by the variable x defined in Eq. (6.13). Taking the ratio of Eq. (6.32) for $2n \geq 4$ to the one for $2n = 2$ and using by definition $\bar{\mathcal{E}}_2 = 1$ we obtain a coupled set of equations for the expectation values of order $2n \geq 4$,

$$\bar{\mathcal{E}}_{2n} = \frac{1}{n}\frac{I^{\rm lin}_{\bar{\mathcal{E}}_{2n}}(n_s, \bar{\mathcal{E}}_4, \bar{\mathcal{E}}_6, \dots)}{I^{\rm lin}_{\bar{\mathcal{E}}_2}(n_s, \bar{\mathcal{E}}_4, \bar{\mathcal{E}}_6, \dots)}\,, \tag{6.34}$$

which is independent of x. They can be viewed as a generalization of Eq. (6.31) to beyond fourth order. Note that also the integral $I^{\rm lin}_{\bar{\mathcal{E}}_2}$ implicitly depends on the background values $\bar{\mathcal{E}}_6$, $\bar{\mathcal{E}}_8$ and so on since the explicit emergence of the third cumulant perturbation π in the source term for ϵ in $I^{\rm lin}$ depends on $\bar{\mathcal{E}}_4 \propto \bar{\omega}$ which in turn depends on higher order expectation values via $J^{\rm lin}$ and so on. Once a solution of Eq. (6.32) is found, we can obtain the solution for x by setting $n = 1$ in Eq. (6.32) which determines the ratio

$$\frac{k_\sigma}{k_{\rm nl}} = \sqrt{3}\left(\frac{n_s+7}{(n_s+3)I^{\rm lin}_{\bar{\mathcal{E}}_2}}\right)^{1/(n_s+3)}\,. \tag{6.35}$$

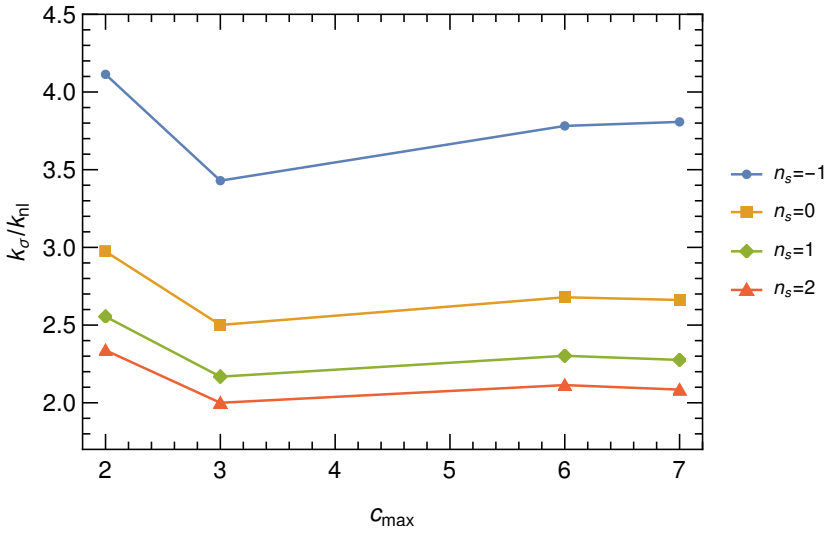

Figure 6.2: Ratio of the velocity dispersion scale $k_\sigma = 1/\sqrt{\epsilon}$ to the nonlinear scale $k_{\rm nl}$ versus the truncation order $c_{\rm max}$ and for various n_s for a power-law initial spectrum $P \propto k^{n_s}$ when solving the linear equations of the background values of the cumulants $\bar{\mathcal{E}}_{2n}$ when including cumulant perturbations up to order $c_{\rm max}$. The values are extracted from Table 6.1. Reprinted from [98].

When truncating at a given $c_{\rm max}$ all dimensionless linear kernels $T_{\ell,2m}(s)$ with $\ell + 2m > c_{\rm max}$ are neglected. So the integral $I^{\rm lin}_{\bar{\mathcal{E}}_2}$ contains background values $\bar{\mathcal{E}}_4, \ldots, \bar{\mathcal{E}}_{c_{\rm max}+1}$ for odd $c_{\rm max}$, and $\bar{\mathcal{E}}_4, \ldots, \bar{\mathcal{E}}_{c_{\rm max}}$ for even $c_{\rm max}$. For $c_{\rm max} = 2$ the results are identical to the ones derived in Sec. 6.1 where Eq. (6.32) becomes Eq. (6.18), and for $c_{\rm max} = 3, 4$, Eq. (6.34) reduces to a single equation Eq. (6.31), derived in Sec. 6.2. For $c_{\rm max} = 5, 6$, Eq. (6.34) yields a coupled set of equations for $\bar{\mathcal{E}}_4, \bar{\mathcal{E}}_6$. For $c_{\rm max} = 7, 8$, one obtains three coupled equations for $\bar{\mathcal{E}}_4, \bar{\mathcal{E}}_6, \bar{\mathcal{E}}_8$. For truncations up to eighth order, there exist a joint self-consistent solution only for $c_{\rm max} = 2, 3, 6, 7$. The values of the solutions are given in Table 6.1 for various n_s. The expectation values have comparable sizes when allowing for various truncations, meaning $\bar{\mathcal{E}}_4$ is similar for $c_{\rm max} = 3, 6, 7$ and $\bar{\mathcal{E}}_6$ is similar for $c_{\rm max} = 6, 7$, which indicates that the overall magnitude of the background values are rather insensitive to the truncation order.

We show the dependence of the dispersion relative to nonlinear scale on the truncation order and for different n_s in Fig. 6.2. We find that the biggest impact occurs when going from $c_{\rm max} = 2$ to $c_{\rm max} = 3$ for each n_s. Even higher cumulants have only a minor impact. This suggests that the scales where the source term Eq. (6.33) mainly contributes are already converged, see Fig. 5.1. In addition, for higher values of n_s the sensitivity to higher cumulants decreases. Despite having large power on small scales initially, it will be erased by the suppression of the efficient buildup of velocity dispersion and higher cumulants which further suppresses the linear kernels making the source term less sensitive to high wavenumbers.

7 Nonlinear kernels with velocity dispersion and higher cumulants

So far, we discussed solutions within VPT in linear approximation. The results laid out by now are very promising to also investigate nonlinear solutions obtained by expanding around the new linear theory. That is we study nonlinear kernels $F_{n,a}(\boldsymbol{k}_1, \ldots, \boldsymbol{k}_n, \eta)$ within VPT that have a crucial decoupling property and satisfy the differential equations Eq. (4.59). For fixed total momentum $\boldsymbol{k} = |\sum_i \boldsymbol{k}_i|$ they become strongly suppressed if any of their wavenumbers k_i cross the dispersion scale k_σ into the nonlinear regime. This is the main feature why VPT accounts for the screening of UV modes. We present analytical results for the nonlinear kernels in Sec. 7.1 and compare them to the full numerical results in Sec. 7.2. We finish this chapter by constraining the VPT kernels from underlying symmetries, such as mass and momentum conservation derived in Sec. 7.3.

In the following, we adopt the **cum3+** approximation scheme, meaning apart from δ, θ, w_i we take the full dispersion tensor (second cumulant) involving its full set of perturbations $g, \delta\epsilon, \nu_i, t_{ij}$ as well as the scalar modes of the third cumulant π, χ into account. Thus, the scalar subset becomes

$$\psi^S = (\delta, \theta, g, \delta\epsilon, A, \pi, \chi), \tag{7.1}$$

including the log-density field A as before, and with linear evolution given in Eq. (4.109), without the last two rows and columns (setting $\Omega_m/f^2 \to 1$). That is, we neglect the scalar modes of the fourth cumulant but keeping track of its background value $\omega(\eta)$ along the background dispersion $\epsilon(\eta)$. At nonlinear level, vector (in particular vorticity) and tensor modes are generated and will also be discussed in Ch. 8.

As we see further below, the generation of the cumulant perturbations due to the background dispersion can be calculated analytically by considering $\epsilon \to 0$, as done in Secs. 4.1 and 4.2 for the *linear* kernels and for a particular time-dependence of ϵ dictated by a scaling universe. We are now interested in finding analytical solutions with a general $\epsilon(\eta)$ and also for the nonlinear kernels $F_{n,a}$ with $n \geq 2$ up to *first order* in ϵ while keeping the cumulant truncation order fixed.

7.1 Analytical results in the limit $\epsilon \to 0$

In Sec. 5.3 we presented how each cumulant scales with ϵ in the limit $\epsilon \to 0$ giving rise to constant dimensionless background values, e.g. $\bar{\omega} = \omega/\epsilon^2$. Thus, we henceforth use the counting that $F_{n,a}$ for $a = \delta, \theta, A$ start at order ϵ^0, the kernels for $a = w_i, g, \delta\epsilon, \nu_i, t_{ij}$ at order ϵ^1, and for $a = \pi, \chi$ at order ϵ^2, in accordance with Eq. (5.26). When going to zeroth order ϵ^0 all perturbations vanish except the contributions coming from SPT, i.e. $F_{n,\delta}|_{\epsilon^0} = F_n$ and $F_{n,\theta}|_{\epsilon^0} = G_n$ coincide with EdS-SPT kernels for all n. In total, one expects a Taylor expansion of the form of Eq. (5.25) for

the corresponding linear kernels. Expanding around these linear solutions ($n = 1$) allows one to derive nonlinear kernels analytically for small ϵ.

First order kernels

Let us start with the expansion of the linear kernels in ϵ. This means we set the right-hand side of Eq. (4.59) to zero. As mentioned above, we already discussed linear solutions but used the power-law ansatz for ϵ. Now we want to refrain from using this ansatz and keep the specific form of ϵ undetermined. The lowest order terms in ϵ are the EdS-SPT results $F_{1,\delta}|_{\epsilon^0} = F_{1,\theta}|_{\epsilon^0} = 1$. Now consider the growing dispersion mode g whose evolution equation can be extracted from the second line of Eq. (4.109) giving

$$(\partial_\eta + 2)F_{1,g}(k,\eta) = 2\epsilon(\eta)F_{1,\theta}(k,\eta) - F_{1,\pi}(k,\eta) + \frac{3}{5}F_{1,\chi}(k,\eta)\,. \tag{7.2}$$

At first order the modes π, χ of the third cumulant do not contribute starting only at order ϵ^2 and inserting the zeroth order expression for $F_{1,\theta}$ being unity gives

$$F_{1,g}(k,\eta) = 2E_2(\eta) + \mathcal{O}(\epsilon^2)\,, \tag{7.3}$$

where we introduced the weighted time integral of the background dispersion $\epsilon(\eta)$,

$$E_m(\eta) \equiv \int^\eta \mathrm{d}\eta'\, e^{m(\eta'-\eta)}\epsilon(\eta')\,, \tag{7.4}$$

which for the power-law ansatz $\epsilon = \epsilon_0\, e^{\alpha\eta}$ gives $E_m(\eta) = \epsilon(\eta)/(m+\alpha)$. Thus, the leading order result for g agrees with Eq. (4.62) derived above, with growing mode $e^{n\eta}$ being factored out as commonly used for the kernels.

The third line of Eq. (4.109) yields the equation for $\delta\epsilon$. One finds that, as stated above, its linear kernel starts only at second order, i.e. $F_{1,\delta\epsilon} = \mathcal{O}(\epsilon^2)$ due to the mixing with π. If it is absent, $\delta\epsilon$ would never be generated (at any order in ϵ), as already discussed within the **cum2** approximation. However, when going to second order in perturbations the kernel starts to contribute already at first order in ϵ, i.e. $F_{n\geq 2,\delta\epsilon} = \mathcal{O}(\epsilon^1)$ which is also true for third and higher order kernels and is also expected from the general scaling of the cumulants.

Let us now consider the density and velocity divergence kernels with evolution equation

$$(\partial_\eta + \mathbf{1} + \Omega_{\mathrm{SPT}}) \begin{pmatrix} F_{1,\delta}(k,\eta) \\ F_{1,\theta}(k,\eta) \end{pmatrix} = -k^2 \begin{pmatrix} 0 \\ F_{1,g}(k,\eta) + F_{1,\delta\epsilon}(k,\eta) + \epsilon(\eta)F_{1,A}(k,\eta) \end{pmatrix}\,, \tag{7.5}$$

where

$$\Omega_{\mathrm{SPT}} = \begin{pmatrix} 0 & -1 \\ -\frac{3}{2} & \frac{1}{2} \end{pmatrix}\,, \tag{7.6}$$

agrees with the commonly known EdS-SPT linear matrix and $\mathbf{1}$ is the unit matrix. The corresponding integral representation of the equation is given by

$$\begin{pmatrix} F_{1,\delta}(k,\eta) \\ F_{1,\theta}(k,\eta) \end{pmatrix} = \begin{pmatrix} 1 \\ 1 \end{pmatrix} + \int^\eta \mathrm{d}\eta'\, e^{\eta'-\eta} g_{\mathrm{SPT}}(\eta-\eta') \begin{pmatrix} 0 \\ \mathcal{S}(k,\eta') \end{pmatrix}\,, \tag{7.7}$$

using SPT initial conditions which specify the lower limit of integration, the SPT linear propagator $g_{\mathrm{SPT}}(\eta-\eta')$ (see Eq. (3.59) and [167]) and the impact of the velocity dispersion

captured in $\mathcal{S}(k,\eta') \equiv -k^2(F_{1,g} + F_{1,\delta\epsilon} + \epsilon F_{1,A})$. Inserting the lowest order results for $\mathcal{S}$ we obtain

$$\begin{aligned} F_{1,\delta}(k,\eta) &= 1 - k^2 I_\delta(\eta) + \mathcal{O}(\epsilon^2)\,, \\ F_{1,\theta}(k,\eta) &= 1 - k^2 I_\theta(\eta) + \mathcal{O}(\epsilon^2)\,, \end{aligned} \tag{7.8}$$

where

$$\begin{aligned} I_\delta(\eta) &\equiv \frac{2}{5}\int^\eta \mathrm{d}\eta' \left(1 - e^{5(\eta'-\eta)/2}\right)\left(\epsilon(\eta') + 2\int^{\eta'} \mathrm{d}\eta''\, e^{2(\eta''-\eta')}\epsilon(\eta'')\right)\,, \\ I_\theta(\eta) &\equiv \frac{2}{5}\int^\eta \mathrm{d}\eta' \left(1 + \frac{3}{2}e^{5(\eta'-\eta)/2}\right)\left(\epsilon(\eta') + 2\int^{\eta'} \mathrm{d}\eta''\, e^{2(\eta''-\eta')}\epsilon(\eta'')\right)\,. \end{aligned} \tag{7.9}$$

We observe that the correction terms $I_{\delta/\theta}$ are strictly positive since $\epsilon \geq 0$ and $\eta \geq \eta'$ which means due to the minus sign the corrections are ultimately negative leading to *suppression* terms compared to SPT. This feature was already found in Ch. 4 and we can now confirm that this occurrence is indeed independent of the precise time-dependence of $\epsilon(\eta)$. Using

$$\int^\eta \mathrm{d}\eta'\, e^{a(\eta'-\eta)} \int^{\eta'} \mathrm{d}\eta''\, e^{b(\eta''-\eta')}\, f(\eta'') = -\frac{1}{a-b}\int^\eta \mathrm{d}\eta' \left(e^{a(\eta'-\eta)} - e^{b(\eta'-\eta)}\right) f(\eta')\,, \quad (a \neq b) \tag{7.10}$$

and the definition of Eq. (7.4) one can simplify the integrals by

$$\begin{aligned} I_\delta(\eta) &= \frac{4}{5}E_0(\eta) - 2E_2(\eta) + \frac{6}{5}E_{5/2}(\eta)\,, \\ I_\theta(\eta) &= \frac{4}{5}E_0(\eta) + 2E_2(\eta) - \frac{9}{5}E_{5/2}(\eta)\,, \end{aligned} \tag{7.11}$$

indicating that the correction term relative to SPT is proportional to ϵ^1. An analogous procedure can be done for the linear kernels of the third cumulant perturbations which contribute at order ϵ^2 given by

$$\begin{aligned} F_{1,\pi}(k,\eta) &= F_{1,\chi} + 3k^2\int^\eta \mathrm{d}\eta'\, e^{5(\eta'-\eta)/2}\epsilon(\eta')F_{1,g}(k,\eta')\,, \\ F_{1,\chi}(k,\eta) &= k^2\int^\eta \mathrm{d}\eta'\, e^{5(\eta'-\eta)/2}\left(5\epsilon(\eta')F_{1,\delta\epsilon}(k,\eta') + \omega(\eta')F_{1,A}(k,\eta')\right)\,, \end{aligned} \tag{7.12}$$

and can be readily seen when inserting the lowest order contributions $F_{1,A}|_{\epsilon^0} = 1$, $F_{1,\delta\epsilon}|_{\epsilon^1} = 0$ and $F_{1,g}|_{\epsilon^1}$ from Eq. (7.3) on the right-hand side and recalling the power counting $\omega \propto \epsilon^2$.

Second order kernels

Going to second order in perturbation theory we have to include the vertices $\gamma_{abc}(\boldsymbol{p},\boldsymbol{q})$ on the right-hand side of Eq. (4.59). For the second order kernel for the g mode we get

$$\begin{aligned} (\partial_\eta + 3)F_{2,g}(\boldsymbol{p},\boldsymbol{q},\eta) &= 2\epsilon(\eta)F_{2,\theta}(\boldsymbol{p},\boldsymbol{q},\eta) - F_{2,\pi}(\boldsymbol{p},\boldsymbol{q},\eta) + \frac{3}{5}F_{2,\chi}(\boldsymbol{p},\boldsymbol{q},\eta) \\ &\quad + \gamma_{gbc}(\boldsymbol{p},\boldsymbol{q})F_{1,b}(p,\eta)F_{1,c}(q,\eta)\,, \end{aligned} \tag{7.13}$$

where in the nonlinear term on the second line we implicitly assume summation over indices b, c. In principle, the vertices $\gamma_{g\theta g}$, $\gamma_{g\theta\epsilon}$, $\gamma_{gA\pi}$, $\gamma_{gA\chi}$, γ_{gw_ig}, $\gamma_{gw_i\epsilon}$, $\gamma_{g\theta\nu_i}$, $\gamma_{g\theta t_{ij}}$, $\gamma_{gw_i\nu_j}$, $\gamma_{gw_it_{jk}}$ can

contribute within the nonlinear term as well as analogous expressions with their last two indices flipped. Each vertex is a function of wavenumbers only and their explicit expressions are given in Appendix B for the mode coupling of second cumulant and in Appendix D with the inclusion of third cumulant modes. Note that whenever we have ϵ in the subscript of the vertices, this is a short-hand notation for the $\delta\epsilon$ mode. Since only scalar modes can contribute to linear kernels and to first order in ϵ modes of the third cumulant (being π and χ) as well as $\delta\epsilon$ do also not contribute we are only left with

$$\gamma_{g\theta g}(\boldsymbol{p},\boldsymbol{q}) = \frac{1}{2}\frac{\boldsymbol{p}\cdot\boldsymbol{q}}{q^2}\left(\frac{(\boldsymbol{p}+\boldsymbol{q})^2}{p^2}+\frac{1}{2}-\frac{3}{2}\frac{((\boldsymbol{p}+\boldsymbol{q})\cdot\boldsymbol{p})^2}{(\boldsymbol{p}+\boldsymbol{q})^2p^2}\right), \tag{7.14}$$

and $\gamma_{gg\theta}(\boldsymbol{p},\boldsymbol{q}) = \gamma_{g\theta g}(\boldsymbol{q},\boldsymbol{p})$ at $\mathcal{O}(\epsilon)$. In the first term on the right-hand side we simply insert the SPT approximation $F_{2,\theta}(\boldsymbol{p},\boldsymbol{q},\eta)|_{\epsilon^0} = G_2(\boldsymbol{p},\boldsymbol{q})$. Then the solution is given by

$$F_{2,g}(\boldsymbol{p},\boldsymbol{q},\eta) = 2G_2(\boldsymbol{p},\boldsymbol{q})E_3(\eta) + 2\left(\gamma_{g\theta g}(\boldsymbol{p},\boldsymbol{q})+\gamma_{g\theta g}(\boldsymbol{q},\boldsymbol{p})\right)\left(E_2(\eta)-E_3(\eta)\right)+\mathcal{O}(\epsilon^2)\,. \tag{7.15}$$

When going to higher order in ϵ the remaining scalar modes (which we left out above) will contribute within the second order kernels as well as in the nonlinear term. At second order we also have $F_{2,\delta\epsilon} = \mathcal{O}(\epsilon)$ as discussed above whose solution can be found analogously,

$$F_{2,\delta\epsilon}(\boldsymbol{p},\boldsymbol{q},\eta) = 2\left(\gamma_{\epsilon\theta g}(\boldsymbol{p},\boldsymbol{q})+\gamma_{\epsilon\theta g}(\boldsymbol{q},\boldsymbol{p})\right)\left(E_2(\eta)-E_3(\eta)\right)+\mathcal{O}(\epsilon^2)\,, \tag{7.16}$$

where

$$\gamma_{\epsilon\theta g}(\boldsymbol{p},\boldsymbol{q}) = \frac{1}{2}\frac{\boldsymbol{p}\cdot\boldsymbol{q}}{2p^2q^2(\boldsymbol{p}+\boldsymbol{q})^2}\left((\boldsymbol{p}\cdot\boldsymbol{q})^2-p^2q^2\right). \tag{7.17}$$

Hence, to first order in ϵ the kernel $F_{n,\delta\epsilon}$ starts to contribute at second order in perturbation theory.

Next, the second order kernels for δ and θ satisfy

$$(\partial_\eta + 2\cdot\mathbf{1}+\Omega_{\rm SPT})\begin{pmatrix}F_{2,\delta}(\boldsymbol{p},\boldsymbol{q},\eta)\\F_{2,\theta}(\boldsymbol{p},\boldsymbol{q},\eta)\end{pmatrix} = \begin{pmatrix}\gamma_{\delta bc}(\boldsymbol{p},\boldsymbol{q})F_{1,b}(p,\eta)F_{1,c}(q,\eta)\\ \gamma_{\theta bc}(\boldsymbol{p},\boldsymbol{q})F_{1,b}(p,\eta)F_{1,c}(q,\eta)+\mathcal{S}_2(\boldsymbol{p},\boldsymbol{q},\eta)\end{pmatrix}, \tag{7.18}$$

where $\mathcal{S}_2(\boldsymbol{p},\boldsymbol{q},\eta) \equiv -(\boldsymbol{p}+\boldsymbol{q})^2(F_{2,g}+F_{2,\delta\epsilon}+\epsilon F_{2,A})$ and possible nonlinear vertices are $\gamma_{\delta\theta\delta}, \gamma_{\delta w_i\delta}$ and $\gamma_{\theta\theta\theta}$, $\gamma_{\theta Ag}$, $\gamma_{\theta A\epsilon}$, $\gamma_{\theta w_i\theta}$, $\gamma_{\theta w_iw_i}$, $\gamma_{\theta A\nu_i}$, $\gamma_{\theta At_{ij}}$ along with the flipped contributions. The actual contributions from the linear kernels goes along with the previous discussion, where in addition to the standard SPT vertices $\gamma_{\delta\theta\delta} \equiv \alpha_{pq}/2$ and $\gamma_{\theta\theta\theta} \equiv \beta_{pq}$, as defined in Eq. (3.41), we get a contribution from

$$\gamma_{\theta Ag}(\boldsymbol{p},\boldsymbol{q}) = -\frac{((\boldsymbol{p}+\boldsymbol{q})\cdot\boldsymbol{q})\,(\boldsymbol{p}\cdot\boldsymbol{q})}{2q^2}\,. \tag{7.19}$$

The integral representation can be written as

$$\begin{pmatrix}F_{2,\delta}(\boldsymbol{p},\boldsymbol{q},\eta)\\F_{2,\theta}(\boldsymbol{p},\boldsymbol{q},\eta)\end{pmatrix} = \int^\eta \mathrm{d}\eta'\, e^{2(\eta'-\eta)}g_{\rm SPT}(\eta-\eta')\begin{pmatrix}\gamma_{\delta bc}(\boldsymbol{p},\boldsymbol{q})F_{1,b}(p,\eta)F_{1,c}(q,\eta)\\ \gamma_{\theta bc}(\boldsymbol{p},\boldsymbol{q})F_{1,b}(p,\eta)F_{1,c}(q,\eta)+\mathcal{S}_2\end{pmatrix}\Bigg|_{\eta'}, \tag{7.20}$$

and expanding the right-hand side up to linear order in ϵ yields

$$\begin{aligned}F_{2,\delta}(\boldsymbol{p},\boldsymbol{q},\eta) &= F_2(\boldsymbol{p},\boldsymbol{q}) - (\boldsymbol{p}+\boldsymbol{q})^2\sum_{j=1}^{7}\Gamma_j(\boldsymbol{p},\boldsymbol{q})J_j^\delta(\eta)+\mathcal{O}(\epsilon^2)\,,\\ F_{2,\theta}(\boldsymbol{p},\boldsymbol{q},\eta) &= G_2(\boldsymbol{p},\boldsymbol{q}) - (\boldsymbol{p}+\boldsymbol{q})^2\sum_{j=1}^{7}\Gamma_j(\boldsymbol{p},\boldsymbol{q})J_j^\theta(\eta)+\mathcal{O}(\epsilon^2)\,,\end{aligned} \tag{7.21}$$

where the time-dependence at linear order in ϵ is completely contained in the $J_j^{\delta/\theta}(\eta)$ and is given in Appendix E. The dependence on the wavenumbers is captured in the functions $\Gamma_j(\boldsymbol{p},\boldsymbol{q})$ which are identical for both δ and θ and read

$$\begin{aligned}
\Gamma_1(\boldsymbol{p},\boldsymbol{q}) &\equiv G_2(\boldsymbol{p},\boldsymbol{q})\,,\\
\Gamma_2(\boldsymbol{p},\boldsymbol{q}) &\equiv \gamma_{g\theta g}(\boldsymbol{p},\boldsymbol{q})+\gamma_{g\theta g}(\boldsymbol{q},\boldsymbol{p})+\gamma_{\epsilon\theta g}(\boldsymbol{p},\boldsymbol{q})+\gamma_{\epsilon\theta g}(\boldsymbol{q},\boldsymbol{p})\,,\\
\Gamma_3(\boldsymbol{p},\boldsymbol{q}) &\equiv F_{2,A}(\boldsymbol{p},\boldsymbol{q},\eta)|_{\epsilon^0}=\left[G_2(\boldsymbol{p},\boldsymbol{q})+\gamma_{A\theta A}(\boldsymbol{p},\boldsymbol{q})+\gamma_{A\theta A}(\boldsymbol{q},\boldsymbol{p})\right]/2\,,\\
\Gamma_4(\boldsymbol{p},\boldsymbol{q}) &\equiv (p^2+q^2)\gamma_{\theta\theta\theta}(\boldsymbol{p},\boldsymbol{q})/(\boldsymbol{p}+\boldsymbol{q})^2\,,\\
\Gamma_5(\boldsymbol{p},\boldsymbol{q}) &\equiv -(\gamma_{\theta Ag}(\boldsymbol{p},\boldsymbol{q})+\gamma_{\theta Ag}(\boldsymbol{q},\boldsymbol{p}))/(\boldsymbol{p}+\boldsymbol{q})^2\,,\\
\Gamma_6(\boldsymbol{p},\boldsymbol{q}) &\equiv (p^2\gamma_{\delta\theta\delta}(\boldsymbol{p},\boldsymbol{q})+q^2\gamma_{\delta\theta\delta}(\boldsymbol{q},\boldsymbol{p}))/(\boldsymbol{p}+\boldsymbol{q})^2=1/2\,,\\
\Gamma_7(\boldsymbol{p},\boldsymbol{q}) &\equiv (q^2\gamma_{\delta\theta\delta}(\boldsymbol{p},\boldsymbol{q})+p^2\gamma_{\delta\theta\delta}(\boldsymbol{q},\boldsymbol{p}))/(\boldsymbol{p}+\boldsymbol{q})^2\,,
\end{aligned} \tag{7.22}$$

with $\gamma_{A\theta A}(\boldsymbol{p},\boldsymbol{q})=\boldsymbol{p}\cdot\boldsymbol{q}/(2q^2)$. They approach a constant when $\boldsymbol{p}+\boldsymbol{q}\to 0$ which ensures mass and momentum conservation, see Sec. 7.3. In fact, by using the explicit expressions for the vertices, each Γ_j can be written in terms of the four basis functions as introduced in [168]. They actually correspond to the shape functions in the context of the effective field theory (EFT) when dealing with the bispectrum [169, 170]. The constant coefficients can then be viewed as a determination from first principles of the counter terms or rather Wilson coefficients by matching the EFT to the exact UV theory. In this case we go to second order in perturbation theory and to first order in the derivative expansion. While the actual EFT counter terms also have to absorb unphysical contributions arising from the lack of knowledge within SPT of small scales, the correction terms obtained here do account for the physical impact of nonlinearly induced dark matter velocity dispersion on the second order kernel. In addition, the correction term I^δ of the linear kernel in Eq. (7.8) would result by matching the EFT to first order in perturbation theory and at leading order in the derivative expansion. When going to higher order in ϵ we would obtain additional higher-derivative operators. However keep in mind, in general we do not expand in orders of ϵ when calculating numerical results (see below), therefore our results go beyond those correction terms, see [99] for the exact expressions and further details.

Finally, the second order kernels of the third cumulant perturbations π and χ contribute at second order in ϵ, so we have to solve

$$\begin{aligned}
\left(\partial_\eta+\frac{7}{2}\right)F_{2,\pi} &= 3k^2\epsilon F_{2,g}+5k^2\epsilon F_{2,\delta\epsilon}+k^2\omega F_{2,A}+\gamma_{\pi bc}F_{1,b}F_{1,c}\,,\\
\left(\partial_\eta+\frac{7}{2}\right)F_{2,\chi} &= 5k^2\epsilon F_{2,\delta\epsilon}+k^2\omega F_{2,A}+\gamma_{\chi bc}F_{1,b}F_{1,c}\,,
\end{aligned} \tag{7.23}$$

where we have suppressed the arguments for brevity. The terms on the right-hand side may be expanded up to second order in ϵ. Recalling that $\omega\propto\epsilon^2$, so we have to insert the zeroth order result $F_{2,A}|_{\epsilon^0}=1$ as well as the first order results of $F_{2,g}$ and $F_{2,\delta\epsilon}$ given in Eqs. (7.15) and (7.16), respectively. The corresponding vertices can be read off from Appendix D. Since we go to second order in ϵ the vertices $\gamma_{\pi gg}$, $\gamma_{\pi\theta\pi}$, $\gamma_{\pi\theta\chi}$ as well as $\gamma_{\chi gg}$, $\gamma_{\chi\theta\pi}$, $\gamma_{\chi\theta\chi}$ along with their flipped arguments will contribute.

Also worth mentioning is that at order $\mathcal{O}(\epsilon)$ also vorticity, vector and tensor modes will be generated when considering second order kernels. They will be discussed in Ch. 8.

The same strategy can be used to obtain third and higher oder kernels (e.g. $F_{3,a} = \mathcal{O}(\epsilon)$) as well as further corrections to higher order in ϵ. This can be done in principle, however the expressions quickly become rather lengthy, so we refer to a numerical treatment of the solutions that do *not* depend on a Taylor expansion in ϵ and are also valid when $k_i^2\epsilon$ becomes sizeable.

7.2 Numerical results

Now we solve the differential equation for the kernels numerically and follow the discussion arguing below Eq. (4.59). That is we do not expand in powers of the background dispersion ϵ and thus seek solutions valid for arbitrary $k_i^2\epsilon$.

As mentioned above, we use the two approximation schemes **cum2** and **cum3+**, as introduced below Eq. (4.114). In order to estimate the contributions sourced by different modes, within the schemes above we additionally consider scheme **s**, where only scalar modes are included, scheme **sw** taking also vorticity into account as well as schemes **sv** and **svt** where on top the vector and tensor modes of ϵ_{ij} are incorporated successively. All the approximation schemes are summarized in Table 7.1. The physically most complex scheme corresponds to **cum3+ (svt)**.

This also means, in the following we have to combine two approximation schemes in order to have full information about the degrees of freedom under consideration. There is one exception that takes place when computing second order kernels. The nonlinear back reaction to $F_{2,a}$ kernels can only be sourced from scalar modes meaning the schemes indicated in the columns are in this case identical and it suffices to only consider either **cum2** or **cum3+**. When computing third order kernels there are back reactions coming from vorticity, vector and tensor modes. On the other hand, when interested in the generation of vorticity, vector and tensor modes, the scheme **s** is of course not sufficient and at second order we also have to go to **sw**, **sv** and **svt**, respectively. This will be discussed in Ch. 8.

Table 7.1: Background values and perturbation modes taken into account in various approximation schemes of VPT.

		s	**sw**	**sv**	**svt**
cum2	$\epsilon(\eta)$	$\delta, \theta, g, \delta\epsilon, A$	$+w_i$	$+\nu_i$	$+t_{ij}$
cum3+	$\epsilon(\eta), \omega(\eta)$	$\delta, \theta, g, \delta\epsilon, A, \pi, \chi$	$+w_i$	$+\nu_i$	$+t_{ij}$

So far, we already discussed the impact of higher cumulants. Within the linear approximation we have seen in Ch. 4 and Ch. 5 that higher cumulants only play a role at very high wavenumbers when considering the linear δ and θ kernels. However, higher cumulants generate back reactions onto lower order cumulants via their background values which can in turn lead to different scaling behaviors for small ϵ as shown in the analytical results. Now, let us extend this investigation to the nonlinear regime considering numerical solutions of the nonlinear kernels.

These modifications are expected to play a role only at late times, i.e. at low redshift. Thus, in our numerical setup, we initialize the kernels at some finite time $\eta_{\rm ini}$ with the EdS-SPT kernels

for the density (plus A) and velocity divergence while setting all other kernels to zero,

$$\begin{aligned} F_{n,\delta}(\boldsymbol{k}_1,\ldots,\boldsymbol{k}_n,\eta_{\rm ini}) &\equiv F_n(\boldsymbol{k}_1,\ldots,\boldsymbol{k}_n)\,, \\ F_{n,\theta}(\boldsymbol{k}_1,\ldots,\boldsymbol{k}_n,\eta_{\rm ini}) &\equiv G_n(\boldsymbol{k}_1,\ldots,\boldsymbol{k}_n)\,, \\ F_{n,A}(\boldsymbol{k}_1,\ldots,\boldsymbol{k}_n,\eta_{\rm ini}) &\equiv F_n(\boldsymbol{k}_1,\ldots,\boldsymbol{k}_n)\,, \\ F_{n,a}(\boldsymbol{k}_1,\ldots,\boldsymbol{k}_n,\eta_{\rm ini}) &\equiv 0, \qquad a = w_i, g, \delta\epsilon, \nu_i, t_{ij}, \pi, \chi\,. \end{aligned} \tag{7.24}$$

So, at linear level, the kernels will be initialized to unity for the upper three lines. At second and higher order, one has to solve the SPT recursion relation Eq. (3.43) to initialize those kernels. In addition, we also have to initialize an infinitesimal small value of the background dispersion ϵ in order to match the evolution of the cumulants in the Vlasov hierarchy to the original Vlasov equation, since otherwise no dispersion and higher cumulants will be generated by time evolution via Eq. (7.24), see further discussion on this in [53]. The results at low redshift of the nonlinear kernels are expected to be insensitive on the precise value of $\eta_{\rm ini}$, as long as it is chosen to be early enough since the dominant contribution arises from the time evolution at late times. In practice we choose $\eta_{\rm ini} = -20$ and explicitly checked that the results are insensitive to this value, what makes sense since potential transients are suppressed by e^{-20}. The implementation of vector and tensor modes is described in Sec. 8.2.

Finally, we henceforth consider kernels only relevant for loop corrections. At one-loop one has Eq. (3.66),

$$\begin{aligned} P_{ab}^{(22)}(k,\eta) &\equiv e^{4\eta}\int \mathrm{d}^3q \Big\{ 2F_{2,a}(\boldsymbol{k}-\boldsymbol{q},\boldsymbol{q},\eta)F_{2,b}(\boldsymbol{k}-\boldsymbol{q},\boldsymbol{q},\eta)P_0(|\boldsymbol{k}-\boldsymbol{q}|)P_0(q)\Big\}\,, \\ 2P_{ab}^{(13)}(k,\eta) &\equiv e^{4\eta}\int \mathrm{d}^3q \Big\{ 3F_{1,a}(k,\eta)F_{3,b}(\boldsymbol{k},\boldsymbol{q},-\boldsymbol{q},\eta)P_0(k)P_0(q) \\ &\quad +3F_{3,a}(\boldsymbol{k},\boldsymbol{q},-\boldsymbol{q},\eta)F_{1,b}(k,\eta)P_0(k)P_0(q)\Big\}\,, \end{aligned} \tag{7.25}$$

where each kernel is *scale- and time-dependent* and the sum $P_{ab}^{(22)} + 2P_{ab}^{(13)}$ is the total one-loop (NLO) correction to the linear power spectrum $P_{ab}^{\rm lin}(k,\eta) = e^{2\eta}F_{1,a}(k,\eta)F_{1,b}(k,\eta)P_0(k)$, where we solve the system within a scaling universe $P_0(k) \propto k^{n_s}$ and using correspondingly the power-law ansatz $\epsilon(\eta) = \epsilon_0 e^{\alpha\eta}$ with $\alpha = 4/(n_s+3)$ and the constant dimensionless ratio $\bar{\omega} = \omega/\epsilon^2$ for the background values of second and fourth cumulant (see Ch. 6). So we will consider the nonlinear kernels $F_{2,a}(\boldsymbol{k}-\boldsymbol{q},\boldsymbol{q},\eta)$ and $F_{3,a}(\boldsymbol{k},\boldsymbol{q},-\boldsymbol{q},\eta)$ in the following, where $\boldsymbol{k}$ is the total momentum (obtained when summing over momenta in each argument) and $\boldsymbol{q}$ the loop momentum.

Furthermore, we discuss kernels $F_{3,a}(\boldsymbol{k}-\boldsymbol{p}-\boldsymbol{q},\boldsymbol{p},\boldsymbol{q},\eta)$ entering the two-loop (NNLO) contribution to consider symmetry constraints for δ and θ in Sec. 7.3. In addition, we compute the one-loop density bispectrum (Sec. 9.3) as well as the full two-loop power spectrum for vorticity (Sec. 9.4).

Dependence on loop wavenumber q

We start with exploring the dependence on the wavenumber $q = |\boldsymbol{q}|$ normalized by the dispersion scale k_σ while keeping the total momentum $k = |\boldsymbol{k}|$ fixed. The numerical results for second (left panels) and third (right panels) order kernels for $a = \delta$ (top), θ (bottom) are shown in Fig. 7.1. The angular dependence is contained in the scalar product $\mu \equiv \cos_{kq} = \boldsymbol{k}\cdot\boldsymbol{q}/(kq)$ and is also fixed in the evaluation. Note that the kernels are dimensionless when plotted against the dimensionless ratio of wavenumbers q/k_σ. In this case the kernel is also independent of the

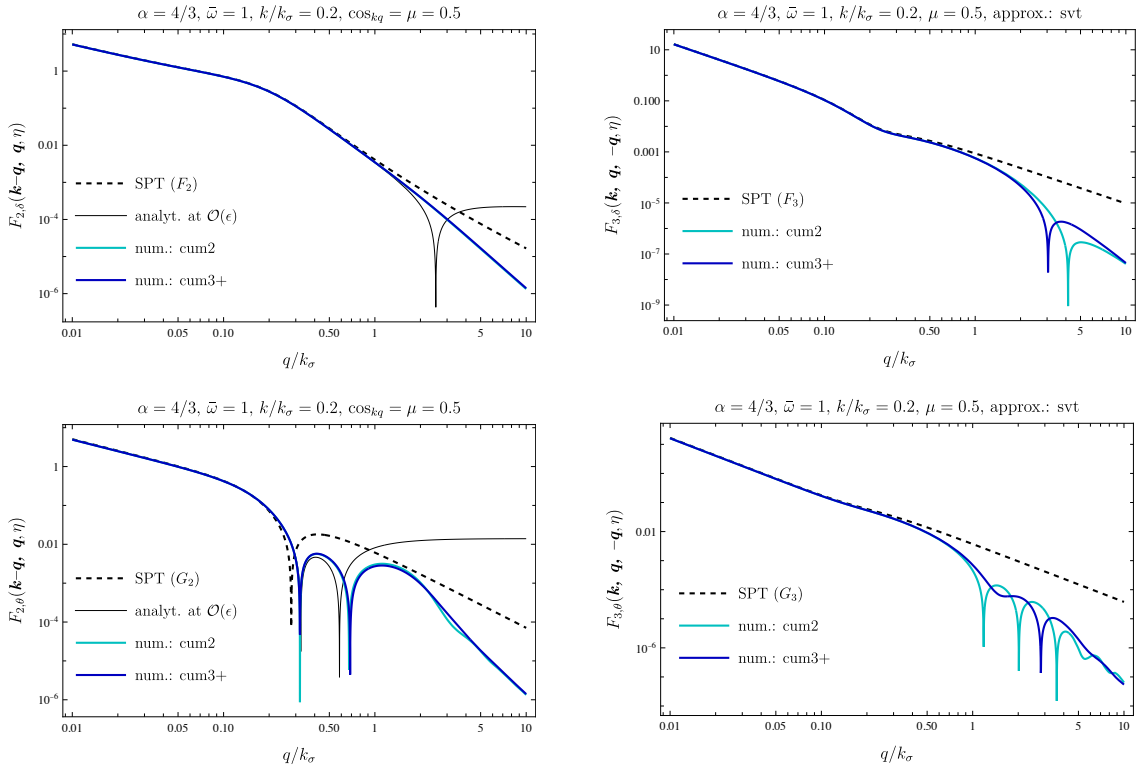

Figure 7.1: Nonlinear VPT kernels $F_{2,a}(\boldsymbol{k}-\boldsymbol{q},\boldsymbol{q},\eta)$ (left) and $F_{3,a}(\boldsymbol{k},\boldsymbol{q},-\boldsymbol{q},\eta)$ (right) for the density $a=\delta$ (top) and the velocity divergence $a=\theta$ (bottom) against the loop wavenumber $q=|\boldsymbol{q}|$ evaluated numerically. For comparison, the EdS-SPT (black-dashed) result of the corresponding kernels as well as the analytical result (thin black) at order ϵ for the second order kernel is shown. In addition, we compare the second (**cum2**) and third (**cum3+**) cumulant approximation (see Table 7.1). We use the power-like growth of the background dispersion $\epsilon(\eta)=\epsilon_0 e^{\alpha\eta}$ where $\alpha=4/3$ such that $n_s=0$ as well as $\bar{\omega}=\omega/\epsilon^2=1$ in the **cum3+** scheme, and $\eta=0$. We fix the total momentum $k=|\boldsymbol{k}|$ to $k/k_\sigma=0.2$ as well as the cosine between both wave vectors to $\cos_{kq}=0.5$. Each numerical evaluation demonstrates the suppression relative to SPT for $q\gtrsim k_\sigma$. Reprinted from [99].

value $\epsilon_0=1/k_\sigma^2$. The numerical kernels approach the EdS-SPT kernels F_n, G_n in the limit when *both* the total momentum $k\ll k_\sigma$ as well as the individual loop momentum $q\ll k_\sigma$ is much smaller than the dispersion scale. Since we choose $k/k_\sigma=0.2$ (which is not very much smaller than one) the numerical density kernels (blue line) as well as the SPT kernels (black-dashed) lie (almost) on top of each other in the limit $q/k_\sigma\ll 1$. In addition, the analytical result at $\mathcal{O}(\epsilon)$, calculated in Eq. (7.21) for the second order kernels $F_{2,\delta}$ and $F_{2,\theta}$, is shown in Fig. 7.1 as thin black line (left panels) and agrees with the numerical result for $q/k_\sigma\lesssim 1$ with a range that is larger for the density kernel while for the velocity divergence one notices a somewhat larger deviation at $q/k_\sigma\sim 1$ which may be due to the direct impact of ϵ_{ij} in the Euler equation highlighting effects beyond $\mathcal{O}(\epsilon)$. Nevertheless, the analytical approximation is able to capture the onset of the deviation of VPT from SPT.

In the opposite limit of large loop wavenumber q we see a significant *suppression* of the numer-

ical kernels relative to EdS-SPT. This observation immediately implies that when integrating over q as done in the one-loop correction the sensitivity of high loop momenta q decreases as compared to SPT, which means within VPT the NLO correction becomes less sensitive to the UV regime. This is expected theoretically [165] and agrees qualitatively when considering simulations of the response of nonlinear power to its linear counterpart indicating the decoupling of small-scale modes [50, 51].

We highlight that the inclusion of velocity dispersion and higher cumulants within VPT addresses one important shortcoming of SPT which is the sensitivity to the UV regime by accounting for the actual physically expected screening of those UV modes.

In addition, we compare the truncations **cum2** (dark blue) and **cum3+** (light blue) in Fig. 7.1, see Table 7.1. In the latter case we choose the most inclusive truncation (**svt**). Regarding the second order kernels (left panels) where only scalar modes contribute, both lines lie almost on top of each other whereas at third order (right panels) both truncations noticeably differ for large q/k_σ. However within the regime $q \lesssim k_\sigma$ where the suppression relative to SPT sets in the impact of higher cumulants is small.

In Fig. 7.2 we show again the third order kernels $F_{3,\delta}(\boldsymbol{k}, \boldsymbol{q}, -\boldsymbol{q}, \eta)$ (left) and $F_{3,\theta}(\boldsymbol{k}, \boldsymbol{q}, -\boldsymbol{q}, \eta)$ (right) within **cum3+** but now we successively turn on vorticity (**sw**), vector (**sv**) and tensor (**svt**) modes. Within the regime $q \lesssim 2k_\sigma$ all curves lie on top of each other except the one corresponding to the **s** scheme which shows a noticeable difference for $F_{3,\delta}$. This tells us that as soon as vorticity is included, i.e. going from **s** to **sw**, we observe even further suppression indicating the importance of the vorticity back reaction on the density kernel which first arises at third order. For $q \gtrsim 2k_\sigma$ there is an additional modification driven by the vector mode of the dispersion tensor (**sv**). A further inclusion of the tensor modes has negligible effects (**svt**). The situation for the velocity kernel $F_{3,\theta}$ is as follows: The impact of the vorticity on $F_{3,\theta}$ is mostly less pronounced. For $q \gtrsim 2k_\sigma$ an impact arises from the vector modes and the tensor back reaction is again negligible. When tuning the parameters k, $\cos_{kq}$, α and $\bar{\omega}$ we find a qualitatively similar behavior including the suppression at large q relative to SPT.

One-loop integrand

Armed with the knowledge how the nonlinear kernels behave at large loop wavenumber q (for fixed k) obtained by numerical computation, we will see that it is even possible to understand this behavior analytically. Finding an asymptotic slope of the nonlinear kernels will lead to a prediction for the asymptotic behavior of the *integrand* of the one-loop correction. We know from SPT that momentum conservation implies

$$\text{SPT:} \qquad F_n(\boldsymbol{k}_1, \ldots, \boldsymbol{k}_n) \propto \frac{k^2}{q^2} \quad \text{for} \quad k \ll k_i \,, \tag{7.26}$$

where $k \equiv |\sum \boldsymbol{k}_i|$, $k_i = |\boldsymbol{k}_i|$ and $q \equiv \max_i |k_i|$, see the equivalent expression for SPT, Eq. (3.81). Within VPT the same factor arises for the kernels $F_{n,\delta}(\boldsymbol{k}_1, \ldots, \boldsymbol{k}_n, \eta)$ in the limit $k \ll k_\sigma \ll k_i$. Now also the time-dependent dispersion scale k_σ becomes relevant. Whenever a mode contributes to the kernel and satisfies $k_i \gg k_\sigma$ it has entered the "dispersion horizon". The moment of entry η_{k_i} is defined as

$$\epsilon(\eta_{k_i}) k_i^2 \equiv 1 \,, \tag{7.27}$$

or equivalently when $k_i \equiv k_\sigma(\eta_{k_i})$. For $\epsilon(\eta) = \epsilon_0 e^{\alpha\eta}$ the moment of entry can be defined as $e^{\eta_{k_i}} = \left(k_\sigma^2/k_i^2\right)^{1/\alpha}$, where $k_\sigma = \epsilon_0^{-1/2}$ and $\alpha = 4/(n_s + 3)$ as before. This tells us that as soon as

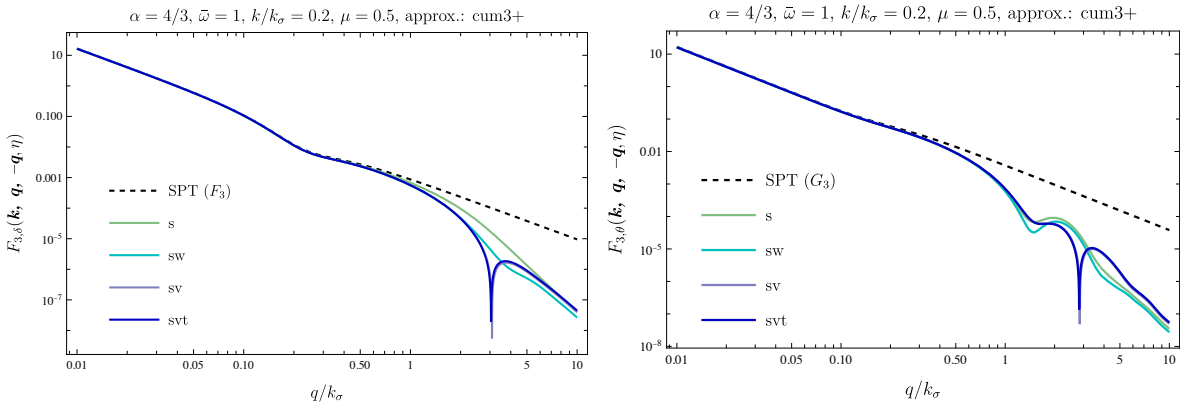

Figure 7.2: Third order kernels $F_{3,a}(\boldsymbol{k},\boldsymbol{q},-\boldsymbol{q},\eta)$ for the density $a=\delta$ (left) and the velocity divergence $a=\theta$ (right) against the loop wavenumber $q=|\boldsymbol{q}|$ evaluated numerically for parameters identical to Fig. 7.1. For comparison, the EdS-SPT (black-dashed) result of the corresponding kernels is shown. In addition, we compare within third cumulant truncation (**cum3+**) various back reactions driven by scalar modes (**s**), vorticity (**sw**), vector (**sv**) and tensor (**svt**) modes of the dispersion tensor (see Table 7.1). In particular, when going from **s** to **sw**, the vorticity back reaction onto $F_{3,\delta}$ plays an important role within the most relevant regime $k_\sigma \lesssim q \lesssim 2k_\sigma$ where the suppression of VPT relative to SPT sets in. Reprinted from [99].

the linear modes entered the dispersion horizon the kernel stops growing in the usual way ($\propto e^\eta$) and this growth is only guaranteed as long as $e^\eta \ll e^{\eta_{k_i}}$. Hence, this implies for the nonlinear kernels which effectively scale with n powers of the linear kernel,

$$\text{VPT:} \qquad F_{n,\delta}(\boldsymbol{k}_1,\ldots,\boldsymbol{k}_n,\eta) \propto \frac{k^2}{q^2}\, e^{\eta_{k_1}}\cdots e^{\eta_{k_n}} \quad \text{for} \quad k \ll k_\sigma \ll q \;\text{ and }\; \eta \gtrsim \eta_{k_i}\,. \tag{7.28}$$

Inserting $e^{\eta_{k_i}} = \left(k_\sigma^2/k_i^2\right)^{1/\alpha}$ gives a power-law screening of UV modes. When applying this to the kernels entering the one-loop integrand, we get

$$\begin{aligned} F_{2,a}(\boldsymbol{k}-\boldsymbol{q},\boldsymbol{q},\eta) &\propto q^{-2-4/\alpha}\,, \\ F_{3,a}(\boldsymbol{k},\boldsymbol{q},-\boldsymbol{q},\eta) &\propto q^{-2-4/\alpha}\,, \end{aligned} \tag{7.29}$$

which denote the slope by which these kernels decay at very large q. Using this for the integrand of the one-loop density power spectrum, which is defined as[1]

$$P_{\delta\delta}^{1L}(k,\eta) = \int \mathrm{d}\ln q\, P_{\delta\delta}^{\text{Integrand}}(k,q,\eta)\,, \tag{7.30}$$

we then get as leading contribution $F_{1,\delta}(k,\eta)F_{3,\delta}(\boldsymbol{k},\boldsymbol{q},-\boldsymbol{q},\eta)P_0(q)\mathrm{d}^3q \sim q^{-2}\mathrm{d}\ln q$ within VPT whereas in SPT the integrand grows as $F_3(\boldsymbol{k},\boldsymbol{q},-\boldsymbol{q})P_0(q)\mathrm{d}^3q \sim q^{n_s+1}\mathrm{d}\ln q$ for large loop wavenumber q with initial power spectrum $P_0(q)\propto q^{n_s}$, see Eq. (3.83). This explains *how VPT accounts for the screening of UV modes* and is illustrated in Fig. 7.3 showing the integrand for various spectral indices $n_s = 2,1,0,-1$. Overall, this gives

$$P_{\delta\delta}^{\text{Integrand}}(k,q,\eta)\big|_{\text{SPT}} \propto q^{n_s+1}\,, \tag{7.31}$$

[1] This is closely related to the one-loop correction of the response function used in [50, 51].

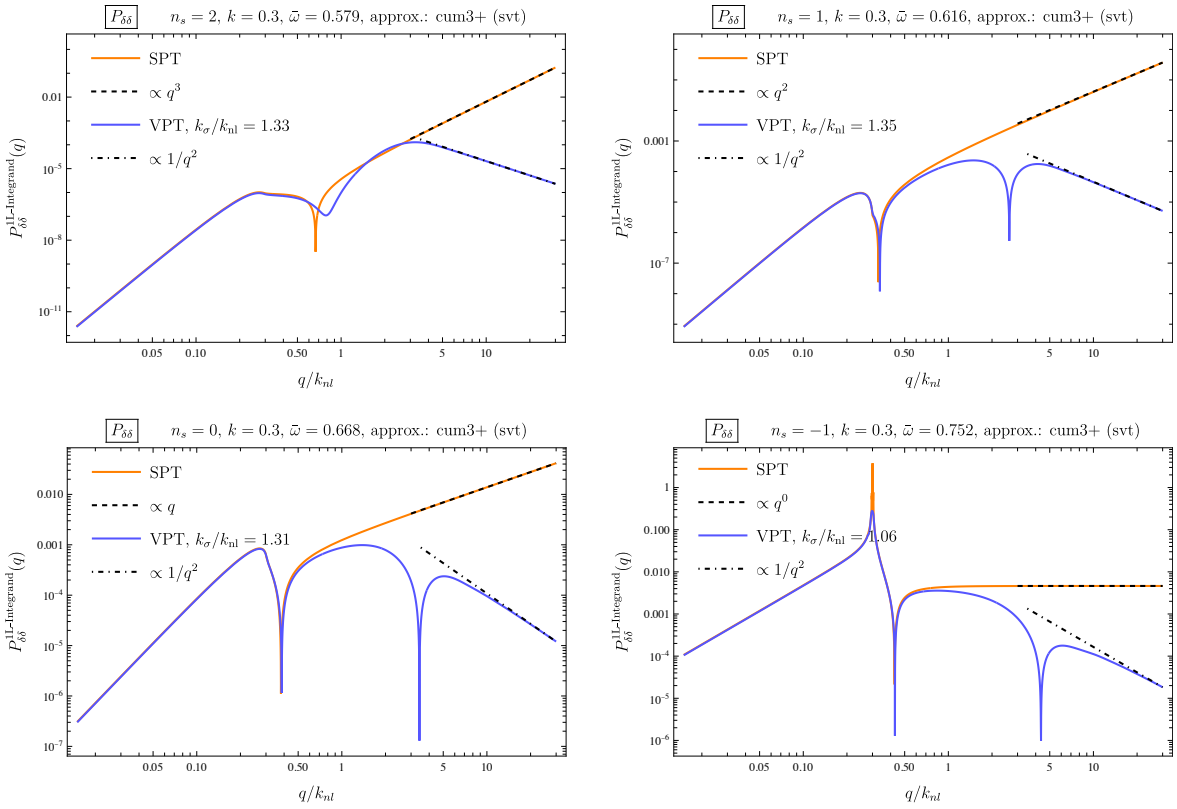

Figure 7.3: *Integrand* of the one-loop contribution to the density power spectrum in VPT (blue lines) and SPT (orange lines) versus the loop wavenumber q normalized by nonlinear scale $k_{\rm nl}$, for fixed total momentum k and for a scaling universe with initial spectrum $P_0(k) \propto k^{n_s}$ with spectral indices $n_s = 2, 1, 0, -1$ (that determine the value of α). We use the most inclusive truncation **cum3+ (svt)** (see Table 7.1) with parameters given in the legends. The values of $\bar{\omega}$ are obtained by self-consistently solving its evolution equation in linear approximation (see Sec. 6.2) while the ratios $k_\sigma/k_{\rm nl}$ are instead obtained by matching the full power spectrum (linear plus NLO correction) to N-body data, see Sec 9.1. Note that the drop at large q within VPT is universal and does not depend on the precise approximation scheme. Each of the SPT curves would lead to UV divergences when integrating over.

in accordance with Eq. (3.83), indicating the fatal shortcoming of SPT as the loop integration is UV divergent for all $n_s \geq -1$. In contrast, the prediction from the Vlasov theory is that the integrand drops as

$$P_{\delta\delta}^{\rm Integrand}(k,q,\eta)\big|_{\rm VPT} \propto q^{-2}\,, \tag{7.32}$$

independently of n_s, making the integrand less sensitive to the UV regime, which means that the modes far inside the dispersion horizon stop contributing, as stated above. Moreover, the argument leading to this scaling is universal and does not depend on the precise way how the linear growth stops when entering the dispersion horizon and therefore leads to the conclusion that the screening of UV modes does not depend on the precise approximation scheme, as shown in Figs. 7.1 and 7.2.

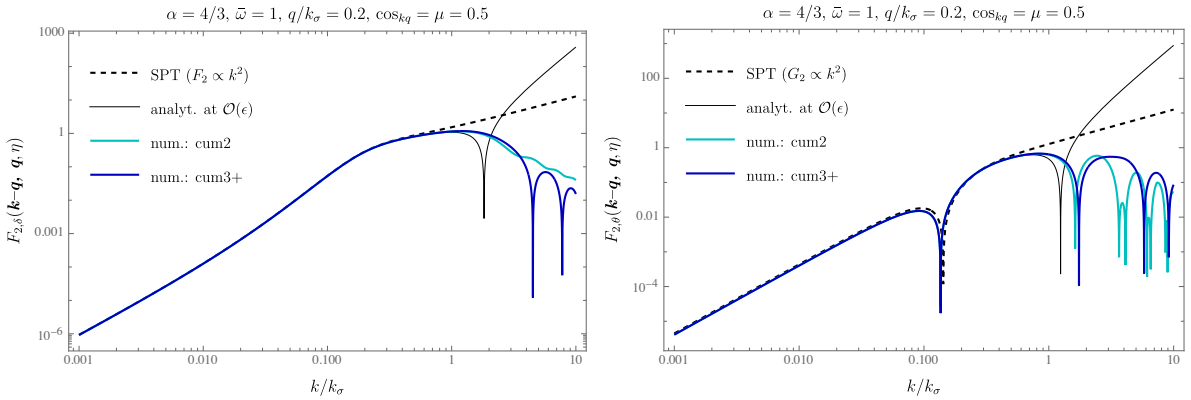

Figure 7.4: Nonlinear kernels $F_{2,\delta}(\boldsymbol{k}-\boldsymbol{q},\boldsymbol{q},\eta)$ (left) and $F_{2,\theta}(\boldsymbol{k}-\boldsymbol{q},\boldsymbol{q},\eta)$ (right) versus the total wavenumber k normalized by the dispersion scale k_σ for the cumulant truncations **cum2** and **cum3+**. The loop wavenumber is fixed to $q/k_\sigma = 0.2$. In addition, we compared the SPT result (black dashed) and the analytical result at order ϵ. The remaining parameters are identical to Fig. 7.1. $F_{2,\delta} \propto k^2$ for $k \to 0$ ensured by mass and momentum conservation, while for $F_{2,\theta}$ it is a consequence by symmetry $\boldsymbol{q} \to -\boldsymbol{q}$ (for $k \to 0$).

Dependence on total wavenumber k

Finally, we want to address the dependence on the total wavenumber k while keeping the loop wavenumber q fixed this time. We show in Fig. 7.4 again the kernels $F_{2,\delta(\theta)}(\boldsymbol{k}-\boldsymbol{q},\boldsymbol{q},\eta)$ but, as opposed to Fig. 7.1, against k/k_σ. We also compare the SPT result as well as the $\mathcal{O}(\epsilon)$ analytical result. They scale as k^2 for small k, as in SPT, which is required by mass and momentum conservation for the density and by the symmetry $\boldsymbol{k} \to -\boldsymbol{k}$ for the velocity divergence, see Sec. 7.3. Apart from that, the behavior is qualitatively similar to the dependence on q including the suppression of VPT kernels compared to SPT in the range $k \gtrsim k_\sigma$, fully captured by the numerical result while the $\mathcal{O}(\epsilon)$ correction only gives the trend of UV screening, and that higher cumulants start to play a role when $k \gtrsim 2k_\sigma$. Note that due to the choice $q/k_\sigma = 0.2$ the VPT curves lie almost on top of the SPT curve for $k \ll k_\sigma$ with a larger difference for the θ kernel.

In Fig. 7.5 we also show the third order kernels $F_{3,a}(\boldsymbol{k},\boldsymbol{q},-\boldsymbol{q},\eta)$ for $a = \delta,\theta$ (left) as well as for the two scalar perturbation modes $a = g,\delta\epsilon$ (right) within the most inclusive truncation **cum3+ (svt)**. The parameters are identical as chosen in Fig. 7.4. We can also confirm the quadratic scaling in the wavenumber k for small k for the density and velocity divergence. While for the former it is ensured up to arbitrary order in perturbation theory (due to mass and momentum conservation) for the latter it only shows up at third order in the configuration entering the one-loop integral and in general we expect a linear scaling, i.e. $F_{n,\theta} \propto k$ for $k \to 0$, see more details in Sec. 7.3.

In contrast, we find a different behavior for the dispersion modes $a = g,\delta\epsilon$ at small k approaching a constant value. This implies a modification of the linear theory even for $k \to 0$, which is quantified by a bias $b_a \equiv P_{a\delta}/P_{\delta\delta}|_{k\to 0}$. For $k \to 0$ it is given by

$$b_a = F_{1,a}(k=0,\eta) + 3\int \mathrm{d}^3q\, F_{3,a}(\boldsymbol{k},\boldsymbol{q},-\boldsymbol{q},\eta)\, P_0(q)\big|_{k\to 0} + \dots\,, \tag{7.33}$$

with linear plus one-loop correction and the ellipsis stands for two and higher loop corrections. For $a = g$ we obtain the analytical result to order ϵ at linear level given by $b_g^{\rm lin} = F_{1,g}(k =$

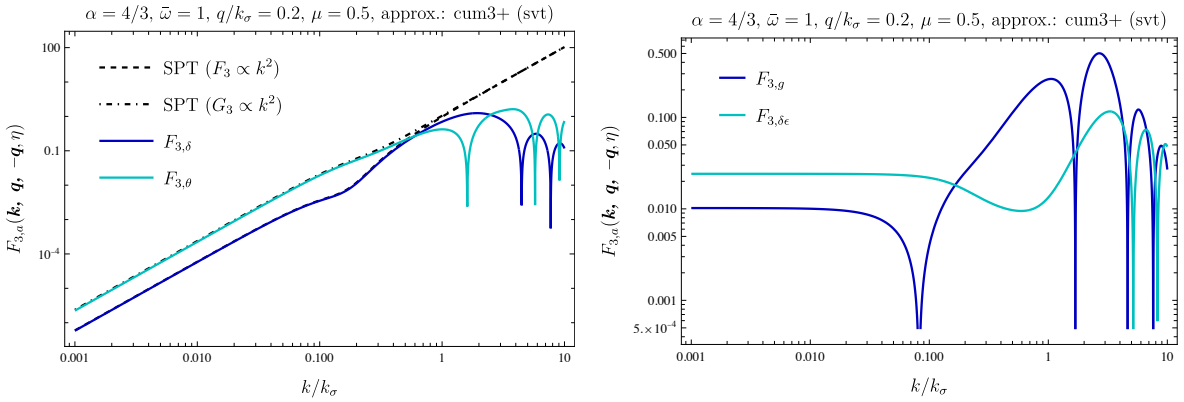

Figure 7.5: Nonlinear kernels $F_{3,a}(\boldsymbol{k}, \boldsymbol{q}, -\boldsymbol{q}, \eta)$ versus $k = |\boldsymbol{k}|$ for $a = \delta, \theta$ (left) and the scalar perturbations $a = g, \delta\epsilon$ of the stress tensor (right). The density and velocity divergence kernels scale with k^2 for $k \to 0$ while the dispersion modes approach a constant at low k. Reprinted from [99].

$0, \eta) = 2E_2(\eta)$, see Eq. (7.3), while for $a = \delta\epsilon$ we have $b^{\rm lin}_{\delta\epsilon} = 0$.

Overall, after having compared nonlinear kernels with multiple approximation schemes facing lower with higher cumulant truncations as well as back reactions of different modes, we can conclude that in particular vorticity, as well as scalar and vector modes of the dispersion should be taken into account when computing one-loop corrections while higher cumulants and especially the tensor mode are less relevant. Including vorticity will also ensure momentum conservation in general, which will be shown in the next section. While the numerical results presented so far are valid for arbitrary $k_i^2\epsilon$ we emphasize that perturbative predictions are limited at some small enough scales and that is why we trust the VPT predictions for scales $k \lesssim 2k_\sigma$.

7.3 Symmetry constraints on nonlinear kernels

The particular symmetries that underlie the Vlasov-Poisson system lead to constraints on the asymptotic behavior of the nonlinear kernels $F_{n,a}(\boldsymbol{k}_1, \ldots, \boldsymbol{k}_n, \eta)$ in appropriate limits. The corresponding constraints are commonly known within EdS-SPT [165, 171, 172] but in the following we want to address the generalization of them when including velocity dispersion and higher cumulants. It is also important to ensure their validity for a given approximation scheme since these constraints rely on delicate cancellations between various terms.

We start by considering the limit where one of the arguments $\boldsymbol{k}_i \to 0$ which corresponds to the impact of very large-scale modes onto smaller ones. The nonrelativistic limit of the Vlasov-Poisson system implies a shift symmetry [173–175]

$$\boldsymbol{x} \to \boldsymbol{x}' = \boldsymbol{x} + \boldsymbol{n}(\tau), \quad \tau \to \tau' = \tau\,, \tag{7.34}$$

with an arbitrary time-dependent shift function $\boldsymbol{n}(\tau)$ and can be seen as a generalized *Galilean invariance*. In [99] it is investigated that under this symmetry all cumulants are scalars, except for the first one, by considering the transformation of the cumulant generating function, Eq. (4.3),

$$\mathcal{C}(\tau, \boldsymbol{x}, \boldsymbol{l}) \to \mathcal{C}(\tau', \boldsymbol{x}', \boldsymbol{l}) = \mathcal{C}'(\tau, \boldsymbol{x}, \boldsymbol{l}) + \boldsymbol{l} \cdot \mathrm{d}\boldsymbol{n}/\mathrm{d}\tau\,. \tag{7.35}$$

In particular we have

$$\begin{aligned}
\delta(\tau,\boldsymbol{x}) &\to \delta(\tau',\boldsymbol{x}') = \delta'(\tau,\boldsymbol{x})\,,\\
\boldsymbol{v}(\tau,\boldsymbol{x}) &\to \boldsymbol{v}(\tau',\boldsymbol{x}') = \boldsymbol{v}'(\tau,\boldsymbol{x}) + \mathrm{d}\boldsymbol{n}/\mathrm{d}\tau\,,\\
\sigma_{ij}(\tau,\boldsymbol{x}) &\to \sigma_{ij}(\tau',\boldsymbol{x}') = \sigma'_{ij}(\tau,\boldsymbol{x})\,,\\
\mathcal{C}_{ijk\ldots}(\tau,\boldsymbol{x}) &\to \mathcal{C}_{ijk\ldots}(\tau',\boldsymbol{x}') = \mathcal{C}'_{ijk\ldots}(\tau,\boldsymbol{x})\,,
\end{aligned} \tag{7.36}$$

but note that the velocity divergence θ as well as the vorticity w_i also transform as scalars, or in general any gradient $\nabla_i v_j$ of the velocity field, as well as second gradients $\nabla_i\nabla_j\phi$ of the gravitational potential. This means that Galilean invariance implies that only gradients of the velocity field, and second gradients of the gravitational potential may appear in the equations of motion, which is indeed the case. However there is one exception, namely the time-derivative which is enforced by Galilean invariance to appear as $D_\eta \equiv \partial_\eta - \boldsymbol{u}\cdot\nabla$ for the rescaled variables in the equations of motion, what can also be confirmed. The latter constraint coming from Galilean invariance implies in Fourier space that the nonlinear vertices satisfy the relation

$$\gamma_{abc}(\boldsymbol{p},\boldsymbol{q}) = \delta^K_{ac}\left(\delta^K_{b\theta}\frac{\boldsymbol{q}\cdot\boldsymbol{p}}{2p^2} - \delta^K_{bw_i}\frac{(\boldsymbol{q}\times\boldsymbol{p})_i}{2p^2}\right) + \mathcal{O}(p^0)\,, \tag{7.37}$$

in the limit $\boldsymbol{p}\to 0$, generalizing the result in [176] to include vorticity. In Ref. [99] it is shown that this implies a recurrence relation for the nonlinear kernels, given by

$$F_{n+1,a}(\boldsymbol{p},\boldsymbol{k}_1,\ldots,\boldsymbol{k}_n,\eta) = \frac{1}{n+1}\frac{\boldsymbol{k}\cdot\boldsymbol{p}}{p^2}F_{n,a}(\boldsymbol{k}_1,\ldots,\boldsymbol{k}_n,\eta) + \mathcal{O}(p^0) \quad \text{for } \boldsymbol{p}\to 0\,, \tag{7.38}$$

where $\boldsymbol{k} = \sum_i \boldsymbol{k}_i$, which is well-known within EdS-SPT [177] but is now generalized to the inclusion of higher cumulants. It is approached when $p \ll k_i$ and $p \ll k_\sigma$ which means the size corresponding to $\sim 1/p$ of the large-scale mode should be larger than the length-scale of the dispersion given by $\sim\sqrt{\epsilon}$. Effectively, Eq. (7.38) ensures the cancellation of the contributions to the equal-time power spectra and bispectra for which the kernels become singular as $\propto 1/p$ for vanishing loop wavenumber, which generalizes the analogous property within SPT [173, 178].

Next, we consider the limit of vanishing total momentum, i.e. $\boldsymbol{k}\equiv\sum_i\boldsymbol{k}_i\to 0$, while the individual $\boldsymbol{k}_i$ remain finite and describes the impact of small-scale modes onto perturbation modes on larger scales. It is well-known from SPT that $F_n(\boldsymbol{k}_1,\ldots,\boldsymbol{k}_n)\propto k^2$ and $G_n(\boldsymbol{k}_1,\ldots,\boldsymbol{k}_n)\propto k^2$ in the large-scale limit when the sum $\boldsymbol{k}\equiv\sum_i\boldsymbol{k}_i$ of wavevectors goes to zero. In the following we show by mass and momentum conservation that for the density this can also be extended to VPT, *provided vorticity is taken into account* and that the scaling of the velocity divergence within VPT is in general different compared to SPT but still conforms with all symmetry requirements.

Density contrast

First, we consider the density contrast with kernels $F_{n,\delta}$. We can write its equation of motion as

$$\partial_\tau\delta + \nabla_i P_i = 0\,, \tag{7.39}$$

where

$$P_i(\tau,\boldsymbol{x}) \equiv (1+\delta)v_i\,, \tag{7.40}$$

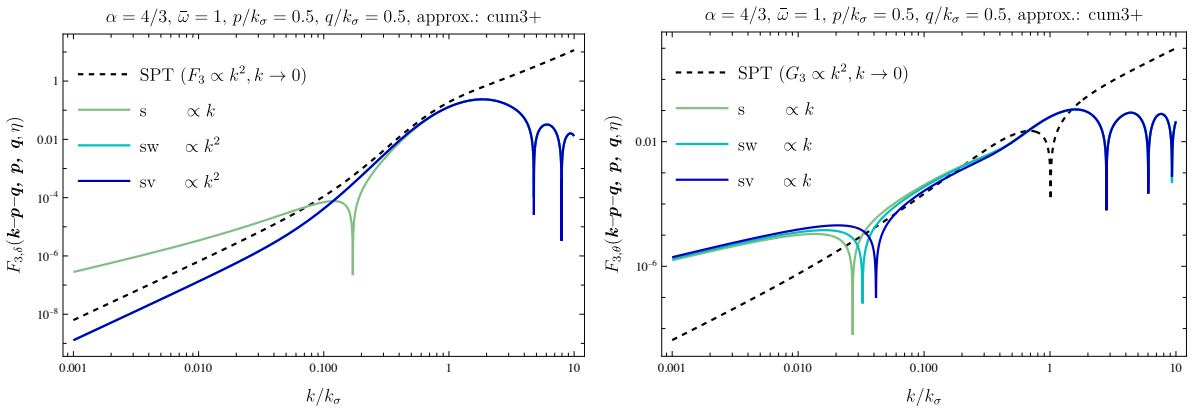

Figure 7.6: Third order kernels $F_{3,a}(\boldsymbol{k}-\boldsymbol{p}-\boldsymbol{q},\boldsymbol{p},\boldsymbol{q},\eta)$ entering the two-loop power spectrum for the density (left) and velocity divergence (right) against k/k_σ as well as their SPT counterparts (black dashed). It is demonstrated that it is mandatory that vorticity should be taken into account (**sw** and sv) to ensure momentum conservation, i.e. have k^2 scaling for the density. Neglecting vorticity (**s**) violates momentum conservation. In contrast, for the velocity divergence we observe a linear scaling $\propto k$ in each approximation scheme which amounts to a physical effect. For the figure we chose cosines $c_{kp}=0.3, c_{kq}=0.5, c_{pq}=0.875, p=0.5k_\sigma, q=0.5k_\sigma$ where $k_\sigma=1/\sqrt{\epsilon_0}$. Reprinted from [99].

is the momentum field. Its equation of motion can be found using the Euler equation

$$\partial_\tau P_i + \mathcal{H}P_i + \nabla_j T_{ij} = 0\,, \tag{7.41}$$

and corresponds to a conservation equation for the (comoving) momentum field aP_i, with

$$T_{ij} \equiv (1+\delta)(\sigma_{ij}+v_iv_j) + \phi\delta^K_{ij} + \frac{1}{3\mathcal{H}^2\Omega_m}\left(\nabla_i\phi\nabla_j\phi - \phi\nabla_i\nabla_j\phi + \phi\delta^K_{ij}\nabla^2\phi\right)\,, \tag{7.42}$$

which can be expected for free particles within general relativity [179]. Momentum conservation then requires that the covariant derivative, which appears in Eq. (7.41), satisfies $\nabla_j T^\phi_{ij} = (1+\delta)\nabla_i\phi$. Here T^ϕ_{ij} contains only the ϕ-dependent terms, described by the scalar metric perturbation, which is the gravitational potential in the Newtonian limit. Combining Eqs. (7.39) and (7.41) gives

$$\partial^2_\tau\delta + \mathcal{H}\partial_\tau\delta = \nabla_i\nabla_j T_{ij}\,, \tag{7.43}$$

including the stress-tensor contribution $(1+\delta)\sigma_{ij}$. Its form is independent of higher cumulants and when inserting the perturbative expansion this gives for the nth order density kernel

$$F_{n,\delta}(\boldsymbol{k}_1,\ldots,\boldsymbol{k}_n,\eta) \propto k^2, \qquad \boldsymbol{k}=\sum_i \boldsymbol{k}_i \to 0\,, \tag{7.44}$$

due to the two overall derivatives on the right-hand side of Eq. (7.43) and is required by mass and momentum conservation. One can check that this holds for all truncation and approximation schemes, in particular for **cum2** and **cum3+**, *given that vorticity is taken into account*. Thus, within the schemes **sw**, **sv** and **svt** this scaling is always guaranteed but within the scheme **s**, momentum conservation is broken. The reason behind this is that the velocity dispersion tensor sources vorticity and neglecting it discards part of the velocity field and thus also parts of the

momentum, which leads to artificial violation of momentum conservation. Therefore, in general the **s** approximation should not be used and we henceforth will not use it and always include vorticity. This can be understood theoretically by considering the scalar projection to the Euler equation, which prevents contributions from different parts to cancel and spuriously keeps linear terms in $\boldsymbol{k}$. Thus, neglecting vorticity generates terms that violate momentum conservation and are at least of third order in perturbation theory (see [99] for further details). So this can only appear in $F_{3,\delta}$ and at higher order. However the third order kernel $F_{3,\delta}(\boldsymbol{k},\boldsymbol{q},-\boldsymbol{q},\eta)$ entering the one-loop correction does not show this effect since it is even under $\boldsymbol{k}\to-\boldsymbol{k}$ due to the property $F_{n,\delta}(\boldsymbol{k}_1,\ldots,\boldsymbol{k}_n,\eta)=F_{n,\delta}(-\boldsymbol{k}_1,\ldots,-\boldsymbol{k}_n,\eta)$. Therefore any linear term in $\boldsymbol{k}$ has to cancel making this violation appear starting at two-loop order. The corresponding kernel $F_{3,\delta}(\boldsymbol{k}-\boldsymbol{p}-\boldsymbol{q},\boldsymbol{p},\boldsymbol{q},\eta)$ entering the two-loop power spectrum is shown in Fig. 7.6 (left). We take the third cumulant truncation and compare the approximation schemes **s**, **sw** and **sv**. The former is only shown for demonstration purposes as it explicitly shows the spurious linear scaling in k. Again, within this scheme momentum conservation is broken and we are not allowed to use this scheme in general. On the other hand the two remaining schemes demonstrate momentum conservation by showing the quadratic scaling Eq. (7.44). We observe suppression of the kernels for large k when compared to SPT, as before. The deviation from SPT even for $k\ll k_\sigma$ arises due to the finite size of the loop wavenumbers $\boldsymbol{p}$ and $\boldsymbol{q}$.

One may wonder whether this violation of momentum conservation is absent within SPT where vorticity is completely neglected. This is the case because velocity dispersion is also absent in SPT which means there are no source terms for vorticity in the Euler equation. Thus, within the perfect fluid approximation vorticity will not be generated at all and consequently the omission of vorticity does not spoil momentum conservation. Therefore, Eq. (7.44) will also hold in SPT even in absence of vorticity. However, *once velocity dispersion is taken into account it is mandatory to also include vorticity in order to guarantee momentum conservation.*

Velocity divergence

As opposed to the density contrast we found that the velocity divergence in general scales differently *even when vorticity as well as higher cumulants are included*, given by

$$F_{n,\theta}(\boldsymbol{k}_1,\ldots,\boldsymbol{k}_n,\eta)\propto k,\qquad \boldsymbol{k}=\sum_i\boldsymbol{k}_i\to 0\,, \tag{7.45}$$

showing a *linear scaling* in k. It satisfies mass and momentum conservation and is therefore allowed by the symmetries of the system. However, we have seen in Figs. 7.4 and 7.5 that $F_{2,\theta}(\boldsymbol{k}-\boldsymbol{q},\boldsymbol{q},\eta)\propto k^2$ and $F_{3,\theta}(\boldsymbol{k},\boldsymbol{q},-\boldsymbol{q},\eta)\propto k^2$ due to $F_{n,\theta}(\boldsymbol{k}_1,\ldots,\boldsymbol{k}_n,\eta)=F_{n,\theta}(-\boldsymbol{k}_1,\ldots,-\boldsymbol{k}_n,\eta)$ for the latter which cancels the linear terms in k, as before for the density contrast. Therefore, the linear scaling does only affect kernels entering two- and higher loops. The simplest kernel that gives the linear scaling is $F_{3,\theta}(\boldsymbol{k}-\boldsymbol{p}-\boldsymbol{q},\boldsymbol{p},\boldsymbol{q},\eta)$, for $\boldsymbol{p}+\boldsymbol{q}\neq 0$ and is shown in Fig. 7.6 (right). Here we see that this scaling appears for any approximation scheme also when vorticity is taken into account, in contrast to the case of the density contrast (left). Different cumulant truncations show the same behavior and we used **cum3+**. One is able to find an analytical

expression for this kernel analogously as in Sec. 7.1 up to first order in k, given by

$$\begin{aligned} F_{3,\theta}(\boldsymbol{k}-\boldsymbol{p}-\boldsymbol{q},\boldsymbol{p},\boldsymbol{q},\eta) &= G_3(\boldsymbol{k}-\boldsymbol{p}-\boldsymbol{q},\boldsymbol{p},\boldsymbol{q}) - \left[\frac{(\boldsymbol{k}\cdot\boldsymbol{p})(\boldsymbol{q}\cdot(\boldsymbol{q}+2\boldsymbol{p}))s^2_{pq}}{(\boldsymbol{p}+\boldsymbol{q})^2} + (\boldsymbol{p}\leftrightarrow\boldsymbol{q})\right] \\ &\times \left(\frac{10}{7}E_2(\eta) + \frac{2}{21}E_3(\eta) - 2E_{5/2}(\eta) + \frac{10}{21}E_{7/2}(\eta)\right) + \mathcal{O}(\epsilon^2,\epsilon k^2)\,, \end{aligned} \tag{7.46}$$

where $s^2_{pq} \equiv 1-(\boldsymbol{p}\cdot\boldsymbol{q})^2/\left(p^2q^2\right)$ and remember that $\boldsymbol{k}$ is the total sum of the wave vectors in the arguments. The term in the square brackets scales linearly in $\boldsymbol{k}$ and the one in round brackets linearly in ϵ since $E_n = \mathcal{O}(\epsilon)$. In the limit $\boldsymbol{p}+\boldsymbol{q}\to 0$ we recover the third order kernel entering the one-loop contribution and the second term indeed vanishes in this limit such that we obtain the k^2 scaling. Up to first order in ϵ there is no contribution coming from third and higher cumulants, such that it is identical for **cum2** and **cum3+** while even higher cumulant orders will also not change Eq. (7.46). Furthermore, the tensor modes of the dispersion tensor will also not affect the result (**sv** is equivalent to **svt**) and when including only vorticity (**sw**) the prefactor alters. Thus, the linear scaling for $\boldsymbol{k}\to 0$ is omnipresent throughout the various approximation schemes and we conclude that it cannot be an artifact of the approximation we are using here but is present in the full Vlasov theory.

On the other hand, we know from the momentum conservation equation Eq. (7.41) that when perturbatively expanding $\nabla_i P_i$ it should scale as k^2 in the limit where the sum of all wave vectors goes to zero. Considering this quantity, which can be written as

$$\nabla_i P_i = \nabla_i\left[(1+\delta)v_i\right] = -\mathcal{H}f\left[\theta + \nabla_i\left(\delta\,\frac{\nabla_i\theta}{\nabla^2}\right) - \nabla_i\left(\delta\,\frac{\varepsilon_{ijk}\nabla_j w_k}{\nabla^2}\right)\right], \tag{7.47}$$

and expanding to third order in perturbation theory using Eq. (4.58), momentum conservation requires that in the following combination of the kernels for δ, θ and w_i, given by

$$\begin{aligned} &F_{3,\theta}(\boldsymbol{k}_1,\boldsymbol{k}_2,\boldsymbol{k}_3,\eta) + \frac{1}{3}\left[\left(\frac{\boldsymbol{k}\cdot\boldsymbol{k}_3}{k_3^2}F_{2,\delta}(\boldsymbol{k}_1,\boldsymbol{k}_2,\eta)F_{1,\theta}(\boldsymbol{k}_3,\eta)\right.\right. \\ &- \frac{(\boldsymbol{k}\times(\boldsymbol{k}_2+\boldsymbol{k}_3))_i}{(\boldsymbol{k}_1+\boldsymbol{k}_3)^2}F_{1,\delta}(\boldsymbol{k}_1,\eta)F_{2,w_i}(\boldsymbol{k}_2,\boldsymbol{k}_3,\eta) \\ &\left.\left. + \frac{\boldsymbol{k}\cdot(\boldsymbol{k}_2+\boldsymbol{k}_3)}{(\boldsymbol{k}_2+\boldsymbol{k}_3)^2}F_{1,\delta}(\boldsymbol{k}_1,\eta)F_{2,\theta}(\boldsymbol{k}_2,\boldsymbol{k}_3,\eta)\right) + 2\,\text{perm.}\right], \end{aligned} \tag{7.48}$$

the linear term in $\boldsymbol{k} = \sum_i \boldsymbol{k}_i$ for $\boldsymbol{k}\to 0$ has to cancel. When using the analytical results at $\mathcal{O}(\epsilon)$ from Secs. 7.1 and 8.3, as well as a generalized form of Eq. (7.46) we indeed obtain the cancellation of linear terms in $\boldsymbol{k}$. This provides an *independent validation* of the linear scaling for the velocity divergence kernels.

However, the leading contribution of this linear scaling shows up starting at two-loop order. At one-loop ($L=1$) we know that the leading term in the limit $k\to 0$ comes from $P^{(13)}_{\theta\theta} \propto k^2 P_0(k)$. Going to two-loop order we get an analogous (propagatorlike) term where one linear and one nonlinear field is correlated, see Eq. (3.64). It contains kernels with $F_{5,\theta}(\boldsymbol{k},\boldsymbol{q},-\boldsymbol{q},\boldsymbol{p},-\boldsymbol{p},\eta)$ which scales as k^2 since any linear terms are cancelled due to symmetry, similarly as for the one-loop. In total, the corresponding contribution to the two-loop power spectrum also gives

$P_{\theta\theta}^{(15)} \propto k^2 P_0(k)$ for $k \to 0$. Now we know there is also a contribution coming from the kernel $F_{3,\theta}(\boldsymbol{k}-\boldsymbol{p}-\boldsymbol{q},\boldsymbol{p},\boldsymbol{q},\eta)$ at two-loop and scales linearly in k. For the auto power spectrum of the velocity divergence this contribution scales as $P_{\theta\theta}^{(33)} \propto k^2$ for $k \to 0$. The latter should therefore dominate over $P_{\theta\theta}^{(15)}$ for large enough scales, when assuming a ΛCDM input power spectrum. Nevertheless, at those scales the linear contribution to $P_{\theta\theta}$ will dominate any loop corrections and it is therefore difficult to verify this feature in practice. Moreover, we will see below, that the same behavior as for the velocity divergence happens for the vorticity. Since vorticity is not generated at linear level, it has no linear contribution to the power spectrum. Therefore it seems promising to find these effects within the vorticity power spectrum at large enough scales.

Next, we describe the generation of vorticity and vector mode kernels along with their numerical implementation in order to correctly calculate the two-loop vorticity power spectrum revealing the features described above. The generation of tensor modes is discussed accordingly.

8 Generation of vorticity, vector and tensor modes

Within SPT or in the pressureless perfect fluid approximation it is commonly known that vorticity is not generated and decays as $(\nabla \times \boldsymbol{v}) \propto 1/a$ within the linear regime [165]. However, when including at least velocity dispersion, i.e. the second cumulant from the Vlasov hierarchy the linear decay remains still valid but *vorticity will be generated nonlinearly* at second order in perturbation theory [166].

In the following we present the joint generation of vorticity and vector modes from nonlinear interactions within VPT for which the equations of motion are coupled to each other. Second (third) order kernels are presented in Sec. 8.3 (Sec. 8.4). An analogous mechanism leads to the generation of tensor modes which will be discussed in Sec. 8.5. In addition, in Sec. 8.2 we discuss an efficient implementation of vorticity, vector and tensor modes in our numerical treatment.

From the equation of motion Eq. (4.47) we can extract the evolution equations of both vorticity $\boldsymbol{w}$ and vector mode $\boldsymbol{\nu}$,

$$\begin{aligned} \partial_\eta w_{k,i} + \left(\frac{3}{2}\frac{\Omega_m}{f^2} - 1\right) w_{k,i} + k^2 \nu_{k,i} &= \int_{pq} \gamma_{w_i bc} \psi_{p,b} \psi_{q,c} \,, \\ \partial_\eta \nu_{k,i} + 2\left(\frac{3}{2}\frac{\Omega_m}{f^2} - 1\right) \nu_{k,i} - \epsilon w_{k,i} &= \int_{pq} \gamma_{\nu_i bc} \psi_{p,b} \psi_{q,c} \,, \end{aligned} \tag{8.1}$$

as well as tensor mode t_{ij} of the dispersion tensor,

$$\partial_\eta t_{k,ij} + 2\left(\frac{3}{2}\frac{\Omega_m}{f^2} - 1\right) t_{k,ij} = \int_{pq} \gamma_{t_{ij} bc} \psi_{p,b} \psi_{q,c} \,, \tag{8.2}$$

and we used subscripts i and j as spatial components for the perturbation fields $\boldsymbol{w}$, $\boldsymbol{\nu}$ and t_{ij}, subscript k as their corresponding wavenumber, as well as p and q as internal wavenumbers adopted from fields ψ_b and ψ_c, respectively.

8.1 Linear approximation

Within the linear approximation one neglects the right-hand side of Eqs. (8.1). and (8.2). When further considering for the background dispersion $\epsilon \to 0$ in the second line and $\Omega_m/f^2 \to 1$ one obtains an approximate solution $\nu_{k,i}(\eta) = \nu_{k,i}(\eta_0) e^{-(\eta-\eta_0)}$ which corresponds to a decaying mode, as expected. Inserting this result into the first line of Eq. (8.1) yields the leading order solution for the vorticity,

$$w_{k,i}(\eta) = \left(w_{k,i}(\eta_0) - 2k^2 \nu_{k,i}(\eta_0)\right) e^{-\frac{1}{2}(\eta-\eta_0)} + 2k^2 \nu_{k,i}(\eta_0) e^{-(\eta-\eta_0)} + \mathcal{O}(\epsilon) \,, \tag{8.3}$$

being a superposition of two decaying modes, corresponding to $\propto a^{-1}$ and $\propto a^{-3/2}$ for the original vorticity $-f\mathcal{H}\boldsymbol{w}$. Due to the presence of the vector mode, the vorticity acquires an additional decaying mode at linear level. Eq. (8.3) can in turn be used to obtain the $\mathcal{O}(\epsilon)$ result for the vector mode $\boldsymbol{\nu}$. One then obtains correction terms at first order in ϵ as hinted in Eq. (8.3). When assuming $\epsilon = \epsilon_0 e^{\alpha\eta}$, there exists a closed-form solution of the linear equations in terms of hypergeometric functions, given by

$$w_{k,i}(\eta) = A\, e^{-\frac{1}{2}\eta}\, {}_0F_1\left(1+\frac{1}{2\alpha};-\frac{\epsilon(\eta)k^2}{\alpha^2}\right) + B\, e^{-\eta}\, {}_0F_1\left(1-\frac{1}{2\alpha};-\frac{\epsilon(\eta)k^2}{\alpha^2}\right), \tag{8.4}$$

for $\alpha > 1/2$ and with coefficients A, B related to the initial vorticity and vector mode. This is analogous to Eq. (4.83) for the density but note that in linear approximation the vorticity contains only decaying modes. For $\epsilon k^2 \to 0$ one recovers Eq. (8.3) since ${}_0F_1 \to 1$ in that limit. In the opposite limit $k^2\epsilon \gg 1$ one finds an oscillatory damping,

$$w_{k,i}(\eta) \to e^{-\frac{3+\alpha}{4}\eta}\left[A' \sin\left(2\sqrt{\epsilon}k + \frac{\alpha-1}{4\alpha}\pi\right) + B' \sin\left(2\sqrt{\epsilon}k + \frac{\alpha+1}{4\alpha}\pi\right)\right], \tag{8.5}$$

where

$$\begin{aligned} A' &\equiv A\left(\frac{\epsilon_0 k^2}{\alpha^2}\right)^{-\frac{1}{4}-\frac{1}{4\alpha}} \frac{\Gamma\left(1+\frac{1}{2\alpha}\right)}{\sqrt{\pi}}, \\ B' &\equiv B\left(\frac{\epsilon_0 k^2}{\alpha^2}\right)^{-\frac{1}{4}+\frac{1}{4\alpha}} \frac{\Gamma\left(1-\frac{1}{2\alpha}\right)}{\sqrt{\pi}}. \end{aligned} \tag{8.6}$$

In linear approximation we only observe decaying modes for both vorticity and vector modes of the dispersion tensor. Furthermore, the tensor modes contain one single decaying mode $\propto e^{-\eta}$ in linear approximation independently of ϵ. In particular, this means that all their linear kernels vanish,

$$F_{1,w_i} = F_{1,\nu_i} = F_{1,t_{ij}} = 0\,, \tag{8.7}$$

as expected. This in turn means that the linear contribution to the vorticity and vector as well as tensor power spectra is zero.

8.2 Numerical treatment of vorticity, vector and tensor modes

Before considering solutions of the nonlinear kernels for vorticity, vector and tensor modes we now address how to incorporate their degrees of freedom within our numerical treatment beyond linear approximation. At linear level, each component evolves independently. However, at nonlinear level the different degrees of freedom for vorticity, vector and tensor modes mix and have in general different solutions. In the following we want to take advantage of the properties of vorticity, vector and tensor modes in order to reduce the independent degrees of freedom leading to efficient numerical computation. We leave the reader to skip this section as it is somewhat advanced and not necessary to understand the solutions from below.

For example, in Fourier space we know that the vorticity $w_{k,i}$ with wave vector $\boldsymbol{k}$ satisfies the transversality condition $\boldsymbol{k}\cdot\boldsymbol{w}_k = 0$ reducing the freedom to two independent degrees. The same holds for the vector mode $\nu_{k,i}$. In turn, the tensor mode $t_{k,ij}$ satisfies $k_i t_{k,ij} = 0, t_{k,ij} =$

$t_{k,ji}, t_{k,ii} = 0$. Then the independent tensor degrees of freedom amount to $3 \times 3 - (3+3+1) = 2$. The corresponding real-space conditions were already introduced in Sec. 4.1.

Within our numerical treatment we use these constraints, where e.g. for the vorticity we can choose two independent degrees of freedom in the plane perpendicular to $\boldsymbol{k}$. The remaining freedom corresponds to the choice of a convenient basis within this plane. If suitably selected one *single* perturbation mode can be sufficient to track the full vorticity as long as one does not go beyond the one-loop approximation for the power spectrum. The same holds for the vector and tensor modes at one-loop. However, for the two-loop power spectrum and one-loop bispectrum, we need to include all independent degrees of freedom. We describe both schemes below and checked their equivalence whenever both are applicable.

Before this, we discuss properties involving power spectra with vector and tensor quantities as well as the circumstance where those modes can appear. Now we will use letter s for all scalar quantities $s \in \{\delta, \theta, g, \delta\epsilon, A, \pi, \chi\}$ up to **cum3+**, v_i for *all* vector quantities $v_i \in \{w_i, \nu_i\}$ and t_{ij} for the tensor modes. The latter two can appear in two physical situations:

(i) During the generation of vector and tensor modes, i.e. when computing vector and tensor power spectra involving kernels F_{n,v_i} or $F_{n,t_{ij}}$ $(n \geq 2)$.

(ii) As nonlinear *back reaction* to the power- (and bi-)spectra of scalar modes via the nonlinear kernels $F_{n,s}$ $(n \geq 3)$.

In a diagrammatic representation as shown in Fig. 8.1 of the perturbative solution of the equations of motion (see e.g. [138]) the vector and tensor modes appear as *external, outgoing lines* in case (i) and as *internal* lines in both (i) and (ii), while "ingoing" lines are always (growing) scalar modes.

In addition, power spectra involving vector and tensor modes are rotationally invariant due to statistical isotropy, i.e. all cross power spectra $P_{v_i s} = P_{t_{ij} s} = P_{v_i t_{jk}} = 0$ vanish. Rotational invariance also requires

$$\begin{aligned} P_{v_i v_j}(k,\eta) &= \frac{1}{2}\left(\delta_{ij} - \frac{k_i k_j}{k^2}\right) \sum_n P_{v_n v_n}(k,\eta)\,, \\ P_{t_{ij} t_{ls}}(k,\eta) &= \frac{1}{2} P^T_{ij,ls}(k) \sum_{m,n} P_{t_{nm} t_{nm}}(k,\eta)\,, \end{aligned} \tag{8.8}$$

where the sum over all n, m was explicitly written down for clarity while being implicitly understood in the rest of this thesis, and i, j, l, s are not summed over. The tensor projector $P^T_{ij,ls}(k)$ can be found in Eq. (4.29) and all v_i can adopt w_i or ν_i. Overall, it is sufficient to compute the power spectra by summing over all indices, as indicated on the right-hand sides of Eq. (8.8).

Simplified algorithm for the one-loop power spectrum

Now we present a treatment applicable for all scalar, vector and tensor power spectra at one-loop level, including the back reaction of vector and tensor modes to the scalar power spectra. Essentially, it can be boiled down to only keep one single degree of freedom of the two independent modes for v_i and t_{ij}. This is the case, since at one-loop the relevant kernels of vector and tensor modes are given by $F_{2,v_i}(\boldsymbol{k}-\boldsymbol{q}, \boldsymbol{q}, \eta)$ and $F_{2,t_{ij}}(\boldsymbol{k}-\boldsymbol{q}, \boldsymbol{q}, \eta)$ either for their generation (i) for the vector- or tensor power spectra $P_{v_i v_i}$ or $P_{t_{ij} t_{ij}}$, respectively, or as for their

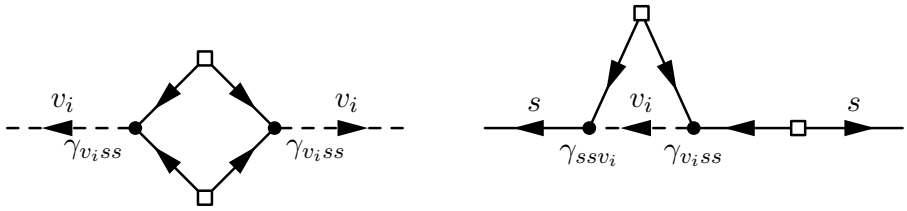

Figure 8.1: Generation of vorticity/vector perturbations at one-loop [left diagram, case (i)] and back reaction on scalar power spectra [right diagram, case(ii)] corresponding to the $P^{(22)}_{v_i v_i}$ and $P^{(13)}_{ss}$ part of the one-loop integrals, respectively. Here $v_i \in \{w_i, \nu_i\}$ corresponds to dashed lines, and solid lines represent any scalar perturbations $s \in \{\delta, \theta, g, \delta\epsilon, A, \pi, \chi\}$ (possibly of different type for each line). The open square denotes the initial power spectrum, and the filled circles are nonlinear vertices. Reprinted from [99].

nonlinear back reaction (ii) to the scalar power spectra involving kernels $F_{3,s}(\boldsymbol{k}, \boldsymbol{q}, -\boldsymbol{q}, \eta)$. Both roles are specific examples of the generic cases (i) and (ii) from above and therefore it is sufficient to compute these kernels. Note also that the one-loop contributions $P^{(13)}_{v_i v_i}$ and $P^{(13)}_{t_{ij} t_{ij}}$ vanish since their linear kernels are zero.

Let us start with the vector modes $v_i \in \{w_i, \nu_i\}$. For the first case we consider nonlinear vertices $\gamma_{abc}(\boldsymbol{k}_1, \boldsymbol{k}_2)$ with $a = v_i(\boldsymbol{k}_1 + \boldsymbol{k}_2, \eta)$ and b, c representing scalar modes $s(\boldsymbol{k}_1, \eta), s'(\boldsymbol{k}_2, \eta)$ as $\gamma_{v_i ss'}(\boldsymbol{k}_1, \boldsymbol{k}_2)$, and analogously for other cases. When inserting the second order kernels into the expression for the one-loop integral Eq. (7.25) we obtain a unique vertex combination given by

$$\gamma_{v_i ss'}(\boldsymbol{q}, \boldsymbol{k} - \boldsymbol{q}) \gamma_{v_i' s'' s'''}(\boldsymbol{q}, \boldsymbol{k} - \boldsymbol{q}) \,, \tag{8.9}$$

with appropriate factors of linear kernels for scalar modes which we left out here for brevity and corresponds to the case (i), see also Fig. 8.1. We implicitly assume the summation over the spatial index $i = x, y, z$. For the second case (ii) we can find an analogous contribution given by

$$\gamma_{ss' v_i}(\boldsymbol{q}, \boldsymbol{k} - \boldsymbol{q}) \gamma_{v_i' s'' s'''}(-\boldsymbol{q}, \boldsymbol{k}) \,, \tag{8.10}$$

where now a linear kernel of a scalar mode as well as a second order kernel of a vector mode is involved (on top of two linear scalar kernels). Note that here we have two contributions due to the sum in m in Eq. (4.59) but this identical to the one from above upon symmetrization of the corresponding kernels. In total, we observe that all vertices of the form $\gamma_{v_i ss'}(\boldsymbol{k}_1, \boldsymbol{k}_2)$ as well as $\gamma_{sv_i s'}(\boldsymbol{k}_1, \boldsymbol{k}_2) = \gamma_{ss' v_i}(\boldsymbol{k}_2, \boldsymbol{k}_1)$ are proportional to $(\boldsymbol{k}_1 \times \boldsymbol{k}_2)_i$ (see Appendix B). Therefore the vorticity vector has to lie along $\boldsymbol{k} \times \boldsymbol{q}$ and it is sufficient to *track a single effective degree of freedom for each vector mode*. So we can replace $w_i \mapsto w_{\text{eff}}$ and $\nu_i \mapsto \nu_{\text{eff}}$, and the factor $(\boldsymbol{k}_1 \times \boldsymbol{k}_2)_i$ contained in the relevant vertices by $\sigma_{\boldsymbol{k}_1 \boldsymbol{k}_2} |\boldsymbol{k}_1 \times \boldsymbol{k}_2|$. The prefactor $\sigma_{\boldsymbol{k}_1 \boldsymbol{k}_2} \in \{\pm 1, 0\}$ is needed to track the correct sign. These replacements are obtained by multiplying the vectorial terms with $(\boldsymbol{k} \times \boldsymbol{q})_i / |\boldsymbol{k} \times \boldsymbol{q}|$ such that

$$F_{2,v_i}(\boldsymbol{k}_1, \boldsymbol{k}_2, \eta) = F_{2,v_{\text{eff}}}(\boldsymbol{k}_1, \boldsymbol{k}_2, \eta) \frac{(\boldsymbol{k} \times \boldsymbol{q})_i}{|\boldsymbol{k} \times \boldsymbol{q}|}, \qquad (\boldsymbol{k}_1 \times \boldsymbol{k}_2)_i = \sigma_{\boldsymbol{k}_1 \boldsymbol{k}_2} |\boldsymbol{k}_1 \times \boldsymbol{k}_2| \frac{(\boldsymbol{k} \times \boldsymbol{q})_i}{|\boldsymbol{k} \times \boldsymbol{q}|} \,, \tag{8.11}$$

for all relevant vectors $\boldsymbol{k}_{1,2} \in \{\pm \boldsymbol{q}, \pm \boldsymbol{k}, \pm(\boldsymbol{k} - \boldsymbol{q}), \pm(\boldsymbol{k} + \boldsymbol{q})\}$ that occur when evaluating the integrand of the one-loop power spectrum. We use $\sigma_{\boldsymbol{k}_1 \boldsymbol{k}_2} = \frac{(\boldsymbol{k}_1 \times \boldsymbol{k}_2) \cdot (\boldsymbol{k} \times \boldsymbol{q})}{|\boldsymbol{k}_1 \times \boldsymbol{k}_2| \, |\boldsymbol{k} \times \boldsymbol{q}|}$. Then the corresponding

vertices involving one vorticity and vector mode can e.g. be written down as

$$\gamma_{\delta w_{\rm eff}\delta}(\boldsymbol{k}_1,\boldsymbol{k}_2) = \gamma_{Aw_{\rm eff}A}(\boldsymbol{k}_1,\boldsymbol{k}_2) = \frac{1}{2}\sigma_{\boldsymbol{k}_1\boldsymbol{k}_2}\frac{|\boldsymbol{k}_1\times\boldsymbol{k}_2|}{k_1^2}\,, \tag{8.12}$$

and analogously for the remaining vertices. Altogether, these replacements leading to a single-component vector mode $v_{\rm eff}$ also correctly take into account the back reaction on the scalar kernels $F_{3,s}(\boldsymbol{k},\boldsymbol{q},-\boldsymbol{q},\eta)$. This allows the computation of the vector power spectra according to

$$P_{w_iw_i} = P_{w_{\rm eff}w_{\rm eff}}, \quad P_{w_i\nu_i} = P_{w_{\rm eff}\nu_{\rm eff}}, \quad P_{\nu_i\nu_i} = P_{\nu_{\rm eff}\nu_{\rm eff}}\,. \tag{8.13}$$

Next, we focus on the treatment of tensor modes. As mentioned above, here we also find at one-loop that one single effective tensor mode will be sufficient since the relevant combinations of vertices is analogous to Eqs. (8.9), (8.10) and Fig. 8.1 with v_i, v_i' replaced by t_{ij}, t_{ij}'. Similarly, we observe that for vertices of the form $\gamma_{t_{ij}ss'}(\boldsymbol{k}_1,\boldsymbol{k}_2)$ the dependence on the indices i,j is uniquely given by the factor

$$f_{ij}(\boldsymbol{k}_1,\boldsymbol{k}_2) \equiv \delta_{ij} - \frac{(\boldsymbol{k}_1+\boldsymbol{k}_2)_i(\boldsymbol{k}_1+\boldsymbol{k}_2)_j}{(\boldsymbol{k}_1+\boldsymbol{k}_2)^2} - 2\frac{(\boldsymbol{k}_1\times\boldsymbol{k}_2)_i(\boldsymbol{k}_1\times\boldsymbol{k}_2)_j}{(\boldsymbol{k}_1\times\boldsymbol{k}_2)^2}\,, \tag{8.14}$$

which fulfills the transversality and trace conditions $0 = (\boldsymbol{k}_1+\boldsymbol{k}_2)_i\, f_{ij}(\boldsymbol{k}_1,\boldsymbol{k}_2)$, $0 = f_{ii}$. This will be relevant for tensor mode generation, corresponding to case (i). Furthermore, for vertices of the form $\gamma_{st_{ij}s'}(\boldsymbol{k}_1,\boldsymbol{k}_2) = \gamma_{ss't_{ij}}(\boldsymbol{k}_2,\boldsymbol{k}_1)$, relevant for tensor mode back reaction [case(ii)], we find an index dependence captured by $g_{ij}(\boldsymbol{k}_1,\boldsymbol{k}_2) \equiv (\boldsymbol{k}_2)_i(\boldsymbol{k}_2)_j$. This then allows us replace the two independent tensor modes by a *single effective tensor mode* $t_{ij} \mapsto t_{\rm eff}$, as before for the vector modes by replacing

$$\begin{aligned}
\gamma_{t_{ij}ss'}(\boldsymbol{k}_1,\boldsymbol{k}_2) &= f_{ij}(\boldsymbol{k}_1,\boldsymbol{k}_2)\,\gamma_{t_{\rm eff}ss'}(\boldsymbol{k}_1,\boldsymbol{k}_2)\,,\\
k_2^2\sin^2(\boldsymbol{k}_1,\boldsymbol{k}_2)\gamma_{st_{ij}s'}(\boldsymbol{k}_1,\boldsymbol{k}_2) &= g_{ij}(\boldsymbol{k}_1,\boldsymbol{k}_2)\,\gamma_{st_{\rm eff}s'}(\boldsymbol{k}_1,\boldsymbol{k}_2)\,,
\end{aligned} \tag{8.15}$$

where $\sin^2(\boldsymbol{k}_1,\boldsymbol{k}_2) = (\boldsymbol{k}_1\times\boldsymbol{k}_2)^2/(k_1^2k_2^2)$ and the second line effectively means that we replace the index-dependence as $g_{ij}(\boldsymbol{k}_1,\boldsymbol{k}_2) \mapsto k_2^2\sin^2(\boldsymbol{k}_1,\boldsymbol{k}_2)$ for the vertices with effective tensor mode. This replacement can be obtained when considering the only relevant contraction $q_iq_j\gamma_{t_{ij}s''s'''}(-\boldsymbol{q},\boldsymbol{k}) = q^2\sin^2(\boldsymbol{k}-\boldsymbol{q},\boldsymbol{q})\gamma_{t_{\rm eff}s''s'''}(-\boldsymbol{q},\boldsymbol{k})$ in the combination of vertices in Eq. (8.10), such that the relevant vertices given in Appendix B for the effective tensor mode can e.g. be written as

$$\begin{aligned}
\gamma_{t_{\rm eff}\theta g}(\boldsymbol{k}_1,\boldsymbol{k}_2) &= -\frac{1}{2}\frac{(\boldsymbol{k}_1\times\boldsymbol{k}_2)^2\,\boldsymbol{k}_1\cdot\boldsymbol{k}_2}{2(\boldsymbol{k}_1+\boldsymbol{k}_2)^2k_1^2k_2^2}\,,\\
\gamma_{\theta At_{\rm eff}}(\boldsymbol{k}_1,\boldsymbol{k}_2) &= -\frac{1}{2}\frac{(\boldsymbol{k}_1\times\boldsymbol{k}_2)^2}{k_2^2}\,.
\end{aligned} \tag{8.16}$$

Note that, in contrast to vorticity and the vector modes the replacement for the tensor modes is differently for cases (i) and (ii). Again, case (i) corresponds to the vertex in the first line and case (ii) to the vertex in the second line. The remaining vertices for the effective tensor mode are obtained analogously. Altogether, with Eq. (8.9), the combinations of vertices entering the one-loop integral can be replaced as

$$\begin{aligned}
\gamma_{t_{ij}ss'}(\boldsymbol{q},\boldsymbol{k}-\boldsymbol{q})\gamma_{t'_{ij}s''s'''}(\boldsymbol{q},\boldsymbol{k}-\boldsymbol{q}) &= 2\gamma_{t_{\rm eff}ss'}(\boldsymbol{q},\boldsymbol{k}-\boldsymbol{q})\gamma_{t'_{\rm eff}s''s'''}(\boldsymbol{q},\boldsymbol{k}-\boldsymbol{q})\,,\\
\gamma_{ss't_{ij}}(\boldsymbol{q},\boldsymbol{k}-\boldsymbol{q})\gamma_{t'_{ij}s''s'''}(-\boldsymbol{q},\boldsymbol{k}) &= \gamma_{ss't_{\rm eff}}(\boldsymbol{q},\boldsymbol{k}-\boldsymbol{q})\gamma_{t'_{\rm eff}s''s'''}(-\boldsymbol{q},\boldsymbol{k})\,.
\end{aligned} \tag{8.17}$$

The first line implies that the tensor power spectrum can be computed according to

$$P_{t_{ij}t_{ij}}(k,\eta) = 2P_{t_{\rm eff}t_{\rm eff}}(k,\eta)\,, \tag{8.18}$$

and the second line shows that the effective tensor mode correctly accounts for the back reaction on the scalar kernels $F_{3,s}(\boldsymbol{k},\boldsymbol{q},-\boldsymbol{q},\eta)$.

General case

Now we want to introduce a numerical treatment which is valid for any approximation scheme, in particular beyond one-loop order for the power spectrum. This generalized treatment will apply e.g. for the one-loop matter density bispectrum and the two-loop vorticity power spectrum discussed in Secs. 9.3 and 9.4, respectively. Within the current treatment we need to take both of the two independent degrees of freedom for the vorticity and vector mode into account. This can be straightforwardly extended to the full treatment of tensor modes but is beyond the scope of this work. Nevertheless, the vector modes still satisfy $\boldsymbol{p}\cdot\boldsymbol{v}(\boldsymbol{p},\eta)=0$ with $v_i\in\{w_i,\nu_i\}$, so we will project v_i on a basis that depends on $\boldsymbol{p}$. In particular, we use the $\boldsymbol{p}$-dependent orthogonal basis vectors given by

$$\begin{aligned}
\boldsymbol{b}_{p1} &\equiv \mathcal{N}_{p1}(\boldsymbol{p}\times\boldsymbol{Q}_p)\,,\\
\boldsymbol{b}_{p2} &\equiv \mathcal{N}_{p2}(\boldsymbol{p}\times(\boldsymbol{p}\times\boldsymbol{Q}_p)) = \mathcal{N}_{p2}\left(\boldsymbol{p}\,(\boldsymbol{p}\cdot\boldsymbol{Q}_p)-\boldsymbol{Q}_p\,p^2\right)\,,\\
\boldsymbol{b}_{p3} &\equiv \mathcal{N}_{p3}\,\boldsymbol{p}\,,
\end{aligned} \tag{8.19}$$

where $\boldsymbol{Q}_p$ is an *a priori* arbitrary reference vector which will be chosen for each $\boldsymbol{p}$ with the only condition that $\boldsymbol{p}\times\boldsymbol{Q}_p\neq 0$, i.e. it must not be collinear to $\boldsymbol{p}$. In addition, the $\mathcal{N}_{p1,2,3}$ are normalization factors. Usually they are chosen such that the basis vectors are normalized to unity, however this is not required. This basis is then referred to as *transverse basis* for which e.g. the vorticity can be decomposed as

$$\boldsymbol{w}_p = w_{p1}\boldsymbol{b}_{p1} + w_{p2}\boldsymbol{b}_{p2}\,, \tag{8.20}$$

where $w_{p1,2}$ are the two transverse vorticity components and when projected along $\boldsymbol{b}_{p3}$ it vanishes by construction. The vector mode is decomposed analogously. This means in the vector of perturbation variables ψ we have to include $w_{p\alpha}$ and $\nu_{p\alpha}$ for $\alpha=1,2$. This choice of basis will not affect the linear dynamics and each component has the same equation, while for the nonlinear part we have to transform the vertices from Cartesian coordinates to the transverse basis via

$$\begin{aligned}
\gamma_{aw_{p\alpha}c}(\boldsymbol{p},\boldsymbol{q}) &= \gamma_{aw_ic}(\boldsymbol{p},\boldsymbol{q})b_{p\alpha,i}\,,\\
\gamma_{abw_{q\alpha}}(\boldsymbol{p},\boldsymbol{q}) &= \gamma_{abw_i}(\boldsymbol{p},\boldsymbol{q})b_{q\alpha,i}\,,\\
\gamma_{w_{k\alpha}bc}(\boldsymbol{p},\boldsymbol{q}) &= \frac{b_{p+q\alpha,i}}{|\boldsymbol{b}_{p+q\alpha}|^2}\gamma_{w_ibc}(\boldsymbol{p},\boldsymbol{q})\,,
\end{aligned} \tag{8.21}$$

where summation over $i=x,y,z$ is implied. In each case for $\boldsymbol{p}$, $\boldsymbol{q}$ and $\boldsymbol{p}+\boldsymbol{q}$ the appropriate transverse basis is applied. For vertices with the vector mode ν_i the projection is analogous and if more than one index a,b,c is a vorticity or vector mode multiple projections apply correspondingly. For example for the vertex with vorticity self coupling we have

$$\gamma_{w_{p+q\alpha}w_{p\beta}w_{q\gamma}}(\boldsymbol{p},\boldsymbol{q}) = \frac{b_{p+q\alpha,i}}{|\boldsymbol{b}_{p+q\alpha}|^2}\gamma_{w_iw_jw_k}(\boldsymbol{p},\boldsymbol{q})b_{p\beta,j}b_{q\gamma,k}\,, \tag{8.22}$$

with summation over $i,j,k = x,y,z$ and for $\alpha,\beta,\gamma = 1,2$. Thus the www vertex involves a total of $2^3 = 8$ distinct vertices instead of $3^3 = 27$ vertices in Cartesian coordinates. This demonstrates the advantage of our numerical treatment using the transverse basis.

Note that when using the transverse basis, and using well-known relations from vector algebra, the projected vertices can be brought into a form that solely depends on scalar products $\boldsymbol{p}\cdot\boldsymbol{q}$, $\boldsymbol{p}\cdot\boldsymbol{Q}_r$ and $\boldsymbol{q}\cdot\boldsymbol{Q}_r$, as well as on

$$D_{rs} \equiv \det(\boldsymbol{s},\boldsymbol{r},\boldsymbol{Q}_r) = (\boldsymbol{r}\times\boldsymbol{Q}_r)\cdot\boldsymbol{s}\,, \tag{8.23}$$

with $\boldsymbol{r},\boldsymbol{s} \in \{\boldsymbol{p},\boldsymbol{q},\boldsymbol{p}+\boldsymbol{q}\}$. This is advantageous when following the algorithm outlined in [163]. Note that the $\boldsymbol{Q}_p$ from above are a special case of $\boldsymbol{Q}_r$. These scalar products are computed initially for a given configuration of wave vectors $\boldsymbol{r}$ which generically enter the kernels and vertices (for the power spectrum) as

$$\boldsymbol{r} = \sum_{n=1}^{L} c_n \boldsymbol{Q}_n + c_{L+1}\boldsymbol{k} \tag{8.24}$$

corresponding to a single evaluation of the integrand for the loop evaluation, with coefficients $c_n = 0,\pm 1$ and loop wavenumbers $\boldsymbol{Q}_{1\ldots L}$ at L-loop order. The additional c_{L+1} is the coefficient in front of the external wavenumber $\boldsymbol{k}$. In case of the bispectrum we would have a further coefficient c_{L+2} for in total two external wavenumbers $\boldsymbol{k}_1,\boldsymbol{k}_2$. For a given $\boldsymbol{r}$ we define the corresponding $\boldsymbol{Q}_r$ entering the definition of the transverse basis as a possible vector within the set $\mathcal{B} = \{\boldsymbol{k},\boldsymbol{Q}_1,\ldots,\boldsymbol{Q}_L\}$ (or $\mathcal{B} = \{\boldsymbol{k}_1,\boldsymbol{k}_2,\boldsymbol{Q}_1,\ldots,\boldsymbol{Q}_L\}$ for the bispectrum) that has the largest projection within the plane perpendicular to $\boldsymbol{r}$, i.e. for which $s^2_{rQ} = 1 - \frac{(\boldsymbol{r}\cdot\boldsymbol{Q})^2}{r^2Q^2}$ is maximal out of all $\boldsymbol{Q}_r \in \mathcal{B}$.

Altogether, this allows for an efficient implementation of vertices involving vector modes, in particular when two or more vector modes are involved. This treatment is based on [161–163, 180]. In practice, we define projection functions entering the vertices involving vector modes which are e.g. given by

$$\begin{aligned}
V^{p1}_{1,pq} &\equiv (\boldsymbol{p}\times\boldsymbol{q})\cdot\boldsymbol{b}_{p1} = \mathcal{N}_{p1}\left(p^2(\boldsymbol{q}\cdot\boldsymbol{Q}_p) - (\boldsymbol{p}\cdot\boldsymbol{Q}_p)(\boldsymbol{q}\cdot\boldsymbol{p})\right)\,,\\
V^{p2}_{1,pq} &\equiv (\boldsymbol{p}\times\boldsymbol{q})\cdot\boldsymbol{b}_{p2} = \mathcal{N}_{p2}p^2 D_{pq}\,,\\
V^{q1}_{1,pq} &\equiv (\boldsymbol{p}\times\boldsymbol{q})\cdot\boldsymbol{b}_{q1} = -V^{q1}_{1,qp}\,,\\
V^{q2}_{1,pq} &\equiv (\boldsymbol{p}\times\boldsymbol{q})\cdot\boldsymbol{b}_{q2} = -V^{q2}_{1,qp}\,,\\
V^{k1}_{1,pq} &\equiv \boldsymbol{P}_{k1}\cdot(\boldsymbol{p}\times\boldsymbol{q}) = \frac{1}{\mathcal{N}_{k1}}\frac{k(\boldsymbol{k}\cdot\boldsymbol{Q}_k) - (\boldsymbol{k}\cdot\boldsymbol{q})(\boldsymbol{Q}_k\cdot\boldsymbol{p})}{k^2Q_k^2 - (\boldsymbol{k}\cdot\boldsymbol{Q}_k)^2}\,,\\
V^{k2}_{1,pq} &\equiv \boldsymbol{P}_{k2}\cdot(\boldsymbol{p}\times\boldsymbol{q}) = \frac{1}{\mathcal{N}_{k2}}\frac{D_{kq}}{k^2Q_k^2 - (\boldsymbol{k}\cdot\boldsymbol{Q}_k)^2}\,,
\end{aligned} \tag{8.25}$$

which contribute at one-loop, with $\boldsymbol{k} = \boldsymbol{p}+\boldsymbol{q}$ and $\boldsymbol{P}_{k\alpha} = \boldsymbol{b}_{p+q\alpha}/|\boldsymbol{b}_{p+q\alpha}|^2$. Then the vertices can e.g. be written as

$$\begin{aligned}
\gamma_{\delta w_{p\alpha}\delta}(\boldsymbol{p},\boldsymbol{q}) &= \gamma_{Aw_{p\alpha}A}(\boldsymbol{p},\boldsymbol{q}) = \frac{1}{2}\frac{V^{p\alpha}_{1,pq}}{p^2}\,,\\
\gamma_{w_{k\alpha}Ag}(\boldsymbol{p},\boldsymbol{q}) &= -\frac{1}{2}\frac{\boldsymbol{p}\cdot\boldsymbol{q}}{q^2}V^{k\alpha}_{1,pq}\,,
\end{aligned} \tag{8.26}$$

in terms of the projection functions in the transverse basis with $\alpha = 1, 2$, and we refer to Appendix C for the remaining projection functions and vertices which contribute also at two-loop.

In the following we are armed with a treatment that allows us to capture vorticity and vector mode generation at one- and two-loop order while for the former the simplified treatment with only one single degree of freedom for each vector mode is sufficient, for the latter we need to use the general case with two independent degrees of freedom for each vector mode. This means that the corresponding kernels entering at one-loop only one unique result suffices to track vorticity and vector modes. However when going to kernels relevant at two-loop order (or one-loop order for bispectrum) we have to account for two solutions for each kernel, which we present below. In particular, the vorticity power spectrum up to two-loop order can be computed as

$$P_{w_i w_i} = P_{w_1 w_1} + P_{w_2 w_2} \,, \tag{8.27}$$

where the cross terms $w_1 w_2 = w_2 w_1 = 0$ vanish by construction. Note that this definition is in general true also at one-loop when using the transverse basis. Regarding the tensor mode, we will only use the simplified treatment tracking one effective tensor mode as we only consider one-loop corrections for tensor mode generation in the remaining part of the work.

8.3 Vorticity generation at second order

At second order in perturbation theory one observes nonlinear vorticity generation [166]. It arises from the coupling of two scalar modes which similarly generates the vector modes of the dispersion tensor. The form of the involved vertices is presented in the previous section. The evolution equations for the corresponding kernels are given by

$$\begin{aligned} \left(\partial_\eta + \frac{5}{2}\right) F_{2,w_i}(\boldsymbol{p},\boldsymbol{q},\eta) + (\boldsymbol{p}+\boldsymbol{q})^2 F_{2,\nu_i}(\boldsymbol{p},\boldsymbol{q},\eta) &= \gamma_{w_i bc}(\boldsymbol{p},\boldsymbol{q}) F_{1,b}(p,\eta) F_{1,c}(q,\eta) \,, \\ (\partial_\eta + 3)\, F_{2,\nu_i}(\boldsymbol{p},\boldsymbol{q},\eta) - \epsilon(\eta) F_{2,w_i}(\boldsymbol{p},\boldsymbol{q},\eta) &= \gamma_{\nu_i bc}(\boldsymbol{p},\boldsymbol{q}) F_{1,b}(p,\eta) F_{1,c}(q,\eta) \,. \end{aligned} \tag{8.28}$$

The list of potential vertices for vorticity is $\gamma_{w_i A g}$, $\gamma_{w_i A \epsilon}$, $\gamma_{w_i A \nu_j}$, $\gamma_{w_i A t_{jk}}$, $\gamma_{w_i \theta w_j}$, $\gamma_{w_i w_j w_k}$, and for the vector mode $\gamma_{\nu_i \theta g}$, $\gamma_{\nu_i \theta \epsilon}$, $\gamma_{\nu_i w_j g}$, $\gamma_{\nu_i w_j \epsilon}$, $\gamma_{\nu_i \theta \nu_j}$, $\gamma_{\nu_i \theta t_{jk}}$, $\gamma_{\nu_i w_j \nu_k}$, $\gamma_{\nu_i w_j t_{k\ell}}$. When considering the solution of second order kernels then the linear kernels $F_{1,b}$ and $F_{1,c}$ can contribute if b and c are scalars. Thus, only $\gamma_{w_i A g}$, $\gamma_{w_i A \epsilon}$ and $\gamma_{\nu_i \theta g}$, $\gamma_{\nu_i \theta \epsilon}$ contribute at second order, and describe the generation of vorticity and vector modes from two scalar perturbations at nonlinear level. The linear mixing of both vector fields is contained on the left-hand side of Eq. (8.28). The leading contribution, i.e. the one-loop of the vorticity power spectrum then has only one contribution, given by

$$P^{1L}_{w_i w_i}(k,\eta) = 2 e^{4\eta} \int \mathrm{d}^3 q \, F_{2,w_i}(\boldsymbol{k}-\boldsymbol{q},\boldsymbol{q},\eta) F_{2,w_i}(\boldsymbol{k}-\boldsymbol{q},\boldsymbol{q},\eta) P_0(|\boldsymbol{k}-\boldsymbol{q}|) P_0(q) \,. \tag{8.29}$$

There are analogous expressions for the vector power spectra and their cross spectrum. In addition, we will see below that it is in fact necessary to include the two-loop correction in order to get the correct scaling for $k \to 0$, see Sec. 8.4 and Sec. 9.4. But first we discuss the kernels entering the one-loop contribution, i.e. $F_{2,w_i/\nu_i}(\boldsymbol{k}-\boldsymbol{q},\boldsymbol{q},\eta)$.

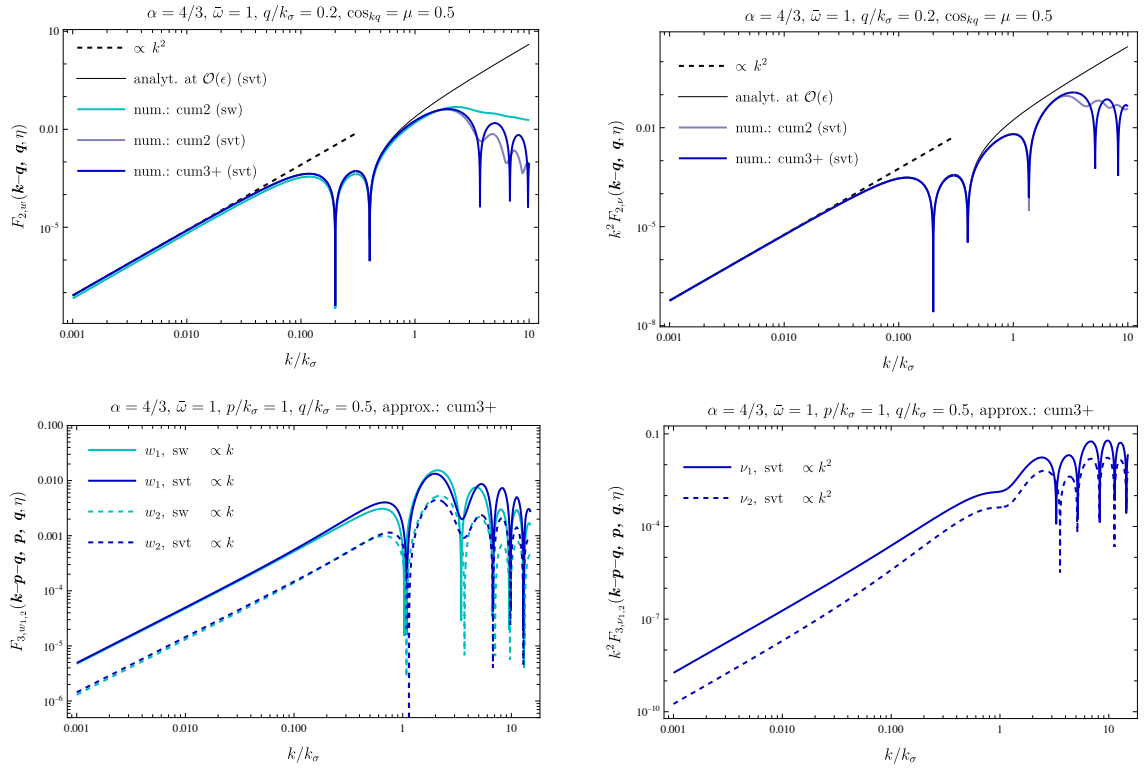

Figure 8.2: Nonlinear VPT kernels for the vorticity F_{n,w_i} (left column) and the vector mode of the dispersion tensor $k^2 F_{n,\nu_i}$ (right column). The second order kernels ($n = 2$) shown in the upper panels commonly scale as $\propto k^2$. At this order, both kernels point in the direction perpendicular to the plane spanned by $\boldsymbol{k}$ and $\boldsymbol{q}$, and we show its projection on $\boldsymbol{k} \times \boldsymbol{q}/|\boldsymbol{k} \times \boldsymbol{q}|$. The kernels are shown for various approximation schemes as indicated in the legend (see Table 7.1). In addition, when showing the third order kernels ($n = 3$) entering the two-loop power spectrum we show the two independent modes perpendicular $\boldsymbol{k}$, finding that $F_{3,w_{k1,2}} \propto k$ for $k \to 0$, similarly to θ (see Sec. 7.3). When comparing **sw** $\leftrightarrow$ **svt** in the left panels we find a noticeable impact of the vector mode on vorticity for $k \gtrsim k_\sigma$, while the impact of third cumulant perturbations (**cum2** $\leftrightarrow$ **cum3+**) is relatively mild for vorticity and vector mode kernels in the upper row. The analytical results Eqs. (8.30) and (8.32) at first order in ϵ are shown as thin black lines, and agree well for $k \ll k_\sigma$. In SPT all these kernels are zero. For the figure we chose $\epsilon = \epsilon_0 e^{\alpha\eta}$ with $\alpha = 4/3$, and $c_{kp} = 0.3, c_{kq} = 0.5, c_{pq} = 0.875, p = k_\sigma, q = 0.5 k_\sigma$, where $k_\sigma = 1/\sqrt{\epsilon_0}$. Reprinted from [98].

Analytical results for $\epsilon \to 0$

Let us first discuss an analytical expression within the second cumulant approximation (**cum2**) for the vorticity when expanding in powers of ϵ, similar as for the kernels of the scalar modes in Sec. 7.1. Recalling the results of Sec. 5.3 we expect both vorticity and the vector mode to be generated at first order in ϵ. Thus, the term $\epsilon F_{2,w_i}$ can be neglected at $\mathcal{O}(\epsilon)$ and we can solve the equation for $\nu_{k,i}$ independently, giving

$$F_{2,\nu_i}(\boldsymbol{p},\boldsymbol{q},\eta) = 2\left(\gamma_{\nu_i\theta g}(\boldsymbol{p},\boldsymbol{q}) + \gamma_{\nu_i\theta g}(\boldsymbol{q},\boldsymbol{p})\right) \int^{\eta} \mathrm{d}\eta' e^{3(\eta'-\eta)} \int^{\eta'} \mathrm{d}\eta'' \, e^{2(\eta''-\eta')} \epsilon(\eta'') + \mathcal{O}(\epsilon^2)\,, \quad (8.30)$$

where we used the fact that $F_{1,\delta\epsilon}$ starts at order ϵ^2 (for **cum2**), so only the vertex $\gamma_{\nu_i\theta g}$ is relevant. Inserting this result into the vorticity equation and using that only $\gamma_{w_i Ag}$ contributes gives the first order correction for the vorticity, given by

$$\begin{aligned} F_{2,w_i}(\boldsymbol{p},\boldsymbol{q},\eta) &= -(\boldsymbol{p}+\boldsymbol{q})^2 \int^\eta \mathrm{d}\eta' e^{\frac{5}{2}(\eta'-\eta)} F_{2,\nu_i}(\boldsymbol{p},\boldsymbol{q},\eta') \\ &\quad + 2(\gamma_{w_i Ag}(\boldsymbol{p},\boldsymbol{q}) + \gamma_{w_i Ag}(\boldsymbol{q},\boldsymbol{p})) \int^\eta \mathrm{d}\eta' e^{\frac{5}{2}(\eta'-\eta)} \int^{\eta'} \mathrm{d}\eta'' \, e^{2(\eta''-\eta')}\epsilon(\eta'') + \mathcal{O}(\epsilon^2)\,. \end{aligned} \tag{8.31}$$

Then we can explicitly insert the form of the vertices given in Appendix B to obtain

$$F_{2,w_i}(\boldsymbol{p},\boldsymbol{q},\eta) = \frac{(\boldsymbol{p}\times\boldsymbol{q})_i(\boldsymbol{p}\cdot\boldsymbol{q})\,(q^2-p^2)}{p^2q^2}\, J^w(\eta) + \mathcal{O}(\epsilon^2)\,, \tag{8.32}$$

with

$$\begin{aligned} J^w(\eta) &= \int^\eta \mathrm{d}\eta' e^{\frac{5}{2}(\eta'-\eta)} \left[\int^{\eta'} \mathrm{d}\eta'' \, e^{2(\eta''-\eta')}\epsilon(\eta'') + \int^{\eta'} \mathrm{d}\eta'' e^{3(\eta''-\eta')} \int^{\eta''} \mathrm{d}\eta''' \, e^{2(\eta'''-\eta'')}\epsilon(\eta''') \right] \\ &= 4E_2(\eta) - 6E_{5/2}(\eta) + 2E_3(\eta)\,, \end{aligned} \tag{8.33}$$

using Eq. (7.4). The combination of the integrals in the second summand (in the first line) would be missed when neglecting the vector mode, corresponding to the approximation scheme **sw**. We also know from Sec. 8.2 that vorticity and vector mode are perpendicular to the plane spanned by the wave vectors $\boldsymbol{p}$ and $\boldsymbol{q}$. Thus, the vectorial factor $(\boldsymbol{p}\times\boldsymbol{q})_i$ can be projected with $(\boldsymbol{p}\times\boldsymbol{q})_i/|\boldsymbol{p}\times\boldsymbol{q}|$ in order to use the effective vorticity mode w_{eff}. In addition, the vorticity kernel $F_{2,w_i}(\boldsymbol{k}-\boldsymbol{q},\boldsymbol{q},\eta)$ scales as k^2 for $\boldsymbol{k}\to 0$. This can be checked from the analytical result Eq. (8.32) at order ϵ. This analytical result can in turn be inserted in the one-loop integral Eq. (8.29) giving a dependence on the loop wavenumber which agrees with Eq. (70) in [68]. However in general we do not expand in powers of ϵ and within our numerical results (see below) we effectively collect *all* orders in ϵ and fully consider the impact of the vector mode on vorticity.

Numerical results

Similarly as for the scalar kernels one can solve the differential equation for the vorticity and vector mode of the dispersion tensor numerically. Using the treatment presented in Sec. 8.2 for the second order kernels entering the one-loop correction $F_{2,w}(\boldsymbol{k}-\boldsymbol{q},\boldsymbol{q},\eta)$ and $F_{2,\nu}(\boldsymbol{k}-\boldsymbol{q},\boldsymbol{q},\eta)$ we get results shown in the upper left and right panels of Fig. 8.2, respectively, and we used the short-hand notation $w \equiv w_{\mathrm{eff}}$ and $\nu \equiv \nu_{\mathrm{eff}}$. The agreement with the analytical results given above is well within the regime $k \lesssim k_\sigma$. In addition, the scaling $F_{2,w}(\boldsymbol{k}-\boldsymbol{q},\boldsymbol{q},\eta) \propto k^2$ for $k\to 0$ holds also for the numerical result. For the vector mode, we show the dimensionless quantity $k^2F_{2,\nu}$ which also scales as k^2 indicating that the kernel for the vector mode itself is constant in the large-scale limit which is in accordance with kernels for the scalar modes of the dispersion tensor, see Fig. 7.5. The simplest approximation involving vorticity generation corresponds to **sw** in the second cumulant approximation **cum2**. We observe that when including in addition the impact of the vector mode a slight horizontal shift at all scales and a moderate modification for $k \gtrsim k_\sigma$. Taking also scalar modes of the third cumulant into account, denoted by **cum3+**, a further impact arises for scales $k \gtrsim 2k_\sigma$ for the vorticity and at $k \gtrsim k_\sigma$ for the vector mode. Note

that using the scheme **svt** is equivalent to **sv** as one needs the latter to capture vector mode generation while the former does not contribute to $F_{2,w}$ and $F_{2,\nu}$. We adopted the simplified numerical treatment valid at one-loop introduced in Sec. 8.2 for the results in the upper panels.

8.4 Vorticity generation at third order

Also for the vorticity, we find in general that it scales with the first power of the total wavenumber,

$$F_{n,w_i}(\boldsymbol{k}_1,\ldots,\boldsymbol{k}_n,\eta) \propto k, \qquad \boldsymbol{k}=\sum_i \boldsymbol{k}_i \to 0\,. \tag{8.34}$$

Similarly as for the velocity divergence it only appears starting at two-loop order, i.e. for kernels F_{n,w_i} with $n \geq 3$ while $F_{2,w_i} \propto k^2$ as for the velocity divergence, see Fig. 7.4. In the lower left panel of Fig. 8.2 we show the kernel $F_{3,w_i}(\boldsymbol{k}-\boldsymbol{p}-\boldsymbol{q},\boldsymbol{p},\boldsymbol{q},\eta)$ entering the two-loop correction versus k for both vorticity modes w_{k1} and w_{k2} perpendicular to $\boldsymbol{k}$. In addition, we compared the approximations **sw** and **sv** where the impact of the vector modes of the dispersion tensor is only included in the latter scheme. We observe a minor impact also for this kernel. Using the transverse basis introduced in Sec. 8.2 we find that the mode in the direction of $\boldsymbol{b}_{k1}$ has a higher amplitude than its perpendicular counterpart. Most importantly, the linear scaling in k is shown for all cases and agrees with analogous results for the velocity divergence θ. However when $\boldsymbol{p}+\boldsymbol{q}=0$ the scaling would be $\propto k^2$. In particular, this implies that the corresponding contribution to the power spectrum, i.e. the two-loop vorticity power spectrum scales as

$$P_{w_iw_i}(k,\eta) \propto k^2\,, \tag{8.35}$$

for $k \ll k_\sigma$ and can be computed according to Eq. (8.27). However, since $F_{2,w_i} \propto k^2$, *this scaling can only be observed starting at two-loop order*, while $P^{1L}_{w_iw_i}(k,\eta) \propto k^4$ at one-loop. This behavior will be confirmed in Sec. 9.4 where we compare our results to measurements of the vorticity power spectrum in numerical simulations.

In contrast to the vorticity, the analogous kernel for the vector mode approaches a constant for $k \to 0$ such that the dimensionless kernels scale as $k^2F_{n,\nu_i} \propto k^2$ even for $n \geq 3$ where both independent modes ν_{k1} and ν_{k2} are shown in the lower right panel of Fig. 8.2 which confirms this scaling.

8.5 Generation of tensor modes

We know from above that the impact of the tensor mode on the nonlinear kernels for the density contrast and velocity divergence is very small, see Fig. 7.2, in contrast to the impact of vorticity and vector modes on the density. Therefore, in practice tensor modes can be neglected when interested in the density or velocity divergence, see Ch. 9. However, the generation of tensor modes due to nonlinear coupling of scalar modes gives rise to a tensor power spectrum which interestingly sources a stochastic background of gravitational waves, see Ch. 10. Therefore, it may be interesting to study its generation. As for the vector modes, the leading contribution arises from the second order kernel which satisfies,

$$(\partial_\eta+3)F_{2,t_{ij}}(\boldsymbol{p},\boldsymbol{q},\eta) = \gamma_{t_{ij}bc}(\boldsymbol{p},\boldsymbol{q})F_{1,b}(p,\eta)F_{1,c}(q,\eta)\,, \tag{8.36}$$

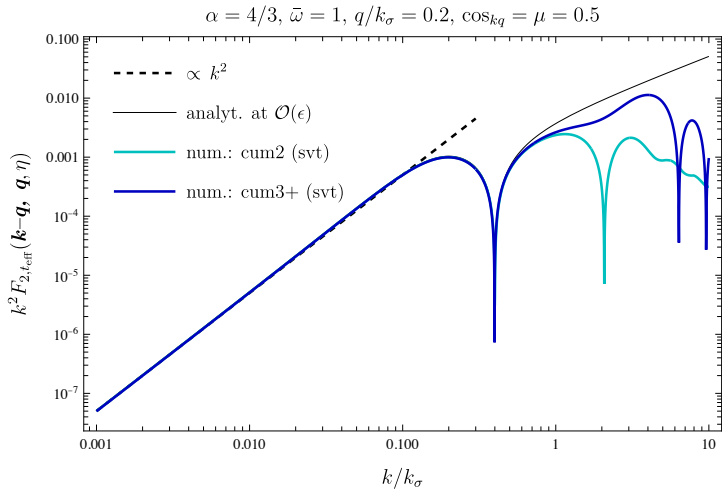

Figure 8.3: Second order kernel for the effective tensor mode in dimensionless units such that $k^2 F_{2,t_{\rm eff}} \propto k^2$ for $k \to 0$ (black dashed). The scheme **svt** is needed in order to take tensor modes into account and the inclusion of third cumulant perturbations (**cum3+**) shows an impact at $k \gtrsim k_\sigma$. For comparison, the analytical result is shown as thin black line. Reprinted from [98].

giving rise to a tensor power spectrum at one-loop,

$$P^{1L}_{t_{ij}t_{ij}}(k,\eta) = 2e^{4\eta} \int \mathrm{d}^3 q\, F_{2,t_{ij}}(\boldsymbol{k}-\boldsymbol{q},\boldsymbol{q},\eta) F_{2,t_{ij}}(\boldsymbol{k}-\boldsymbol{q},\boldsymbol{q},\eta) P_0(|\boldsymbol{k}-\boldsymbol{q}|) P_0(q)\,. \tag{8.37}$$

The relevant vertices which could potentially contribute are $\gamma_{t_{ij}\theta g}$, $\gamma_{t_{ij}\theta\epsilon}$, $\gamma_{t_{ij}w_k g}$, $\gamma_{t_{ij}w_k\epsilon}$, $\gamma_{t_{ij}\theta\nu_k}$, $\gamma_{t_{ij}\theta t_{k\ell}}$, $\gamma_{t_{ij}w_k\nu_\ell}$, $\gamma_{t_{ij}w_k t_{\ell m}}$. As before, $F_{1,b}$ and $F_{1,c}$ are only nonzero for scalar modes which means that only the vertices

$$\begin{aligned}
\gamma_{t_{ij}\theta g}(\boldsymbol{p},\boldsymbol{q}) &= -\frac{1}{2}\frac{(\boldsymbol{p}\times\boldsymbol{q})^2\,\boldsymbol{p}\cdot\boldsymbol{q}}{2(\boldsymbol{p}+\boldsymbol{q})^2 p^2 q^2}\, f_{ij}(\boldsymbol{p},\boldsymbol{q})\,, \\
\gamma_{t_{ij}\theta\epsilon}(\boldsymbol{p},\boldsymbol{q}) &= \frac{1}{2}\frac{(\boldsymbol{p}\times\boldsymbol{q})^2}{(\boldsymbol{p}+\boldsymbol{q})^2 p^2}\, f_{ij}(\boldsymbol{p},\boldsymbol{q})\,,
\end{aligned} \tag{8.38}$$

contribute to $F_{2,t_{ij}}$ and f_{ij} is defined in Eq. (8.14).

There is also an analytical result for the second order kernel at first order in ϵ. At this order, only the vertex $\gamma_{t_{ij}\theta g}$ contributes since $F_{1,\delta\epsilon} \propto \epsilon^2$. For $F_{1,g}$ we use the analytical result at $\mathcal{O}(\epsilon)$ given in Eq. (7.3) and use $F_{1,\theta} \to 1$, giving

$$F_{2,t_{ij}}(\boldsymbol{p},\boldsymbol{q},\eta) = 2(\gamma_{t_{ij}\theta g}(\boldsymbol{p},\boldsymbol{q}) + \gamma_{t_{ij}\theta g}(\boldsymbol{q},\boldsymbol{p})) \int^\eta \mathrm{d}\eta' e^{3(\eta'-\eta)} \int^{\eta'} \mathrm{d}\eta''\, e^{2(\eta''-\eta')}\epsilon(\eta'') + \mathcal{O}(\epsilon^2)\,. \tag{8.39}$$

In Fig. 8.3 we show the analytical result using the treatment of the effective tensor mode defined by

$$F_{2,t_{ij}}(\boldsymbol{p},\boldsymbol{q},\eta) = F_{2,t_{\rm eff}}(\boldsymbol{p},\boldsymbol{q},\eta)\, f_{ij}\,, \tag{8.40}$$

where the index-dependence is factored out which was discussed in Sec. 8.2. Furthermore, we show the dimensionless kernel $k^2 F_{2,t_{\rm eff}}$ along with the numerical result which scales as k^2 for $k \to 0$ such that the effective tensor mode kernel approaches a constant in the large-scale limit,

analogously as for the vector mode of the stress tensor, shown in Fig. 8.2. In both cases the same scaling is expected when going to higher order in perturbation theory such that no modification is expected when going beyond one-loop order. Here we also observe that modifications within **cum3+** only occur for $k \gtrsim k_\sigma$, as for the vector mode (see Fig. 8.2).

In total, $P_{t_{ij}t_{ij}}(k,\eta)$ approaches a constant for $k \to 0$ at all loop orders. For the dimensionless tensor power spectrum, this means that $k^4 P_{t_{ij}t_{ij}}(k,\eta) \propto k^4$ for $k \to 0$. Note that

$$P_{t_{ij}t_{ij}}(k,\eta) \equiv 2P_{t_{\rm eff}t_{\rm eff}}(k,\eta)\,. \tag{8.41}$$

As mentioned above, the nonlinear generation of tensor modes of the stress tensor constitute a *stochastic background of gravitational waves* whose frequency is related to the wavenumber k. Thus, this background exists at ultra-low frequencies related to the dispersion scale $f_{\rm gw} \sim ck_\sigma/(2\pi) \simeq 1.5 \cdot 10^{-15}\,h$ Hz $\times(k_\sigma/(1h/{\rm Mpc}))$. In addition, due to the nonrelativistic velocities of order $\mathcal{H} \times \sqrt{\epsilon} \simeq 100{\rm km/s} \times \sqrt{\epsilon}/({\rm Mpc}/h)$ the amplitude of the gravitational wave background is expected to be tiny. The detailed calculation of this background is presented in Ch. 10.

9 VPT predictions vs Simulations

In this chapter we finally present results for the power spectra for the density $P_{\delta\delta}$ (Sec. 9.1) and velocity divergence $P_{\theta\theta}$ including their cross spectrum $P_{\delta\theta}$ (Sec. 9.2), as well as for the vorticity $P_{w_i w_i}$ (Sec. 9.4) and density bispectrum $B_{\delta\delta\delta}$ (Sec. 9.3) within the VPT framework where we compare all these spectra with N-body simulations.

We still focus on a scaling universe with input power spectrum $P_0 \propto k^{n_s}$ and consider spectral indices $n_s = 2, 1, 0, -1$, which refer to very blue initial spectra demonstrating the strong screening of UV modes as already seen at the level of the kernels when taking velocity dispersion and higher cumulants into account. Note that within SPT the one-loop integrals become UV-divergent for $n_s \geq -1$, i.e. there are no predictions coming from SPT beyond tree-level for our choice of spectral indices. We will see below that this shortcoming is remedied in VPT.

For our results we use the schemes (**cum3+**, **svt**) by default denoting our *fiducial choice* and compare it against various other approximation schemes (see Table 7.1). As before, it includes apart from δ and θ the vorticity w_i, all scalar $(g, \delta\epsilon)$ vector (ν_i) and tensor (t_{ij}) modes of the second cumulant along its background value $\epsilon(\eta)$, as well as the scalar (π, χ) modes of the third cumulant including the background value of the fourth cumulant $\omega(\eta)$.

Finally, in Ch. 10 we predict a stochastic gravitational wave background which is related to the tensor power spectrum $P_{t_{ij}t_{ij}}$ within a more realistic ΛCDM universe.

9.1 Density power spectrum

Now, we start with the observationally most accessible quantity, i.e. the power spectrum of the matter density contrast $P_{\delta\delta}(k, \eta)$. We compute the linear plus one-loop correction involving kernels $F_{1,\delta}(k, \eta)$, $F_{2,\delta}(\boldsymbol{k}-\boldsymbol{q}, \boldsymbol{q}, \eta)$ and $F_{3,\delta}(\boldsymbol{k}, \boldsymbol{q}, -\boldsymbol{q}, \eta)$ which are numerically solved within VPT and finally we compare to N-body results. Scaling symmetry implies

$$\epsilon(\eta) = \epsilon_0\, e^{4\eta/(n_s+3)}\,, \qquad \bar{\omega} = \frac{\omega(\eta)}{\epsilon(\eta)^2} = \text{ const.} \tag{9.1}$$

as before, which means that the only free parameters, apart from n_s, are ϵ_0 and $\bar{\omega}$, where the latter has only a minor impact, as shown below. In addition, we use the value for $\bar{\omega}$ obtained when self-consistently solve its evolution equation in linear approximation, as already done for various cumulant truncations in Sec. 6.2. In particular, see Table 6.1 from which one is able to extract the fiducial values we are using here,

$$\bar{\omega}_{\text{fid}} = 0.579, \quad 0.616, \quad 0.668, \quad 0.752\,, \tag{9.2}$$

for $n_s = 2, 1, 0, -1$, respectively and using $\bar{\omega} = 5\bar{\mathcal{E}}_4/3$ as well as $c_{\max} = 3$. However, below we also study the behavior for different $\bar{\omega}$ for each n_s. Altogether, the *only remaining dimensional parameter* is $\epsilon_0 \equiv 1/k_\sigma^2$, which we quantify by the ratio k_σ/k_{nl}, see also Sec. 6.2. Below, we

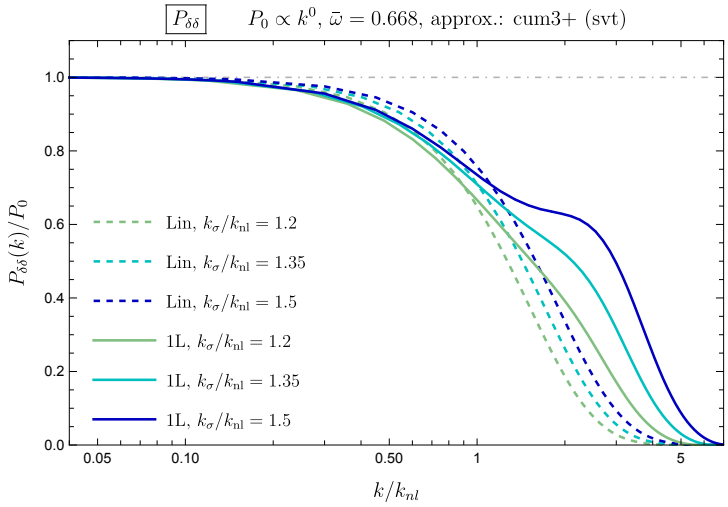

Figure 9.1: Density power spectrum $P_{\delta\delta}(k,\eta)$ relative to the power-law input power spectrum $P_0(k,\eta) \propto k^{n_s}$ versus $k/k_{\rm nl}$. It is computed in linear (dashed) and one-loop (solid) approximation for various values of the background dispersion $\epsilon_0 = 1/k_\sigma^2$ with $\epsilon(\eta) = \epsilon_0 e^{4\eta/(n_s+3)}$. The linear kernel $F_{1,\delta}(k,\eta)$ as well as the nonlinear kernels $F_{2,\delta}(\boldsymbol{k}-\boldsymbol{q},\boldsymbol{q},\eta)$ and $F_{3,\delta}(\boldsymbol{k},\boldsymbol{q},-\boldsymbol{q},\eta)$ enter the power spectrum using third cumulant scalar perturbations in addition to vorticity, vector and tensor modes of the stress tensor (**cum3+**, **svt**). Scaling symmetry also implies a constant value of the dimensionless ratio of the fourth cumulant background value $\bar{\omega} = \omega(\eta)/\epsilon(\eta)^2$, given in the legend. Reprinted from [99].

discuss further approaches involving perturbation theory and halo modeling, how to determine the ratio of dispersion to the nonlinear scale. Remarkably, these distinct determinations yield a value for $k_\sigma/k_{\rm nl}$ within a common range $\sim 1-2$. For our computation we use determinations from fitting the density power spectrum, which in turn give values lying in the same range, as shown below.

In Fig. 9.1 we show the density power spectrum in linear approximation (dashed lines) and when including the one-loop correction (solid lines) based on the (**cum3+**, **svt**) scheme within VPT. They are shown for three different values of $k_\sigma/k_{\rm nl}$ (using as external input without fitting[1]) with $n_s = 0$. The result is normalized to the linear SPT result $P_0(k,\eta) = e^{2\eta}k^{n_s}$. We can eliminate the time-dependence on η by showing the result $P_{\delta\delta}(k,\eta)/P_0(k,\eta)$ versus $k/k_{\rm nl}(\eta)$, thus we omit the time arguments for brevity.

Within the linear approximation, using $P_{\delta\delta}(k,\eta)/P_0(k,\eta) = F_{1,\delta}(k,\eta)^2$, we observe suppression relative to the linear SPT result being unity, which is more pronounced for larger values of the background dispersion ϵ, i.e. for smaller k_σ, as expected. When adding the one-loop correction there is a slightly stronger suppression for $k \lesssim k_{\rm nl}$ and enhancement of the power spectrum relative to linear VPT for $k \gtrsim k_{\rm nl}$, more significantly for higher k_σ. This tells us that the one-loop piece is first negative and then turns positive. This sign change occurs at larger k values when increasing k_σ. Nevertheless, within the regime $k \lesssim \mathcal{O}(k_{\rm nl})$ both linear as well as one-loop approximation are close to each other, indicating the one-loop value being a small perturbative correction and guarantees perturbative stability. Note that there is no one-loop

[1] Note that scaling symmetry can be used to rescale numerical results for power- and bispectra for a given value of $k_\sigma/k_{\rm nl}$, meaning it is not necessary to recompute each result for different $k_\sigma/k_{\rm nl}$, see Ch. 6.

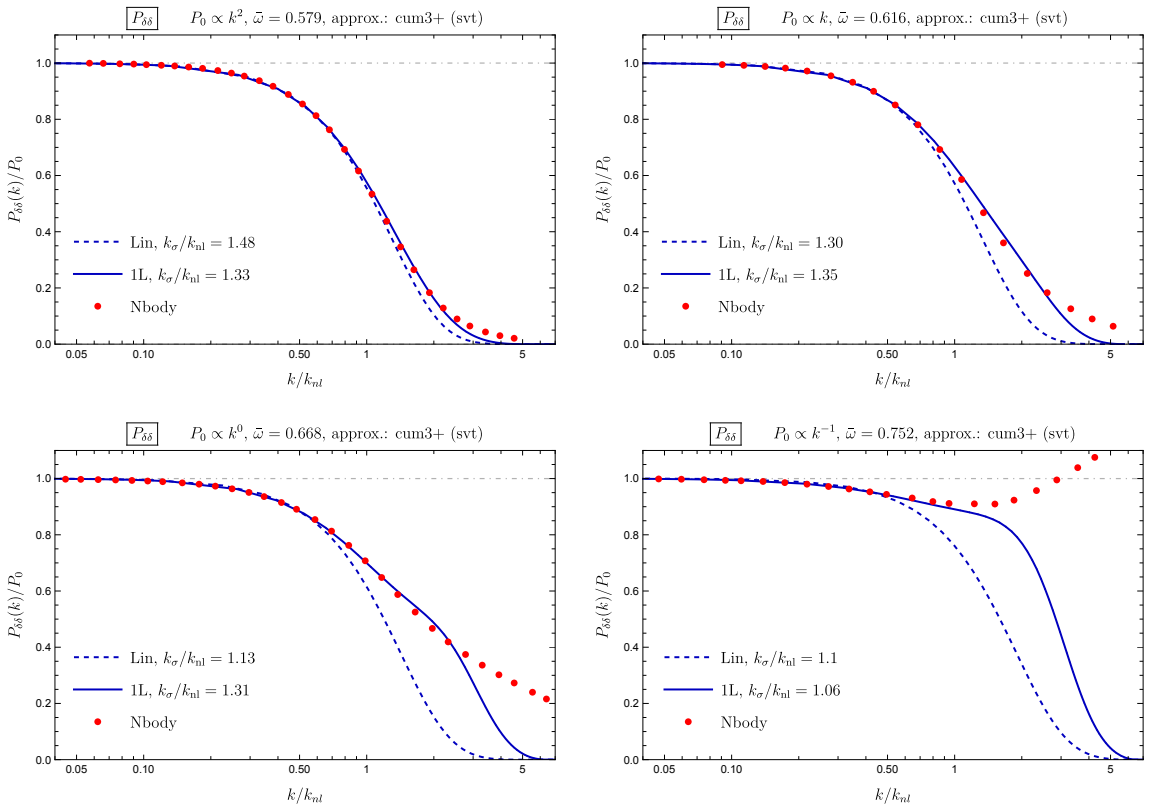

Figure 9.2: VPT density power spectrum $P_{\delta\delta}$ in linear (dashed) and one-loop (solid) approximation within **cum3+** (**svt**) compared to N-body simulations (red circles) for various spectral indices $n_s = 2, 1, 0, -1$. Here we adjusted the value of $k_\sigma/k_{\rm nl}$ by a one-parameter fit up to $k \leq k_{\rm max} = 0.6 k_{\rm nl}$ to match the N-body result, with best-fit values given in the legend for each case. Remarkably, the obtained values of $k_\sigma/k_{\rm nl}$ are consistent with our theoretical predictions, especially when involving one-loop corrections, see Table 9.1. In addition, we use the *same fixed* values of $k_\sigma/k_{\rm nl}$ as given for $P_{\delta\delta}$ when comparing VPT and N-body results for velocity spectra and bispectra below (for each approximation and n_s, respectively) such that for all these statistics there is only a single free parameter that is adjusted once to a common value. Reprinted from [99].

SPT result, since it is UV divergent for all $n_s \geq -1$. Furthermore, we checked that the one-loop integration is finite being a consequence of the screening of UV modes within VPT.

In addition, we performed N-body simulations in order to compare the VPT predictions. They were similarly performed for scaling universes with spectral indices $n_s = 2, 1, 0, -1$. In particular, two sets with 512^3 particles of fixed amplitude initial conditions with opposite phases in order to cancel Gaussian cosmic variance were used in the simulations. We refer to [99] for an extensive description, including tests of self-similarity, initial conditions, and computation of error bars, especially in Appendix F therein.

In Fig. 9.2 we then compare the N-body simulations (red circles) with the VPT linear (dashed) and one-loop (solid) approximation for each $n_s = 2, 1, 0, -1$. Note that the error bars are too small to be visible in $P_{\delta\delta}$. In contrast to Fig. 9.1, we did not choose the values of $k_\sigma/k_{\rm nl}$ by hand, but instead we adjusted the value by fitting the perturbative to the N-body result at

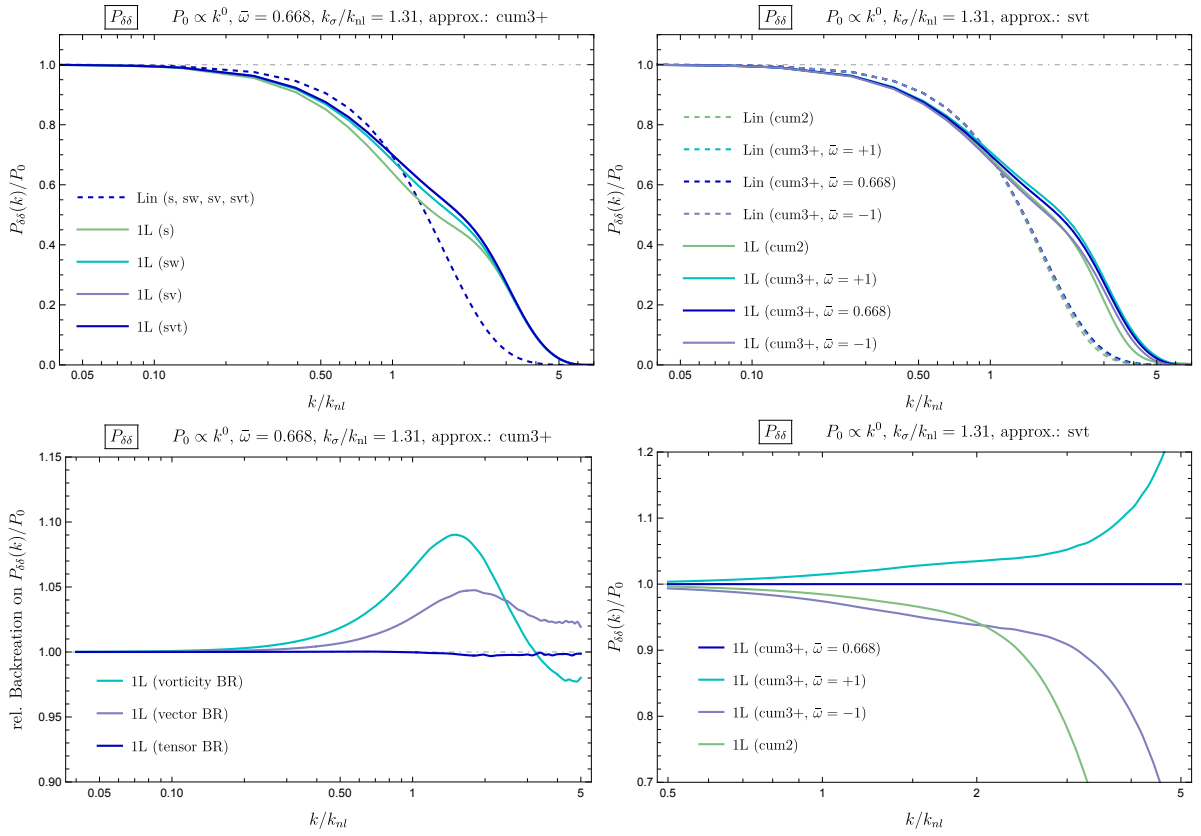

Figure 9.3: Left panels: impact of vorticity (**sw**), as well as vector and tensor back reactions of the stress tensor (**sv** and **svt**) on the density power spectrum $P_{\delta\delta}(k,\eta)$ in linear (dashed) and one-loop (solid) approximation (upper panels). As those back reactions enter through the kernel $F_{3,\delta}(\boldsymbol{k},\boldsymbol{q},-\boldsymbol{q},\eta)$ *all* linear curves are identical. In addition, as before, tensor modes are negligible. In the lower panels we show the ratios of the one-loop curves shown on the upper panel quantifying the corresponding back reactions. Right panels: impact of third cumulant perturbations (**cum2** vs **cum3+**) as well as sensitivity of magnitude of background value of fourth cumulant $\bar{\omega}$ with a common value $k_\sigma = 1.31 k_{\rm nl}$.

low wavenumbers, i.e. for $k \leq k_{\rm max} = 0.6 k_{\rm nl}$. Nevertheless, the approximation scheme (**cum3+**, **svt**) is identical in both figures and we emphasize that it is *not necessary* to determine the value of $k_\sigma/k_{\rm nl}$ (or the background dispersion) by matching to simulations. It only circumvents the difficulty to accurately determine the spatial average of the stress tensor being indeed a well-defined physical quantity whose evolution equation we are in principle able to solve, and is also done below.

It is also noteworthy that within our fitting procedure we use the *same value* of $k_\sigma/k_{\rm nl}$ obtained from the density power spectrum for all further comparisons including power- and bispectra. Thus, each value of $k_\sigma/k_{\rm nl}$ is keeping fixed for a given approximation scheme and n_s which further tests the viability of the fitting procedure. Moreover, the results are stable under changing $k_{\rm max}$ as long as it is below the nonlinear scale, which we have explicitly checked. Note that we adopted the optimal value of $k_\sigma/k_{\rm nl}$ for both the linear approximation as well as for the sum of linear and one-loop approximations, respectively, giving rise to two distinct values of

$k_\sigma/k_{\rm nl}$ for each panel with distinct spectral index n_s. This is helpful since one then has a direct observation of the improvement stemming from one-loop corrections. Remarkably, the obtained values of $k_\sigma/k_{\rm nl}$ are again within the expected range of $k_\sigma \sim (1-2)k_{\rm nl}$.

Indeed, the VPT density power spectrum can reproduce the N-body result up to $k \lesssim \mathcal{O}(k_{\rm nl})$ with significant improvement when adding the one-loop correction. In particular, the one-loop approximation gives values of $k_\sigma/k_{\rm nl}$ which are much less sensitive to n_s[2]. However, we observe that the agreement with N-body is better the larger n_s. This is a consequence, as already discussed for the kernels, that for higher initial power at small scales (large n_s) velocity dispersion and higher cumulants are quickly generated such that UV screening is most efficient and the small-scale sensitivity is most suppressed. Nevertheless, the linear approximation agrees with N-body up to $k \lesssim 0.5k_{\rm nl}$ which is also remarkable as it is only the square of the linear density kernel and hence very fast to compute. When interested in an improved determination of $k_\sigma/k_{\rm nl}$ one requires the one-loop approximation despite being a relatively small correction in both $k_\sigma/k_{\rm nl}$ and in $P_{\delta\delta}$ up to $k \lesssim k_{\rm nl}$, appropriate for a perturbative expansion.

Notwithstanding, the fitting procedure we are using potentially exaggerates the level of agreement and could obscure the importance of two-loop corrections, at least to some degree. We comment on the impact of the two-loop further below. In the following, we study the impact of various approximation schemes on the density power spectrum.

Impact of vorticity, vector and tensor modes

We first discuss how strong vorticity, as well as vector and tensor modes of the stress tensor impact the density contrast. Those back reactions enter the kernel $F_{3,\delta}(\boldsymbol{k},\boldsymbol{q},-\boldsymbol{q},\eta)$ in the one-loop integral. To assess the size of these back reactions, we show various results within approximations **s**, **sw**, **sv** and **svt** within scheme **cum3+** in Fig. 9.3 (upper left panel) for a fixed common value of $k_\sigma/k_{\rm nl}$ for all cases with $n_s = 0$, in analogy to Fig. 7.2 for a specific configuration of the third order kernel. Let us first focus on the left panels. Here we find a significant back reaction arising from vorticity, i.e. there is a sizeable shift between the one-loop results in the **s** and **sw** approximation. In turn, there is a further impact when turning on vector modes, i.e. going to the **sv** scheme with no further modifications coming from the tensor modes (**svt**). Note also that the scale at which the one-loop part turns positive is also affected by the different back reactions. The amount of those back reactions can be quantified when taking the ratio of the corresponding approximation scheme at one-loop, shown in Fig. 9.3 (lower left panel). To assess e.g. the impact of vorticity we take the ratio of power spectra as $P_{\delta\delta}^{(\mathbf{sw})}/P_{\delta\delta}^{(\mathbf{s})}$, and analogously for the other cases. We find around the nonlinear scale the vorticity back reaction amounts to 10% and vector back reaction to another 5% while the tensor back reaction is negligible (sub-percent), as expected. Overall, taking vorticity *and* vector modes of the stress tensor into account we find a modification of around 16% to density power spectrum at the nonlinear scale for $n_s = 0$. The magnitude of back reactions change for different n_s. For bluer indices $n_s = 1, 2$ the vorticity back reaction grows to about 15%, while for $n_s = -1$ it drops to 3%, reflecting again the effectiveness of velocity dispersion and higher cumulants for larger n_s.

As discussed in Sec. 7.3, it is necessary to include vorticity to ensure momentum conservation in general. However, when restricting to the one-loop approximation momentum conservation is also fulfilled within scheme **s**, i.e. without including vorticity. This is so, as shown in Sec. 7.3, all kernels relevant at one-loop have to satisfy momentum conservation due to symmetry regardless

[2] except for $n_s = -1$ where the two-loop corrections could be most important, see below.

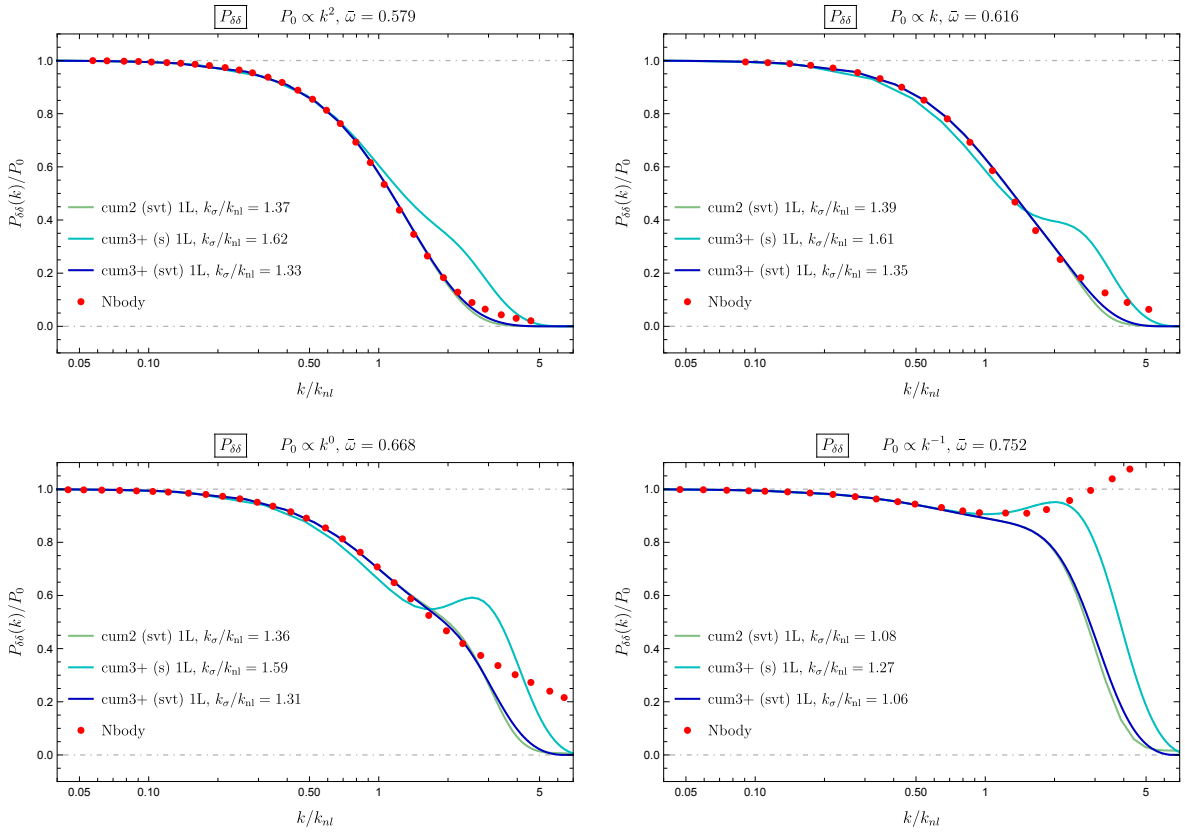

Figure 9.4: One-loop density power spectrum in VPT compared to N-body results for $n_s = 2, 1, 0, -1$ and three distinct approximation schemes. When using only scalar perturbations (**cum3+**, **s**) there is a significant difference to our fiducial case (**cum3+**, **svt**), including vorticity, vector and tensor modes. On the contrary, when only neglecting third cumulant perturbations (**cum2**, **svt**) we observe almost no difference in both best-fit values of $k_\sigma/k_{\rm nl}$ and $P_{\delta\delta}$ to the fiducial choice. This means that the impact of vorticity is important and required to take into account in order to get trustable results, while third cumulant yields a mild effect. Therefore one should use schemes **cum2/3+**, **sv(t)**. Reprinted from [99].

of the approximation scheme. However when going to two-loop inclusion of vorticity is actually required. Therefore, we find $P_{\delta\delta}/P_0 \to 1$ for $k \to 0$, also for scheme **s** at one-loop, and the vorticity back reaction becomes noticeable at $k \gtrsim 0.3k_{\rm nl}$.

One may wonder, why these back reactions become less important for even smaller scales. The reason behind this is that the impact of vorticity plus vector and tensor modes of the stress tensor becomes relevant for $q \gtrsim k$ (or $q \gtrsim k_\sigma$ if $k_\sigma > k$). The impact of loop wavenumbers with $q > k$ on the one-loop result diminishes as k rises, attributed to UV screening within VPT. Consequently, the vorticity backreaction vanishes for high-k in the one-loop contribution. Therefore all lines in the upper left panel of Fig. 9.3 lie on top of each other and the back reactions in the lower left panel become negligible for $k \gtrsim 3k_{\rm nl}$. This is also in line with the vorticity back reaction shown in Fig. 7.2 and Fig. 7.6. However, one expects that two- and higher loops are relevant at these scales which are in turn affected by vorticity back reaction. Overall, our results show that at scales relevant for perturbative approaches, i.e. within the

mildly nonlinear regime *vorticity back reaction is significant.*

There is yet another way to show the importance of vorticity inclusion. In Fig. 9.4 we compare our one-loop results against N-body simulations, within different approximations, in particular **cum2** (**svt**) and **cum3+** (**svt**) with vorticity as well as **cum3+** (**s**) without for $n_s = 2, 1, 0, -1$. We adopt the ratio $k_\sigma/k_{\rm nl}$ for each scheme, respectively. Both the best-fit values and the power spectra change significantly for the case without vorticity and show a worse agreement with N-body data. The case $n_s = -1$ is again an exception since here small-scale sensitivity is most pronounced and the difference occurs at scales where the two-loop becomes relevant.

In addition, for spectral indices $n_s = 0, 1$ we observe a poor match to N-body for **cum3+** (**s**) even for relatively small k. The reason for this is the interplay between linear and one-loop contribution. The sum of both features a maximum when varying k_σ at a fixed scale k, i.e. the one-loop $P_{\delta\delta}$ is constrained to be below a certain maximal possible value for any choice of k_σ. This can be understood by the following argument. As quoted above, the one-loop piece experiences a sign change in k which happens due to a sign change in $F_{3,\delta}(\boldsymbol{k}, \boldsymbol{q}, -\boldsymbol{q}, \eta)$ for $k \lesssim q$ in the one-loop integral while in SPT this kernel is negative throughout as long as $k \lesssim q$, see Fig. 7.2. Now when k_σ is *decreased* (corresponding to larger background dispersion) the linear part also decreases (see Fig. 9.1), while the one-loop increases as long as $k \lesssim k_{\rm nl}$ due to the UV screening in VPT. This means at $k \lesssim k_{\rm nl}$ it becomes less negative such that the suppression relative to linear VPT becomes weaker for smaller k_σ. However at $k \simeq k_{\rm nl}$ it eventually turns positive. This opposite interplay between both linear and one-loop parts explains the occurrence of this maximum when changing k_σ. In particular, this maximum is below the N-body data for $n_s = 0, 1$ meaning that regardless how well k_σ is tuned the result cannot reach the N-body value. In turn, this tells us that *including vorticity back reaction is essential in order to have agreement with N-body results.*

To conclude, it is very important to take vorticity into account both for momentum conservation and due to its quantitative impact on the density contrast. Moreover, vector modes of the stress tensor have a further quantitative impact while the back reaction of tensor modes is completely negligible at one-loop.

Impact of higher cumulants and loops

Now we focus on the impact of higher cumulants which is assessed by comparing schemes **cum2** and **cum3+**, adopting **svt** in both cases. We show in the right panels of Fig. 9.3 both approximations for $n_s = 0$ and fixed $k_\sigma/k_{\rm nl}$ where for **cum3+** we choose three different values of $\bar{\omega} = \pm 1, \bar{\omega}_{\rm fid}$ to estimate the impact of the background value of the fourth cumulant (see Eq. 9.2). At linear approximation, there is hardly any difference in $P_{\delta\delta}$ between all the schemes, see also Fig. 4.3 for the corresponding linear kernels. When adding the one-loop contribution, one finds a slightly smaller value for the second cumulant approximation (**cum2**) compared to the fiducial case (**cum3+**, $\bar{\omega}_{\rm fid}$). For $\bar{\omega} = +1$ one obtains a slightly larger result while for $\bar{\omega} = -1$ the result drops down to a value similar to **cum2**. Overall, the differences are relatively small in the relevant range $k \lesssim k_{\rm nl}$. In the lower right panel we address the impact of third cumulant dependent on the choice of $\bar{\omega}$ by plotting the ratios to the fiducial case in one-loop approximation (similar to the back reactions on the lower left panel) and find modifications $\lesssim 3\%$ for $k \leq k_{\rm nl}$. Importantly, *in stark contrast to vorticity*, these effects can largely be compensated by a small shift in k_σ, as shown in Fig. 9.4 by comparing **cum2** (**svt**) and **cum3+** (**svt**) with both lines being almost identical for $k \lesssim k_{\rm nl}$, while for the latter the best-fit value of $k_\sigma/k_{\rm nl}$ is somewhat smaller for all n_s. In addition, we checked that an analogous comparison to N-body

with a choice of $\bar{\omega} = -1$ the difference can also be compensated by a shift in k_σ with best-fit values being somewhat larger than the ones within **cum2**. Note that the strong modifications at $k \gtrsim 2k_{\rm nl}$ are a consequence of persistent deviations along the various schemes into the high-k regime with absolute values dropping rapidly due to UV screening making those modifications insignificant. Nevertheless, two- and higher loops become relevant at these scales.

Altogether, we find no evidence that cumulants beyond the velocity dispersion tensor invalidate the VPT approach for $k \lesssim \mathcal{O}(k_{\rm nl})$. On the contrary, the fact that both the agreement between **cum2** and **cum3+** as well as the weak sensitivity on the background value of fourth cumulant $\bar{\omega}$ indicates an acceptable uncertainty for the one-loop $P_{\delta\delta}$ when disregarding higher cumulants, at least within the mildly nonlinear regime and for the considered values of n_s. This is remarkable, since for a single shell crossing event, *all* higher cumulants are generated at once, rendering the relevance of them unclear a priori. Moreover, the findings at one-loop are consistent with those in linear approximation. While higher cumulants are indeed important to capture the suppression behavior of the linear kernels at $k \gg k_\sigma$ they only play a minor role in the transition region between the low-k regime and the onset of suppression $k \simeq k_\sigma$ corresponding to the UV screening, as highlighted in Fig. 5.1.

Finally we comment on neglecting two- and higher loop corrections. The findings above conclude that **cum2** is a reasonable approximation scheme for $P_{\delta\delta}$ at one-loop. However, higher cumulants are expected to become more relevant at higher order in perturbation theory with stronger back reaction effects. A profound analysis of two-loop corrections is important and will be conducted in future. So far, we only made an explorative study of the *two-loop matter power spectrum*, finding only minor changes within the regime $k \lesssim \mathcal{O}(k_{\rm nl})$ with an agreement with N-body similar or slightly improved compared to the one-loop **cum3+** (**svt**) case. However, as mentioned above, for $n_s = -1$ the best-fit value of the dispersion relative to nonlinear scale changes noticeably yielding a unique trend of k_σ as a function of n_s. We find by fitting the two-loop (**cum2, sv**)

$$k_\sigma/k_{\rm nl} = 1.32,\ 1.36,\ 1.39,\ 1.40\,, \tag{9.3}$$

for $n_s = 2, 1, 0, -1$, respectively, i.e. the larger n_s the smaller the dispersion relative to nonlinear scale. These values are also specified in Table 9.1 and the same trend is obtained when self-consistently determine the value of $k_\sigma/k_{\rm nl}$ in *any approximation scheme*. We summarize all different determinations of $k_\sigma/k_{\rm nl}$ in Table 9.1 with additional dispersion estimates from halos. Altogether, we conclude that the lack of this trend when matching $P_{\delta\delta}$ to N-body measurements is most likely a shortcoming within the linear and one-loop approximation.

Dispersion scale k_σ

We now summarize all the different results of the dispersion scale, in particular the ratio $k_\sigma/k_{\rm nl}$ was determined. This is an important estimate since within VPT all the perturbation variables are coupled to the background values and vice versa. The most relevant background value is then related to the dispersion scale. So far, we presented two ways how to determine the value of $k_\sigma/k_{\rm nl}$:

(i) self-consistent calculation from the equation of motion for $\epsilon(\eta)$

(ii) one-parameter fit of matter density spectrum $P_{\delta\delta}$ to N-body data

(iii) halo calculations

Table 9.1: Various determinations for the velocity dispersion scale $k_\sigma = \epsilon_0^{-1/2}$ relative to the nonlinear scale [described within (i)–(iii) in the main text], for scaling universes with spectral indices $n_s = 2, 1, 0, -1$ and using different approximation schemes (see Table 7.1). Note that vorticity+vector (**sv**) and tensor (**svt**) modes enter starting at one-loop only. We show linear as well as one- and two-loop results. For **cum3+**, we show results for three choices $\bar{\omega} = \bar{\omega}_{\rm fid} = 0.579, 0.616, 0.668, 0.752$ for $n_s = 2, 1, 0, -1$ and $\bar{\omega}_\pm = \pm 1$, respectively (see text for details).

n_s	*self-consistent solution*								*matching $P_{\delta\delta}$ to N-body*								*NFW halos*	
	$\frac{k_\sigma}{k_{\rm nl}}$ (linear)			$\frac{k_\sigma}{k_{\rm nl}}$ (one-loop)					$\frac{k_\sigma}{k_{\rm nl}}$ (lin.)	$\frac{k_\sigma}{k_{\rm nl}}$ (one-loop)				$\frac{k_\sigma}{k_{\rm nl}}$ (two-loop)			$\frac{k_\sigma}{k_{\rm nl}}$	$\frac{k_\sigma}{k_{\rm nl}}$
	cum2	**cum3+**		**cum2**			**cum3+**		**cum3+**	**cum2**	**cum3+**			**cum2**	**cum3+**		-	-
	-	-	-	**s**	**sv**	**svt**	**svt**	**svt**	-	**svt**	**s**	**svt**	**svt**	**sv**	**sv**	**sv**	-	-
	-	$\bar{\omega}_{\rm fid}$	$\bar{\omega}_+$	-	-	-	$\bar{\omega}_{\rm fid}$	$\bar{\omega}_+$	$\bar{\omega}_{\rm fid}$	-	$\bar{\omega}_{\rm fid}$	$\bar{\omega}_-$	$\bar{\omega}_{\rm fid}$	-	$\bar{\omega}_-$	$\bar{\omega}_{\rm fid}$	$\beta = 0$	$\beta = \frac{1}{2}$
2	2.34	2.00	1.85	1.80	1.74	1.74	1.62	1.51	1.48	1.37	1.62	1.37	1.33	1.32	1.32	1.27	0.85	0.86
1	2.55	2.17	2.00	1.96	1.86	1.87	1.69	1.64	1.30	1.39	1.61	1.42	1.35	1.36	1.37	1.30	0.96	0.98
0	2.97	2.50	2.29	2.28	2.11	2.11	2.13	1.97	1.13	1.36	1.59	1.41	1.31	1.39	1.38	1.32	1.08	1.11
−1	4.1	3.4	-	-	-	-	-	-	1.10	1.08	1.27	1.10	1.06	1.40	1.41	1.37	1.22	1.24

We evaluate both cases (i) and (ii) in various approximation schemes (see Table 7.1). The third case (iii) will be explained below. Note that in Table 6.1 we already determined this ratio self-consistently within linear approximation, among calculations of further background values $\bar{\mathcal{E}}_{2n}$. At one-loop, there is also only one physical solution for $k_\sigma/k_{\rm nl}$, despite solving a quadratic equation, see Eq. (6.19) and Eq. (6.21). The results are presented in Table 9.1. We find that the inclusion of the one-loop correction within the self-consistent solution leads to an enhancement of the background dispersion ϵ, i.e. to a reduction in the dispersion scale k_σ by about 20% within **cum3+** and about 30% within **cum2**. This is a significant shift but still in line with a perturbative correction. Furthermore, when adding third cumulant perturbations (i.e. using **cum3+**) we observe a trend towards smaller values of k_σ both in linear and one-loop approximation. This is also the case when including vorticity and vector modes (**sv**) but with no further effect coming from the tensor mode (**svt**), as expected. To assess the dependence on the background value of the fourth cumulant $\bar{\omega}$ we use as fiducial value $\bar{\omega}_{\rm fid}$ obtained from self-consistently solving its equation of motion in linear approximation, as well as alternative values $\bar{\omega} = \pm 1$. A self-consistent determination of $\bar{\omega}$ in one-loop approximation is beyond the scope of this work but would be an interesting extension. Nevertheless the dependence of $k_\sigma/k_{\rm nl}$ on $\bar{\omega}$ is noticeable but relatively mild and it is convenient to work with the fiducial value $\bar{\omega}_{\rm fid}$.

When focusing on the values obtained by matching the density power spectrum to N-body data we essentially have similar findings. There is an overall tendency to increase the background dispersion $\epsilon(\eta)$ (such that k_σ decreases) when allowing for more complex approximation schemes, i.e. when successively including one- and two-loop, vorticity/vector mode and higher cumulant effects. Note that the approximation using only scalar modes (**cum3+**, **s**) yields unphysical results (see Fig. 9.4 and discussion in Sec. 7.3) which can also not be compensated by third cumulant effects. As stated above, the choice $\bar{\omega} = -1$ yields values being similar or slightly larger than a corresponding matching within second cumulant approximation (**cum2**). Also noteworthy is, that for $n_s = -1$ only at two-loop a value is obtained which recovers the trend

that k_σ *increases* when n_s decreases. Hence, we conclude that the fitting procedure within linear approximation, despite looking promising in Fig. 9.2, works not very well for a proper determination of $k_\sigma/k_{\rm nl}$ due to the lack of the features argued above. One-loop cures the drawbacks of the matching with linear results and gives reasonable results, while the two-loop further decreases k_σ and changes significantly the value for $n_s = -1$ towards the expected range.

In addition, we checked that the integral in the source term $I^{L-\rm loop}(n_s)$ for the background dispersion, Eq. (6.19), is converged, in particular for $n_s = 2, 1$ the difference between cutoffs $30k_\sigma$ and $40k_\sigma$ is negligible and for $n_s = 0$, the difference is at percent level. Note that there are no estimated values for $n_s = -1$ within the self-consistent solution at one-loop. This is so since here the UV sensitivity is most pronounced and performing an integral which in principle includes arbitrarily high UV modes is not reliable anymore.

Furthermore, we considered calculations of the velocity dispersion within halo models, corresponding to case (iii). We used NFW halos which are isotropic ($\beta = 0$) and radially biased ($\beta = 1/2$), see [99] for a detailed derivation. The estimated background dispersion via the ratio $k_\sigma/k_{\rm nl}$ based on halo calculations is given in the last two columns. Interestingly, those halo-based calculations yield a larger velocity dispersion (or smaller k_σ) than predictions from perturbation theory, but at most by about 30% when comparing with the most complex perturbative prediction (in fact combined with simulations) we are considering (**two-loop**, **cum3+**, **sv**). This is remarkable, given the quite distinct assumptions used within perturbative dynamics with generated dispersion everywhere on the one hand and dispersion only inside NFW halos on the other hand. We note that those predictions arising purely from solving perturbative evolution equations yield somewhat larger values *at one-loop*, but with values at most twice the size of the halo results. Matching perturbative solutions with N-body simulations yields values which are closer to the latter results, with the advantage of having (preliminary) *two-loop results*. This is encouraging and tells us that through our fitting procedure we are determining the spatial average of the velocity dispersion which is indeed a well-defined physical quantity.

Note that when matching $P_{\delta\delta}$ to N-body not all values given in Table 9.1 are shown in the plots above. For example all two-loop results are not presented and are only considered as a first approach to two-loop corrections, in particular those within **cum3+** may be changed significantly when including e.g. additional perturbations modes of the third cumulant which may be relevant at two-loop order, however the further decrease in k_σ using the two-loop seems promising. Overall, it is quite impressing that the various estimations of the dispersion scale $k_\sigma/k_{\rm nl}$ all lie within the same range $\sim 1 - 2$.

In the following we consider different power spectra and compare again with N-body simulations. We first start with the velocity divergence spectra.

9.2 Velocity divergence and cross power spectrum

When interested in the velocity divergence spectrum $P_{\theta\theta}$ and its correlation with the density contrast $P_{\delta\theta}$ it turns out that within N-body measurements a reconstruction of the velocity field is required. This procedure is described in detail in Appendix H in [99].

However, within VPT those power spectra at one-loop can be computed analogously to density power spectrum by replacing $a = b = \theta$ or $a = \delta, b = \theta$, respectively. Importantly, we use the *same* value of $k_\sigma/k_{\rm nl}$ as determined when matching $P_{\delta\delta}$ to the N-body measurements, for each approximation scheme and n_s. This means, there are *no free parameters* in $P_{\theta\theta}$ and $P_{\delta\theta}$ which are therefore predicted uniquely. The related results for linear (dashed) and one-loop (solid)

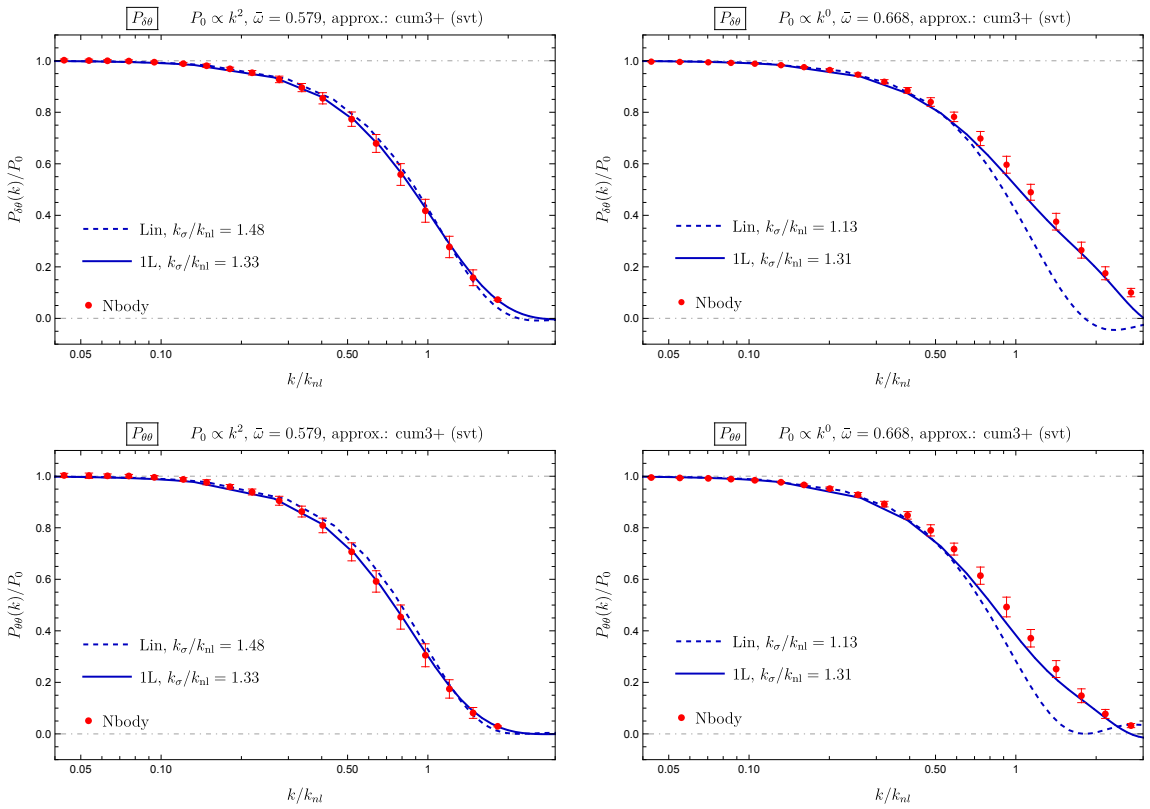

Figure 9.5: Velocity divergence and cross power spectra $P_{\delta\theta}$ (first row) and $P_{\theta\theta}$ (second row) for $n_s = 2$ (left column) and $n_s = 0$ (right column), compared against N-body measurements (red circles with error bars). Linear (dashed) and one-loop (solid) results within the VPT **cum3+** (**svt**) scheme are shown, with the *same* value of $k_\sigma/k_{\rm nl}$ as for $P_{\delta\delta}$ for each case (see Fig. 9.2), respectively. These are then unique predictions within VPT as no free parameter is fitted to the measurements. Reprinted from [99].

approximation are shown in Fig. 9.5 for $n_s = 2$ (left panels) and $n_s = 0$ (right panels). We adopt the fiducial scheme **cum3+** (**svt**) and observe an agreement with N-body for $k \lesssim k_{\rm nl}$ being somewhat better for $n_s = 2$, as for the matter power spectrum $P_{\delta\delta}$. Regarding the uncertainty in the velocity reconstruction (via the error bars), the VPT framework is also able to predict promising results for the velocity divergence, which represents a further consistency check of the formalism. Again, there were no additional parameters adjusted to obtain the velocity and cross power spectra, which is also true when comparing another statistics, i.e. the bispectrum.

9.3 Bispectrum

Now we present a further statistics within VPT, i.e. the density bispectrum $B_{\delta\delta\delta}$ which is then compared to N-body measurements. For the tree-level and one-loop bispectrum there are

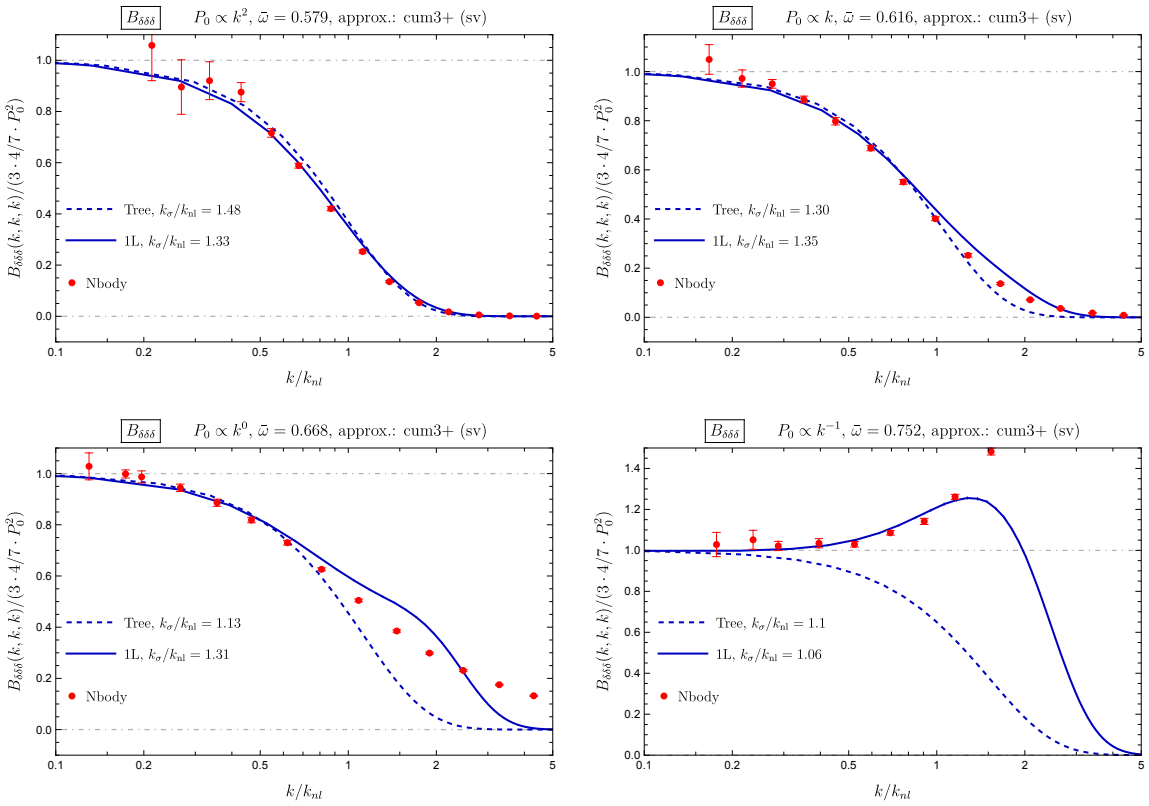

Figure 9.6: Equilateral bispectrum at tree-level (dashed) and one-loop (solid) VPT compared to N-body results for $n_s = 2, 1, 0, -1$, respectively. The bispectra are normalized to the SPT tree-level bispectrum. In each case $k_\sigma/k_{\rm nl}$ is fixed to the *same* value as for $P_{\delta\delta}$ (see Fig. 9.2). Therefore, these can be regarded as unique predictions of VPT as there is no free parameter being fit to the measurements. Reprinted from [99].

analogous expressions as in SPT, with kernels replaced by the VPT ones $F_{n,\delta}$, giving

$$
\begin{aligned}
B^{\rm tree}(k_1,k_2,k_3,\eta) &= 2e^{4\eta}F_{2,\delta}(\boldsymbol{k}_1,\boldsymbol{k}_2,\eta)F_{1,\delta}(k_1,\eta)F_{1,\delta}(k_2,\eta)P_0(k_1)P_0(k_2) + 2 \text{ perm.}\,, \\
B^{1L}(k_1,k_2,k_3,\eta) &= e^{6\eta}\int d^3q P_0(q)\Big\{8F_{2,\delta}(\boldsymbol{q}+\boldsymbol{k}_1,-\boldsymbol{q},\eta) \\
&\times\ F_{2,\delta}(\boldsymbol{q}-\boldsymbol{k}_2,-\boldsymbol{q}-\boldsymbol{k}_1,\eta)F_{2,\delta}(\boldsymbol{q},\boldsymbol{k}_2-\boldsymbol{q},\eta)P_0(|\boldsymbol{q}+\boldsymbol{k}_1|) \\
&\times\ P_0(|\boldsymbol{q}-\boldsymbol{k}_2|) + 6\Big[F_{1,\delta}(k_3,\eta)F_{3,\delta}(\boldsymbol{q}-\boldsymbol{k}_2,-\boldsymbol{q},-\boldsymbol{k}_3,\eta) \\
&\times\ F_{2,\delta}(\boldsymbol{q},\boldsymbol{k}_2-\boldsymbol{q},\eta)P_0(|\boldsymbol{q}-\boldsymbol{k}_2|)P_0(k_3) + F_{2,\delta}(\boldsymbol{k}_2,\boldsymbol{k}_3,\eta) \\
&\times\ F_{1,\delta}(k_2,\eta)F_{3,\delta}(\boldsymbol{k}_3,\boldsymbol{q},-\boldsymbol{q},\eta)P_0(k_2)P_0(k_3) + 5 \text{ perm.}\Big] \\
&+\ 12\Big[F_{1,\delta}(k_2,\eta)F_{1,\delta}(k_3,\eta)F_{4,\delta}(\boldsymbol{k}_2,\boldsymbol{k}_3,\boldsymbol{q},-\boldsymbol{q},\eta)P_0(k_2)P_0(k_3) + 2 \text{ perm.}\Big]\Big\}\,.
\end{aligned}
\tag{9.4}
$$

In contrast to SPT, also the VPT linear kernels $F_{1,\delta}$ need to be included as they are nontrivial. Here, we need already at one-loop the general treatment of vorticity and the vector mode of the dispersion tensor to correctly describe their back reactions, introduced in Sec. 8.2. Note that when using this advanced algorithm we do not include the tensor modes in the numerical kernels as its impact was found to be negligible, hence we adopt at most **sv** within **cum3+** for the one-loop bispectrum.

We choose again power-law initial spectra with spectral indices $n_s = 2, 1, 0, -1$ as for the power spectra and for which the one-loop SPT results would diverge. We normalize our results to the tree-level SPT bispectrum $B^{\rm tree}_{\rm SPT}(k_1, k_2, k_3, \eta) = 2e^{4\eta} F_2(\boldsymbol{k}_1, \boldsymbol{k}_2) P_0(k_1) P_0(k_2) + 2$ perm., with EdS-SPT kernel $F_2(\boldsymbol{k}_1, \boldsymbol{k}_2)$. In the equilateral configuration $k_1 = k_2 = k_3$, the relevant SPT kernels are given by $F_2(\boldsymbol{k}_1, \boldsymbol{k}_2) = F_2(\boldsymbol{k}_1, \boldsymbol{k}_3) = F_2(\boldsymbol{k}_2, \boldsymbol{k}_3) = 2/7$.

We then compare the tree-level (dashed) and one-loop (solid) equilateral bispectrum within VPT to N-body results in Fig. 9.6 for each spectral index. The bispectrum is predicted without any free parameter as we use the same value of $k_\sigma/k_{\rm nl}$ as determined for the density power spectrum $P_{\delta\delta}$. Even at tree-level the bispectrum yields reasonable results. For smaller n_s the one-loop amounts to larger corrections and gives an improved agreement with N-body relative to the tree-level result. This can be understood by the stronger damping for larger n_s which overcompensates the increased weight of larger wavenumbers due to $P_0(q) \propto q^{n_s}$. Overall, the agreement is better the larger n_s. The difference between schemes **cum2** and **cum3+** are rather small, as for the power spectra. Thus, the VPT framework does not only give an accurate prediction of density and velocity power spectra but also of the bispectrum.

9.4 Vorticity power spectrum

Finally, we turn to the vorticity power spectrum $P_{w_i w_i}$ which is particularly sensitive to velocity dispersion as it is generated only in presence of velocity dispersion and higher cumulants. The leading contribution within VPT is at one-loop level, since vorticity vanishes at the linear level. We are now to predict two interesting issues, i.e. the overall amplitude and the scaling in the large-scale limit of the vorticity power spectrum, while for the latter we know from Sec. 8.4 that

$$P_{w_i w_i}(k, \eta) \propto k^2 \quad \text{for} \quad k \to 0\,, \tag{9.5}$$

which however occurs only *starting at two-loop order* with the one-loop piece scaling as k^4. It is therefore expected, that the two-loop piece eventually dominates in the limit $k \to 0$. Nevertheless, this behavior on *large scales* is surely not a sign of perturbative breakdown, as opposed to the opposite regime. It only arises due to the accidentally strong suppression of the one-loop piece and all higher loops show the quadratic scaling.

However, the k^2 scaling can only be observed at small enough k as also the one-loop piece contributes on intermediate scales. We therefore compute the vorticity power spectrum *up to two-loop order*. This means we have go up to fifth order in perturbation theory involving in addition the F_{3,w_i} kernels shown in the lower left panel of Fig. 8.2. Now we work with approximation schemes **cum2** (**sv**) as third cumulant as well as tensor modes have negligible effects, see Table 7.1. As for the one-loop bispectrum we here also have to adopt the advanced algorithm for vorticity and vector modes, introduced in Sec. 8.2. That is we use both modes w_{k1} and w_{k2} which are perpendicular to the vorticity Fourier mode $\boldsymbol{k}$, and similarly for the vector mode $\boldsymbol{\nu}_k$. The vorticity power spectrum is then a sum over both independent modes as $P_{ww} = P_{w_{k1} w_{k1}} + P_{w_{k2} w_{k2}}$, identical to Eq. (8.27).

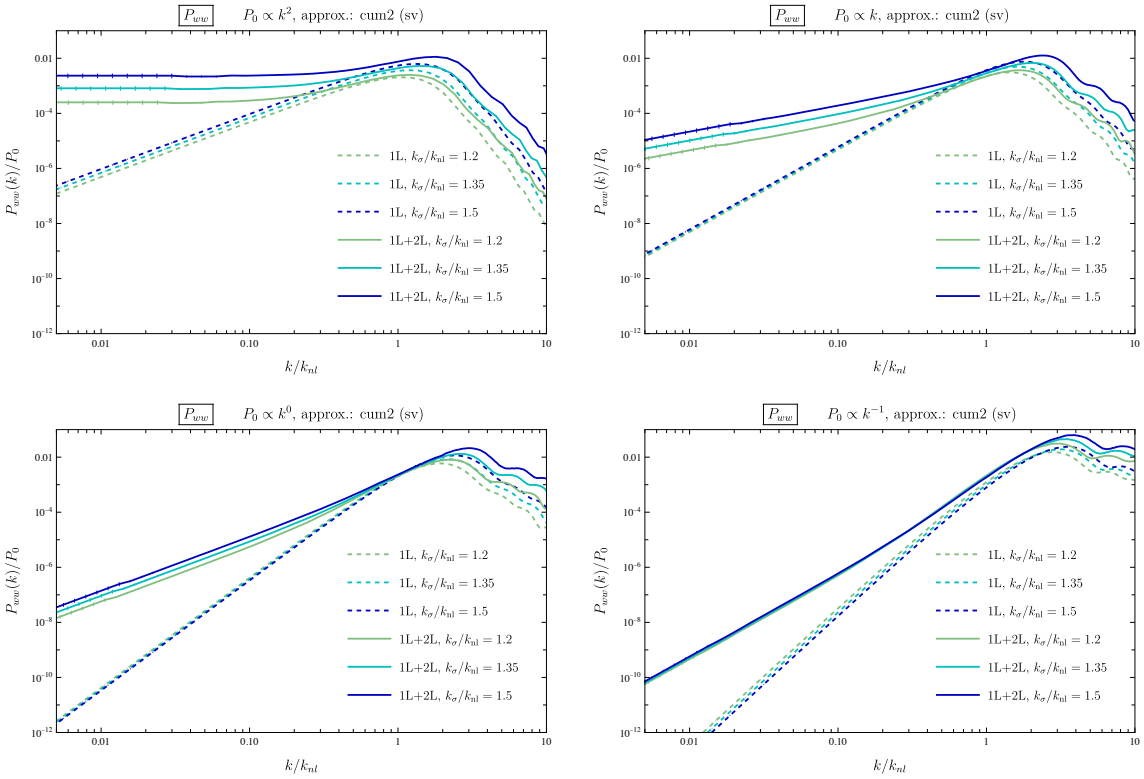

Figure 9.7: One-loop (dashed) and two-loop (solid) vorticity power spectrum $P_{w_i w_i}$ within VPT, see Eq. (8.27), and for various $n_s = 2, 1, 0, -1$. The general scaling $P_{w_i w_i} \propto k^2$ occurs only starting at two-loop order, while the one-loop result accidentally scales as k^4 for $k \to 0$. In each panel the actual scaling is different as the final result is normalized to the initial power spectrum $P_0 \sim k^{n_s}$. LO and NLO results depend on $k_\sigma/k_{\rm nl}$ which is different for a given spectral index n_s, see Eq. (9.6). The error bars correspond to the Monte Carlo integration error which is visible only at low k and at two-loop. Reprinted from [99].

We show the one-loop (dashed) as well as the sum of one- and two-loop (solid) vorticity power spectrum in Fig. 9.7 for $n_s = 2, 1, 0, -1$. The different scaling of one- ($\propto k^4$) and two-loop ($\propto k^2$) results for $k \ll k_{\rm nl}$ is clearly shown and occurs gradually for $k/k_{\rm nl} \lesssim 0.1 - 0.2$. Thus, the power spectrum is dominated by the two-loop piece at $k \lesssim 0.5 k_{\rm nl}$. Each panel of Fig. 9.7 shows the dependence on $k_\sigma/k_{\rm nl}$ for a given n_s. These dependencies can be understood analytically within scaling universes. The dimensionless power spectrum $k^3 P_{w_i w_i}$ only depends on dimensionless ratios which we take as k/k_σ and $k_\sigma/k_{\rm nl}$. Moreover, the power of the nonlinear scale $k_{\rm nl}$ is given by the L-loop order in perturbation theory as P_0^{L+1} with $P_0 = A k^{n_s}$ and $A \propto 1/k_{\rm nl}^{n_s+3}$. Using in addition that $P^{1L}_{w_i w_i} \propto k^4$ and $P^{2L}_{w_i w_i} \propto k^2$ for small k implies

$$\begin{aligned} k^3 P^{1L}_{w_i w_i} &\propto \left(\frac{k}{k_\sigma}\right)^{4+3} \left(\frac{k_\sigma}{k_{\rm nl}}\right)^{2(n_s+3)} \propto k_\sigma^{2n_s-1}\,, \\ k^3 P^{2L}_{w_i w_i} &\propto \left(\frac{k}{k_\sigma}\right)^{2+3} \left(\frac{k_\sigma}{k_{\rm nl}}\right)^{3(n_s+3)} \propto k_\sigma^{3n_s+4}\,, \\ &\qquad\qquad \text{for } k \ll k_{\rm nl}, k_\sigma\,. \end{aligned} \tag{9.6}$$

This explains the dependence on $k_\sigma/k_{\rm nl}$ in Fig. 9.7. It shows an increase (decrease) of $P^{1L}_{w_i w_i}$

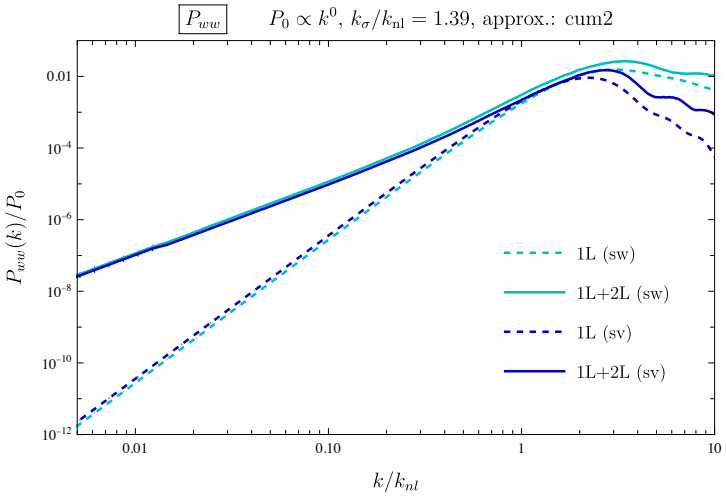

Figure 9.8: One-loop (dashed) and two-loop (solid) vorticity power spectrum $P_{w_i w_i}$ within VPT, see Eq. (8.27), and for $n_s = 0$. The difference between the two colors **(cum2 (sw) ↔ cum2 (sv))** quantifies the impact of the vector mode of velocity dispersion on the vorticity power spectrum and only mildly shows up within $k \lesssim k_{\rm nl}$. Reprinted from [99].

when increasing k_σ for some fixed $k/k_{\rm nl} \ll 1$ (dashed lines in each panel of Fig. 9.7) for $n_s = 2, 1$ ($n_s = 0, -1$). For the two-loop it explains the increase for all $n_s = 2, 1, 0, -1$ which is least pronounced for $n_s = -1$ (solid lines which are dominated by the two-loop part at low k).

Next, we investigate the impact of the vector mode on the vorticity power spectrum at one- and two-loop approximation in Fig. 9.8. In both approximations the impact is moderate and rather negligible within the perturbative regime $k \lesssim \mathcal{O}(k_{\rm nl})$ and becomes larger at smaller scales. However note that there is an overall small vertical shift for the entire k-range when including vector modes which can be understood analytically at the kernel level, as discussed below Eq. (8.33).

Finally, we compare our results with N-body measurements in Fig. 9.9 for $n_s = 0$ (left panel) and $n_s = -1$ (right panel). Here we show one-loop (dashed) and two-loop (dot-dashed) pieces as well as their sum (solid). Measuring vorticity from N-body data is highly challenging and requires a careful treatment which is described in Appendix H in [99]. Specifically, the overall amplitude of the vorticity power spectrum is rather sensitive to the mass resolution in simulations as opposed to the *shape* of the spectrum being quite robust [166, 181, 182]. This feature we take into consideration within our VPT predictions. Indeed, for scale-free simulations with $n_s = 0, -1$ we compare the vorticity power spectrum within VPT in Fig. 9.9. For the former case the simulations may not be fully converged yet and note that in particular for the cases $n_s = 2, 1$ the simulations do not have enough resolution in order to reliably capture the amplitude. Therefore we discard those cases in our comparison. Likewise, the prediction of the two-loop vorticity power spectrum within VPT also has some uncertainty as it is restricted to **cum2**, neglecting higher cumulants as well as their corresponding vector modes being more relevant at two-loop level. As this is beyond the scope of this work we focus on the large-scale limit and the overall shape of the vorticity power spectrum. For this we have multiplied the N-body results for $n_s = -1$ by a factor of four, while the $n_s = 0$ result is unchanged.

Within this setup we observe a good agreement with N-body data. The dip of the two-loop

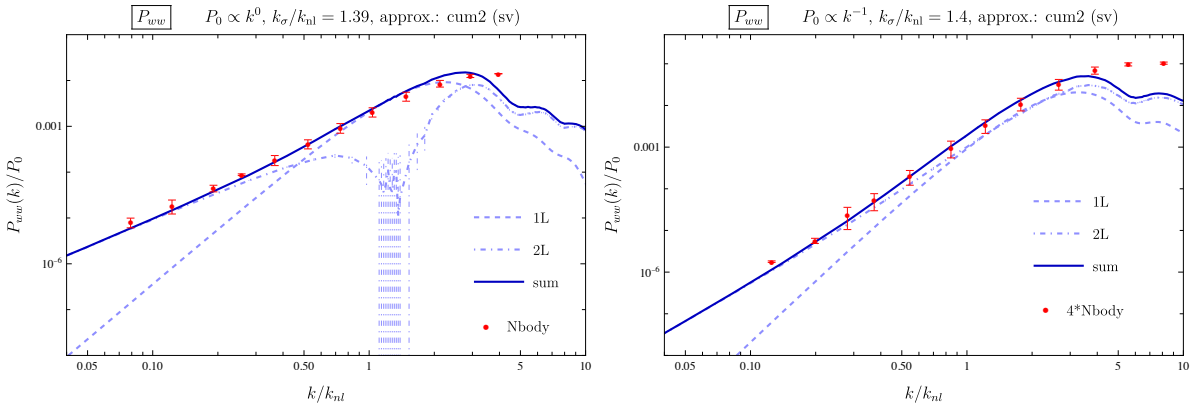

Figure 9.9: Two-loop vorticity power spectrum with $P^{1L}_{w_i w_i}$ (dashed), $P^{2L}_{w_i w_i}$ (dot-dashed) as well as $P^{1L+2L}_{w_i w_i}$ (solid) for $n_s = 0$ (left) and $n_s = -1$ (right). The cross-over from k^4 to k^2 scaling is clearly shown up in both the two-loop VPT and N-body results. Note that for $n_s = -1$ we multiplied the N-body results by a factor of four and the actual scalings in the right panel are k^5 and k^3 for one- and two-loop, respectively. This is due to the normalization of the initial power spectrum $P_0 \sim k^{n_s}$. The value of $k_\sigma/k_{\rm nl}$ is fixed to the one obtained from $P_{\delta\delta}$ in the same VPT approximation, two-loop (**cum2**, **sv**), see Eq. (9.3). Reprinted from [99].

part at $k \sim 1.5 k_{\rm nl}$ for $n_s = 0$ is due to an (almost) cancellation among the two perpendicular vorticity modes $P^{2L}_{w_1 w_1}$ and $P^{2L}_{w_2 w_2}$ (see Sec. 8.2), but the sum is positive below and above, as is the one-loop result. In addition, we fixed the value of $k_\sigma/k_{\rm nl}$ to the value obtained when fitting $P_{\delta\delta}$ to N-body within the same approximation scheme and going up to two-loop order, see Eq. (9.3). In particular, adding the two-loop contribution significantly improves the agreement of the shape of $P_{w_i w_i}$ with N-body and thereby captures the correct scaling $\propto k^2$ at large scales. Remarkably, the transition from quartic to quadratic scaling when both one- and two-loop pieces merge is consistent in both two-loop VPT and N-body results for $n_s = 0, -1$. Although the overall normalization requires further investigation, the *shape* of the perturbative and N-body results agree very well in the mildly nonlinear regime. This demonstrates another nontrivial consistency check of the VPT approach.

The large-scale limit of the vorticity power spectrum was already studied in literature. ΛCDM simulations performed in [182] yield a low-k asymptotic behavior $P_{ww} \propto k^{n_w}$ with $n_w = 2.55 \pm 0.02$ (for $k \lesssim 0.4\,h/\text{Mpc}$) in agreement with [181] which quote $n_w \simeq 2.5$ for $k \simeq 0.1\,h/\text{Mpc}$. However note that due to the somewhat smaller simulation boxes, $256\,\text{Mpc}/h$ and $100 - 300\,\text{Mpc}/h$, respectively, they may have not reached the regime where VPT predicts the k^2 scaling at around $k \simeq (0.1 - 0.2)\,k_{\rm nl}$. Perturbative predictions based on EFT on the other hand yield a "leading order" contribution at the one-loop level $n_w = 7 + 3n_s$ including a stochastic component $n_w = 4$ [183] as well as $n_w = 7 + 2n_s$ plus $n_w = 4$ [184]. Further predictions from Lagrangian perturbation theory (LPT) contain $n_w = 4$ [68]. For the indices relevant for our predictions ($n_s \geq -1$) all these perturbative predictions would lead to a low-k slope of $n_w = 4$. However, predictions of the collisionless Vlasov dynamics, captured by VPT, unambiguously yield $n_w = 2$, i.e. *a quadratic low-k slope*, in agreement with our N-body results. This is independent of the input power spectrum (and thus n_s) holding also e.g. for ΛCDM power spectra.

10 Stochastic gravitational wave background

In this chapter we turn to a somewhat different computation. It is related to a physical application within VPT, in particular to the tensor mode of the velocity dispersion tensor. That is, the corresponding tensor power spectrum $P_{t_{ij}t_{ij}}$ can be seen as a source for gravitational waves. In the following we present a calculation of the spectrum of a *stochastic gravitational wave background*, denoted by $\Omega_{\rm GW}$ and computed within VPT. In addition, we turn away from scaling universes with power-law initial spectra and use instead the more realistic ΛCDM cosmology with initial power spectrum given in Eq. (2.25), containing a maximal value at the scale of matter-radiation equality $k_{\rm eq}$.

To see this, we recall that perturbations in the particle distributions will affect the gravitational field. That is, we have to supplement the Vlasov equation Eq. (3.1) by a more general treatment of the Einstein field equations describing perturbations in gravitational fields. So far, we used the Newtonian limit within scalar perturbations giving rise to the Poisson equation Eq. (3.2) which tells that the matter density contrast δ sources the gravitational field perturbation ϕ. Within VPT further perturbation modes are added revealing further effects in the gravitational field such that the description with a single gravitational potential ϕ is not sufficient to capture all gravitational physics. In particular, the anisotropic part of the stress tensor sources additional metric perturbations. By making a proper scalar, vector and tensor decomposition of the stress tensor, as done in Sec. 4.1, we are able to relate those modes to scalar, vector and tensor fields in the metric, giving rise to effects related to *gravitational slip*, the *gravitomagnetic field* and to *gravitational waves*, respectively.

10.1 Einstein field equations in SVT decomposition

Now we want to study the perturbed FLRW (isotropic and homogeneous) metric which in general reads [4],

$$\begin{aligned} g_{00}(\boldsymbol{x},\tau) &= a^2(\tau)[-1+h_{00}(\boldsymbol{x},\tau)]\,, \\ g_{0i}(\boldsymbol{x},\tau) &= a^2(\tau)h_{0i}(\boldsymbol{x},\tau) = a^2(\tau)h_{i0}(\boldsymbol{x},\tau)\,, \\ g_{ij}(\boldsymbol{x},\tau) &= a^2(\tau)[\delta^K_{ij}+h_{ij}(\boldsymbol{x},\tau)]\,, \end{aligned} \tag{10.1}$$

with conformal time τ and $\delta g_{\mu\nu} \equiv h_{\mu\nu}$ being a small perturbation compared to the background metric $\bar{g}_{\mu\nu}$. The first line corresponds to a scalar metric perturbation h_{00}, the second line to a vector perturbation $h_{i0} = h_{0i}$ and the third line to a tensor perturbation h_{ij} in the metric. In total, the symmetric tensor $g_{\mu\nu}$ contains 10 independent components. The invariant line element $\mathrm{d}s^2 = g_{\mu\nu}\mathrm{d}x^\mu \mathrm{d}x^\nu$ can then be written as

$$\mathrm{d}s^2 = a^2(\tau)\Big\{-(1+2A)\mathrm{d}\tau^2 - 2B_i\mathrm{d}\tau\mathrm{d}x^i + [(1+2D)\delta^K_{ij}+2E_{ij}]\mathrm{d}x^i\mathrm{d}x^j\Big\}\,, \tag{10.2}$$

where we introduced two scalar fields $A(\boldsymbol{x},\tau)$ and $D(\boldsymbol{x},\tau)$ (2 components), one vector field $B_i(\boldsymbol{x},\tau)$ (3 components) and one symmetric and traceless tensor field $E_{ij}(\boldsymbol{x},\tau)$ (5 components). The vector and tensor fields can be decomposed according to their behavior under spatial rotations as $B_i = B_i^S + B_i^V$ and $E_{ij} = E_{ij}^S + E_{ij}^V + E_{ij}^T$, analogously as for the velocity vector and velocity dispersion tensor in Eq. (4.24) and Eq. (4.30), respectively. Within the conformal Newtonian gauge one eliminates four components by setting $B_i^S = 0$ and $E_{ij}^S = E_{ij}^V = 0$ to zero. In addition, the scalar fields are related to the gravitational potentials as $A = \phi$ and $D = -\psi$. Note in the Newtonian limit we have $\phi = \psi$. This leaves *six independent physical degrees of freedom*:

- two scalar fields ϕ and ψ
- two components of the divergenceless vector field B_i^V
- two components of the transverse, symmetric and traceless tensor field E_{ij}^T

The Einstein equations relate any source of energy and momentum to the curvature of spacetime as

$$R_{\mu\nu} - \frac{1}{2} g_{\mu\nu} R = 8\pi G T_{\mu\nu} \,, \tag{10.3}$$

where the spatial part of the Ricci tensor reads

$$R_{ij} = \Gamma^{\alpha}_{\ ij,\alpha} - \Gamma^{\alpha}_{\ i\alpha,j} + \Gamma^{\alpha}_{\ \alpha\beta}\Gamma^{\beta}_{\ ij} - \Gamma^{\alpha}_{\ \beta j}\Gamma^{\beta}_{\ i\alpha} \tag{10.4}$$

and the Christoffel symbols solely depend on the metric itself

$$\Gamma^{\alpha}_{\ ij} = \frac{1}{2} g^{\alpha k} \left(g_{ik,j} + g_{jk,i} - g_{ij,k} \right) \tag{10.5}$$

where commata denote partial derivatives with respect to the spatial components. $T_{\mu\nu}$ is the *stress-energy-momentum tensor* and in the fluid context is given by

$$T^{\mu\nu} = (\rho + p) u^{\mu} u^{\nu} + p g^{\mu\nu} + \Sigma^{\mu\nu} \,, \tag{10.6}$$

where ρ the overall matter density, p the pressure, $g^{\mu\nu}$ the inverse metric tensor, $u^{\mu} = \mathrm{d}x^{\mu}/\mathrm{d}s \simeq (1-\phi, v^i)$ the four-velocity vector and $v^i = \mathrm{d}x^i/\mathrm{d}\tau$ the peculiar velocity field. Here we assume non-relativistic velocities for which $v^i \ll 1$ as well as the weak-field limit indicating small metric perturbations. $\Sigma^{\mu\nu}$ is the *anisotropic stress tensor* and takes deviations from an ideal fluid into account. It is related to the velocity dispersion tensor. Now, to obtain evolution equations one needs the mixed component form, given by

$$G^{\mu}_{\ \nu} = 8\pi G T^{\mu}_{\ \nu} \,, \tag{10.7}$$

where $G^{\mu}_{\ \nu}$ is the Einstein tensor and corresponds to the left-hand side of Eq. (10.3). This is obtained by contracting with the inverse metric tensor as $g^{\mu\kappa} G_{\kappa\nu}$. Then one proceeds as follows. We treat $\boldsymbol{v}$ and Σ_{ij} as perturbed quantities and in addition decompose density and pressure into background plus perturbation around it, giving

$$\begin{aligned} \rho(\boldsymbol{x},\tau) &= \bar{\rho}(\tau) + \delta\rho(\boldsymbol{x},\tau) = \bar{\rho}(\tau)[1 + \delta(\boldsymbol{x},\tau)] \,, \\ p(\boldsymbol{x},\tau) &= \bar{p}(\tau) + \delta p(\boldsymbol{x},\tau), \quad \bar{p} = w\bar{\rho} \,, \end{aligned} \tag{10.8}$$

which defines the usual density contrast δ as well as a pressure perturbation δp. In addition, we defined the ratio of background pressure to density as w which is usually neglected for a matter species. Now, we face a nonzero contribution from the velocity dispersion which effectively generates a *pressure of the dark matter fluid at the background level*, given by [153]

$$\langle T_{ij}(\boldsymbol{x},\tau)\rangle = \bar{p}(\tau)\delta^K_{ij}\,. \tag{10.9}$$

Using the energy-momentum tensor

$$T_{ij}(\boldsymbol{x},\tau) = \frac{1}{a^2}\int \mathrm{d}^3p\,\frac{p_i p_j}{m} f(\boldsymbol{x},\boldsymbol{p},\tau) \tag{10.10}$$

for a dark matter fluid in comoving coordinates and comparing with Eq. (3.7) one obtains for the pressure of the dark matter fluid

$$\bar{p}(\tau) = \bar{\rho}(\tau)(\mathcal{H}f)^2\Big[\epsilon(\tau) + \langle\delta(\boldsymbol{x},\tau)\,\delta\epsilon(\boldsymbol{x},\tau)\rangle\Big]\,, \tag{10.11}$$

after inserting the decomposition of the velocity dispersion tensor Eq. (4.30). This would affect the background expansion but is suppressed by two powers of the Hubble constant. A further investigation of this kind of back reaction is beyond the scope of this work and we refer to [185] for further details. Next, we make a proper scalar, vector, and tensor decomposition of the Einstein equations Eq. (10.7). This yields four scalar mode equations using [186]

$$G^0_0,\ \left(G^0_i\right)^S,\ G^i_i,\ \left(G^i_j\right)^S\,, \tag{10.12}$$

two vector mode equations using

$$\left(G^0_i\right)^V,\ \left(G^i_j\right)^V\,, \tag{10.13}$$

and one tensor mode equation via

$$\left(G^i_j\right)^T\,. \tag{10.14}$$

However, we know that only two scalar, two vector, and two tensor modes are independent degrees of freedom. Combining the above equations properly gives in total four linearized Einstein equations [186] ,

$$\left(\nabla_i\nabla_j - \frac{1}{3}\delta^K_{ij}\nabla^2\right)(\phi-\psi) = -8\pi G a^2\Sigma^S_{ij}\,, \tag{10.15}$$

$$\nabla^2\psi = 4\pi G\bar{\rho}a^2[\delta - 3\mathcal{H}(1+w)\chi]\,, \tag{10.16}$$

$$\nabla^2 B^V_i = -16\pi G\bar{\rho}a^2(1+w)\left(v^V_i - B^V_i\right)\,, \tag{10.17}$$

$$\left(\partial^2_\tau + 2\mathcal{H}\partial_\tau - \nabla^2\right)E^T_{ij} = 8\pi G a^2\Sigma^T_{ij}\,, \tag{10.18}$$

where χ is the velocity potential ($\nabla_i\chi = v^S_i$) related to the velocity divergence θ (but not being identical, see Eq. (4.24)) and note that $v_i = -\mathcal{H}fu_i$ which in total implies that Eq. (10.16) simplifies to the usual Poisson equation Eq. (3.2) in the sub-horizon limit, i.e. for $k^2 \gg \mathcal{H}^2$. In absence of any scalar anisotropic stress ($\Sigma^S_{ij} = 0$) one recovers the Newtonian limit $\phi = \psi$, i.e. both gravitational potentials are identical, and any deviation therefrom quantifies a so-called *gravitational slip*. From Eq. (10.17) we observe that the vorticity, related to v^V_i, sources

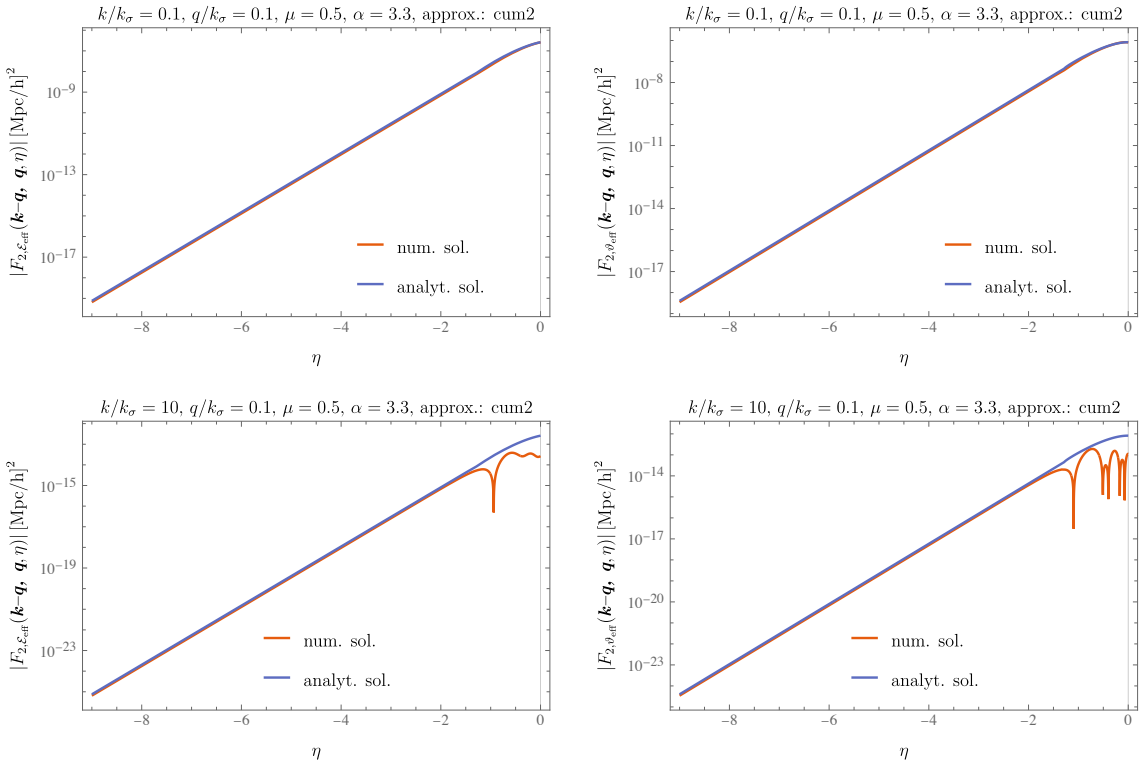

Figure 10.1: Nonlinear kernels $F_{2,\mathcal{E}_{\rm eff}}(\boldsymbol{k}-\boldsymbol{q},\boldsymbol{q},\eta)$ (left column) and $F_{2,\vartheta_{\rm eff}}(\boldsymbol{k}-\boldsymbol{q},\boldsymbol{q},\eta)$ (right column) versus η (time). In the upper panels we chose $k/k_\sigma = q/k_\sigma = 0.1$ meaning the modes have not entered the dispersion scale yet such that the analytical (sub-horizon + super-dispersion) approximation (blue) agrees with the numerical solution (orange). The lower panels have instead wavenumbers $k/k_\sigma = 10$ showing the dispersion induced suppression at time $\eta_\sigma < 0$ in the past. The numerical solution therefore shows deviations as scales inside the dispersion scale ($k > k_\sigma$) are here taken into account. The leading time-dependence for EdS is $\propto e^{(-1+\alpha)\eta}$ where $\alpha = 3.3$, see Eq. (10.33). The suppression induced by dark energy can be seen at very late times. We initialized Eq. (8.36) with $F_{2,t_{\rm eff}}(\boldsymbol{k}-\boldsymbol{q},\boldsymbol{q},\eta_{\rm ini}) \equiv 0$ where $\eta_{\rm ini} = -10$ and used Eq. (10.34).

gravitomagnetic or frame-dragging effects encoded by B_i^V. Finally, the transverse, symmetric, and traceless part of the anisotropic stress tensor Σ_{ij}^T sources the propagation of *gravitational waves* with amplitude E_{ij}^T, see Eq. (10.18). Note that Σ_{ij}^S, Σ_{ij}^V and Σ_{ij}^T are related to the scalar, vector and tensor modes of the velocity dispersion tensor. Therefore, the propagation of gravitational waves are sourced by the tensor mode of velocity dispersion t_{ij} which we focus on in the following.

10.2 Perturbation kernel of gravitational wave amplitude

Now we want to systematically incorporate the evolution equation for the gravitational wave amplitude Eq. (10.18) into the VPT framework. First, we switch to Fourier space, giving

$$\left(\partial_\tau^2 + 2\mathcal{H}\partial_\tau + k^2\right) E_{ij}^T(\tau,\boldsymbol{k}) = 8\pi G a^2 \Sigma_{ij}^T(\tau,\boldsymbol{k})\,. \tag{10.19}$$

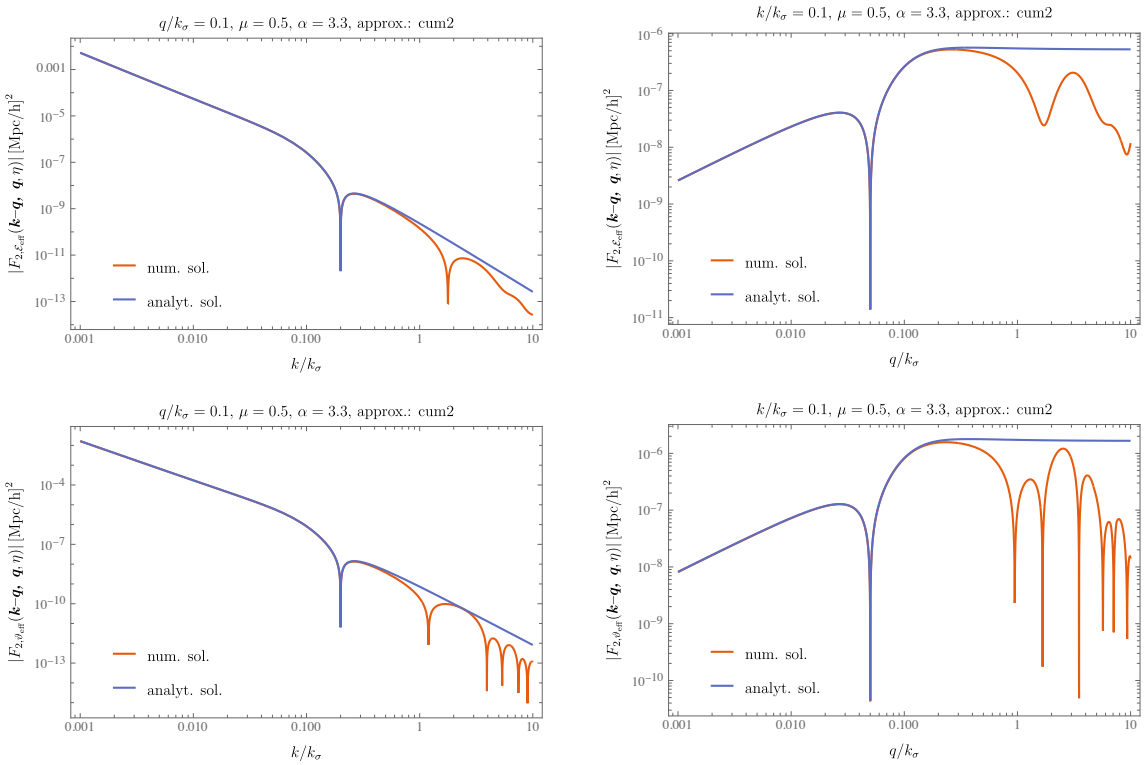

Figure 10.2: Nonlinear kernels $F_{2,\mathcal{E}_{\rm eff}}(\boldsymbol{k}-\boldsymbol{q},\boldsymbol{q},\eta)$ (top panels) and $F_{2,\vartheta_{\rm eff}}(\boldsymbol{k}-\boldsymbol{q},\boldsymbol{q},\eta)$ (bottom panels) versus $k \equiv |\boldsymbol{k}|$ (left column with $q/k_\sigma = 0.1$) and $q \equiv |\boldsymbol{q}|$ (right column with $k/k_\sigma = 0.1$) evaluated today, i.e. $\eta = 0$. For comparison we show the analytical result at order ϵ obtained for the tensor mode of velocity dispersion Eq. (8.39) using $\epsilon = \epsilon_0 e^{\alpha\eta}$ which yields the result for the GW modes via Eq. (10.34). One observes suppression relative to the analytical result when modes enter the regime $k, q \gtrsim k_\sigma$. Both kernels show a scaling with total wavenumber as $\propto 1/k^2$ for $k \to 0$.

In the following, we seek an expression for the spectrum of gravitational waves which requires a statistical ensemble average or power spectrum in Fourier space as $\Omega_{\rm GW} \sim \langle E^T_{ij}(\tau,\boldsymbol{k}) E^T_{ij}(\tau,\boldsymbol{k}')\rangle$. Since we are interested in the transverse, traceless and symmetric part we immediately find the relationship of the anisotropic stress tensor to the dispersion tensor as

$$\Sigma^T_{ij} = \bar{\rho}\,\delta\sigma^T_{ij} = \bar{\rho}\,(\mathcal{H}f)^2\,t_{ij}\,, \tag{10.20}$$

where the density $\bar{\rho}$ enters due to dimensional reasons and we keep only linear terms in perturbations. It is related to the dimensionless energy density parameter Ω_m via

$$\bar{\rho} = \Omega_m \rho_{\rm cr} a^{-3}, \qquad \rho_{\rm cr} = \frac{3H_0^2}{8\pi G}\,. \tag{10.21}$$

Next, we we switch time variable from conformal time τ to $\eta = \ln D_+$ and define the rescaled gravitational wave amplitude as

$$\mathcal{E}_{ij}(\eta,\boldsymbol{k}) \equiv \frac{E^T_{ij}(\eta,\boldsymbol{k})}{(\mathcal{H}f)^2}\,, \tag{10.22}$$

in accordance with Eq. (4.10) for the rescaled cumulants, and the growth rate $f \equiv \mathrm{d}\ln D_+/\mathrm{d}\ln a$ satisfies the Mészáros equation Eq. (3.21). In addition, we will use the time-dependent energy density parameter

$$\Omega_m(\tau) = \frac{H_0^2}{H^2(\tau)}\Omega_m a(\tau)^{-3}\,, \tag{10.23}$$

where Ω_m is the present-day matter energy density parameter. Note that we do not consider the simplified Einstein-de Sitter (EdS) universe and thus a nonzero dark energy contribution $\Omega_\Lambda \neq 0$ enters the Friedmann equation as

$$H^2(\tau) = H_0^2\left(\Omega_m\, a(\tau)^{-3} + \Omega_\Lambda\right)\,. \tag{10.24}$$

When rescaling the time variables one uses the relation

$$\frac{\mathrm{d}(\mathcal{H}f)}{\mathrm{d}\tau} = \mathcal{H}^2\left(\frac{3}{2}\Omega_m(\tau) - f(\tau) - f^2(\tau)\right) \tag{10.25}$$

such that

$$\partial_\tau = \mathcal{H}f\partial_\eta\,, \tag{10.26}$$

$$\partial_\tau^2 = (\mathcal{H}f)^2\left[\partial_\eta^2 + \left(\frac{3}{2}\frac{\Omega_m(\eta)}{f^2} - 1 - \frac{1}{f}\right)\partial_\eta\right]. \tag{10.27}$$

Finally, for ΛCDM, Eq. (10.19) becomes

$$\left[\partial_\eta^2 + \left(\frac{3}{2}\frac{\Omega_m(\eta)}{f^2} - 1 + \frac{1}{f}\right)\partial_\eta + \frac{k^2}{(\mathcal{H}f)^2}\right]\mathcal{E}_{ij}(\eta,\boldsymbol{k}) = \frac{3\,\Omega_m(\eta)}{f^2}\,t_{ij}(\eta,\boldsymbol{k})\,. \tag{10.28}$$

In this form it is possible to cast the evolution equation into the usual (slightly modified) compact matrix notation as used in SPT and VPT, see Eq. (4.47). In absence of any nonlinear terms the matrix form of the gravitational wave equations may be written as

$$\partial_\eta\psi_a^{\mathrm{GW}} + \Omega_{ab}^{\mathrm{GW}}\psi_b^{\mathrm{GW}} = \mathcal{S}_a \tag{10.29}$$

where the superscript denotes the inclusion of gravitational wave modes only using $\psi^{\mathrm{GW}}(\eta,\boldsymbol{k}) = \left(\mathcal{E}_{ij}, \mathcal{E}'_{ij}\right)$. The linear evolution matrix is given by

$$\Omega^{\mathrm{GW}}(\eta,|\boldsymbol{k}|) = \begin{pmatrix} 0 & -1 \\ \frac{k^2}{(\mathcal{H}f)^2} & \frac{3}{2}\frac{\Omega_m(\eta)}{f^2} - 1 + \frac{1}{f} \end{pmatrix} \tag{10.30}$$

and $\mathcal{S}(\eta,\boldsymbol{k}) = \left(0, \frac{3\,\Omega_m(\eta)}{f^2}\,t_{ij}(\eta,\boldsymbol{k})\right)$ is the source term related to the tensor mode of velocity dispersion. Without it, Eq. (10.29) would describe freely propagating gravitational waves without any driving source. The first row describes the evolution of the GW mode itself while the second row tracks its η-derivative. Then one straightforwardly obtains the corresponding kernels by expanding in initial density fields (see Eq. 4.58) and inserting into Eq. (10.29). We know from Sec. 8.5 that the tensor mode t_{ij} is generated at second order due to the nonlinear coupling of scalar modes. This can then be seen as driving force for the gravitational wave modes *at nonlinear level*. Technically, this kernel is used as input from the solution of Eq. (8.36). This is possible since within the solutions of the cumulant perturbations any back reactions from metric

perturbations are neglected. Therefore, Eq. (10.29) can be translated to a system of differential equations for second order kernels as

$$\left(\partial_\eta + 2 + \Omega_{ab}^{\mathrm{GW}}\right) \begin{pmatrix} F_{2,\mathcal{E}_{ij}}(\boldsymbol{p},\boldsymbol{q},\eta) \\ F_{2,\vartheta_{ij}}(\boldsymbol{p},\boldsymbol{q},\eta) \end{pmatrix} - \begin{pmatrix} 0 \\ \frac{3\,\Omega_m(\eta)}{f^2}\, F_{2,t_{ij}}(\boldsymbol{p},\boldsymbol{q},\eta) \end{pmatrix} = 0 \tag{10.31}$$

where we defined

$$\begin{aligned} \partial_\eta \mathcal{E}_{ij} &\equiv \vartheta_{ij}\,, \\ \partial_\eta \left(e^{2\eta} F_{2,\mathcal{E}_{ij}}\right) &= e^{2\eta} F_{2,\mathcal{E}'_{ij}} = e^{2\eta} F_{2,\vartheta_{ij}}\,. \end{aligned} \tag{10.32}$$

Note that in particular the second line implies that $F_{2,\mathcal{E}'_{ij}} \neq \partial_\eta F_{2,\mathcal{E}_{ij}}$ and as we see further below both $\mathcal{E}_{ij}$ and ϑ_{ij} enter the gravitational wave spectrum. From Eq. (10.28) we see that in the sub-horizon limit ($k^2 \gg \mathcal{H}^2$) we immediately obtain a solution given by

$$F_{2,\bar{\mathcal{E}}_{ij}}(\boldsymbol{p},\boldsymbol{q},\eta) = 3\left(\frac{\mathcal{H}}{k}\right)^2 \Omega_m(\eta)\, F_{2,\bar{t}_{ij}}(\boldsymbol{p},\boldsymbol{q},\eta) \tag{10.33}$$

such that the η-derivative terms can simply be neglected. And we introduced the dimensionless kernels $F_{2,\bar{\mathcal{E}}_{ij}} \equiv F_{2,\mathcal{E}_{ij}}/\epsilon(\eta)$ and $F_{2,\bar{t}_{ij}} \equiv F_{2,t_{ij}}/\epsilon(\eta)$. This implies for the time-derivative of the gravitational wave mode

$$\begin{aligned} F_{2,\bar{\vartheta}_{ij}}(\boldsymbol{p},\boldsymbol{q},\eta) &\equiv (\partial_\eta + 2 + \alpha)\, F_{2,\bar{\mathcal{E}}_{ij}}(\boldsymbol{p},\boldsymbol{q},\eta) \\ &= 3\left(\frac{\mathcal{H}}{k}\right)^2 \Omega_m(\eta)\, \left(\partial_\eta + 2 + \alpha - \frac{1}{f}\right) F_{2,\bar{t}_{ij}}(\boldsymbol{p},\boldsymbol{q},\eta) \end{aligned} \tag{10.34}$$

where $\alpha \equiv \frac{\mathrm{d}\log\epsilon}{\mathrm{d}\eta}|_{\eta=0}$ comes from the definition of the dimensionless kernels and we used $\partial_\eta\left(\mathcal{H}^2\Omega_m(\eta)\right) = -\frac{1}{f}\mathcal{H}^2\Omega_m(\eta)$. Note that Eq. (10.28) in principle allows to be solved for scales outside the Hubble horizon, i.e. for super-horizon scales $k^2 \ll \mathcal{H}^2$. However this is beyond the scope of this work and is also technically not allowed since the solution of the dispersion modes and hence of $F_{2,t_{ij}}$ originates from the Vlasov equation for sub-horizon scales. Therefore, the way how we solve for $F_{2,\mathcal{E}_{ij}}$ and $F_{2,\vartheta_{ij}}$ in Eq. (10.33) is only allowed in the sub-horizon limit $k^2 \gg \mathcal{H}^2$. However, the solution Eq. (10.34) is totally applicable for scales beyond the dispersion scale, i.e. for $k \gtrsim k_\sigma$ as we numerically solve for $F_{2,t_{ij}}$. This in turn means that we only have to solve for the tensor mode given by the evolution equation Eq. (8.36) without the need of explicitly solving the differential equation Eq. (10.31). Therefore Eq. (10.34) is sufficient to obtain a solution for the gravitational wave modes once a solution for $F_{2,t_{ij}}$ is found.

Analogously as for the tensor mode, these kernels enter the one-loop integral and constitute a *gravitational wave power spectrum*, see Eq. (8.37). In addition, we can separate the index dependence at one-loop level dictated by Eq. (8.40) which correspondingly defines an effective single degree of freedom of the gravity modes which in turn implies

$$P_{\vartheta_{ij}\vartheta_{ij}}(k,\eta) \equiv 2P_{\vartheta_{\mathrm{eff}}\vartheta_{\mathrm{eff}}}(k,\eta)\,, \tag{10.35}$$

and analogously for the auto spectrum of $\mathcal{E}_{ij}$. Since the kernels scale as $\propto 1/k^2$ for $k \to 0$ (see Eq. 10.33) we expect for the power spectra a scaling as

$$P_{\vartheta_{\mathrm{eff}}\vartheta_{\mathrm{eff}}} \propto P_{\mathcal{E}_{\mathrm{eff}}\mathcal{E}_{\mathrm{eff}}} \propto 1/k^4\,, \quad \text{for } k \to 0\,. \tag{10.36}$$

Using Eq. (10.33) and Eq. (8.40) we plot the time-dependence in Fig. 10.1 as well as the dependence on wavenumbers k and q for the GW modes $F_{2,\mathcal{E}_{\rm eff}}(\boldsymbol{k}-\boldsymbol{q},\boldsymbol{q},\eta)$ and $F_{2,\vartheta_{\rm eff}}(\boldsymbol{k}-\boldsymbol{q},\boldsymbol{q},\eta)$ in Fig. 10.2. We compare the full numerical computation with analytical results using the approximate solution for $F_{2,t_{ij}}$ given by

$$F_{2,t_{ij}}(\boldsymbol{p},\boldsymbol{q},\eta) = -\frac{\epsilon(\eta)\,(\boldsymbol{p}\cdot\boldsymbol{q})(\boldsymbol{p}\times\boldsymbol{q})^2}{(2+\alpha)(3+\alpha)(\boldsymbol{p}+\boldsymbol{q})^2p^2q^2}\,f_{ij}\,, \tag{10.37}$$

where f_{ij} is given in Eq. (8.14). Note that once a mode enters the dispersion horizon, i.e. if it satisfies $k_i \geq k_\sigma(\eta_{k_i})$ suppression due to velocity dispersion occurs. On the other hand, regarding the η-dependence, a given mode k_i experiences suppression as soon as time η_{k_i} is reached and for $\epsilon = \epsilon_0 e^{\alpha\eta}$ is given by

$$\eta_{k_i} \equiv -2\ln\left(k_i/k_\sigma\right)/\alpha \tag{10.38}$$

where $k_\sigma \equiv k_\sigma(\eta=0) = \epsilon_0^{-1/2}$. It tells us that for $k_i > k_\sigma$ the instant of time where dispersion suppresses the mode happened in the past ($\eta_{k_i} < 0$), while for $k_i < k_\sigma$ it will only happen in future ($\eta_{k_i} > 0$). Directly at the dispersion scale $k_i = k_\sigma$ dispersion effects set in today, i.e. $\eta_{k_i} = 0$. This behavior is shown in Fig. 10.1 where the upper panels ($k/k_\sigma = 0.1$) show no suppression at all until today, while the lower panels ($k/k_\sigma = 10$) clearly demonstrate a suppression relative to the analytical results which happened in the past at around $\eta_{k_i} \sim \ln(0.1)$.

10.3 Gravitational wave background

Next, we want to calculate the energy density from those gravitational wave modes. In general, the energy-momentum tensor for gravitational waves, [187, 188] for further details, is given by

$$\begin{aligned} T^{(\rm GW)}_{\mu\nu} &= \frac{4}{32\pi G}\Big\langle (E^T)_{\alpha\beta\,;\mu}\,(E^T)^{\alpha\beta}_{\;\;;\nu}\Big\rangle \\ &= \frac{4}{32\pi G}\Big\langle \partial_\mu (E^T)_{\alpha\beta}\,\partial_\nu (E^T)^{\alpha\beta}\Big\rangle + \mathcal{O}\left((E^T)^3\right)\,, \end{aligned} \tag{10.39}$$

where ; denotes the covariant derivative with respect to the background metric, $\bar{g}_{\mu\nu}$ and we treat $E^T(t,\boldsymbol{x})$ as a small perturbation around $\bar{g}_{\mu\nu}$. It tells us how the back reaction from the energy density of gravitational waves would affect the background expansion history. The contribution to the energy density is obtained when setting $\mu=\nu=0$. We directly go from physical time t to time $\eta = \ln D_+$ leading to an overall prefactor $\mathcal{H}f/a$ per GW mode. Then the energy density in terms of the rescaled gravitational wave modes (Eq. 10.22) is given by

$$\rho_{\rm GW}(\eta) = \frac{(\mathcal{H}f)^6}{8\pi G a^2}\Big[\langle \vartheta_{ij}(\eta,\boldsymbol{x})\,\vartheta_{ij}(\eta,\boldsymbol{x})\rangle + 4\,b(\eta)^2\langle \mathcal{E}_{ij}(\eta,\boldsymbol{x})\mathcal{E}_{ij}(\eta,\boldsymbol{x})\rangle\Big] \tag{10.40}$$

where

$$b(\eta) \equiv \left(\frac{3}{2}\frac{\Omega_m(\eta)}{f^2} - 1 - \frac{1}{f}\right)\,, \tag{10.41}$$

and note that $b(\eta) \to -\frac{1}{2}$ for EdS. In general, there are only two independent modes for gravitational waves,

$$E^T = \begin{pmatrix} E_+ & E_\times & 0 \\ E_\times & -E_+ & 0 \\ 0 & 0 & 0 \end{pmatrix}\,. \tag{10.42}$$

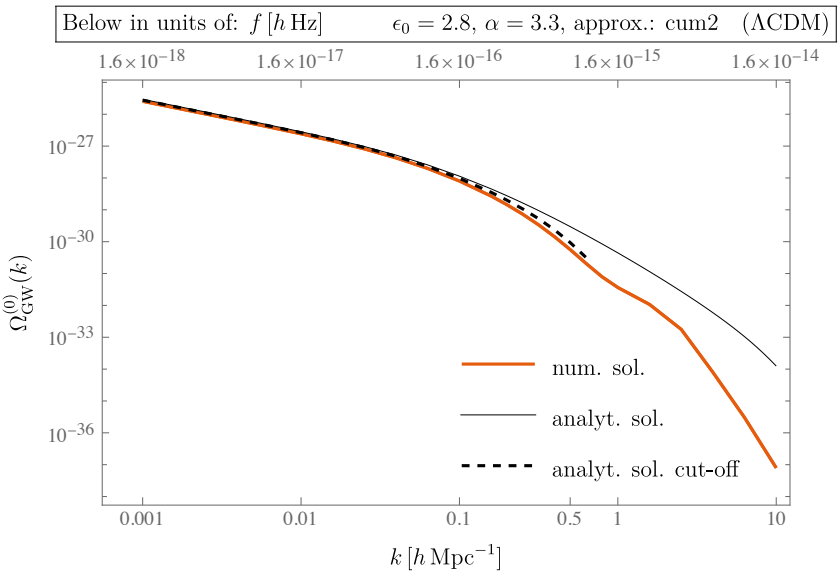

Figure 10.3: Spectrum of the stochastic gravitational wave background $\Omega_{\mathrm{GW}}(k,\eta)$ in the sub-horizon regime $k^2 \gg \mathcal{H}^2$. It is defined as the dimensionless energy density parameter per logarithmic wavenumber interval, see Eq. (10.52). It scales as $\Omega_{\mathrm{GW}}(k,\eta) \propto 1/k$ for $\mathcal{H} \ll k \ll k_\sigma$ and the overall amplitude is very tiny ($\lesssim 10^{-26}$). We compare the numerical computation with analytical approximations. The latter differ in two choices of the UV cut-off, $q_{\mathrm{UV}} = 10\,h/\mathrm{Mpc}$ (thin line) and $q_{\mathrm{UV}} = k_\sigma$ (dashed line) within the one-loop integral. We note that up to the dispersion scale $k_\sigma = 1/\sqrt{\epsilon_0}$ the agreement with the numerical result is improved when using the modified cut-off scale since UV modes not applicable within the analytical approximation are thrown away. Moreover, we added a frequency scale, using the relation $f_{\mathrm{gw}} \sim ck_\sigma/(2\pi) \simeq 1.5{\cdot}10^{-15}\,h$ Hz $\times(k_\sigma/(1h/\mathrm{Mpc}))$, emphasizing that such a GW background occurs at ultra-low frequencies.

This allows to decompose the tensor E^T_{ij} into Fourier modes as well as into the independent polarization modes $p = +, \times$ [18, 22] as

$$E^T_{ij}(\eta, \boldsymbol{x}) = \sum_{p=+,\times} \int \mathrm{d}^3k\, E_p(\eta, \boldsymbol{k}) e^{i\boldsymbol{k}\cdot\boldsymbol{x}} e^p_{ij}(\hat{\boldsymbol{k}})\,, \tag{10.43}$$

where the polarization tensors $e^p_{ij}(\hat{\boldsymbol{k}})$ are real, symmetric in ij, transverse ($\hat{k}_i e^p_{ij} = 0$), traceless ($e^p_{ii} = 0$) and satisfy $e^p_{ij}(\hat{\boldsymbol{k}}) = e^p_{ij}(-\hat{\boldsymbol{k}})$. In fact they only depend on the direction $\hat{\boldsymbol{k}}$ (see Eq. 4.29) and can be written as

$$\begin{aligned} e^+_{ij}(\hat{\boldsymbol{k}}) &= \hat{x}_i\hat{x}_j - \hat{y}_i\hat{y}_j\,, \\ e^\times_{ij}(\hat{\boldsymbol{k}}) &= \hat{x}_i\hat{y}_j + \hat{y}_i\hat{x}_j\,, \end{aligned} \tag{10.44}$$

where $\hat{x}$ and $\hat{y}$ are the unit vectors orthogonal to $\hat{\boldsymbol{k}} = \hat{z}$ which yields Eq. (10.42). We then have the orthonormal and completeness relations

$$\begin{aligned} e^p_{ij}(\hat{\boldsymbol{k}}) e^{p'}_{ij}(\hat{\boldsymbol{k}}) &= 2\delta_{pp'}\,, \\ \sum_{p=+,\times} e^p_{ij}(\hat{\boldsymbol{k}}) e^p_{lm}(\hat{\boldsymbol{k}}) &= 2[\Delta_{il}\Delta_{jm} + \Delta_{im}\Delta_{jl} - \Delta_{ij}\Delta_{lm}]\,, \end{aligned} \tag{10.45}$$

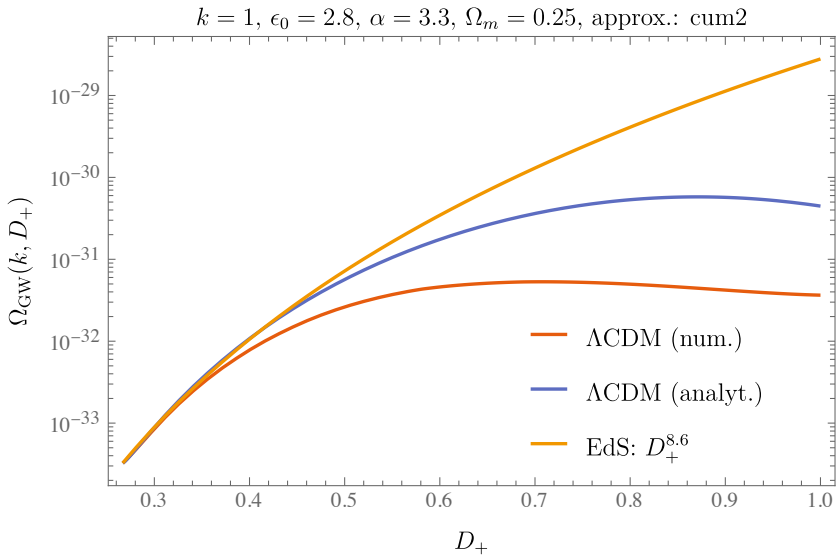

Figure 10.4: Gravitational wave spectrum $\Omega_{\rm GW}(k, \eta)$ versus growth factor $D_+ = e^\eta$ for $k = 1\,h/\text{Mpc}$. We compare ΛCDM with EdS cosmology where the latter is only valid at early times and in addition, we show the analytical approximation which shows deviations from the numerical result at later times, i.e. when the mode has entered the dispersion horizon. Only the numerical ΛCDM computation gives the correct amplitude of the gravitational wave background which is lower when compared to the other approximations. Note the value of $\alpha = 3.3$, as given in the legend, is the approximate power-law index for $D_+ = 1$. This value changes when going to earlier times and eventually becomes $\alpha_{\rm early} = 4.3$ for $D_+ \ll 1$. This value is also used for the EdS approximation in the plot.

where the projector Δ_{ij} can be defined as $\Delta_{ij} = \frac{1}{\sqrt{2}}\left(\hat{x}_i\hat{x}_j + \hat{y}_i\hat{y}_j\right)$ in comparison to Eq. (4.29), which we used for the analogeous definition of the tensor mode t_{ij}. The decomposition Eq. (10.43) analogously holds for $\mathcal{E}_{ij}$ and ϑ_{ij}. When inserting the first line of Eq. (10.45) and Eq. (10.43) into Eq. (10.40) one obtains for the energy density

$$\rho_{\rm GW}(\eta) = \frac{(\mathcal{H}f)^6}{4\pi G a^2}\sum_{p,p'}\int_{\boldsymbol{k},\boldsymbol{k}'}\delta_{pp'}e^{i(\boldsymbol{k}+\boldsymbol{k}')\cdot\boldsymbol{x}}\left[\langle\vartheta_p(\eta,\boldsymbol{k})\vartheta_{p'}(\eta,\boldsymbol{k}')\rangle + 4\,b(\eta)^2\langle\mathcal{E}_p(\eta,\boldsymbol{k})\mathcal{E}_{p'}(\eta,\boldsymbol{k}')\rangle\right], \tag{10.46}$$

where $\int_{\boldsymbol{k}} \equiv \int \mathrm{d}^3k$. For stochastic modes, the spatial average over several wavelengths, $\langle\ \ \rangle$, is equivalent to the ensemble average in $\boldsymbol{k}$ space, which implies

$$\langle\vartheta_p(\eta,\boldsymbol{k})\vartheta_p(\eta,\boldsymbol{k}')\rangle = \delta_D^{(3)}(\boldsymbol{k}+\boldsymbol{k}')|\vartheta_p(\eta,\boldsymbol{k})|^2\,. \tag{10.47}$$

With this, Eq. (10.46) simplifies to

$$\rho_{\rm GW}(\eta) = \frac{(\mathcal{H}f)^6}{2\pi G a^2}\int_{\boldsymbol{k}}\left[|\vartheta_{\rm eff}(\eta,\boldsymbol{k})|^2 + 4\,b(\eta)^2|\mathcal{E}_{\rm eff}(\eta,\boldsymbol{k})|^2\right], \tag{10.48}$$

where we used $\sum_{p,p'}\delta_{pp'}\vartheta_p\vartheta_{p'} = \sum_p\vartheta_p\vartheta_p$ as well as for unpolarized gravitational waves $|\vartheta_{+,k}|^2 = |\vartheta_{\times,k}|^2 \equiv |\vartheta_{{\rm eff},k}|^2$. This ensemble average exactly corresponds to the power spectrum with

kernels $F_{2,\vartheta_{\rm eff}}$ contributing at one-loop level. The overall time-dependence to leading order in an EdS background can be estimated as

$$\rho_{\rm GW}(\eta) \propto \frac{a^{2\alpha}}{a} = e^{(-1+2\alpha)\eta}\,, \tag{10.49}$$

using Eq. (10.33) as well as Eq. (3.66). For $\alpha > 1/2$ the energy density overweighs cosmological redshift and increases with time due to the nonlinear amplification because of scalar mode coupling. However nonlinear dispersion effects further suppress the energy density of GW at late times in addition to dark energy. Eq. (10.48) can be rewritten per logarithmic scale

$$\rho_{\rm GW}(\eta) = \frac{(\mathcal{H}f)^6\epsilon(\eta)^2}{2\pi G a^2}\int \mathrm{d}\log k\Big[\Delta_{\bar{\vartheta}_{\rm eff}\bar{\vartheta}_{\rm eff}}(\eta,k) + 4\,b(\eta)^2\Delta_{\bar{\mathcal{E}}_{\rm eff}\bar{\mathcal{E}}_{\rm eff}}(\eta,k)\Big]\,, \tag{10.50}$$

where the dimensionless power spectrum is defined via

$$\Delta_{\bar{\vartheta}_{\rm eff}\bar{\vartheta}_{\rm eff}}(\eta,k) = 4\pi k^3\, P_{\bar{\vartheta}_{\rm eff}\bar{\vartheta}_{\rm eff}}(\eta,k)\,. \tag{10.51}$$

Finally, we define the *energy density spectrum of gravitational waves* with

$$\begin{aligned}\Omega_{\rm GW}(\eta,k) &\equiv \frac{\tilde{\rho}_{\rm GW}(\eta,k)}{\rho_{\rm cr}}\,,\\ \tilde{\rho}_{\rm GW}(\eta,k) &\equiv \frac{\mathrm{d}\rho_{\rm GW}(\eta)}{\mathrm{d}\log k}\,,\end{aligned} \tag{10.52}$$

which then yields

$$\Omega_{\rm GW}(\eta,k) = \frac{4}{3}\mathcal{H}^4 f^6\epsilon(\eta)^2\Big[\Delta_{\bar{\vartheta}_{\rm eff}\bar{\vartheta}_{\rm eff}}(\eta,k) + 4\,b(\eta)^2\Delta_{\bar{\mathcal{E}}_{\rm eff}\bar{\mathcal{E}}_{\rm eff}}(\eta,k)\Big]\,, \tag{10.53}$$

and the time-dependent critical density is given by $\rho_{\rm cr}(\tau) = 3H(\tau)^2/(8\pi G)$. This result can in turn be expressed in terms of the tensor power spectrum when inserting the prefactors given in Eq. (10.33) and Eq. (10.34),

$$\begin{aligned}\Omega_{\rm GW}(\eta,k) &= 12\,\mathcal{H}^8 f^6\epsilon(\eta)^2\Omega_m(\eta)^2\frac{\Delta_{\bar{t}_{\rm eff}\bar{t}_{\rm eff}}(\eta,k)}{k^4}\\ &\quad\times\left\{4\,b(\eta)^2 + \frac{1}{f^2} + (2+\alpha)\left[\alpha + 2\left(1-\frac{1}{f}\right)\right]\right\}.\end{aligned} \tag{10.54}$$

Finally, we obtained an expression for the spectrum of the gravitational wave background in terms of the dimensionless tensor power spectrum $\Delta_{\bar{t}_{\rm eff}\bar{t}_{\rm eff}}$ for a ΛCDM cosmology. In the limit of an EdS cosmology this result reduces to

$$\Omega_{\rm GW}(\eta,k) = 12\,\mathcal{H}^8\epsilon(\eta)^2\,(2+\alpha(2+\alpha))\,\frac{\Delta_{\bar{t}_{\rm eff}\bar{t}_{\rm eff}}(\eta,k)}{k^4}\,. \tag{10.55}$$

We plot the full numerical result of the spectrum in Fig. 10.3 for $\eta = 0$. We observe that the gravitational wave spectrum scales as $\propto 1/k$ at large scales and is stronger suppressed at scales $k \gtrsim k_\sigma$. This means the signal is largest at scales around the horizon scale. At even larger scales, Eq. (10.54) is not valid anymore. However when solving the full Eq. (10.28) one finds a scaling of $\Omega_{\rm GW}(k) \propto k^3$ in the super-horizon regime ($k^2/\mathcal{H}^2 \ll 1$) where the Hubble

rate today in units of wavenumbers reads $H_0 \simeq 2998^{-1}\, h\,\mathrm{Mpc}^{-1}$. The full solution also agrees with the sub-horizon limit given in Eq. (10.54). Therefore this suggests that at the cross over from k^3 to $1/k$ scaling there is indeed a maximal value of $\Omega_{\rm GW}$ occurring at the horizon scale. Nevertheless, this super-horizon solution will most likely be changed when in addition having a correct super-horizon solution for $F_{2,t_{ij}}$. For comparison also the analytical results are plotted. Those use Eq. (10.37) as input and shows a good agreement at large scales. To further improve the analytical result we show an additional computation where we cut the loop integral off at $q_{\rm UV} = k_\sigma = 1/\sqrt{\epsilon_0}$. Otherwise we just set the cut-off to $q_{\rm UV} = 10\, h/\mathrm{Mpc}$ as for the numerical computation and include scales ($q_{\rm UV} > k_\sigma$) where in principle the analytical approximation breaks down. For ΛCDM we performed simulations, using the LasDamas cosmology, in order to get a more correct time-dependence of the velocity dispersion background $\epsilon(\eta)$ which differs from a mere power-law behavior $\propto e^{\alpha\eta}$. Using $\Omega_m = 0.25$ for the present-day matter density parameter we obtained for the background dispersion today a value of $\epsilon_0 \simeq 2.8\,(\mathrm{Mpc}/h)^2$ which gives a dispersion scale of $k_\sigma \simeq 0.6\, h/\mathrm{Mpc}$. Nevertheless we still assumed an approximate power-law at any instant of time while fixing α in the results above to the power-law index today and obtained $\alpha = \frac{\mathrm{d}\log\epsilon}{\mathrm{d}\eta}|_{\eta=0} \simeq 3.3$.

Regarding the time-dependence we obtain to leading order

$$\Omega_{\rm GW}(\eta) \propto D_+^{2\alpha_{\rm early}} = e^{2\alpha_{\rm early}}\,, \tag{10.56}$$

which corresponds to the EdS approximation. Note that $\alpha_{\rm early} = \frac{\mathrm{d}\log\epsilon}{\mathrm{d}\eta}|_{\eta\to-\infty} \simeq 4.3$ differs from α defined above and corresponds to the approximate power-law index at early times. In Fig. 10.4 we show $\Omega_{\rm GW}(k,\eta)$ versus $D_+ = e^\eta$ for $k = 1\, h\,\mathrm{Mpc}^{-1}$. The growth factor is normalized to unity, i.e. $D_+(a=1) = 1$ and for ΛCDM it has to satisfy Eq. (3.21) for $a < 1$. We compare the full numerical result with the analytical approximation as well as with the EdS approximation. We observe that EdS is only valid at very early times until $D_+ \lesssim 0.35$ while the analytical approximation shows deviations from the full numerical result starting from $D_+ \gtrsim 0.5$ for the choice of $k = 1\, h\,\mathrm{Mpc}^{-1}$. For smaller wavenumbers, EdS as well as analytical approximations are valid for a longer period of time, as expected.

10.4 Detecting gravitational waves

It is intriguing to connect the gravitational wave (GW) background originating from the cosmic epochs of primordial inflation and late-time cosmic structure formation. The former represents an irreducible GW background stemming from tensor metric fluctuations during inflation, while the latter arises as a second-order consequence of dark matter anisotropic stress during structure formation, peaking around the dispersion horizon. Observationally, we can detect stochastic gravitational waves within specific frequency ranges that correspond to perturbation modes evolving over cosmic time. For such ultra-low frequencies, the only accessible tool is the detection via the imprint of tensor modes on CMB photons. Tensor modes would induce a particular polarization pattern in the CMB, so-called B-modes [4].

The polarization signal in the CMB is generated at last scattering and is decomposed into E and B polarization modes, where E-mode is sourced by all metric perturbations and B-mode is primarily sourced by vector and tensor perturbations, representing an imprint of primordial inflationary gravitational waves. However, B-polarization is also affected by gravitational lensing and galactic foregrounds like dust and synchrotron emission, posing challenges for detecting the primordial tensor spectrum. Distinguishing these sources can be achieved through angular

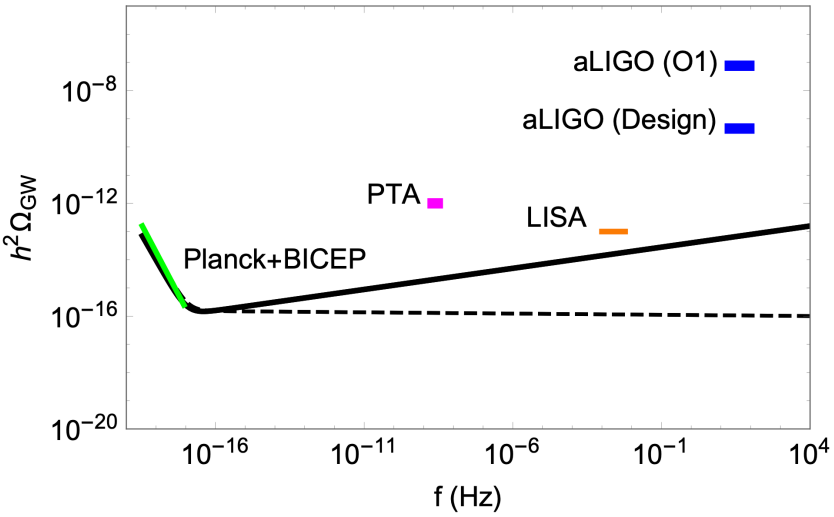

Figure 10.5: Theoretical prediction for the GW energy density of inflation for various scenarios: $n_T = -r/8$ and $n_T = 0.2$ (black dashed and black solid lines respectively), where n_T is the power-law index of the primordial tensor power spectrum. The constraint from Planck+BICEP2+Keck Array data (green solid line) is also presented, with $r = 0.07$ and $n_T = 0$. The figure further includes the sensitivity ranges of current and future gravitational wave (GW) detectors: Pulsar Timing Arrays (PTA) in magenta, advanced LIGO at first run, and design sensitivity in blue, and LISA in orange. Figure extracted from [18]

spectrum shape and frequency measurements, aided by ground and space observations of less foreground-contaminated regions. Several ongoing or planned experiments aim to detect or constrain the irreducible gravitational wave (GW) background from inflation using CMB polarization B-mode observations. However, due to the small amplitude of this background, current and planned direct GW detectors like aLIGO/Virgo [189, 190], LISA [15], and ET [191] are not expected to detect it. The observable frequency window corresponds respectively to modes that enter the Horizon today and at the epoch of photon decoupling, corresponding to $f \sim 10^{-19}\,\mathrm{Hz}$ and $f \sim 10^{-17}\,\mathrm{Hz}$, respectively. Futuristic detectors like BBO [192, 193] might have a chance if inflation's energy scale is high enough. Despite challenges, GWs from inflation remain an important target for upcoming interferometers on the ground and in space. The current upper limit from a combination of space (Planck) and ground-based (BICEP/Keck array BK15) observations quantified by the *tensor-to-scalar ratio* r yields [127]

$$r_* < 0.056 \qquad (95\%\ \text{C.L., Planck})\,, \tag{10.57}$$

measured at the pivot scale $k_* = 0.002\,\mathrm{Mpc}^{-1}$, which lies in the frequency range quoted above (see [194] for more recent constraints on r for a different pivot scale). It is defined as the amplitude of primordial gravitational waves relative to scalar perturbations in the cosmic microwave background. This translates into an upper bound for the primordial GW background as [18]

$$\Omega_{\mathrm{GW}}(k_*) \lesssim 10^{-14.3}\, r_* \simeq 5 \times 10^{-16}\,. \tag{10.58}$$

Thus, dark matter anisotropic stress limits the ability to detect primordial gravitational waves if $r_* \lesssim 10^{-12}$. Unfortunately, this seems non-detectable from near-future experiments, even though the observable frequency window covers the highest impact of the GW spectrum in Fig. 10.3. An analogous effect coming from anisotropic stresses of photons and neutrinos on the secondary generated GWs from density perturbations was treated in [195] in which the authors found accountable corrections at small scales $k \gtrsim 1\,h\,\mathrm{Mpc}^{-1}$. We provide a concise overview of past endeavors aimed at detecting gravitational waves, with a particular focus on the pursuit of identifying a background spectrum of these waves.

The first generation of earth-based GW detectors, including LIGO [196], Virgo [197], GEO 600 [198], and TAMA [199], played a crucial role in testing technical innovations and paving the way for the second generation detectors. Advanced LIGO [189] and Advanced Virgo [190] achieved the first direct detection of GWs, including black hole and neutron star mergers. However, detections of stochastic backgrounds have yet to be made, only upper bounds have been determined. The next technological step involves the use of cryogenic mirrors, which is being explored by the KAGRA collaboration [200]. Additionally, a conceptual design study for the third generation Einstein Telescope (E.T.) [191] has been funded, aiming to provide a strain sensitivity ten times better than second generation detectors and probe the stochastic background down to a level of $\Omega_{\mathrm{GW}} \sim 10^{-12}$ [191].

On the other hand, space-based detectors, like LISA [15], overcome the limitations of Earth-based detectors by placing drag-free spacecraft in orbit. LISA consists of three spacecraft forming an equilateral triangle and can detect GWs in the frequency range of 0.1 mHz to 0.1 Hz. It aims to study sources like galactic binaries, stellar black hole binaries, and coalescing massive black hole binaries. LISA is expected to probe a SGWB down to a level of $\Omega_{\mathrm{GW}} \sim 10^{-13}$ [15]. Other proposed missions, like DECIGO [201, 202] and BBO [192, 193], have similar configurations and target the detection of the primordial GW background and are designed to probe the $0.1 - 10\,\mathrm{Hz}$ frequency band with aimed sensitivity of about $\Omega_{\mathrm{GW}} \sim 10^{-17}$ [203, 204]. There are also proposals for space-based missions utilizing atom interferometry, such as AGIS and AGIS-LEO [205, 206], which can probe frequencies from $0.01 - 10\,\mathrm{Hz}$ with high sensitivity. These space-based detectors open up new possibilities for observing GWs at lower frequencies and exploring a wide range of astrophysical and cosmological phenomena. We present a collection of sensitivity bounds from various detectors in Fig. 10.5.

Moreover, there are natural detectors residing in the cosmos. Pulsars, rotating neutron stars emitting radiation along their magnetic axes, act as stable cosmic clocks for precise astronomical measurements. Pulsar timing involves assigning arrival times to pulses and comparing them to models, making millisecond pulsars ideal for detecting gravitational wave (GW) backgrounds. This technique, pioneered by Sazhin [207] and Detweiler [208], yields upper bounds on GW background amplitudes. Collaborations like PPTA [209], EPTA [210], NANOGrav [211], and IPTA [212] collectively aim to detect GW backgrounds using pulsar timing. Pulsar timing arrays (PTA) are expected to enhance their sensitivity like the IPTA's anticipated $\Omega_{\mathrm{GW}} \sim 10^{-11}$ [212]. The SKA projects sensitivities down to $\Omega_{\mathrm{GW}} \sim 10^{-15}$ [213], but supermassive black hole binaries from galaxy mergers can obscure other backgrounds with smaller amplitudes. In fact, very recently the NANOGrav collaboration reported evidence for an isotropic stochastic gravitational wave background (GWB) using the 15-year NANOGrav data set. Previous analyses of the 12.5-year data showed evidence of excess low-frequency noise with common properties across the array, but inconclusive evidence for Hellings–Downs interpulsar correlations, which would indicate a GW origin. However, the 12.5-year data did not support purely monopolar or dipolar correlations. Independent analyses by PPTA [214] and EPTA [215] collaborations, as well

as a combined data set [216], yielded consistent results, most reasonable for a signal from a population of supermassive black hole binaries. This highlights the promising emergence of low-frequency GW astronomy.

11 Conclusions

Over the past few decades, the field of cosmology has witnessed a significant surge in experimental information, enabling us to delve deeper into understanding the fundamental structure and evolutionary trajectory of the universe. Notably, ongoing and forthcoming surveys focusing on the universe's large-scale structure offer the potential to elucidate aspects of dark matter and dark energy, the behavior of gravity on cosmic scales, and even ascertain the initial state of the early universe. As the volume of observational data expands, there arises a pressing need for a substantial and complementary theoretical endeavor to effectively extract invaluable insights from this wealth of information.

In this thesis, a new perspective on understanding gravitational clustering in cosmology is introduced through the lens of Vlasov Perturbation Theory (VPT), offering a systematic improvement over the traditional Standard Perturbation Theory (SPT). The fundamental motivation for this exploration lies in the desire to overcome the limitations of SPT and gain a more comprehensive understanding of the dynamics that govern large-scale structures in the universe. The main conclusions are:

1. ***The foundation of Vlasov Perturbation Theory (VPT)***: The VPT approach laid out in Ch. 4 decomposes cumulants into average values and fluctuations. The evolution of perturbations depends on average values, and vice versa. Treating background values of even cumulants as "$\mathcal{O}(1)$" quantities yields a systematic perturbative expansion for fluctuations and enables the description of UV mode screening for better convergence. This leads to VPT equations that resemble SPT but include an extended set of perturbation variables and nonlinear interactions, in presence of a background determined by even cumulant average values.

2. ***Richer linear theory and non-local in time behavior***: Unlike SPT, which truncates at density and velocity fields, VPT incorporates second and higher cumulants. This leads to a significantly richer linear theory involving the generation of a dispersion perturbation (see Sec. 4.1). As we are dealing with collisionless particles interacting only by gravity, this transcends (fluid-like) local in time contributions in the Euler equation which are prohibited due to their violation of the cosmic energy equation.

3. ***Decoupling of modes and dispersion scale***: A key insight emerges with the concept of the (time-dependent) dispersion scale k_σ, a hallmark of VPT and is related to the background value of velocity dispersion. It signifies that modes experience suppression when crossing the dispersion scale, an effect resulting from the back reaction due to orbit crossing (see Sec. 4.1). This feature enters the linear kernel ($n = 1$), which deviates from unity except for the $k \to 0$ limit. This modification accounts for the suppression of linear growth at smaller scales when $k > k_\sigma$, dictated by the velocity dispersion tensor's expectation value. The suppression is influenced by even higher cumulants only at

scales where $k \gg k_\sigma$, and their presence only enhances the effectiveness of the screening mechanism. This suppression is a crucial mechanism that is absent in SPT and leads to the convergence of the cumulant expansion for all wavenumbers (see Sec. 5.1, in particular Fig. 5.1).

4. ***Stability conditions and Gaussian case***: Stability considerations within the context of VPT revealed that the absence of exponential instabilities is tied to the non-Gaussian nature of the distribution function (see Sec. 5.4). Interestingly, the Gaussian case (vanishing average values of fourth and higher cumulants) remains stable, and these stability conditions (derived up to the eighth cumulant within linear approximation) are independent of the value of the velocity dispersion and spectral index.

5. ***Self-consistent solutions***: A significant achievement is the derivation of self-consistent solutions by solving the coupled equations for perturbations and background values (see Ch. 6). Our findings reveal that the screening of UV modes is more evident for higher spectral indices n_s. This is due to blue initial spectra inducing substantial orbit crossing on smaller scales, leading to rapid dispersion generation. Notably, this behavior causes convergence in the integral over the power spectra of cumulant perturbations that influence average values, even for considerably large n_s values. Importantly, the resulting background values for cumulants in this self-consistent approach also adhere to stability criteria.

6. ***Nonlinear VPT solutions and UV screening***: VPT closely resembles SPT, however with different nonlinear kernels, denoted as $F_{n,a}$ involving a broader set of perturbation modes labeled by $a = \delta, \theta, w_i, \ldots$ with additional degrees of freedom corresponding to the velocity dispersion and higher cumulants of the distribution function. In terms of nonlinear kernels within loop corrections, their suppression compared to equivalent SPT kernels occurs even when their total momentum $k < k_\sigma$, provided the loop momenta q_i intersect the dispersion scale (see Sec. 7.2). Consequently, once such a crossover transpires, the linear modes stop their growth and cease sourcing the nonlinear kernels, effectively reducing the UV sensitivity of VPT loops in contrast to SPT. This behavior allows for the computation of nonlinear corrections to power spectra, even in cosmologies featuring very blue power-law input spectra that do not converge in SPT (see Ch. 9). Insights into the corrections made to SPT can be provided by analytical results however, they do not fully capture the UV screening (see Sec. 7.1). Constraints on the VPT nonlinear kernels are derived from symmetries such as mass and momentum conservation, revealing the importance of including vorticity to respect these symmetries (see Sec. 7.3).

7. ***Validation through N-body simulations***: A pivotal aspect of this thesis is the validation of VPT predictions through comparisons with N-body simulation results. In a scaling universe scenario, we compare in Ch. 9 one-loop VPT predictions for density and velocity divergence power spectra, along with the bispectrum, against N-body simulations across a range of spectral indices ($-1 \leq n_s \leq +2$). The density power spectrum is used to fix the precise value of the background dispersion (see Fig. 9.2), which then fully determines all other power- and bispectra. Our findings exhibit good agreement up to the nonlinear scale across all cases, with an extended reach for higher n_s values. Despite the expectation of UV dominance within SPT for larger n_s, our inclusion of higher cumulants and efficient screening of small-scale modes by VPT shows the opposite behavior with improved UV screening the larger n_s. Consequently, VPT resolves perturbation theory predictions

with the observed suppression of nonlinear power in simulations, decoding the correlation between nonlinear and linear power with the spectral index.

8. ***Vorticity back reaction and power spectrum***: An intriguing prediction arising from VPT is the correct incorporation of vorticity. We find that it significantly influences the density contrast at third and higher orders. At the nonlinear scale, its impact on the density power spectrum is approximately in the range of 10% (see Fig. 9.3), while being reduced to a percent correction for lower n_s (see Sec. 9.1). Moreover, VPT makes a nontrivial prediction of the vorticity power spectrum, which we compute up to two-loop order to recover the correct large-scale behavior (see Sec. 9.4). Our comparison with N-body measurements confirms the transition from k^4 (one-loop) to k^2 (two-loop) scaling on large scales impliying a vorticity index of $n_w = 2$. In conclusion, considering vorticity back reaction is crucial both for physical reasons and due to its measurable impact on the density contrast.

9. ***Higher cumulants, vector and tensor modes***: The impact of higher cumulants as well as vorticity, vector and tensor modes on the nonlinear kernels of VPT is meticulously analyzed (see Sec. 9.1). The effects of vector modes of the stress tensor on $P_{\delta\delta}$ are noticeable, while the back reaction of tensor modes is negligible at one-loop. Our findings suggest that higher cumulants beyond the velocity dispersion tensor do not invalidate the VPT approach for $k \leq \mathcal{O}(k_{\rm nl})$. On the contrary, the agreement between second and third cumulant approximation and the low sensitivity to the fourth cumulant expectation value imply that truncating higher cumulants leads to an acceptable uncertainty for the one-loop density power spectrum in the mildly nonlinear regime and for the considered spectral indices n_s.

10. ***Stochastic gravitational wave background***: Incorporating dark matter anisotropic stress into perturbation theory inevitably leads to the generation of gravitational tensor modes. In fact, this sources an irreducible background of gravitational waves due to nonlinear velocity dispersion, induced by coupling of two scalar perturbations. This was explicitly carried out in Ch. 10. At ultra-low frequencies, corresponding to the horizon scale, this stochastic GW background peaks but has an overall tiny amplitude potentially unreachable for prospective GW experiments.

This thesis introduces VPT as a potent framework that bridges the gap between theoretical understanding and computational simulations, offering a compelling demonstration that perturbative techniques for understanding dark matter clustering can be systematically enhanced by leveraging the inherent collisionless dynamics. This novel approach addresses a significant limitation of the widely used SPT approximation through the effective screening of UV modes. This success serves as a basis for further advancements in cosmological perturbation theory, including its application within ΛCDM cosmologies. Future endeavors involve the exploration of two-loop corrections and the assessment of VPT's convergence, expected to excel particularly with blue spectra—a contrast to SPT. Additionally, investigating power spectra response functions, which reveal the nonlinear power spectrum's sensitivity to the initial spectrum, will provide further insight and serve as another test for the efficacy of VPT. Finally, redshift-space distortions (RSD) are an essential feature of the observed galaxy clustering statistics but are notoriously difficult to model in perturbation theory setups. RSD and related effects are known to be highly sensitive to velocity dispersion and higher moments of the velocity distribution which serves as an excellent issue to address in future.

Appendix A

Equations of motion up to the second cumulant

In this appendix we give the equations of motion up to the second cumulant when neglecting third and higher order cumulants in nonlinear terms (see Appendix D for those). We use non-bold symbols to denote wavevectors here and below as well as $k = p + q$.

Continuity equations

$$\delta_k' - \theta_k = \int_{pq} \left\{ \alpha_{pq} \theta_p \delta_q + \frac{(p \times q) \cdot w_p}{p^2} \delta_q \right\}, \tag{A.1}$$

$$A_k' - \theta_k = \int_{pq} \left\{ \frac{q \cdot p}{p^2} \theta_p A_q + \frac{(p \times q) \cdot w_p}{p^2} A_q \right\}, \tag{A.2}$$

where $A_k \equiv [\ln(1+\delta)]_k$.

Euler equation

$$\begin{aligned} &\theta_k' + \left(\frac{3}{2} \frac{\Omega_m}{f^2} - 1 \right) \theta_k - \frac{3}{2} \frac{\Omega_m}{f^2} \delta_k + k^2 \left(\delta\epsilon_k + g_k + \epsilon A_k \right) \\ &= \int_{pq} \left\{ \gamma_{pq} \theta_p \theta_q + \left(1 + \frac{2p \cdot q}{q^2} \right) \frac{(p \times q) \cdot w_p}{p^2} \theta_q - \frac{(p \times q) \cdot w_p}{p^2} \frac{(p \times q) \cdot w_q}{q^2} \right. \\ &\quad \left. - k \cdot p A_p \delta\epsilon_q - k \cdot q \, \frac{q \cdot p}{q^2} A_p g_q + \left(1 + \frac{2p \cdot q}{q^2} \right) A_p (p \times q) \cdot \nu_q - A_p p_i p_j t_{q,ij} \right\}, \end{aligned} \tag{A.3}$$

Equation of motion for the vorticity

$$\begin{aligned} &w_{k,i}' + \left(\frac{3}{2} \frac{\Omega_m}{f^2} - 1 \right) w_{k,i} + k^2 \nu_{k,i} \\ &= \int_{pq} \left\{ -\frac{1}{p^2} \theta_p (k \times (p \times w_q))_i + \frac{1}{p^2} (k \times ((p \times w_p) \times w_q))_i - \frac{p \cdot q}{q^2} (p \times q)_i A_p g_q + (p \times q)_i A_p \delta\epsilon_q \right. \\ &\quad \left. - \frac{1}{q^2} \Big[(p \cdot q)(k \cdot q \delta_{ij}^K - k_j q_i) - (p \times q)_i (p \times q)_j \Big] A_p \nu_{q,j} - \varepsilon_{ijn} k_j p_m A_p t_{q,nm} \right\}. \end{aligned} \tag{A.4}$$

Equations of motion for scalar, vector and tensor perturbations of ϵ_{ij}

$$
\begin{aligned}
&g_k' + 2\left(\frac{3}{2}\frac{\Omega_m}{f^2} - 1\right) g_k - 2\epsilon\theta_k \\
&= \int_{pq}\Bigg\{ \left(3\frac{(k\cdot p)^2}{k^2p^2} - 1\right)\theta_p\delta\epsilon_q + \frac{p\cdot q}{q^2}\left(\frac{k^2}{p^2} + \frac{1}{2} - \frac{3}{2}\frac{(k\cdot p)^2}{k^2p^2}\right)\theta_p g_q + 3\frac{k\cdot p}{p^2k^2}(p\times q)\cdot w_p\delta\epsilon_q \\
&\quad + \frac{1}{p^2}\left(\frac{3}{2}\frac{(k\cdot q)^2}{k^2q^2} + 3\frac{k\cdot qp\cdot q}{k^2q^2} - \frac{p\cdot q}{q^2} - \frac{1}{2}\right)(p\times q)\cdot w_p g_q - \frac{1}{k^2p^2q^2}\left(p\cdot qk^2 + 3k\cdot pk\cdot q\right)\theta_p(p\times q)\cdot\nu_q \\
&\quad - \frac{p\cdot q}{p^2q^2}(p\cdot q\delta^K_{ij} - q_ip_j)w_{p,i}\nu_{q,j} - \frac{6k\cdot q - k^2 + 3p\cdot q}{k^2p^2q^2}(p\times q)\cdot w_p(p\times q)\cdot\nu_q \\
&\quad - \frac{2k^2 - 3p\cdot q - 6k\cdot p}{2k^2p^2}p_ip_j\theta_p t_{q,ij} + \frac{2k^2(p\times w_p)_i + 9(p\times q)\cdot w_p p_i}{2k^2p^2}p_j t_{q,ij}\Bigg\},
\end{aligned}
\tag{A.5}
$$

$$
\begin{aligned}
&\delta\epsilon_k' + 2\left(\frac{3}{2}\frac{\Omega_m}{f^2} - 1\right)\delta\epsilon_k \\
&= \int_{pq}\Bigg\{ \frac{k\cdot pk\cdot q}{k^2p^2}\theta_p\delta\epsilon_q + \frac{p\cdot q}{2p^2q^2k^2}((k\cdot p)^2 - p^2k^2)\theta_p g_q + \frac{k\cdot q}{p^2k^2}(p\times q)\cdot w_p\delta\epsilon_q \\
&\quad + \frac{k^2q^2 - (k\cdot q)^2 + 2p\cdot qk\cdot p}{2p^2q^2k^2}(p\times q)\cdot w_p g_q + \frac{1}{q^2}\left(1 - \frac{(k\cdot p)^2}{k^2p^2}\right)\theta_p(p\times q)\cdot\nu_q \\
&\quad + \frac{p\cdot q}{p^2q^2}(p\cdot q\delta^K_{ij} - q_ip_j)w_{p,i}\nu_{q,j} + \frac{2k\cdot q - k^2 + p\cdot q}{k^2p^2q^2}(p\times q)\cdot w_p(p\times q)\cdot\nu_q \\
&\quad + \frac{2k\cdot q - p\cdot q}{2k^2p^2}p_ip_j\theta_p t_{q,ij} - \frac{2k^2(p\times w_p)_i + 3(p\times q)\cdot w_p p_i}{2k^2p^2}p_j t_{q,ij}\Bigg\} - Q\delta^{(3)}(k)\,,
\end{aligned}
\tag{A.6}
$$

$$
\begin{aligned}
&\nu_{k,i}' + 2\left(\frac{3}{2}\frac{\Omega_m}{f^2} - 1\right)\nu_{k,i} - \epsilon w_{k,i} \\
&= \int_{pq}\Bigg\{ -2\frac{k\cdot p(p\times q)_i}{k^2p^2}\theta_p\delta\epsilon_q + \frac{p\cdot qk\cdot p(p\times q)_i}{k^2p^2q^2}\theta_p g_q \\
&\quad + \frac{k\cdot p(k\cdot p\delta^K_{ij} - p_ik_j) - (p\times q)_i(p\times q)_j}{k^2p^2}w_{p,j}\delta\epsilon_q \\
&\quad + \frac{k\cdot qp\cdot q(k\cdot p\delta^K_{ij} - p_ik_j) + (p\times q)_i(p\times q)_j(k^2 - p^2)}{k^2p^2q^2}w_{p,j}g_q \\
&\quad + \frac{k^2p\cdot q(k\cdot q\delta^K_{ij} - q_ik_j) - (p\times q)_i(p\times q)_j(p^2 - q^2)}{k^2p^2q^2}\theta_p\nu_{q,j} \\
&\quad + \frac{k^2 - p^2}{k^2p^2q^2}\left[(k\times(p\times w_p))_i(p\times q)\cdot\nu_q - (p\times q)\cdot w_p(k\times(q\times\nu_q))_i\right] \\
&\quad - 2\frac{(p\times q)_i}{k^2p^2q^2}(p\times q)\cdot w_p(p\times q)\cdot\nu_q + \frac{(k^2 - q^2)\epsilon_{inm}k_n - (p\times q)_ip_m}{k^2p^2}p_j\theta_p t_{q,mj} \\
&\quad + \frac{2(p\times q)\cdot w_p\epsilon_{inm}k_n - (k\times(p\times w_p))_ip_m}{k^2p^2}p_j t_{q,mj}\Bigg\},
\end{aligned}
\tag{A.7}
$$

$$
\begin{aligned}
& t'_{k,ij} + 2\left(\frac{3}{2}\frac{\Omega_m}{f^2} - 1\right) t_{k,ij} \\
&= \int_{pq} \Bigg\{ \left[\left(\delta^K_{ij} - \frac{k_i k_j}{k^2}\right) - 2\frac{(p\times q)_i (p\times q)_j}{(p\times q)^2} \right] \frac{(p\times q)^2}{k^2 p^2} \left[\theta_p \delta\epsilon_q - \frac{1}{2}\frac{p\cdot q}{q^2}\theta_p g_q + \theta_p \frac{(p\times q)\cdot \nu_q}{q^2} \right] \\
&\quad + \frac{1}{k^2 p^2} \Bigg[(q^2 k_i - k^2 q_i)(p_m \delta^K_{j\ell} + p_\ell \delta^K_{jm}) + (q^2 k_j - k^2 q_j)(p_m \delta^K_{i\ell} + p_\ell \delta^K_{im}) \\
&\quad + p\cdot q \left(\delta^K_{i\ell}\delta^K_{jm} + \delta^K_{im}\delta^K_{j\ell} - \frac{p_\ell p_m}{k^2}\left(\delta^K_{ij} - \frac{k_i k_j}{k^2}\right)\right) \\
&\quad - 2\frac{p_\ell p_m}{k^2}\left(k_i p_j + k_j p_i - k_i k_j + q^2 \delta^K_{ij} - k\cdot p \frac{k_i k_j}{k^2}\right) \Bigg] \theta_p t_{q,\ell m} \\
&\quad + \frac{1}{k^2 p^2} \Bigg[(p\times w_p)_i \left(k_j (k\cdot p) - k^2 p_j)\right) + (p\times w_p)_j \left(k_i (k\cdot p) - k^2 p_i)\right) \\
&\quad + (p\times q)\cdot w_p \left(k\cdot p \left(\delta^K_{ij} + \frac{k_i k_j}{k^2}\right) - k_i p_j - k_j p_i \right) \Bigg] \delta\epsilon_q \\
&\quad + \frac{1}{p^2 q^2} \Bigg[(p\times w_p)_i (p\cdot q)\left(k\cdot q \frac{k_j}{k^2} - q_j\right) + (p\times w_p)_j (p\cdot q)\left(k\cdot q\frac{k_i}{k^2} - q_i\right) \\
&\quad + (p\times q)\cdot w_p \Bigg\{ \left(\delta^K_{ij} + \frac{k_i k_j}{k^2}\right) \frac{k\cdot q(k\cdot q + 2p\cdot q)}{2k^2} + q_i q_j \\
&\quad + \frac{1}{2}(k^2 - p^2)\left(\delta^K_{ij} - \frac{k_i k_j}{k^2} + 2\frac{k_i q_j + k_j q_i}{k^2}\right) \Bigg\} \Bigg] g_q \\
&\quad + \frac{p^2 k_i - k^2 p_i}{k^2 p^2 q^2} \left[(p\times q)\cdot \nu_q (p\times w_p)_j - (p\times q)\cdot w_p (q\times \nu_q)_j \right] \\
&\quad + \frac{p^2 k_j - k^2 p_j}{k^2 p^2 q^2} \left[(p\times q)\cdot \nu_q (p\times w_p)_i - (p\times q)\cdot w_p (q\times \nu_q)_i \right] \\
&\quad + \frac{p\cdot q}{p^2 q^2} \Bigg[(p\times w_p)_i (q\times \nu_q)_j + (p\times w_p)_j (q\times \nu_q)_i - (p\times w_p)\cdot(q\times\nu_q)\left(\delta^K_{ij} - \frac{k_i k_j}{k^2}\right) \Bigg] \\
&\quad - \frac{(p\times q)\cdot w_p (p\times q)\cdot \nu_q}{p^2 q^2} \left[\left(\delta^K_{ij} + \frac{k_i k_j}{k^2}\right)\frac{3p\cdot q + 2q^2}{k^2} - 2\frac{k_i q_j + k_j q_i}{k^2} - \left(\delta^K_{ij} - \frac{k_i k_j}{k^2}\right) \right] \\
&\quad + \frac{1}{2p^2} \Bigg[2\left(\delta^K_{ij} - \frac{k_i k_j}{k^2}\right)\left[(p\times w_p)_m p_n + (p\times w_p)_n p_m\right] \\
&\quad - 2(p\times w_p)_i \left(p_n \delta^K_{jm} + p_m \delta^K_{jn} - 2\frac{p_m p_n k_j}{k^2}\right) - 2(p\times w_p)_j \left(p_n \delta^K_{im} + p_m \delta^K_{in} - 2\frac{p_m p_n k_i}{k^2}\right) \\
&\quad + (p\times q)\cdot w_p \Bigg(6\frac{p_m p_n}{k^2}\left(\delta^K_{ij} + \frac{k_i k_j}{k^2}\right) + \delta^K_{im}\left(\delta^K_{jn} - 4\frac{p_n k_j}{k^2}\right) \\
&\quad + \delta^K_{jn}\left(\delta^K_{ik} - 4\frac{p_m k_i}{k^2}\right) + \delta^K_{in}\left(\delta^K_{jm} - 4\frac{p_m k_j}{k^2}\right) + \delta^K_{jm}\left(\delta^K_{in} - 4\frac{p_n k_i}{k^2}\right) \Bigg) \Bigg] t_{q,mn} \Bigg\}. \qquad \text{(A.8)}
\end{aligned}
$$

Appendix B

Vertices up to the second cumulant

In this appendix, we collect all vertices $\gamma_{abc}(p,q)$ for perturbation modes up to the second cumulant. We write ϵ instead of $\delta\epsilon$ in the index for simplicity. Furthermore $k \equiv p+q$ in the vectorial sense.

Vertices involving only scalar perturbations

$$\begin{aligned}
\gamma_{\delta\theta\delta}(p,q) &= \frac{1}{2}\alpha_{pq} = \frac{(p+q)\cdot p}{2p^2}\,, \\
\gamma_{\theta\theta\theta}(p,q) &= \gamma_{pq} = \frac{(p+q)^2 p\cdot q}{2p^2q^2}\,, \\
\gamma_{A\theta A}(p,q) &= \frac{1}{2}\frac{q\cdot p}{p^2}\,, \\
\gamma_{\theta A g}(p,q) &= -\frac{1}{2}(p+q)\cdot q\ \frac{q\cdot p}{q^2}\,, \\
\gamma_{\theta A \epsilon}(p,q) &= -\frac{1}{2}(p+q)\cdot p\,,
\end{aligned} \tag{B.1}$$

$$\begin{aligned}
\gamma_{g\theta g}(p,q) &= \frac{1}{2}\frac{p\cdot q}{q^2}\left(\frac{k^2}{p^2}+\frac{1}{2}-\frac{3}{2}\frac{(k\cdot p)^2}{k^2p^2}\right)\,, \\
\gamma_{g\theta\epsilon}(p,q) &= \frac{1}{2}\left(3\frac{(k\cdot p)^2}{k^2p^2}-1\right)\,, \\
\gamma_{\epsilon\theta g}(p,q) &= \frac{1}{2}\frac{p\cdot q}{2p^2q^2k^2}((k\cdot p)^2-p^2k^2)\,, \\
\gamma_{\epsilon\theta\epsilon}(p,q) &= \frac{1}{2}\frac{k\cdot pk\cdot q}{k^2p^2}\,.
\end{aligned} \tag{B.2}$$

Vertices involving at most one vorticity, vector or tensor perturbation

$$
\begin{aligned}
\gamma_{\delta w_i \delta}(p,q) &= \gamma_{A w_i A}(p,q) = \frac{1}{2}\frac{(p\times q)_i}{p^2}\,,\\
\gamma_{\theta w_i \theta}(p,q) &= \frac{1}{2}\left(1+\frac{2p\cdot q}{q^2}\right)\frac{(p\times q)_i}{p^2}\,,\\
\gamma_{\theta A \nu_i}(p,q) &= \frac{1}{2}\left(1+\frac{2p\cdot q}{q^2}\right)(p\times q)_i\,,\\
\gamma_{\theta A t_{ij}}(p,q) &= -\frac{1}{2}p_i p_j\,,
\end{aligned}
\tag{B.3}
$$

$$
\begin{aligned}
\gamma_{g w_i g}(p,q) &= \frac{1}{2}\frac{1}{p^2}\left(\frac{3}{2}\frac{(k\cdot q)^2}{k^2q^2}+3\frac{k\cdot q p\cdot q}{k^2q^2}-\frac{p\cdot q}{q^2}-\frac{1}{2}\right)(p\times q)_i\,,\\
\gamma_{g w_i \epsilon}(p,q) &= \frac{1}{2}3\frac{k\cdot p}{p^2k^2}(p\times q)_i\,,\\
\gamma_{g\theta \nu_i}(p,q) &= -\frac{1}{2}\frac{1}{k^2p^2q^2}\left(p\cdot q k^2+3k\cdot p k\cdot q\right)(p\times q)_i\,,\\
\gamma_{g\theta t_{ij}}(p,q) &= -\frac{1}{2}\frac{2k^2-3p\cdot q-6k\cdot p}{2k^2p^2}p_i p_j\,,
\end{aligned}
\tag{B.4}
$$

$$
\begin{aligned}
\gamma_{\epsilon w_i g}(p,q) &= \frac{1}{2}\frac{k^2q^2-(k\cdot q)^2+2p\cdot q k\cdot p}{2p^2q^2k^2}(p\times q)_i\,,\\
\gamma_{\epsilon w_i \epsilon}(p,q) &= \frac{1}{2}\frac{k\cdot q}{p^2k^2}(p\times q)_i\,,\\
\gamma_{\epsilon\theta \nu_i}(p,q) &= \frac{1}{2}\frac{1}{q^2}\left(1-\frac{(k\cdot p)^2}{k^2p^2}\right)(p\times q)_i\,,\\
\gamma_{\epsilon\theta t_{ij}}(p,q) &= \frac{1}{2}\frac{2k\cdot q-p\cdot q}{2k^2p^2}p_i p_j\,,
\end{aligned}
\tag{B.5}
$$

$$
\begin{aligned}
\gamma_{w_i A g}(p,q) &= -\frac{1}{2}\frac{p\cdot q}{q^2}(p\times q)_i\,,\\
\gamma_{w_i A \epsilon}(p,q) &= \frac{1}{2}(p\times q)_i\,,\\
\gamma_{\nu_i\theta g}(p,q) &= \frac{1}{2}\frac{p\cdot q k\cdot p(p\times q)_i}{k^2p^2q^2}\,,\\
\gamma_{\nu_i\theta \epsilon}(p,q) &= -\frac{1}{2}2\frac{k\cdot p(p\times q)_i}{k^2p^2}\,,
\end{aligned}
\tag{B.6}
$$

$$
\begin{aligned}
\gamma_{t_{ij}\theta g}(p,q) &= -\frac{1}{2}\frac{(p\times q)^2\,p\cdot q}{2k^2p^2q^2}\left\{\left(\delta^K_{ij}-\frac{k_ik_j}{k^2}\right)-2\frac{(p\times q)_i(p\times q)_j}{(p\times q)^2}\right\},\\
\gamma_{t_{ij}\theta \epsilon}(p,q) &= \frac{1}{2}\frac{(p\times q)^2}{k^2p^2}\left\{\left(\delta^K_{ij}-\frac{k_ik_j}{k^2}\right)-2\frac{(p\times q)_i(p\times q)_j}{(p\times q)^2}\right\}.
\end{aligned}
\tag{B.7}
$$

Vertices involving two vorticity, vector or tensor perturbations

$$
\begin{aligned}
\gamma_{\theta w_i w_j}(p,q) &= -\frac{(p\times q)_i (p\times q)_j}{p^2 q^2}\,, \\
\gamma_{\epsilon w_i \nu_j}(p,q) &= \frac{1}{2}\,\frac{(p\cdot q - p^2 + q^2)(p\times q)_i (p\times q)_j}{p^2 q^2 k^2}\,, \\
&\quad + \frac{1}{2}\frac{k^2 (p\cdot q)\left(\delta^K_{ij}\, p\cdot q - p_j q_i\right)}{p^2 q^2 k^2}\,, \\
\gamma_{g w_i \nu_j}(p,q) &= \frac{1}{2}\,\frac{(p^2 - 5q^2 - 7p\cdot q)(p\times q)_i (p\times q)_j}{p^2 q^2 k^2}\,, \\
&\quad - \frac{1}{2}\frac{k^2 (p\cdot q)\left(\delta^K_{ij}\, p\cdot q - p_j q_i\right)}{p^2 q^2 k^2}\,, \\
\gamma_{g w_i t_{jm}}(p,q) &= \frac{1}{2}\,\frac{9(p\times q)_i p_j + 2k^2 \varepsilon_{ijl} p_l}{2k^2 p^2} p_m\,, \\
\gamma_{\epsilon w_i t_{jm}}(p,q) &= -\frac{1}{2}\,\frac{3(p\times q)_i p_j + 2k^2 \varepsilon_{ijl} p_l}{2k^2 p^2} p_m\,,
\end{aligned}
\tag{B.8}
$$

$$
\begin{aligned}
\gamma_{w_i \theta w_j}(p,q) &= \frac{1}{2}\,\frac{\delta^K_{ij} p\cdot k - p_i p_j}{p^2}\,, \\
\gamma_{w_i A \nu_j}(p,q) &= \frac{1}{2}\,\frac{(p\times q)_i (p\times q)_j + (p\cdot q)\left(p_j q_i - \delta^K_{ij}(k\cdot q)\right)}{q^2}\,, \\
\gamma_{w_i A t_{nm}}(p,q) &= -\frac{1}{2}\varepsilon_{ijn} k_j p_m\,, \\
\gamma_{\nu_i w_j g}(p,q) &= \frac{1}{2}\,\frac{\left(\delta^K_{ij} p\cdot k - p_i q_j\right)(q\cdot k)(p\cdot q)}{p^2 q^2 k^2} \\
&\quad + \frac{1}{2}\frac{(p\times q)_i (p\times q)_j (k^2 - p^2)}{p^2 q^2 k^2}\,, \\
\gamma_{\nu_i w_j \epsilon}(p,q) &= \frac{1}{2}\,\frac{\left(\delta^K_{ij} p\cdot k - p_i q_j\right)(p\cdot k) - (p\times q)_i (p\times q)_j}{p^2 k^2}\,, \\
\gamma_{\nu_i \theta \nu_j}(p,q) &= \frac{1}{2}\,\frac{\left(\delta^K_{ij} q\cdot k - p_j q_i\right)(p\cdot q) k^2 + (p\times q)_i (p\times q)_j (q^2 - p^2)}{p^2 q^2 k^2}\,, \\
\gamma_{\nu_i \theta t_{mj}}(p,q) &= \frac{1}{2}\,\frac{(k^2 - q^2)\varepsilon_{inm} k_n - (p\times q)_i p_m}{k^2 p^2} p_j\,,
\end{aligned}
$$

$$
\begin{aligned}
\gamma_{t_{ij}w_\ell g}(p,q) &= \frac{1}{2}\,\frac{1}{p^2q^2}\Bigg[\varepsilon_{in\ell}\,p_n(p\cdot q)\left(k\cdot q\frac{k_j}{k^2}-q_j\right)+\varepsilon_{jn\ell}\,p_n(p\cdot q)\left(k\cdot q\frac{k_i}{k^2}-q_i\right)\\
&\quad+\varepsilon_{\ell nm}\,p_nq_m\Bigg\{\left(\delta^K_{ij}+\frac{k_ik_j}{k^2}\right)\frac{k\cdot q(k\cdot q+2p\cdot q)}{2k^2}+q_iq_j\\
&\quad+\frac{1}{2}(k^2-p^2)\left(\delta^K_{ij}-\frac{k_ik_j}{k^2}+2\frac{k_iq_j+k_jq_i}{k^2}\right)\Bigg\}\Bigg],\\
\gamma_{t_{ij}w_\ell\epsilon}(p,q) &= \frac{1}{2}\,\frac{p_n}{k^2p^2}\Bigg[\varepsilon_{in\ell}\left(k_j(k\cdot p)-k^2p_j)\right)+\varepsilon_{jn\ell}\left(k_i(k\cdot p)-k^2p_i)\right)\\
&\quad+\varepsilon_{\ell nm}\,q_m\left(k\cdot p\left(\delta^K_{ij}+\frac{k_ik_j}{k^2}\right)-k_ip_j-k_jp_i\right)\Bigg],\\
\gamma_{t_{ij}\theta\nu_\ell}(p,q) &= \frac{1}{2}\,\frac{\varepsilon_{mn\ell}\,p_mq_n(p\times q)^2}{k^2p^2q^2}\left[\left(\delta^K_{ij}-\frac{k^ik^j}{k^2}\right)-2\frac{(p\times q)_i(p\times q)_j}{(p\times q)^2}\right],\\
\gamma_{t_{ij}\theta t_{\ell m}}(p,q) &= \frac{1}{2}\,\frac{1}{k^2p^2}\Bigg[(q^2k_i-k^2q_i)(p_m\delta^K_{j\ell}+p_\ell\delta^K_{jm})+(q^2k_j-k^2q_j)(p_m\delta^K_{i\ell}+p_\ell\delta^K_{im})\\
&\quad+p\cdot q\left(\delta^K_{i\ell}\delta^K_{jm}+\delta^K_{im}\delta^K_{j\ell}-\frac{p_\ell p_m}{k^2}\left(\delta^K_{ij}-\frac{k_ik_j}{k^2}\right)\right)\\
&\quad-2\frac{p_\ell p_m}{k^2}\left(k_ip_j+k_jp_i-k_ik_j+q^2\delta^K_{ij}-k\cdot p\frac{k_ik_j}{k^2}\right)\Bigg].
\end{aligned}
\tag{B.9}
$$

Vertices involving three vorticity, vector or tensor perturbations

$$
\begin{aligned}
\gamma_{w_iw_jw_\ell}(p,q) &= \frac{\varepsilon_{imj}\,p_\ell p_m+\delta^K_{i\ell}(p\times q)_j}{2p^2}+\frac{\varepsilon_{im\ell}\,q_jq_m-\delta^K_{ij}(p\times q)_\ell}{2q^2},\\
\gamma_{\nu_iw_j\nu_\ell}(p,q) &= \frac{1}{2}\,\frac{1}{p^2q^2k^2}\Bigg\{\left[\delta^K_{i\ell}\,q\cdot k-p_\ell q_i\right](p\times q)_j(k^2-p^2)\\
&\quad-\left[\delta^K_{ij}\,p\cdot k-p_iq_j\right](p\times q)_\ell(k^2-p^2)\\
&\quad-2(p\times q)_i(p\times q)_j(p\times q)_\ell\Bigg\},\\
\gamma_{\nu_iw_\ell t_{mj}}(p,q) &= \frac{1}{2}\,\frac{2(p\times q)_\ell\,\varepsilon_{inm}k_n-p_m\left(p_iq_\ell-k\cdot p\delta^K_{i\ell}\right)}{k^2p^2}p_j\,,
\end{aligned}
$$

$$
\begin{aligned}
\gamma_{t_{ij}w_\ell\nu_m}(p,q) &= \frac{1}{2}\frac{p^2k_i-k^2p_i}{k^2p^2q^2}\left[\varepsilon_{mns}\,\varepsilon_{jr\ell}\,p_r-\varepsilon_{\ell ns}\,\varepsilon_{jrm}\,q_r\right]p_nq_s \\
&\quad+\frac{1}{2}\frac{p^2k_j-k^2p_j}{k^2p^2q^2}\left[\varepsilon_{mns}\,\varepsilon_{ir\ell}\,p_r-\varepsilon_{\ell ns}\,\varepsilon_{irm}\,q_r\right]p_nq_s \\
&\quad+\frac{1}{2}\frac{p\cdot q}{p^2q^2}p_nq_r\left[\varepsilon_{in\ell}\,\varepsilon_{jrm}+\varepsilon_{jn\ell}\,\varepsilon_{irm}-\varepsilon_{sn\ell}\,\varepsilon_{srm}\left(\delta^K_{ij}-\frac{k_ik_j}{k^2}\right)\right] \\
&\quad-\frac{1}{2}\frac{\varepsilon_{\ell ns}\,\varepsilon_{mkr}\,p_np_kq_sq_r}{p^2q^2}\left[\left(\delta^K_{ij}+\frac{k_ik_j}{k^2}\right)\frac{3p\cdot q+2q^2}{k^2}-2\frac{k_iq_j+k_jq_i}{k^2}-\left(\delta^K_{ij}-\frac{k_ik_j}{k^2}\right)\right], \\
\gamma_{t_{ij}w_\ell t_{mn}}(p,q) &= \frac{1}{2}\frac{1}{2p^2}\left[2\left(\delta^K_{ij}-\frac{k_ik_j}{k^2}\right)\left[\varepsilon_{mr\ell}\,p_n+\varepsilon_{nr\ell}\,p_m\right]p_r\right. \\
&\quad-2\varepsilon_{ir\ell}\,p_r\left(p_n\delta^K_{jm}+p_m\delta^K_{jn}-2\frac{p_mp_nk_j}{k^2}\right)-2\varepsilon_{jr\ell}\,p_r\left(p_n\delta^K_{im}+p_m\delta^K_{in}-2\frac{p_mp_nk_i}{k^2}\right) \\
&\quad+\varepsilon_{\ell rs}\,p_rq_s\left(6\frac{p_mp_n}{k^2}\left(\delta^K_{ij}+\frac{k_ik_j}{k^2}\right)+\delta^K_{im}\left(\delta^K_{jn}-4\frac{p_nk_j}{k^2}\right)\right. \\
&\quad\left.\left.+\delta^K_{jn}\left(\delta^K_{ik}-4\frac{p_mk_i}{k^2}\right)+\delta^K_{in}\left(\delta^K_{jm}-4\frac{p_mk_j}{k^2}\right)+\delta^K_{jm}\left(\delta^K_{in}-4\frac{p_nk_i}{k^2}\right)\right)\right]. \qquad \text{(B.10)}
\end{aligned}
$$

Appendix C

Vertices in transverse basis up to the second cumulant

In this appendix we present nonlinear vertices involving vorticity and vector perturbations when using the transverse basis, i.e. keeping track of the two independent degrees of freedom for the vector perturbations (see Sec. 8.2 for details). To achieve this, we define *projection functions*, which project the cartesian index dependence onto the transverse components. Finally, the resulting vertices do depend on these projection functions. In the following, we give results for vertices which only show up starting at two-loop order.

Vertices involving at most two vorticity or vector perturbations in transverse basis

For this type of vertices we have to incorporate following projection functions given by

$$
\begin{aligned}
V_{1,pq}^{p\alpha,q\beta} &\equiv (p\times q)_i (p\times q)_j b_{p\alpha,i} b_{q\beta,j} = V_{1,pq}^{p\alpha} V_{1,pq}^{q\beta}\,,\\
V_{1,pq}^{k\alpha,q\beta} &\equiv (p\times q)_i (p\times q)_j P_{k\alpha,i} b_{q\beta,j} = V_{1,pq}^{k\alpha} V_{1,pq}^{q\beta}\,,\\
V_{1,pq}^{k\alpha,p\beta} &\equiv (p\times q)_i (p\times q)_j P_{k\alpha,i} b_{p\beta,j} = V_{1,pq}^{k\alpha} V_{1,pq}^{p\beta}\,,\\
V_{2,pq}^{p\alpha,q\beta} &\equiv \delta_{ij} b_{p\alpha,i} b_{q\beta,j}\,,\\
V_{2,pq}^{k\alpha,q\beta} &\equiv \delta_{ij} P_{k\alpha,i} b_{q\beta,j}\,,\\
V_{2,pq}^{k\alpha,p\beta} &\equiv \delta_{ij} P_{k\alpha,i} b_{p\beta,j}\,,\\
V_{3,pq}^{p\alpha,q\beta} &\equiv p_j q_i b_{p\alpha,i} b_{q\beta,j}\,,\\
V_{3,pq}^{k\alpha,q\beta} &\equiv p_j q_i P_{k\alpha,i} b_{q\beta,j}\,,\\
V_{4,pq}^{k\alpha,q\beta} &\equiv p_i p_j P_{k\alpha,i} b_{q\beta,j}\,,\\
V_{5,pq}^{k\alpha,p\beta} &\equiv p_i q_j P_{k\alpha,i} b_{p\beta,j}\,,
\end{aligned}
\tag{C.1}
$$

where $\alpha,\beta = 1,2$. Introducing the following determinants

$$
D_{pQ_q} \equiv \det(p, Q_p, Q_q) = (p\times Q_p)\cdot Q_q\,,
\tag{C.2}
$$

and using Eq. (C.1), the vertices involving at most two vorticity or vector perturbations become,

$$
\begin{aligned}
\gamma_{\theta w_{p\alpha} w_{q\beta}}(p,q) &\equiv -\frac{V_{1,pq}^{p\alpha,q\beta}}{p^2 q^2}\,, \\
\gamma_{\epsilon w_{p\alpha} \nu_{q\beta}}(p,q) &\equiv \frac{V_{1,pq}^{p\alpha,q\beta}(p\cdot q - p^2 + q^2) + k^2 (p\cdot q)\left(V_{2,pq}^{p\alpha,q\beta}\, p\cdot q - V_{3,pq}^{p\alpha,q\beta}\right)}{p^2 q^2 k^2}\,, \\
\gamma_{g w_{p\alpha} \nu_{q\beta}}(p,q) &\equiv \frac{V_{1,pq}^{p\alpha,q\beta}(p^2 - 5q^2 - 7p\cdot q) - k^2 (p\cdot q)\left(V_{2,pq}^{p\alpha,q\beta}\, p\cdot q - V_{3,pq}^{p\alpha,q\beta}\right)}{p^2 q^2 k^2}\,, \\
\gamma_{w_{k\alpha} \theta w_{q\beta}}(p,q) &\equiv (p\cdot k)\frac{V_{2,pq}^{k\alpha,q\beta}}{p^2} - \frac{V_{4,pq}^{k\alpha,q\beta}}{p^2}\,, \\
\gamma_{w_{k\alpha} A \nu_{q\beta}}(p,q) &\equiv \frac{V_{1,pq}^{k\alpha,q\beta} + (p\cdot q)\left(V_{3,pq}^{k\alpha,q\beta} - V_{2,pq}^{k\alpha,q\beta}(k\cdot q)\right)}{q^2}\,, \\
\gamma_{\nu_{k\alpha} w_{p\beta} \epsilon}(p,q) &\equiv \frac{\left(V_{2,pq}^{k\alpha,p\beta}\, p\cdot k - V_{5,pq}^{k\alpha,p\beta}\right)(p\cdot k) - V_{1,pq}^{k\alpha,p\beta}}{p^2 k^2}\,, \\
\gamma_{\nu_{k\alpha} w_{p\beta} g}(p,q) &\equiv \frac{\left(V_{2,pq}^{k\alpha,p\beta}\, p\cdot k - V_{5,pq}^{k\alpha,p\beta}\right)(q\cdot k)(p\cdot q) + V_{1,pq}^{k\alpha,p\beta}(k^2 - p^2)}{p^2 q^2 k^2}\,, \\
\gamma_{\nu_{k\alpha} \theta \nu_{q\beta}}(p,q) &\equiv \frac{\left(V_{2,pq}^{k\alpha,q\beta}\, q\cdot k - V_{3,pq}^{k\alpha,q\beta}\right)(p\cdot q)k^2 + V_{1,pq}^{k\alpha,q\beta}(q^2 - p^2)}{p^2 q^2 k^2}\,,
\end{aligned}
\tag{C.3}
$$

where each of the above vertices is expanded into four individual vertices, given the definitions using Eq. (C.1). Those can explicitly expressed in terms of the projection functions expressed in Eq. (8.25), given by

$$
\begin{aligned}
V_{1,pq}^{p\alpha,q\beta} &= V_{1,pq}^{p\alpha} V_{1,pq}^{q\beta}\,, \\
V_{1,pq}^{k\alpha,q\beta} &= V_{1,pq}^{k\alpha} V_{1,pq}^{q\beta}\,, \\
V_{1,pq}^{k\alpha,p\beta} &= V_{1,pq}^{k\alpha} V_{1,pq}^{p\beta}\,, \\
V_{2,pq}^{p\alpha,q\beta} &\to \text{explicit}\,, \\
V_{2,pq}^{k\alpha,q\beta} &\to \text{explicit}\,, \\
V_{2,pq}^{k\alpha,p\beta} &= V_{2,qp}^{k\alpha,p\beta}\,, \\
V_{3,pq}^{p\alpha,q\beta} &\propto V_{1,pq}^{p\tilde{\alpha},q\tilde{\beta}}\,, \\
V_{3,pq}^{k\alpha,q\beta} &\propto V_{1,pq}^{k\tilde{\alpha},q\tilde{\beta}}\,, \\
V_{4,pq}^{k\alpha,q\beta} &= -V_{3,pq}^{k\alpha,q\beta}\,, \\
V_{5,pq}^{k\alpha,p\beta} &= V_{3,qp}^{k\alpha,p\beta}
\end{aligned}
\tag{C.4}
$$

where $\tilde{\alpha}, \tilde{\beta} = 1, 2$ but $\tilde{\alpha} \neq \alpha$ and $\tilde{\beta} \neq \beta$. The remaining explicit expressions are given by

$$
\begin{aligned}
V_{2,pq}^{p1,q1} &= b_{p1} \cdot b_{q1} = \mathcal{N}_{p1}\mathcal{N}_{q1}(p \times Q_p) \cdot (q \times Q_q) \\
&= \mathcal{N}_{p1}\mathcal{N}_{q1}[(p \cdot q)(Q_p \cdot Q_q) - (p \cdot Q_q)(\boldsymbol{Q}_p \cdot \boldsymbol{q})] \,, \\
V_{2,pq}^{p1,q2} &= (p \times Q_p) \cdot (q \times (q \times Q_q))\mathcal{N}_{p1}\mathcal{N}_{q2} \\
&= [D_{pq}(\boldsymbol{q} \cdot \boldsymbol{Q}_q) - D_{pQ_q}q^2]\mathcal{N}_{p1}\mathcal{N}_{q2} \,, \\
V_{2,pq}^{p2,q1} &= (p \times (p \times Q_p)) \cdot (q \times Q_q)\mathcal{N}_{p2}\mathcal{N}_{q1} \\
&= [D_{qp}(\boldsymbol{p} \cdot \boldsymbol{Q}_p) - D_{qQ_p}p^2]\mathcal{N}_{p2}\mathcal{N}_{q1} = V_{2,qp}^{p1,q2} \,, \\
V_{2,pq}^{p2,q2} &= (q \times (q \times Q_q)) \cdot (p \times (p \times Q_p))\mathcal{N}_{p2}\mathcal{N}_{q2} \\
&= [(\boldsymbol{p} \cdot \boldsymbol{Q}_p)(\boldsymbol{p} \cdot \boldsymbol{q})(\boldsymbol{q} \cdot \boldsymbol{Q}_q) + (\boldsymbol{Q}_p \cdot \boldsymbol{Q}_q)p^2q^2 \\
&\qquad - (\boldsymbol{p} \cdot \boldsymbol{Q}_q)(\boldsymbol{p} \cdot \boldsymbol{Q}_p)q^2 - (\boldsymbol{q} \cdot \boldsymbol{Q}_p)(\boldsymbol{q} \cdot \boldsymbol{Q}_q)p^2]\mathcal{N}_{p2}\mathcal{N}_{q2} \,, \\
V_{2,pq}^{k1,q1} &= P_{k1} \cdot b_{q1} = \frac{b_{k1} \cdot b_{q1}}{|b_{k1}|^2} \\
&= \frac{\mathcal{N}_{q1}}{\mathcal{N}_{k1}} \frac{(\boldsymbol{k} \times \boldsymbol{Q}_k) \cdot (\boldsymbol{q} \times \boldsymbol{Q}_q)}{(\boldsymbol{k} \times \boldsymbol{Q}_k)^2} \\
&= \frac{\mathcal{N}_{q1}}{\mathcal{N}_{k1}} \frac{(\boldsymbol{k} \cdot \boldsymbol{q})(\boldsymbol{Q}_k \cdot \boldsymbol{Q}_q) - (\boldsymbol{k} \cdot \boldsymbol{Q}_q)(\boldsymbol{q} \cdot \boldsymbol{Q}_k)}{(\boldsymbol{k} \times \boldsymbol{Q}_k)^2} \,, \\
V_{2,pq}^{k1,q2} &= \frac{\mathcal{N}_{q2}}{\mathcal{N}_{k1}} \frac{(\boldsymbol{k} \times \boldsymbol{Q}_k) \cdot (\boldsymbol{q} \times (\boldsymbol{q} \times \boldsymbol{Q}_q))}{(\boldsymbol{k} \times \boldsymbol{Q}_k)^2} \\
&= \frac{\mathcal{N}_{q2}}{\mathcal{N}_{k1}} \frac{D_{kq}(\boldsymbol{q} \cdot \boldsymbol{Q}_q) - D_{kQ_q}q^2}{(\boldsymbol{k} \times \boldsymbol{Q}_k)^2} \,, \\
V_{2,pq}^{k2,q1} &= \frac{\mathcal{N}_{q1}}{\mathcal{N}_{k2}} \frac{(\boldsymbol{q} \times \boldsymbol{Q}_q) \cdot (\boldsymbol{k} \times (\boldsymbol{k} \times \boldsymbol{Q}_k))}{k^2(\boldsymbol{k} \times \boldsymbol{Q}_k)^2} \\
&= \frac{\mathcal{N}_{q1}}{\mathcal{N}_{k2}} \frac{D_{qk}(\boldsymbol{k} \cdot \boldsymbol{Q}_k) - D_{qQ_k}k^2}{k^2(\boldsymbol{k} \times \boldsymbol{Q}_k)^2} \,, \\
V_{2,pq}^{k2,q2} &= \frac{\mathcal{N}_{q2}}{\mathcal{N}_{k2}} \frac{(\boldsymbol{q} \times (\boldsymbol{q} \times \boldsymbol{Q}_q)) \cdot (\boldsymbol{k} \times (\boldsymbol{k} \times \boldsymbol{Q}_k))}{k^2(\boldsymbol{k} \times \boldsymbol{Q}_k)^2} \\
&= \frac{\mathcal{N}_{q2}}{\mathcal{N}_{k2}} \Bigg(\frac{(\boldsymbol{k} \cdot \boldsymbol{q})(\boldsymbol{k} \cdot \boldsymbol{Q}_k)(\boldsymbol{q} \cdot \boldsymbol{Q}_q) + (\boldsymbol{Q}_k \cdot \boldsymbol{Q}_q)q^2k^2}{k^2(\boldsymbol{k} \times \boldsymbol{Q}_k)^2} \\
&\qquad - \frac{(\boldsymbol{q} \cdot \boldsymbol{Q}_k)(\boldsymbol{q} \cdot \boldsymbol{Q}_q)k^2 + (\boldsymbol{k} \cdot \boldsymbol{Q}_q)(\boldsymbol{k} \cdot \boldsymbol{Q}_k)q^2}{k^2(\boldsymbol{k} \times \boldsymbol{Q}_k)^2} \Bigg) \,,
\end{aligned}
\tag{C.5}
$$

$$
\begin{aligned}
V_{3,pq}^{k1,q1} &= (\boldsymbol{q}\cdot\boldsymbol{P}_{k1})(\boldsymbol{p}\cdot\boldsymbol{b}_{q1}) \\
&= \frac{\mathcal{N}_{q1}}{\mathcal{N}_{k1}}\frac{D_{kq}D_{qp}}{(\boldsymbol{k}\times\boldsymbol{Q}_k)^2} = -\frac{\mathcal{N}_{q1}\mathcal{N}_{k2}}{\mathcal{N}_{q2}\mathcal{N}_{k1}}\frac{V_{1,pq}^{k2,q2}}{q^2}\,, \\
V_{3,pq}^{k2,q1} &= \frac{\mathcal{N}_{q1}}{\mathcal{N}_{k2}}\frac{\boldsymbol{q}\cdot(\boldsymbol{k}(\boldsymbol{k}\cdot\boldsymbol{Q}_k)-\boldsymbol{Q}_k k^2)D_{qp}}{k^2(\boldsymbol{k}\times\boldsymbol{Q}_k)^2} \\
&= \frac{\mathcal{N}_{q1}\mathcal{N}_{k1}}{\mathcal{N}_{q2}\mathcal{N}_{k2}}\frac{V_{1,pq}^{k1,q2}}{k^2q^2}\,, \\
V_{3,pq}^{k1,q2} &= \frac{\mathcal{N}_{q2}}{\mathcal{N}_{k1}}\frac{\boldsymbol{q}\cdot(\boldsymbol{k}\times\boldsymbol{Q}_k)\boldsymbol{p}\cdot(\boldsymbol{q}\times(\boldsymbol{q}\times\boldsymbol{Q}_q))}{(\boldsymbol{k}\times\boldsymbol{Q}_k)^2} \\
&= \frac{\mathcal{N}_{q2}\mathcal{N}_{k2}}{\mathcal{N}_{q1}\mathcal{N}_{k1}}V_{1,pq}^{k2,q1}\,, \\
V_{3,pq}^{k2,q2} &= \frac{\mathcal{N}_{q2}}{\mathcal{N}_{k2}}\frac{\boldsymbol{q}\cdot(\boldsymbol{k}\times(\boldsymbol{k}\times\boldsymbol{Q}_k))\boldsymbol{p}\cdot(\boldsymbol{q}\times(\boldsymbol{q}\times\boldsymbol{Q}_q))}{k^2(\boldsymbol{k}\times\boldsymbol{Q}_k)^2} \\
&= -\frac{\mathcal{N}_{q2}\mathcal{N}_{k1}}{\mathcal{N}_{q1}\mathcal{N}_{k2}}\frac{V_{1,pq}^{k1,q1}}{k^2}\,, \\
V_{3,pq}^{p1,q1} &= (\boldsymbol{p}\cdot\boldsymbol{b}_{q1})(\boldsymbol{q}\cdot\boldsymbol{b}_{p1}) \\
&= \boldsymbol{p}\cdot(\boldsymbol{q}\times\boldsymbol{Q}_q)\boldsymbol{q}\cdot(\boldsymbol{p}\times\boldsymbol{Q}_p)\mathcal{N}_{p1}\mathcal{N}_{q1} \\
&= D_{qp}D_{pq}\mathcal{N}_{p1}\mathcal{N}_{q1} = -\frac{\mathcal{N}_{p1}\mathcal{N}_{q1}}{\mathcal{N}_{p2}\mathcal{N}_{q2}}\frac{V_{1,pq}^{p2,q2}}{p^2q^2}\,, \\
V_{3,pq}^{p1,q2} &= \boldsymbol{p}\cdot(\boldsymbol{q}\times(\boldsymbol{q}\times\boldsymbol{Q}_q))\boldsymbol{q}\cdot(\boldsymbol{p}\times\boldsymbol{Q}_p)\mathcal{N}_{p1}\mathcal{N}_{q2} \\
&= D_{pq}((\boldsymbol{p}\cdot\boldsymbol{q})(\boldsymbol{q}\cdot\boldsymbol{Q}_q)-(\boldsymbol{p}\cdot\boldsymbol{Q}_p)q^2)\mathcal{N}_{p1}\mathcal{N}_{q2} \\
&= \frac{\mathcal{N}_{p1}\mathcal{N}_{q2}}{\mathcal{N}_{p2}\mathcal{N}_{q1}}\frac{V_{1,pq}^{p2,q1}}{p^2}\,, \\
V_{3,pq}^{p2,q1} &= \frac{\mathcal{N}_{p2}\mathcal{N}_{q1}}{\mathcal{N}_{p1}\mathcal{N}_{q2}}\frac{V_{1,pq}^{p1,q2}}{q^2} = V_{3,qp}^{q1,p2}\,, \\
V_{3,pq}^{p2,q2} &= \boldsymbol{p}\cdot(\boldsymbol{q}\times(\boldsymbol{q}\times\boldsymbol{Q}_q))\boldsymbol{q}\cdot(\boldsymbol{p}\times(\boldsymbol{p}\times\boldsymbol{Q}_p))\mathcal{N}_{p2}\mathcal{N}_{q2} \\
&= -\frac{\mathcal{N}_{p2}\mathcal{N}_{q2}}{\mathcal{N}_{p1}\mathcal{N}_{q1}}V_{1,pq}^{p1,q1}\,,
\end{aligned}
\tag{C.6}
$$

where $(\boldsymbol{k}\times\boldsymbol{Q}_k)^2 = k^2Q_k^2 - (\boldsymbol{k}\cdot\boldsymbol{Q}_k)^2$ and e.g. $V_{2,qp}$ indicates the projection where p and q are interchanged everywhere.

Vertices involving three vorticity or vector perturbations in transverse basis

Vertices with three vorticity or vector modes require three vector projections, which gives following projection functions,

$$\begin{aligned}
V_{1,pq}^{k\alpha,p\beta,q\gamma} &\equiv (\boldsymbol{p}\times\boldsymbol{q})_i(\boldsymbol{p}\times\boldsymbol{q})_j(\boldsymbol{p}\times\boldsymbol{q})_k P_{k\alpha,i} b_{p\beta,j} b_{q\gamma,k} = V_{1,pq}^{k\alpha} V_{1,pq}^{p\beta} V_{1,pq}^{q\gamma}\,,\\
V_{2,pq}^{k\alpha,p\beta,q\gamma} &\equiv \delta_{ij}(\boldsymbol{p}\times\boldsymbol{q})_k P_{k\alpha,i} b_{p\beta,j} b_{q\gamma,k}\,,\\
V_{3,pq}^{k\alpha,p\beta,q\gamma} &\equiv \delta_{ik}(\boldsymbol{p}\times\boldsymbol{q})_j P_{k\alpha,i} b_{p\beta,j} b_{q\gamma,k}\,,\\
V_{4,pq}^{k\alpha,p\beta,q\gamma} &\equiv p_i q_j(\boldsymbol{p}\times\boldsymbol{q})_k P_{k\alpha,i} b_{p\beta,j} b_{q\gamma,k}\,,\\
V_{5,pq}^{k\alpha,p\beta,q\gamma} &\equiv p_k q_i(\boldsymbol{p}\times\boldsymbol{q})_j P_{k\alpha,i} b_{p\beta,j} b_{q\gamma,k}\,,\\
V_{6,pq}^{k\alpha,p\beta,q\gamma} &\equiv \varepsilon_{ilj} p_k p_l P_{k\alpha,i} b_{p\beta,j} b_{q\gamma,k}\,,
\end{aligned} \tag{C.7}$$

with $\alpha,\beta,\gamma = 1,2$. Then the vertices become

$$\begin{aligned}
\gamma_{w_{k\alpha}w_{p\beta}w_{q\gamma}}(p,q) &= \frac{V_{3,pq}^{k\alpha,p\beta,q\gamma} + V_{6,pq}^{k\alpha,p\beta,q\gamma}}{p^2}\,,\\
\gamma_{\nu_{k\alpha}w_{p\beta}\nu_{q\gamma}}(p,q) &= \frac{1}{p^2q^2k^2}\Bigg\{\left(V_{3,pq}^{k\alpha,p\beta,q\gamma}(\boldsymbol{k}\cdot\boldsymbol{q}) - V_{5,pq}^{k\alpha,p\beta,q\gamma}\right)(k^2-p^2)\\
&\qquad - \left(V_{2,pq}^{k\alpha,p\beta,q\gamma}(\boldsymbol{k}\cdot\boldsymbol{p}) - V_{4,pq}^{k\alpha,p\beta,q\gamma}\right)(k^2-p^2) - 2V_{1,pq}^{k\alpha,p\beta,q\gamma}\Bigg\}
\end{aligned} \tag{C.8}$$

and the projection functions in terms of the previous V's read

$$\begin{aligned}
V_{1,pq}^{k\alpha,p\beta,q\gamma} &= V_{1,pq}^{k\alpha} V_{1,pq}^{p\beta} V_{1,pq}^{q\gamma}\,,\\
V_{2,pq}^{k\alpha,p\beta,q\gamma} &= V_{2,pq}^{k\alpha,p\beta} V_{1,pq}^{q\gamma}\,,\\
V_{3,pq}^{k\alpha,p\beta,q\gamma} &= V_{2,pq}^{k\alpha,q\gamma} V_{1,pq}^{p\beta}\,,\\
V_{4,pq}^{k\alpha,p\beta,q\gamma} &= V_{3,pq}^{k\alpha,p\beta} V_{1,pq}^{q\gamma}\,,\\
V_{5,pq}^{k\alpha,p\beta,q\gamma} &= V_{3,pq}^{k\alpha,q\gamma} V_{1,pq}^{p\beta}\,,\\
V_{6,pq}^{k\alpha,p\beta,q\gamma} &\propto V_{2,pq}^{k\alpha,p\tilde{\beta}} V_{1,pq}^{q\tilde{\gamma}}
\end{aligned} \tag{C.9}$$

where here also $\tilde{\gamma} = 1, 2$ but $\tilde{\gamma} \neq \gamma$. The last line explicitly reads

$$
\begin{aligned}
V_{6,pq}^{k1,p1,q1} &= (\boldsymbol{p}\cdot\boldsymbol{b}_{q1})\boldsymbol{P}_{k1}\cdot(\boldsymbol{p}\times\boldsymbol{b}_{p1}) \\
&= D_{qp}\frac{\mathcal{N}_{p1}\mathcal{N}_{q1}}{\mathcal{N}_{k1}}\frac{(\boldsymbol{k}\times\boldsymbol{Q}_k)\cdot(\boldsymbol{p}\times(\boldsymbol{p}\times\boldsymbol{Q}_p))}{(\boldsymbol{k}\times\boldsymbol{Q}_k)^2} \\
&= -\frac{\mathcal{N}_{p1}\mathcal{N}_{q1}}{\mathcal{N}_{p2}\mathcal{N}_{q2}}\frac{V_{2,pq}^{k1,p2}V_{1,pq}^{q2}}{q^2}\,,
\end{aligned}
$$

$$
\begin{aligned}
V_{6,pq}^{k1,p1,q2} &= (\boldsymbol{p}\cdot\boldsymbol{b}_{q2})\boldsymbol{P}_{k1}\cdot(\boldsymbol{p}\times\boldsymbol{b}_{p1}) \\
&= \frac{\mathcal{N}_{p1}\mathcal{N}_{q2}}{\mathcal{N}_{k1}}(\boldsymbol{q}\times\boldsymbol{Q}_q)\cdot(\boldsymbol{p}\times\boldsymbol{q})\frac{(\boldsymbol{p}\times(\boldsymbol{p}\times\boldsymbol{Q}_p))\cdot(\boldsymbol{k}\times\boldsymbol{Q}_k)}{(\boldsymbol{k}\times\boldsymbol{Q}_k)^2} \\
&= \frac{\mathcal{N}_{p1}\mathcal{N}_{q2}}{\mathcal{N}_{p2}\mathcal{N}_{q1}}V_{2,pq}^{k1,p2}V_{1,pq}^{q1}\,,
\end{aligned}
$$

$$
\begin{aligned}
V_{6,pq}^{k1,p2,q1} &= (\boldsymbol{p}\cdot\boldsymbol{b}_{q1})\boldsymbol{P}_{k1}\cdot(\boldsymbol{p}\times\boldsymbol{b}_{p2}) \\
&= D_{qp}\frac{\mathcal{N}_{p2}\mathcal{N}_{q1}}{\mathcal{N}_{k1}}\frac{(\boldsymbol{k}\times\boldsymbol{Q}_k)}{(\boldsymbol{k}\times\boldsymbol{Q}_k)^2}\cdot\underbrace{(p\times(\boldsymbol{p}\times(\boldsymbol{p}\times\boldsymbol{Q}_p)))}_{[(\boldsymbol{p}\times\boldsymbol{p})(\boldsymbol{p}\cdot\boldsymbol{Q}_p)-(\boldsymbol{p}\times\boldsymbol{Q}_p)p^2]} \\
&= \frac{\mathcal{N}_{p2}\mathcal{N}_{q1}}{\mathcal{N}_{p1}\mathcal{N}_{q2}}\frac{p^2}{q^2}V_{2,pq}^{k1,p1}V_{1,pq}^{q2}\,,
\end{aligned}
$$

$$
\begin{aligned}
V_{6,pq}^{k1,p2,q2} &= (\boldsymbol{p}\cdot\boldsymbol{b}_{q2})\boldsymbol{P}_{k1}\cdot(\boldsymbol{p}\times\boldsymbol{b}_{p2}) \\
&= -\frac{\mathcal{N}_{p2}\mathcal{N}_{q2}}{\mathcal{N}_{p1}\mathcal{N}_{q1}}p^2V_{2,pq}^{k1,p1}V_{1,pq}^{q1}\,,
\end{aligned}
$$

$$
\begin{aligned}
V_{6,pq}^{k2,p1,q1} &= (\boldsymbol{p}\cdot\boldsymbol{b}_{q1})\boldsymbol{P}_{k2}\cdot(\boldsymbol{p}\times\boldsymbol{b}_{p1}) \\
&= -\frac{\mathcal{N}_{p1}\mathcal{N}_{q1}}{\mathcal{N}_{p2}\mathcal{N}_{q2}}\frac{V_{2,pq}^{k2,p2}V_{1,pq}^{q2}}{q^2}\,,
\end{aligned}
$$

$$
\begin{aligned}
V_{6,pq}^{k2,p1,q2} &= (\boldsymbol{p}\cdot\boldsymbol{b}_{q2})\boldsymbol{P}_{k2}\cdot(\boldsymbol{p}\times\boldsymbol{b}_{p1}) \\
&= \frac{\mathcal{N}_{p1}\mathcal{N}_{q2}}{\mathcal{N}_{p2}\mathcal{N}_{q1}}V_{2,pq}^{k2,p2}V_{1,pq}^{q1}\,,
\end{aligned}
$$

$$
\begin{aligned}
V_{6,pq}^{k2,p2,q1} &= (\boldsymbol{p}\cdot\boldsymbol{b}_{q1})\boldsymbol{P}_{k2}\cdot(\boldsymbol{p}\times\boldsymbol{b}_{p2}) \\
&= \frac{\mathcal{N}_{p2}\mathcal{N}_{q1}}{\mathcal{N}_{p1}\mathcal{N}_{q2}}\frac{p^2}{q^2}V_{2,pq}^{k2,p1}V_{1,pq}^{q2}\,,
\end{aligned}
$$

$$
\begin{aligned}
V_{6,pq}^{k2,p2,q2} &= (\boldsymbol{p}\cdot\boldsymbol{b}_{q2})\boldsymbol{P}_{k2}\cdot(\boldsymbol{p}\times\boldsymbol{b}_{p2}) \\
&= -\frac{\mathcal{N}_{p2}\mathcal{N}_{q2}}{\mathcal{N}_{p1}\mathcal{N}_{q1}}p^2V_{2,pq}^{k2,p1}V_{1,pq}^{q1}\,.
\end{aligned}
\tag{C.10}
$$

Appendix D

Vertices involving third cumulant

In this appendix, we collect all vertices $\gamma_{abc}(p,q)$ for perturbation modes involving third cumulant perturbations π and χ. We write ϵ instead of $\delta\epsilon$ in the index for simplicity. Furthermore $k \equiv p+q$ in the vectorial sense. Note that we do not present the full set of vertices involving π and χ since fourth and higher cumulants as well as nonlinearities involving two vorticity, vector or tensor modes of velocity dispersion are neglected.

Vertices involving scalar modes π and χ of the third cumulant and only scalar perturbations otherwise

$$\begin{aligned}
\gamma_{gA\pi}(p,q) &= \frac{1}{4}\frac{p\cdot q}{q^2} - \frac{3}{4}\frac{(k\cdot q)^2 p\cdot q}{k^2 q^4}\,,\\
\gamma_{gA\chi}(p,q) &= -3\gamma_{\epsilon A\chi}(p,q)\,,\\
\gamma_{\epsilon A\pi}(p,q) &= -\frac{1}{4}\frac{p\cdot q}{q^2} + \frac{1}{4}\frac{(k\cdot q)^2 p\cdot q}{k^2 q^4}\,,\\
\gamma_{\epsilon A\chi}(p,q) &= \frac{1}{4}\left(\frac{p\cdot q}{5q^2} + \frac{2}{5}\frac{k\cdot p k\cdot q}{k^2 q^2} - \frac{(k\cdot q)^2 p\cdot q}{k^2 q^4}\right)\,,
\end{aligned} \tag{D.1}$$

$$\begin{aligned}
\gamma_{\pi gg}(p,q) &= \frac{k^2(p\cdot q)^2}{p^2 q^2} + \frac{1}{2}p\cdot q\left(\frac{k\cdot q}{q^2} + \frac{k\cdot p}{p^2}\right)\,,\\
\gamma_{\pi\epsilon g}(p,q) &= \frac{1}{2}k\cdot q\left(3 + \frac{5p\cdot q}{q^2}\right)\,,\\
\gamma_{\pi\epsilon\epsilon}(p,q) &= \frac{5}{2}k^2\,,\\
\gamma_{\pi\theta\pi}(p,q) &= \frac{1}{2}\frac{k^2 p\cdot q}{p^2 q^2} + \frac{k\cdot q(p\cdot q)^2}{p^2 q^4}\,,\\
\gamma_{\pi\theta\chi}(p,q) &= \frac{1}{5}\frac{k\cdot q}{q^2} + \frac{2}{5}\frac{k\cdot p p\cdot q}{p^2 q^2} - \frac{k\cdot q(p\cdot q)^2}{p^2 q^4}\,,
\end{aligned} \tag{D.2}$$

$$
\begin{aligned}
\gamma_{\chi gg}(p,q) &= -\frac{15}{4}\frac{k\cdot q k\cdot p p\cdot q}{p^2q^2}+\frac{5}{2}\gamma_{\pi gg}(p,q)\,,\\
\gamma_{\chi\epsilon g}(p,q) &= -\frac{15}{4}\left(\frac{k\cdot q p\cdot q}{q^2}+\frac{(k\cdot q)^3}{k^2q^2}\right)+\frac{5}{2}\gamma_{\pi\epsilon g}(p,q)\,,\\
\gamma_{\chi\epsilon\epsilon}(p,q) &= -\frac{15}{4}k^2+\frac{5}{2}\gamma_{\pi\epsilon\epsilon}(p,q)\,,\\
\gamma_{\chi\theta\pi}(p,q) &= -\frac{5}{4}\frac{(k\cdot q)^2 p\cdot q(k^2+2k\cdot p)}{k^2p^2q^4}+\frac{5}{2}\gamma_{\pi\theta\pi}(p,q)\,,\\
\gamma_{\chi\theta\chi}(p,q) &= -\frac{3}{4}\frac{k^2p\cdot q}{p^2q^2}-\frac{3}{2}\frac{(k\cdot p)^2k\cdot q}{k^2p^2q^2}+\frac{5}{4}\frac{(k\cdot q)^2p\cdot q(k^2+2k\cdot p)}{k^2p^2q^4}+\frac{5}{2}\gamma_{\pi\theta\chi}(p,q)\,.
\end{aligned}
\tag{D.3}
$$

Vertices involving scalar modes π and χ of the third cumulant and at most one vorticity, vector or tensor perturbation

$$
\begin{aligned}
\gamma_{\pi w_i\pi}(p,q) &= \frac{1}{2}(p\times q)_i\left(\frac{k\cdot q+p\cdot q}{p^2q^2}+2\frac{k\cdot qp\cdot q}{p^2q^4}\right)\\
\gamma_{\pi w_i\chi}(p,q) &= (p\times q)_i\left(\frac{p\cdot q+p\cdot k}{5p^2q^2}-\frac{k\cdot qp\cdot q}{p^2q^4}\right)\\
\gamma_{\chi w_i\pi}(p,q) &= -\frac{5}{4}(p\times q)_i\frac{(k\cdot q)^2(4p\cdot q+q^2)}{k^2p^2q^4}+\frac{5}{2}\gamma_{\pi w_i\pi}(p,q)\\
\gamma_{\chi w_i\chi}(p,q) &= -\frac{5}{4}(p\times q)_i\left(\frac{3}{5}\frac{k\cdot q+p\cdot q+2k\cdot qk\cdot p}{p^2q^2}-\frac{(k\cdot q)^2(4p\cdot q+q^2)}{k^2p^2q^4}\right)+\frac{5}{2}\gamma_{\pi w_i\chi}(p,q)
\end{aligned}
\tag{D.4}
$$

$$
\begin{aligned}
\gamma_{\nu_iA\pi}(p,q) &= -\frac{1}{2}(p\times q)_i\frac{k\cdot qp\cdot q}{k^2q^4}\\
\gamma_{\nu_iA\chi}(p,q) &= \frac{1}{2}(p\times q)_i\left(\frac{k\cdot q-k\cdot p}{5k^2q^2}+\frac{k\cdot qp\cdot q}{k^2q^4}\right)\\
\gamma_{t_{ij}A\pi}(p,q) &= -\frac{1}{2}\frac{(p\cdot q)(p\times q)^2}{2k^2q^4}\left[\delta_{ij}-\frac{k_ik_j}{k^2}-2\frac{(p\times q)_i(p\times q)_j}{(p\times q)^2}\right]\\
\gamma_{t_{ij}A\chi}(p,q) &= \frac{1}{2}\frac{(p\times q)^2}{5k^2q^2}\left(1+\frac{p\cdot q}{2q^2}\right)\left[\delta_{ij}-\frac{k_ik_j}{k^2}-2\frac{(p\times q)_i(p\times q)_j}{(p\times q)^2}\right]
\end{aligned}
\tag{D.5}
$$

$$
\begin{aligned}
\gamma_{\pi\epsilon\nu_i}(p,q) &= (p\times q)_i\left(1+\frac{5}{2}\frac{k\cdot q+p\cdot q}{q^2}\right)\\
\gamma_{\pi g\nu_i}(p,q) &= \frac{1}{2}(p\times q)_i\left(\frac{(p\cdot q)(k^2+3k\cdot p+p\cdot q)}{p^2q^2}+\frac{k\cdot q+p\cdot q}{q^2}\right)\\
\gamma_{\pi\epsilon t_{ij}}(p,q) &= \frac{5}{2}p_ip_j\\
\gamma_{\pi g t_{ij}}(p,q) &= p_ip_j\left(1+\frac{p\cdot q}{q^2}+\frac{k\cdot p}{p^2}\right)
\end{aligned}
\tag{D.6}
$$

$$
\begin{aligned}
\gamma_{\chi\epsilon\nu_i}(p,q) &= -\frac{15}{4}(p\times q)_i\left(2\frac{(k\cdot q)^2}{k^2q^2}+\frac{k\cdot q+p\cdot q}{q^2}\right)+\frac{5}{2}\gamma_{\pi\epsilon\nu_i}(p,q)\\
\gamma_{\chi g\nu_i}(p,q) &= -\frac{15}{4}(p\times q)_i\left(\frac{(k\cdot p)[(p\cdot q)(2k^2+q^2)+p^2q^2]}{k^2p^2q^2}\right)+\frac{5}{2}\gamma_{\pi g\nu_i}(p,q)\\
\gamma_{\chi\epsilon t_{ij}}(p,q) &= \frac{15}{4}p_ip_j\left(1+\frac{k\cdot q}{q^2}\right)+\frac{5}{2}\gamma_{\pi\epsilon t_{ij}}(p,q)\\
\gamma_{\chi g t_{ij}}(p,q) &= \frac{15}{4}p_ip_j\frac{(k\cdot p)^2+(p\cdot q)(k\cdot p)}{k^2p^2}+\frac{5}{2}\gamma_{\pi g t_{ij}}(p,q)
\end{aligned}
\tag{D.7}
$$

Appendix E

Time integrals

The only time-dependent contributions for the nonlinear kernels $F_{2,\delta}$ and $F_{2,\theta}$ in Eq. (7.21) up to first order in the background dispersion $\epsilon(\eta)$ are given by

$$
\begin{aligned}
J_1^\delta &\equiv \frac{4}{5}\int^\eta d\eta' \left(e^{\eta'-\eta} - e^{7(\eta'-\eta)/2}\right) E_3(\eta') = \frac{2}{5}(E_1(\eta) - 5E_3(\eta) + 4E_{7/2}(\eta))\,,\\
J_2^\delta &\equiv \frac{4}{5}\int^\eta d\eta' \left(e^{\eta'-\eta} - e^{7(\eta'-\eta)/2}\right) (E_2(\eta') - E_3(\eta')) = \frac{2}{15}(3E_1(\eta) - 10E_2(\eta) + 15E_3(\eta) - 8E_{7/2}(\eta))\,,\\
J_3^\delta &\equiv \frac{2}{5}\int^\eta d\eta' \left(e^{\eta'-\eta} - e^{7(\eta'-\eta)/2}\right) \epsilon(\eta') = \frac{2}{5}(E_1(\eta) - E_{7/2}(\eta))\,,\\
J_4^\delta &\equiv \frac{2}{5}\int^\eta d\eta' \left(e^{\eta'-\eta} - e^{7(\eta'-\eta)/2}\right) I_\theta(\eta') = \frac{2}{105}(12E_0(\eta) - 70E_2(\eta) + 63E_{5/2}(\eta) - 5E_{7/2}(\eta))\,,\\
J_5^\delta &\equiv J_1^\delta + J_2^\delta = \frac{4}{15}(3E_1(\eta) - 5E_2(\eta) + 2E_{7/2}(\eta))\,,\\
J_6^\delta &\equiv \frac{2}{5}\int^\eta d\eta' \left(\frac{3}{2}e^{\eta'-\eta} + e^{7(\eta'-\eta)/2}\right) I_\theta(\eta') = \frac{2}{21}(6E_0(\eta) - 7E_2(\eta) + E_{7/2}(\eta))\,,\\
J_7^\delta &\equiv \frac{2}{5}\int^\eta d\eta' \left(\frac{3}{2}e^{\eta'-\eta} + e^{7(\eta'-\eta)/2}\right) I_\delta(\eta') = \frac{2}{105}(30E_0(\eta) - 63E_1(\eta) + 35E_2(\eta) - 2E_{7/2}(\eta))\,,
\end{aligned}
\tag{E.1}
$$

and

$$
\begin{aligned}
J_1^\theta &\equiv \frac{4}{5}\int^\eta d\eta' \left(e^{\eta'-\eta} + \frac{3}{2}e^{7(\eta'-\eta)/2}\right) E_3(\eta') = \frac{2}{5}(E_1(\eta) + 5E_3(\eta) - 6E_{7/2}(\eta))\,,\\
J_2^\theta &\equiv \frac{4}{5}\int^\eta d\eta' \left(e^{\eta'-\eta} + \frac{3}{2}e^{7(\eta'-\eta)/2}\right) (E_2(\eta') - E_3(\eta')) = \frac{2}{5}(E_1(\eta) - 5E_3(\eta) + 4E_{7/2}(\eta))\,,\\
J_3^\theta &\equiv \frac{2}{5}\int^\eta d\eta' \left(e^{\eta'-\eta} + \frac{3}{2}e^{7(\eta'-\eta)/2}\right) \epsilon(\eta') = \frac{1}{5}(2E_1(\eta) + 3E_{7/2}(\eta))\,,\\
J_4^\theta &\equiv \frac{2}{5}\int^\eta d\eta' \left(e^{\eta'-\eta} + \frac{3}{2}e^{7(\eta'-\eta)/2}\right) I_\theta(\eta') = \frac{1}{35}(16E_0(\eta) - 21E_{5/2}(\eta) + 5E_{7/2}(\eta))\,,\\
J_5^\theta &\equiv J_1^\theta + J_2^\theta = \frac{4}{5}(E_1(\eta) - E_{7/2}(\eta))\,,\\
J_6^\theta &\equiv \frac{2}{5}\int^\eta d\eta' \left(\frac{3}{2}e^{\eta'-\eta} - \frac{3}{2}e^{7(\eta'-\eta)/2}\right) I_\theta(\eta') = \frac{1}{35}(12E_0(\eta) - 70E_2(\eta) + 63E_{5/2}(\eta) - 5E_{7/2}(\eta))\,,\\
J_7^\theta &\equiv \frac{2}{5}\int^\eta d\eta' \left(\frac{3}{2}e^{\eta'-\eta} - \frac{3}{2}e^{7(\eta'-\eta)/2}\right) I_\delta(\eta') = \frac{2}{35}(6E_0(\eta) - 21E_1(\eta) + 35E_2(\eta) - 21E_{5/2}(\eta) + E_{7/2}(\eta))\,.
\end{aligned}
\tag{E.2}
$$

Bibliography

[1] E. Kolb, *The early universe*. CRC press, 2018.

[2] A. Einstein, *The foundation of the general theory of relativity*, *Annalen Phys* **49** (1916) 769.

[3] E. Hubble, *A relation between distance and radial velocity among extra-galactic nebulae*, *Proceedings of the national academy of sciences* **15** (1929) 168.

[4] S. Dodelson and F. Schmidt, *Modern cosmology*. Academic press, 2020.

[5] M. S. Turner, *The road to precision cosmology*, *Annual Review of Nuclear and Particle Science* **72** (2022) 1.

[6] M. A. Amin, F.-Y. Cyr-Racine, T. Eifler, R. Flauger, M. M. Ivanov, M. LoVerde et al., *Snowmass2021 theory frontier white paper: data-driven cosmology*, *arXiv preprint arXiv:2203.07946* (2022) .

[7] G. F. Smoot, C. L. Bennett, A. Kogut, E. Wright, J. Aymon, N. Boggess et al., *Structure in the cobe differential microwave radiometer first-year maps*, *Astrophysical Journal, Part 2-Letters (ISSN 0004-637X), vol. 396, no. 1, Sept. 1, 1992, p. L1-L5. Research supported by NASA.* **396** (1992) L1.

[8] B. D. Fields, K. A. Olive, T.-H. Yeh and C. Young, *Big-bang nucleosynthesis after planck*, *Journal of Cosmology and Astroparticle Physics* **2020** (2020) 010.

[9] S. Perlmutter, G. Aldering, G. Goldhaber, R. Knop, P. Nugent, P. G. Castro et al., *Measurements of and from 42 high-redshift supernovae*, *The Astrophysical Journal* **517** (1999) 565.

[10] A. G. Riess, A. V. Filippenko, P. Challis, A. Clocchiatti, A. Diercks, P. M. Garnavich et al., *Observational evidence from supernovae for an accelerating universe and a cosmological constant*, *The astronomical journal* **116** (1998) 1009.

[11] S. Cole, W. J. Percival, J. A. Peacock, P. Norberg, C. M. Baugh, C. S. Frenk et al., *The 2df galaxy redshift survey: power-spectrum analysis of the final data set and cosmological implications*, *Monthly Notices of the Royal Astronomical Society* **362** (2005) 505.

[12] K. S. Dawson, J.-P. Kneib, W. J. Percival, S. Alam, F. D. Albareti, S. F. Anderson et al., *The sdss-iv extended baryon oscillation spectroscopic survey: overview and early data*, *The Astronomical Journal* **151** (2016) 44.

[13] V. Springel, C. S. Frenk and S. D. White, *The large-scale structure of the universe*, *nature* **440** (2006) 1137.

[14] B. P. Abbott, R. Abbott, T. Abbott, F. Acernese, K. Ackley, C. Adams et al., *Gw170814: a three-detector observation of gravitational waves from a binary black hole coalescence*, *Physical review letters* **119** (2017) 141101.

[15] P. Amaro-Seoane, H. Audley, S. Babak, J. Baker, E. Barausse, P. Bender et al., *Laser interferometer space antenna*, *arXiv preprint arXiv:1702.00786* (2017) .

[16] H. Atek, M. Shuntov, L. J. Furtak, J. Richard, J.-P. Kneib, G. Mahler et al., *Revealing galaxy candidates out to z16 with jwst observations of the lensing cluster smacs0723*, *Monthly Notices of the Royal Astronomical Society* **519** (2023) 1201.

[17] B. Wang, S. Fujimoto, I. Labbe, L. J. Furtak, T. B. Miller, D. J. Setton et al., *Uncover: Illuminating the early universe–jwst/nirspec confirmation of $ z> 12$ galaxies*, *arXiv preprint arXiv:2308.03745* (2023) .

[18] C. Caprini and D. G. Figueroa, *Cosmological backgrounds of gravitational waves*, *Classical and Quantum Gravity* **35** (2018) 163001.

[19] G. Agazie, A. Anumarlapudi, A. M. Archibald, Z. Arzoumanian, P. T. Baker, B. Bécsy et al., *The nanograv 15 yr data set: Evidence for a gravitational-wave background*, *The Astrophysical Journal Letters* **951** (2023) L8.

[20] P. J. E. Peebles, *Principles of physical cosmology*, vol. 27. Princeton university press, 1993.

[21] V. F. Mukhanov, *Physical foundations of cosmology*. Cambridge university press, 2005.

[22] S. Weinberg, *Cosmology*. Oxford university press, 2008.

[23] L. Amendola, S. Appleby, A. Avgoustidis, D. Bacon, T. Baker, M. Baldi et al., *Cosmology and fundamental physics with the euclid satellite*, *Living reviews in relativity* **21** (2018) 1.

[24] O. Doré, J. Bock, M. Ashby, P. Capak, A. Cooray, R. de Putter et al., *Cosmology with the spherex all-sky spectral survey*, *arXiv preprint arXiv:1412.4872* (2014) .

[25] Ž. Ivezić, S. M. Kahn, J. A. Tyson, B. Abel, E. Acosta, R. Allsman et al., *Lsst: from science drivers to reference design and anticipated data products*, *The Astrophysical Journal* **873** (2019) 111.

[26] M. E. Levi, L. E. Allen, A. Raichoor, C. Baltay, S. BenZvi, F. Beutler et al., *The dark energy spectroscopic instrument (desi)*, *arXiv preprint arXiv:1907.10688* (2019) .

[27] D. Spergel, N. Gehrels, C. Baltay, D. Bennett, J. Breckinridge, M. Donahue et al., *Wide-field infrarred survey telescope-astrophysics focused telescope assets wfirst-afta 2015 report*, *arXiv preprint arXiv:1503.03757* (2015) .

[28] M. Takada, R. S. Ellis, M. Chiba, J. E. Greene, H. Aihara, N. Arimoto et al., *Extragalactic science, cosmology, and galactic archaeology with the subaru prime focus spectrograph*, *Publications of the Astronomical Society of Japan* **66** (2014) R1.

[29] F. Beutler, C. Blake, M. Colless, D. H. Jones, L. Staveley-Smith, L. Campbell et al., *The 6df galaxy survey: baryon acoustic oscillations and the local hubble constant*, *Monthly Notices of the Royal Astronomical Society* **416** (2011) 3017.

[30] C. Blake, E. A. Kazin, F. Beutler, T. M. Davis, D. Parkinson, S. Brough et al., *The wigglez dark energy survey: mapping the distance–redshift relation with baryon acoustic oscillations*, *Monthly Notices of the Royal Astronomical Society* **418** (2011) 1707.

[31] A. S. Bolton, D. J. Schlegel, É. Aubourg, S. Bailey, V. Bhardwaj, J. R. Brownstein et al., *Spectral classification and redshift measurement for the sdss-iii baryon oscillation spectroscopic survey*, *The Astronomical Journal* **144** (2012) 144.

[32] D. J. Eisenstein, D. H. Weinberg, E. Agol, H. Aihara, C. A. Prieto, S. F. Anderson et al., *Sdss-iii: Massive spectroscopic surveys of the distant universe, the milky way, and extra-solar planetary systems*, *The Astronomical Journal* **142** (2011) 72.

[33] A. J. Ross, F. Beutler, C.-H. Chuang, M. Pellejero-Ibanez, H.-J. Seo, M. Vargas-Magana et al., *The clustering of galaxies in the completed sdss-iii baryon oscillation spectroscopic survey: Observational systematics and baryon acoustic oscillations in the correlation function*, *Monthly Notices of the Royal Astronomical Society* **464** (2017) 1168.

[34] S. Alam, M. Aubert, S. Avila, C. Balland, J. E. Bautista, M. A. Bershady et al., *Completed sdss-iv extended baryon oscillation spectroscopic survey: Cosmological implications from two decades of spectroscopic surveys at the apache point observatory*, *Physical Review D* **103** (2021) 083533.

[35] C. Desi, A. Aghamousa, J. Aguilar, S. Ahlen, S. Alam, L. Allen et al., *The desi experiment part i: science, targeting, and survey design*, .

[36] R. Laureijs, J. Amiaux, S. Arduini, J. L. Augueres, J. Brinchmann, R. Cole et al., *Euclid Definition Study Report*, *arXiv e-prints* (2011) arXiv:1110.3193 [1110.3193].

[37] M. Asgari, C.-A. Lin, B. Joachimi, B. Giblin, C. Heymans, H. Hildebrandt et al., *Kids-1000 cosmology: Cosmic shear constraints and comparison between two point statistics*, *Astronomy & Astrophysics* **645** (2021) A104.

[38] T. M. Abbott, F. B. Abdalla, A. Alarcon, J. Aleksić, S. Allam, S. Allen et al., *Dark energy survey year 1 results: Cosmological constraints from galaxy clustering and weak lensing*, *Physical Review D* **98** (2018) 043526.

[39] H. D. M. Des Bourboux, J. Rich, A. Font-Ribera, V. de Sainte Agathe, J. Farr, T. Etourneau et al., *The completed sdss-iv extended baryon oscillation spectroscopic survey: baryon acoustic oscillations with lyforests*, *The Astrophysical Journal* **901** (2020) 153.

[40] G. Hinshaw, D. Larson, E. Komatsu, D. N. Spergel, C. Bennett, J. Dunkley et al., *Nine-year wilkinson microwave anisotropy probe (wmap) observations: cosmological parameter results*, *The Astrophysical Journal Supplement Series* **208** (2013) 19.

[41] N. Aghanim, Y. Akrami, M. Ashdown, J. Aumont, C. Baccigalupi, M. Ballardini et al., *Planck 2018 results-vi. cosmological parameters*, *Astronomy & Astrophysics* **641** (2020) A6.

[42] K. N. Abazajian, P. Adshead, Z. Ahmed, S. W. Allen, D. Alonso, K. S. Arnold et al., *Cmb-s4 science book*, *arXiv preprint arXiv:1610.02743* (2016) .

[43] F. Bernardeau, S. Colombi, E. Gaztanaga and R. Scoccimarro, *Large-scale structure of the Universe and cosmological perturbation theory.*, *Phys. Rep.* **367** (2002) 1.

[44] M. M. Ivanov, M. Simonović and M. Zaldarriaga, *Cosmological Parameters from the BOSS Galaxy Power Spectrum*, *arXiv e-prints* (2019) arXiv:1909.05277 [1909.05277].

[45] G. D'Amico, J. Gleyzes, N. Kokron, D. Markovic, L. Senatore, P. Zhang et al., *The Cosmological Analysis of the SDSS/BOSS data from the Effective Field Theory of Large-Scale Structure*, *arXiv e-prints* (2019) arXiv:1909.05271 [1909.05271].

[46] T. Sousbie and S. Colombi, *ColDICE: A parallel Vlasov-Poisson solver using moving adaptive simplicial tessellation*, *Journal of Computational Physics* **321** (2016) 644 [1509.07720].

[47] S. Colombi, F. R. Bouchet and L. Hernquist, *Self-Similarity and Scaling Behavior of Scale-free Gravitational Clustering*, *ApJ* **465** (1996) 14.

[48] N. Makino, M. Sasaki and Y. Suto, *Analytic approach to the perturbative expansion of nonlinear gravitational fluctuations in cosmological density and velocity fields*, *Phys. Rev. D* **46** (1992) 585.

[49] R. Scoccimarro and J. A. Frieman, *Loop Corrections in Nonlinear Cosmological Perturbation Theory. II. Two-Point Statistics and Self-Similarity*, *ApJ* **473** (1996) 620 [arXiv:astro-ph/9602070].

[50] T. Nishimichi, F. Bernardeau and A. Taruya, *Response function of the large-scale structure of the universe to the small scale inhomogeneities*, *Physics Letters B* **762** (2016) 247 [1411.2970].

[51] T. Nishimichi, F. Bernardeau and A. Taruya, *Moving around the cosmological parameter space: A nonlinear power spectrum reconstruction based on high-resolution cosmic responses*, *Phys. Rev. D* **96** (2017) 123515 [1708.08946].

[52] R. Scoccimarro, *Redshift-space distortions, pairwise velocities, and nonlinearities*, *Physical Review D* **70** (2004) 083007.

[53] S. Pueblas and R. Scoccimarro, *Generation of vorticity and velocity dispersion by orbit crossing*, *Physical Review D* **80** (2009) 043504.

[54] J. J. M. Carrasco, M. P. Hertzberg and L. Senatore, *The effective field theory of cosmological large scale structures*, *Journal of High Energy Physics* **2012** (2012) 82.

[55] D. Baumann, A. Nicolis, L. Senatore and M. Zaldarriaga, *Cosmological non-linearities as an effective fluid*, *Journal of Cosmology and Astro-Particle Physics* **2012** (2012) 051.

[56] M. Davis and P. J. E. Peebles, *On the integration of the BBGKY equations for the development of strongly nonlinear clustering in an expanding universe*, *ApJS* **34** (1977) 425.

[57] P. J. E. Peebles, *The Gravitational-Instability Picture and the Nature of the Distribution of Galaxies*, *ApJ* **189** (1974) L51.

[58] P. J. E. Peebles, *The large-scale structure of the universe*. Princeton university press, 1980.

[59] P. McDonald, *How to generate a significant effective temperature for cold dark matter, from first principles*, *J. Cosmology Astropart. Phys.* **2011** (2011) 032 [0910.1002].

[60] A. Erschfeld and S. Floerchinger, *Evolution of dark matter velocity dispersion*, *J. Cosmology Astropart. Phys.* **2019** (2019) 039 [1812.06891].

[61] A. A. Erschfeld, *Functional methods for cosmic structure formation.*, Ph.D. thesis, U. Heidelberg (main), 2021. 10.11588/heidok.00030982.

[62] T. Buchert and A. Domínguez, *Modeling multi-stream flow in collisionless matter: approximations for large-scale structure beyond shell-crossing*, *A&A* **335** (1998) 395 [astro-ph/9702139].

[63] S. Adler and T. Buchert, *Lagrangian theory of structure formation in pressure-supported cosmological fluids*, *A&A* **343** (1999) 317 [astro-ph/9806320].

[64] T. Tatekawa, M. Suda, K.-I. Maeda, M. Morita and H. Anzai, *Perturbation theory in Lagrangian hydrodynamics for a cosmological fluid with velocity dispersion*, *Phys. Rev. D* **66** (2002) 064014 [astro-ph/0205017].

[65] M. Morita and T. Tatekawa, *Extending Lagrangian perturbation theory to a fluid with velocity dispersion*, *MNRAS* **328** (2001) 815 [astro-ph/0108289].

[66] S. Colombi, *Vlasov-Poisson in 1D for initially cold systems: post-collapse Lagrangian perturbation theory*, *MNRAS* **446** (2015) 2902 [1411.4165].

[67] A. Aviles, *Dark matter dispersion tensor in perturbation theory*, *Phys. Rev. D* **93** (2016) 063517 [1512.07198].

[68] G. Cusin, V. Tansella and R. Durrer, *Vorticity generation in the Universe: A perturbative approach*, *Phys. Rev. D* **95** (2017) 063527 [1612.00783].

[69] A. Taruya and S. Colombi, *Post-collapse perturbation theory in 1D cosmology - beyond shell-crossing*, *MNRAS* **470** (2017) 4858 [1701.09088].

[70] C. Rampf and U. Frisch, *Shell-crossing in quasi-one-dimensional flow*, *MNRAS* **471** (2017) 671 [1705.08456].

[71] P. McDonald and Z. Vlah, *Large-scale structure perturbation theory without losing stream crossing*, *Phys. Rev. D* **97** (2018) 023508 [1709.02834].

[72] S. Saga, A. Taruya and S. Colombi, *Lagrangian Cosmological Perturbation Theory at Shell Crossing*, *Phys. Rev. Lett.* **121** (2018) 241302 [1805.08787].

[73] A. Halle, T. Nishimichi, A. Taruya, S. Colombi and F. Bernardeau, *Power spectrum response of large-scale structure in 1D and in 3D: tests of prescriptions for post-collapse dynamics*, *MNRAS* **499** (2020) 1769 [2001.10417].

[74] C. Rampf and O. Hahn, *Shell-crossing in a ΛCDM Universe*, *MNRAS* **501** (2021) L71 [2010.12584].

[75] P. Valageas, *Impact of shell crossing and scope of perturbative approaches, in real space and redshift space*, *ArXiv e-prints* (2010) [1009.0106].

[76] P. Valageas and T. Nishimichi, *Combining perturbation theories with halo models*, *A&A* **527** (2011) A87 [1009.0597].

[77] P. Valageas and T. Nishimichi, *Combining perturbation theories with halo models for the matter bispectrum*, *A&A* **532** (2011) A4 [1102.0641].

[78] P. Valageas, T. Nishimichi and A. Taruya, *Matter power spectrum from a Lagrangian-space regularization of perturbation theory*, *Phys. Rev. D* **87** (2013) 083522 [1302.4533].

[79] U. Seljak and Z. Vlah, *Halo Zel'dovich model and perturbation theory: Dark matter power spectrum and correlation function*, *Phys. Rev. D* **91** (2015) 123516 [1501.07512].

[80] T. Abel, O. Hahn and R. Kaehler, *Tracing the dark matter sheet in phase space*, *MNRAS* **427** (2012) 61 [1111.3944].

[81] O. Hahn, T. Abel and R. Kaehler, *A new approach to simulating collisionless dark matter fluids*, *MNRAS* **434** (2013) 1171 [1210.6652].

[82] S. Colombi and J. Touma, *Vlasov-Poisson in 1D: waterbags*, *MNRAS* **441** (2014) 2414.

[83] O. Hahn and R. E. Angulo, *An adaptively refined phase-space element method for cosmological simulations and collisionless dynamics*, *MNRAS* **455** (2016) 1115 [1501.01959].

[84] J. Stucker, O. Hahn, R. E. Angulo and S. D. M. White, *Simulating the Complexity of the Dark Matter Sheet I: Numerical Algorithms*, *Mon. Not. Roy. Astron. Soc.* **495** (2020) 4943 [1909.00008].

[85] S. Colombi, *Phase-space structure of protohalos: Vlasov versus particle-mesh*, *A&A* **647** (2021) A66 [2012.04409].

[86] S. Saga, A. Taruya and S. Colombi, *Cold dark matter protohalo structure around collapse: Lagrangian cosmological perturbation theory versus Vlasov simulations*, *A&A* **664** (2022) A3 [2111.08836].

[87] R. E. Angulo and O. Hahn, *Large-scale dark matter simulations*, *Living Reviews in Computational Astrophysics* **8** (2022) 1 [2112.05165].

[88] L. M. Widrow and N. Kaiser, *Using the Schroedinger Equation to Simulate Collisionless Matter*, *ApJ* **416** (1993) L71+.

[89] H.-Y. Schive, T. Chiueh and T. Broadhurst, *Cosmic Structure as the Quantum Interference of a Coherent Dark Wave*, *Nature Phys.* **10** (2014) 496 [1406.6586].

[90] M. Kopp, K. Vattis and C. Skordis, *Solving the Vlasov equation in two spatial dimensions with the Schrödinger method*, *Phys. Rev. D* **96** (2017) 123532 [1711.00140].

[91] M. Garny and T. Konstandin, *Gravitational collapse in the Schrödinger-Poisson system*, *J. Cosmology Astropart. Phys.* **2018** (2018) 009 [1710.04846].

[92] C. Uhlemann, *Finding closure: approximating Vlasov-Poisson using finitely generated cumulants*, *J. Cosmology Astropart. Phys.* **2018** (2018) 030 [1807.07274].

[93] P. Mocz, L. Lancaster, A. Fialkov, F. Becerra and P.-H. Chavanis, *Schrödinger-Poisson–Vlasov-Poisson correspondence*, *Phys. Rev. D* **97** (2018) 083519 [1801.03507].

[94] X. Li, L. Hui and G. L. Bryan, *Numerical and Perturbative Computations of the Fuzzy Dark Matter Model*, *Phys. Rev. D* **99** (2019) 063509 [1810.01915].

[95] C. Uhlemann, C. Rampf, M. Gosenca and O. Hahn, *Semiclassical path to cosmic large-scale structure*, *Phys. Rev. D* **99** (2019) 083524 [1812.05633].

[96] M. Garny, T. Konstandin and H. Rubira, *The Schrödinger-Poisson method for Large-Scale Structure*, *JCAP* **04** (2020) 003 [1911.04505].

[97] S. May and V. Springel, *Structure formation in large-volume cosmological simulations of fuzzy dark matter: impact of the non-linear dynamics*, *Mon. Not. Roy. Astron. Soc.* **506** (2021) 2603 [2101.01828].

[98] M. Garny, D. Laxhuber and R. Scoccimarro, *Perturbation theory with dispersion and higher cumulants: Framework and linear theory*, *Phys. Rev. D* **107** (2023) 063539 [2210.08088].

[99] M. Garny, D. Laxhuber and R. Scoccimarro, *Perturbation theory with dispersion and higher cumulants: Nonlinear regime*, *Phys. Rev. D* **107** (2023) 063540 [2210.08089].

[100] P. Peebles, *Aa penzias and rw wilson: A measurement of excess antenna temperature at 4080 mc/s (apj, 142, 419 [1965])*, *ASTROPHYSICAL JOURNAL* **525** (1999) 1065.

[101] R. A. Alpher, H. Bethe and G. Gamow, *The origin of chemical elements*, *Physical Review* **73** (1948) 803.

[102] D. S. Gorbunov and V. A. Rubakov, *Introduction to the theory of the early universe: Cosmological perturbations and inflationary theory*. World Scientific, 2011.

[103] L. Amendola and S. Tsujikawa, *Dark energy: theory and observations*. Cambridge University Press, 2010.

[104] A. Friedmann, *On the possibility of a world with constant negative curvature of space*, *General Relativity and Gravitation* **31** (1999) 2001.

[105] H. P. Robertson, *Kinematics and world-structure*, *Astrophysical Journal, vol. 82, p. 284* **82** (1935) 284.

[106] A. G. Walker, *On milne's theory of world-structure*, *Proceedings of the London Mathematical Society* **2** (1937) 90.

[107] G. Lemaitre, *A homogeneous universe of constant mass and increasing radius accounting for the radial velocity of extra-galactic nebulae*, in *A Source Book in Astronomy and Astrophysics, 1900–1975*, pp. 844–848, Harvard University Press, (1979).

[108] E. Abdalla et al., *Cosmology intertwined: A review of the particle physics, astrophysics, and cosmology associated with the cosmological tensions and anomalies*, *JHEAp* **34** (2022) 49 [2203.06142].

[109] L. Bergström, *Non-baryonic dark matter: observational evidence and detection methods*, *Reports on Progress in Physics* **63** (2000) 793.

[110] G. Bertone, D. Hooper and J. Silk, *Particle dark matter: Evidence, candidates and constraints*, *Physics reports* **405** (2005) 279.

[111] J. L. Feng, *Dark matter candidates from particle physics and methods of detection*, *Annual Review of Astronomy and Astrophysics* **48** (2010) 495.

[112] A. A. Penzias and R. W. Wilson, *A measurement of excess antenna temperature at 4080 mhz*, in *A Source Book in Astronomy and Astrophysics, 1900–1975*, pp. 873–876, Harvard University Press, (1979).

[113] D. Fixsen, *The temperature of the cosmic microwave background*, *The Astrophysical Journal* **707** (2009) 916.

[114] P. J. E. Peebles and B. Ratra, *The cosmological constant and dark energy*, *Reviews of modern physics* **75** (2003) 559.

[115] S. Nojiri and S. D. Odintsov, *Introduction to modified gravity and gravitational alternative for dark energy*, *International Journal of Geometric Methods in Modern Physics* **4** (2007) 115.

[116] T. Clifton, P. G. Ferreira, A. Padilla and C. Skordis, *Modified gravity and cosmology*, *Physics reports* **513** (2012) 1.

[117] A. Joyce, L. Lombriser and F. Schmidt, *Dark energy versus modified gravity*, *Annual Review of Nuclear and Particle Science* **66** (2016) 95.

[118] S. Weinberg, *The cosmological constant problem*, *Reviews of modern physics* **61** (1989) 1.

[119] R. Barkana and A. Loeb, *In the beginning: the first sources of light and the reionization of the universe*, *Physics reports* **349** (2001) 125.

[120] A. Starobinskii, *Spectrum of relict gravitational radiation and the early state of the universe*, *JETP Letters* **30** (1979) 682.

[121] V. F. Mukhanov and G. Chibisov, *Quantum fluctuations and a nonsingular universe*, *ZhETF Pisma Redaktsiiu* **33** (1981) 549.

[122] A. H. Guth, *Inflationary universe: A possible solution to the horizon and flatness problems*, *Physical Review D* **23** (1981) 347.

[123] A. D. Linde, *A new inflationary universe scenario: a possible solution of the horizon, flatness, homogeneity, isotropy and primordial monopole problems*, *Physics Letters B* **108** (1982) 389.

[124] V. F. Mukhanov, H. A. Feldman and R. H. Brandenberger, *Theory of cosmological perturbations*, *Physics Reports* **215** (1992) 203.

[125] V. Desjacques, D. Jeong and F. Schmidt, *Large-scale galaxy bias*, *Phys. Rep.* **733** (2018) 1.

[126] D. Baumann, *Tasi lectures on inflation*, *arXiv preprint arXiv:0907.5424* (2009) .

[127] Y. Akrami, F. Arroja, M. Ashdown, J. Aumont, C. Baccigalupi, M. Ballardini et al., *Planck 2018 results-x. constraints on inflation*, *Astronomy & Astrophysics* **641** (2020) A10.

[128] S. Das, T. Louis, M. R. Nolta, G. E. Addison, E. S. Battistelli, J. R. Bond et al., *The atacama cosmology telescope: temperature and gravitational lensing power spectrum measurements from three seasons of data*, *Journal of Cosmology and Astroparticle Physics* **2014** (2014) 014.

[129] J. Dunkley, E. Calabrese, J. Sievers, G. Addison, N. Battaglia, E. Battistelli et al., *The atacama cosmology telescope: likelihood for small-scale cmb data*, *Journal of Cosmology and Astroparticle Physics* **2013** (2013) 025.

[130] J. L. Sievers, R. A. Hlozek, M. R. Nolta, V. Acquaviva, G. E. Addison, P. A. Ade et al., *The atacama cosmology telescope: Cosmological parameters from three seasons of data*, *Journal of Cosmology and Astroparticle Physics* **2013** (2013) 060.

[131] Z. Hou, C. Reichardt, K. Story, B. Follin, R. Keisler, K. Aird et al., *Constraints on cosmology from the cosmic microwave background power spectrum of the 2500${\rm deg}^ 2$ spt-sz survey*, *arXiv preprint arXiv:1212.6267* (2012) .

[132] K. Story, C. Reichardt, Z. Hou, R. Keisler, K. Aird, B. Benson et al., *A measurement of the cosmic microwave background damping tail from the 2500-square-degree spt-sz survey*, *The Astrophysical Journal* **779** (2013) 86.

[133] Particle Data Group collaboration, *Review of Particle Physics*, *PTEP* **2022** (2022) 083C01.

[134] P. Ade, J. Aguirre, Z. Ahmed, S. Aiola, A. Ali, D. Alonso et al., *The simons observatory: science goals and forecasts*, *Journal of Cosmology and Astroparticle Physics* **2019** (2019) 056.

[135] *LiteBIRD satellite: JAXA's new strategic L-class mission for all-sky surveys of cosmic microwave background polarization*, vol. 11443, SPIE, 2020.

[136] J. Delabrouille, P. De Bernardis, F. Bouchet, A. Achúcarro, P. Ade, R. Allison et al., *Exploring cosmic origins with core: Survey requirements and mission design*, *Journal of Cosmology and Astroparticle Physics* **2018** (2018) 014.

[137] *PICO-the probe of inflation and cosmic origins*, vol. 10698, SPIE, 2018.

[138] F. Bernardeau, S. Colombi, E. Gaztanaga and R. Scoccimarro, *Large-scale structure of the universe and cosmological perturbation theory*, *Physics reports* **367** (2002) 1.

[139] L. Landau and E. Lifshitz, *Fluid Mechanics: Volume 6*, vol. 6. Elsevier, 1987.

[140] V. Silveira and I. Waga, *Decaying Lambda cosmologies and power spectrum*, *Phys. Rev. D* **50** (1994) 4890.

[141] M. Goroff, B. Grinstein, S.-J. Rey and M. B. Wise, *Coupling of modes of cosmological mass density fluctuations*, *The Astrophysical Journal* **311** (1986) 6.

[142] B. Jain and E. Bertschinger, *Second order power spectrum and nonlinear evolution at high redshift*, *arXiv preprint astro-ph/9311070* (1993) .

[143] R. Scoccimarro, *A New Angle on Gravitational Clustering*, *ArXiv:astro-ph/0008277, Annals New York Academy Sciences* **927** (2001) 13.

[144] R. Scoccimarro, *A New Angle on Gravitational Clustering*, in *The Onset of Nonlinearity in Cosmology*, J. N. Fry, J. R. Buchler and H. Kandrup, eds., vol. 927, pp. 13–23, Jan., 2001, DOI [astro-ph/0008277].

[145] T. Evans and D. Steer, *Wick's theorem at finite temperature*, *Nuclear Physics B* **474** (1996) 481.

[146] M. Crocce and R. Scoccimarro, *Renormalized cosmological perturbation theory*, *Physical Review D* **73** (2006) 063519.

[147] B. Jain and E. Bertschinger, *Second order power spectrum and nonlinear evolution at high redshift*, *arXiv preprint astro-ph/9311070* (1993) .

[148] D. Blas, J. Lesgourgues and T. Tram, *The Cosmic Linear Anisotropy Solving System (CLASS) II: Approximation schemes*, *JCAP* **07** (2011) 034 [1104.2933].

[149] A. Lewis, A. Challinor and A. Lasenby, *Efficient computation of CMB anisotropies in closed FRW models*, *Astrophys. J.* **538** (2000) 473 [astro-ph/9911177].

[150] D. Blas, M. Garny and T. Konstandin, *On the non-linear scale of cosmological perturbation theory*, *JCAP* **09** (2013) 024 [1304.1546].

[151] M. Crocce and R. Scoccimarro, *Memory of initial conditions in gravitational clustering*, *Physical Review D* **73** (2006) 063520.

[152] D. Blas, M. Garny and T. Konstandin, *On the non-linear scale of cosmological perturbation theory*, *Journal of Cosmology and Astroparticle Physics* **2013** (2013) 024.

[153] A. Erschfeld and S. Floerchinger, *Evolution of dark matter velocity dispersion*, *Journal of Cosmology and Astroparticle Physics* **2019** (2019) 039.

[154] C. Uhlemann, *Finding closure: approximating vlasov-poisson using finitely generated cumulants*, *Journal of Cosmology and Astroparticle Physics* **2018** (2018) 030.

[155] A. Dominguez, *Hydrodynamic approach to the evolution of cosmological structures*, *Physical Review D* **62** (2000) 103501.

[156] M. C. Neyrinck, I. Szapudi and A. S. Szalay, *Rejuvenating the Matter Power Spectrum: Restoring Information with a Logarithmic Density Mapping*, *ApJ* **698** (2009) L90 [0903.4693].

[157] X. Wang, M. Neyrinck, I. Szapudi, A. Szalay, X. Chen, J. Lesgourgues et al., *Perturbation Theory of the Cosmological Log-Density Field*, *Astrophys. J.* **735** (2011) 32 [1103.2166].

[158] J. Carron and I. Szapudi, *Optimal non-linear transformations for large-scale structure statistics*, *MNRAS* **434** (2013) 2961 [1306.1230].

[159] H. Rubira and R. Voivodic, *The Effective Field Theory and Perturbative Analysis for Log-Density Fields*, *JCAP* **03** (2021) 070 [2011.12280].

[160] J. Binney and S. Tremaine, *Galactic Dynamics: Second Edition*. 2008.

[161] D. Blas, S. Floerchinger, M. Garny, N. Tetradis and U. A. Wiedemann, *Large scale structure from viscous dark matter*, *JCAP* **11** (2015) 049 [1507.06665].

[162] M. Garny and P. Taule, *Loop corrections to the power spectrum for massive neutrino cosmologies with full time- and scale-dependence*, *JCAP* **01** (2021) 020 [2008.00013].

[163] D. Blas, M. Garny and T. Konstandin, *Cosmological perturbation theory at three-loop order*, *ArXiv e-prints* (2013) [1309.3308].

[164] A. A. Abolhasani, M. Mirbabayi and E. Pajer, *Systematic Renormalization of the Effective Theory of Large Scale Structure*, *JCAP* **05** (2016) 063 [1509.07886].

[165] P. Peebles, *The large-scale structure of the universe*. Princeton University Press, 1980.

[166] S. Pueblas and R. Scoccimarro, *Generation of vorticity and velocity dispersion by orbit crossing*, *Phys. Rev. D* **80** (2009) 043504 [0809.4606].

[167] R. Scoccimarro, *Transients from initial conditions: a perturbative analysis*, *MNRAS* **299** (1998) 1097 [astro-ph/9711187].

[168] A. Eggemeier, R. Scoccimarro and R. E. Smith, *Bias Loop Corrections to the Galaxy Bispectrum*, *Phys. Rev. D* **99** (2019) 123514 [1812.03208].

[169] T. Baldauf, L. Mercolli, M. Mirbabayi and E. Pajer, *The bispectrum in the Effective Field Theory of Large Scale Structure*, *Journal of Cosmology and Astro-Particle Physics* **2015** (2015) 007 [1406.4135].

[170] R. E. Angulo, S. Foreman, M. Schmittfull and L. Senatore, *The one-loop matter bispectrum in the Effective Field Theory of Large Scale Structures*, *Journal of Cosmology and Astro-Particle Physics* **2015** (2015) 039 [1406.4143].

[171] Y. B. Zeldovich, *Survey of Modern Cosmology*, *Advances in Astronomy and Astrophysics* **3** (1965) 241.

[172] M. Goroff, B. Grinstein, S.-J. Rey and M. Wise, *Coupling of modes of cosmological mass density fluctuations*, *ApJ* **311** (1986) 6.

[173] R. Scoccimarro and J. Frieman, *Loop Corrections in Nonlinear Cosmological Perturbation Theory*, *ApJS* **105** (1996) 37 [arXiv:astro-ph/9509047].

[174] A. Kehagias and A. Riotto, *Symmetries and Consistency Relations in the Large Scale Structure of the Universe*, *Nucl. Phys. B* **873** (2013) 514 [1302.0130].

[175] M. Peloso and M. Pietroni, *Galilean invariance and the consistency relation for the nonlinear squeezed bispectrum of large scale structure*, *JCAP* **05** (2013) 031 [1302.0223].

[176] M. Crocce and R. Scoccimarro, *Memory of initial conditions in gravitational clustering*, *Phys. Rev. D* **73** (2006) 063520 [arXiv:astro-ph/0509419].

[177] N. S. Sugiyama and T. Futamase, *Relation between standard perturbation theory and regularized multi-point propagator method*, *Astrophys. J.* **769** (2013) 106 [1303.2748].

[178] B. Jain and E. Bertschinger, *Self-similar Evolution of Gravitational Clustering: Is N = -1 Special?*, *ApJ* **456** (1996) 43 [astro-ph/9503025].

[179] C.-P. Ma and E. Bertschinger, *Cosmological Perturbation Theory in the Synchronous and Conformal Newtonian Gauges*, *ApJ* **455** (1995) 7 [astro-ph/9506072].

[180] S. Floerchinger, M. Garny, A. Katsis, N. Tetradis and U. A. Wiedemann, *The dark matter bispectrum from effective viscosity and one-particle irreducible vertices*, *JCAP* **09** (2019) 047 [1907.10729].

[181] O. Hahn, R. E. Angulo and T. Abel, *The properties of cosmic velocity fields*, *MNRAS* **454** (2015) 3920 [1404.2280].

[182] G. Jelic-Cizmek, F. Lepori, J. Adamek and R. Durrer, *The generation of vorticity in cosmological N-body simulations*, *J. Cosmology Astropart. Phys.* **2018** (2018) 006 [1806.05146].

[183] J. J. M. Carrasco, S. Foreman, D. Green and L. Senatore, *The Effective Field Theory of Large Scale Structures at two loops*, *J. Cosmology Astropart. Phys.* **2014** (2014) 057 [1310.0464].

[184] L. Mercolli and E. Pajer, *On the velocity in the Effective Field Theory of Large Scale Structures*, *J. Cosmology Astropart. Phys.* **2014** (2014) 006 [1307.3220].

[185] S. Floerchinger, N. Tetradis and U. A. Wiedemann, *Backreaction from inhomogeneous matter fields during large-scale structure formation*, *Physical Review D* **104** (2021) 083522.

[186] R. Scoccimarro, "Scalar-Vector-Tensor decomposition of FLRW perturbations." unpublished.

[187] Y. Watanabe and E. Komatsu, *Improved calculation of the primordial gravitational wave spectrum in the standard model*, *Physical Review D* **73** (2006) 123515.

[188] C. W. Misner, K. S. Thorne and J. A. Wheeler, *Gravitation*. Macmillan, 1973.

[189] J. Aasi, B. Abbott, R. Abbott, T. Abbott, M. Abernathy, K. Ackley et al., *Advanced ligo*, *Classical and quantum gravity* **32** (2015) 074001.

[190] F. a. Acernese, M. Agathos, K. Agatsuma, D. Aisa, N. Allemandou, A. Allocca et al., *Advanced virgo: a second-generation interferometric gravitational wave detector*, *Classical and Quantum Gravity* **32** (2014) 024001.

[191] B. Sathyaprakash, M. Abernathy, F. Acernese, P. Ajith, B. Allen, P. Amaro-Seoane et al., *Scientific objectives of einstein telescope*, *Classical and Quantum Gravity* **29** (2012) 124013.

[192] J. Crowder and N. J. Cornish, *Beyond lisa: Exploring future gravitational wave missions*, *Physical Review D* **72** (2005) 083005.

[193] G. M. Harry, P. Fritschel, D. A. Shaddock, W. Folkner and E. S. Phinney, *Laser interferometry for the big bang observer*, *Classical and Quantum Gravity* **23** (2006) 4887.

[194] M. Tristram, A. J. Banday, K. M. Górski, R. Keskitalo, C. Lawrence, K. J. Andersen et al., *Improved limits on the tensor-to-scalar ratio using bicep and p l a n c k data*, *Physical Review D* **105** (2022) 083524.

[195] S. Saga, K. Ichiki and N. Sugiyama, *Impact of anisotropic stress of free-streaming particles on gravitational waves induced by cosmological density perturbations*, *Physical Review D* **91** (2015) 024030.

[196] G. M. Harry and forthe LIGO Scientific Collaboration, *Advanced ligo: the next generation of gravitational wave detectors*, *Classical and Quantum Gravity* **27** (2010) 084006.

[197] *The advanced Virgo detector*, vol. 610, IOP Publishing, 2015.

[198] H. Grote and forthe LIGO Scientific Collaboration, *The geo 600 status*, *Classical and Quantum Gravity* **27** (2010) 084003.

[199] M. Ando and T. collaboration, *Current status of the tama300 gravitational-wave detector*, *Classical and Quantum Gravity* **22** (2005) S881.

[200] *Kagra: 2.5 generation interferometric gravitational wave detector*, *Nature Astronomy* **3** (2019) 35.

[201] S. Kawamura, T. Nakamura, M. Ando, N. Seto, K. Tsubono, K. Numata et al., *The japanese space gravitational wave antenna—decigo*, *Classical and Quantum Gravity* **23** (2006) S125.

[202] N. Seto, S. Kawamura and T. Nakamura, *Possibility of direct measurement of the acceleration of the universe using 0.1 hz band laser interferometer gravitational wave antenna in space*, *Physical Review Letters* **87** (2001) 221103.

[203] C. Cutler and D. E. Holz, *Ultrahigh precision cosmology from gravitational waves*, *Physical Review D* **80** (2009) 104009.

[204] H. Kudoh, A. Taruya, T. Hiramatsu and Y. Himemoto, *Detecting a gravitational-wave background with next-generation space interferometers*, *Physical Review D* **73** (2006) 064006.

[205] S. Dimopoulos, P. W. Graham, J. M. Hogan, M. A. Kasevich and S. Rajendran, *Atomic gravitational wave interferometric sensor*, *Physical Review D* **78** (2008) 122002.

[206] J. M. Hogan, D. M. Johnson, S. Dickerson, T. Kovachy, A. Sugarbaker, S.-w. Chiow et al., *An atomic gravitational wave interferometric sensor in low earth orbit (agis-leo)*, *General Relativity and Gravitation* **43** (2011) 1953.

[207] M. Sazhin, *The registration of gravitational waves by concentrated electromagnetic systems*, *Moskovskii Universitet Vestnik Seriia Fizika Astronomiia* **18** (1977) 82.

[208] S. Detweiler, *Pulsar timing measurements and the search for gravitational waves*, *Astrophysical Journal, Part 1, vol. 234, Dec. 15, 1979, p. 1100-1104.* **234** (1979) 1100.

[209] R. Manchester, G. Hobbs, M. Bailes, W. Coles, W. Van Straten, M. Keith et al., *The parkes pulsar timing array project*, *Publications of the Astronomical Society of Australia* **30** (2013) e017.

[210] R. D. Ferdman, R. van Haasteren, C. G. Bassa, M. Burgay, I. Cognard, A. Corongiu et al., *The european pulsar timing array: current efforts and a leap toward the future*, *Classical and Quantum Gravity* **27** (2010) 084014.

[211] F. Jenet, L. Finn, J. Lazio, A. Lommen, M. McLaughlin, I. Stairs et al., *The north american nanohertz observatory for gravitational waves*, *arXiv preprint arXiv:0909.1058* (2009) .

[212] G. Hobbs, A. Archibald, Z. Arzoumanian, D. Backer, M. Bailes, N. Bhat et al., *The international pulsar timing array project: using pulsars as a gravitational wave detector*, *Classical and Quantum Gravity* **27** (2010) 084013.

[213] C. J. Moore, R. H. Cole and C. P. Berry, *Gravitational-wave sensitivity curves*, *Classical and Quantum Gravity* **32** (2014) 015014.

[214] B. Goncharov, R. M. Shannon, D. J. Reardon, G. Hobbs, A. Zic, M. Bailes et al., *On the evidence for a common-spectrum process in the search for the nanohertz gravitational-wave background with the parkes pulsar timing array*, *The Astrophysical Journal Letters* **917** (2021) L19.

[215] S. Chen, R. Caballero, Y. Guo, A. Chalumeau, K. Liu, G. Shaifullah et al., *Common-red-signal analysis with 24-yr high-precision timing of the european pulsar timing array: inferences in the stochastic gravitational-wave background search*, *Monthly Notices of the Royal Astronomical Society* **508** (2021) 4970.

[216] J. Antoniadis, Z. Arzoumanian, S. Babak, M. Bailes, A. Bak Nielsen, P. Baker et al., *The international pulsar timing array second data release: Search for an isotropic gravitational wave background*, *Monthly Notices of the Royal Astronomical Society* **510** (2022) 4873.